ISSN 2542-1565

Vol. 15 2022 No. 03

GEOGRAPHY ENVIRONMENT SUSTAINABILITY

«The journal GEOGRAPHY, ENVIRONMENT, SUSTAINABILITY was founded in 2008 by Russian Geographical Society, the Lomonosov Moscow State University Geography Department, and the Russian Academy of Sciences Institute of Geography. Since that time the journal publishes **4 issues per year**, containing original research papers and reviews. The journal issues are open source and distributed through subscriptions, library exchanges of leading universities, and via the website through the world»

FOUNDERS OF THE JOURNAL: Russian Geographical Society, Faculty of Geography, Lomonosov Moscow State University and Institute of Geography of the Russian Academy of Sciences

The journal is published with financial support of the Russian Geographical Society.

The journal is registered in Federal service on supervision of observance of the legislation in sphere of mass communications and protection of a cultural heritage. The certificate of registration: ПИ № ФС77-67752, 2016, December 21.

PUBLISHER
Russian Geographical Society
Moscow, 109012 Russia
Novaya ploshchad, 10, korp. 2
Phone 8-800-700-18-45
E-mail: press@rgo.ru
www.rgo.ru/en

EDITORIAL OFFICE
Lomonosov Moscow State University
Moscow 119991 Russia
Leninskie Gory, 1,
Faculty of Geography, 1806a
Phone 7-495-9391552
Fax 7-495-9391552
E-mail: ges-journal@geogr.msu.ru
www.ges.rgo.ru

DESIGN
Layout designer: Tereshkin Anton
Moscow, 115088,
26 Simonovsky Val str., bldg. One
Phone: +7 (903) 108-04-44
E-mail: smile.tai@gmail.com

DOI prefix: 10.24057

Format A4 (210x297mm)

"GEOGRAPHY, ENVIRONMENT, SUSTAINABILITY" is the only original English-language journal in the field of geography and environmental sciences published in Russia. It is supposed to be an outlet from the Russian-speaking countries to Europe and an inlet from Europe to the Russian-speaking countries regarding environmental and Earth sciences, geography and sustainability. The main sections of the journal are the theory of geography and ecology, the theory of sustainable development, use of natural resources, natural resources assessment, global and regional changes of environment and climate, social-economical geography, ecological regional planning, sustainable regional development, applied aspects of geography and ecology, geoinformatics and ecological cartography, ecological problems of oil and gas sector, nature conservations, health and environment, and education for sustainable development.

Date of publication: October 1st, 2022.

CONTENTS

RESEARCH PAPER

RADON FLUX DENSITY IN CONDITIONS OF PERMAFROST THAWING: SIMULATION EXPERIMENT

Andrey V. Puchkov[1*], Elena V. Berezina[2], Evgeny Yu. Yakovlev[1], Nicholas R. Hasson[3], Sergey V. Druzhinin[1], Alexey S. Tyshov[1], Ekaterina V. Ushakova[4], Lev S. Koshelev[1], Pavel I. Lapikov[1]
[1]N. Laverov Federal Centre for Integrated Arctic Research of the Ural Branch of Russian Academy of Sciences, 109 Severnoj Dviny Emb., Arkhangelsk, 163000, Russia.
[2]A.M. Obukhov Institute of Atmospheric Physics, Russian Academy of Sciences, 119017 Moscow, Russia
[3]Water and Environmental Research Center, University of Alaska Fairbanks, 1764 Tanana Loop, Fairbanks, AK 99775, USA
[4]Yuri Gagarin State Technical University of Saratov, 77 Politechnicheskaya street, Saratov, 410054, Russia.
*Corresponding author: andrey.puchkov@fciarctic.ru
Received: March 6th, 2022 / Accepted: August 8th, 2022 / Published: October 1st, 2022
https://DOI-10.24057/2071-9388-2022-023

ABSTRACT. This paper describes a five-month experiment (February – July 2021) measuring the gradual thaw diffusion of radon-222 (further in the article – radon) from a frozen environment in NW Russia (i.e. Arhangelsk region). Red clay substrate containting a high content of ^{226}Ra filled the bottom insides of 200-liter barrel holding the source of radon and buried at 1.6 m depth (e.g., the radium source zone), then covered with native soil, filled with water and frozen under in-situ conditions. Radon measurements were carried out from soil surface above the container (disturbed soil layer) and at background location (undisturbed soil layer). Several periods of increased radon flux density were observed, which was related to radium source zone thawing. It was shown that in 1-2 days after thawing of the radium source zone and drying of the upper soil layer, the radon flux increases sharply – more than 8 times compared to background values. These results show a strong relationship between radon flux density and soil temperature profiles at different depths. The calculations of radon sourced from frozen and thawed zones show how temperature phase of substrate (e.g. clays) control the barrier influence of radon migration. It reduced them by 10-20 times (according to the results of a theoretical calculation), depending on the characteristics of frozen rocks (density, porosity). Thus, the barrier function of permafrost is related to the physical properties of ice and frozen rocks. These temperture phases controls radon emanation coefficients and significantly influences the migration of radon to the earth's surface.

KEYWORDS: Radon hazard, permafrost, Arctic, climate warming, natural radioactivity, frozen soil

CITATION: Puchkov A. V., Berezina E. V., Yakovlev E. Yu., Hasson N. R., Druzhinin S. V., Tyshov A. S., Ushakova E. V., Koshelev L. S., Lapikov P. I. (2022). Radon Flux Density In Conditions Of Permafrost Thawing: Simulation Experiment. Geography, Environment, Sustainability, 3(15), 5-18
https://DOI-10.24057/2071-9388-2022-023

ACKNOWLEDGEMENTS: This work was supported by the grant of the Russian Science Foundation No 20-77-10057, the grant of the Project Office For Arctic Development No. 245G dated 04/19/2021 and the grant of the Ministry of Science and Higher Education of Russia No 075-15-2021-934.

Conflict of interests: The authors reported no potential conflict of interest.

INTRODUCTION

Over the past few years, the problem of climate change has grown to the most pressing issue in the world. As the arctic regions warm twice the global rate, changes in the relief, vegetation, fauna and property intensify (Zolkos et al. 2021). Rapid thawing leads to distinct ground collapse and high topographical relief, leading to thermokarst wetlands that further accelerate thawing by increasing talik formation and wetland development (Farquaharson et al. 2019).

One of the most important negative results of climate warming is the thawing of permafrost soils. Thermokarst wetlands and abrupt thawing promote greenhouse gas (GHG) emissions of carbon dioxide (CO_2) and methane (CH_4), which in turn accelerate polar amplification, which promote further ground thaw/collapse, and leading to a potential permafrost carbon feedback. (Walter Anthony et al. 2018; Obu et al. 2019, Biscaborn et al. 2019). Recent studies indicated that the permafrost boundary is gradually shifting from south to north and its depth is progressively increasing (Zhang et al. 2021). Few examples of such behaviors are noticeable such has the giant sinkhole-blow out craters in the Yamalo-Nenets Autonomous Okrug (Buldovicz et al. 2018), the collapse of major industrial buildings in Norilsk (Koptev 2020) and rapid relief changes in the boreal and/or tundra ecoystems (Ji et al. 2019, Doloisio et al. 2020).

While changes in the parameters of permafrost leads to the redistribution of macro- and microelements in the geological environment (Shirokova 2021, Dahédrey Payandi-Rolland 2021, Pokrovsky 2021), one poorly understood factor has so far remained underdeveloped here but is related to the afermomented permafrost degradation processes – natural radioactivity – which everywhere in the geological environment, including landforms developed under permafrost conditions. Our prior work concerning radioactivity and the radioactive radon gas emerging from permafrost provides the justified context for these above concerns, as we investigated both the policy and shortfalls of environmental monitoring of radioactive elements in permafrost settings (Puchkov et al. 2021).

Radon is a member of the uranium-238 radioactive decay chain, which makes up over 99% of all uranium on earth. Radon is constantly formed in all geological environments. The physical and chemical properties of radon allow it to be used as a tracer for studying many geological and atmospheric processes (Sabbarese et al. 2021, Giustini et al. 2019, Miklyaev et al. 2010, Baskaran et al. 2016, Daraktchieva et al. 2021, Selvam et al. 2021). At the same time, radon is a dangerous radioactive element that can lead to lung cancer where high concentrations are present, for example, in dwellings (Lorenzo-Gonzalez et al. 2020, Maier et al. 2021, Petrova et al. 2020, Rodríguez-Martínez et al. 2018, Rosenberger et al. 2018).

Until now, there are few scientific works devoted to the behavior of radon in frozen rocks and permafrost, while at the same time thawing and changing phase boundaries, thereby altering the pathways for radon migration to the surface. Most of those works are of a theoretical nature (Puchkov et al. 2021). Technically, there is existing scientific works showing permafrost is an excellent barrier to migiate upward migration of radon from the ground (Glover et al. 2022) which shows the need to extend these results elsewhere, as permafrost conditions are heterogenious and geographically unique. This concerns drives our investigations into how radioactive gas will migrate and to flow to the earth surface if permafrost thaws.

The purpose of this scientific paper is to demonstrate the influence of the process of thawing of frozen soils on radon flux during a laboratory experiment. For this, an experimental site with a frozen container containing ^{226}Ra (radioactive source) was prepared. The total activity of the radioactive source was about 4200 Bq and the radon flux density (RFD) was measured over a 5-month period. These experimental results will contribute to the fate and transport of radon emissions from permafrost to post-permafrost conditions.

MATERIALS AND METHODS

The experimental site is located in the Arkhangelsk region (NW Russia), 30 km from the city of Severodvinsk (Fig. 1). This territory belongs to the northern part of the East European plain. The region is characterised by a glacially formed landscape of flat plains, laterally extensive terraces and moraine belts dissected by river valleys (Jensen 2009). At the experimental site, the overburden layer is made of a mixture of gley-podzolic soils and loams, that is typical for this territory and the northern taiga. The upper soil layers were exposed to anthropogenic impacts after its agricultural use making them mix layers (urban soils). The content of ^{226}Ra in these soils is low and equal to about 10 Bq·kg^{-1}. For this reason, the background radon flux did not interfere with the experiment. Site and container preparations were carried out in February 2021. During this period, the air temperature reached -40°C. A red clay with an increased content of ^{226}Ra was used as a source of radon. Detailed radiation and physical characteristics of the radon source and the «background» soils are presented. During 5 months (March – July 2021, n days = 132), the RFD was measured in the control and background points coupled with soil temperature of 0.5, 1.0 and 1.5 m depths. The average daily temperatures at the city of Arkhangelsk, Russia according to the Northern Directorate for Hydrometeorology and Environmental Monitoring (http://www.sevmeteo.ru/) was used as the temperature of the atmospheric air.

Experimental site

The experimental setup uses a container placed in a pit of 1.6 m deep. The height of the container is 86 cm. The bottom inside container holds 40 kg of red clay (e.g radium source zone). The radium source zone was covered with surrounding soil up to the top of the container (overlapping layer). Holes were drilled at the bottom of the container for drainage of melt water. A detailed diagram of the experimental setup, its location and geometric characteristics are shown in Fig. 1. The container was then filled with water daily and reached a volume of 50 liters for 7 days (total 350 liters of water). We specially prepared more water in the container because some of the water went through the drainage holes and also through the top of the container, allowing it to freeze on all sides of the outside. In extremely low temperatures (down to -40°C), the content of the container was quickly and naturally frozen. After freezing is achieved by temperature logger observations, the pit was backfilled with prior in-situ soil. Thus, the frozen container and prior soils filled the exgivated pit.

Measurements of the RFD were carried out at two points. The control point was above the container and the background point was also at the surface at 10

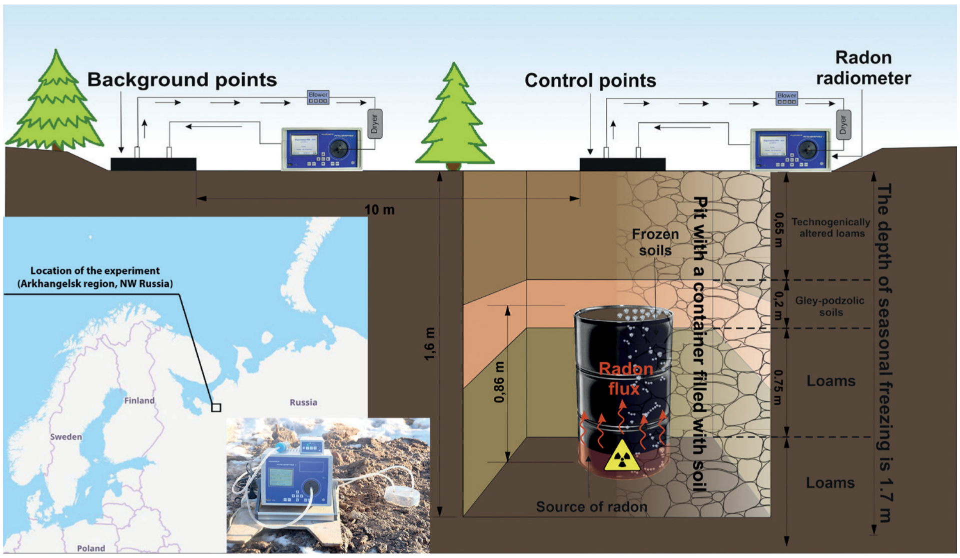

Fig. 1. The location of the experimental site and its geometric characteristics

meters away from the control point. When the topsoil subsided under thawing conditions, soils were added so that the measurement height above control point of the measurement did not change.

Radiometric measurement method

The measurement of the RFD using the radon radiometer «Alpharad plus» (Manufacturer – «NTM» Protection, Moscow city, Russia) (Fig. 2) is based on the electrostatic deposition of charged ^{218}Po ions from the air sample to the surface of the semiconductor detector. The electrical impulses generated by alpha particles on the detector were amplified with a preamplifier, fed to the input of an analogue-to-digital converter and then processed with a computer. The measurements were displayed on a colour LCD screen and stored in a non-volatile memory. The radon radiation was determined by the number of registered alpha particles during the decay of ^{218}Po atoms deposited on the detector (Afonin 2013).

The samplers were installed on a leveled ground. The sampler is made of plastic. The depth of immersion in the soil is 1 cm. The edges of the sampler were covered with soil to prevent contact with the atmosphere. The sampler was stored for 30 minutes to allow radon accumulation. Air was then pumped through the radiometer chamber for 20 minutes. The measurement was carried out twice for 20 minutes. Before the second measurement, air was pumped again through the radiometer chamber. About 2 hours are necessary between the moment the sampler is installed and the measurement is obtained. Since the measurements were carried out at two points (background and control), two radon radiometers of the same type were used. A reference sample was initially used to test the convergence of the measurements using the two radiometers. The relative standard deviation of the measurements from the reference sample was no more than 5-8%. As a reference sample, a 5-liter container with granite having a ^{226}Ra activity of about 95 Bq·kg^{-1} and an emanation rate of 15% was used.

Gamma Spectrometry Measurements

Gamma spectrometry is a widely used method to measure gamma radiation from radionuclides of natural origin, including Ra-226. It is a universal, non-destructive and easy-to-use method, especially at the stage of sample preparation and in the measurement process (Syam et al. 2020, IAEA 2013). A semiconductor gamma-spectrometric complex with nitrogen cooling ORTEC with a GEM 10 P4-70 HPGe detector (Ametek Ortec, Oak Ridge, TN, USA) complete with lead shielding was used to determine radionuclide Ra-226 in soils and radium source zone. The gamma spectrometer resolution along the 1.33 MeV (60Co) line is 1.75 keV and its relative efficiency is 15%. The measurement geometry is a 1-L Marinelli vessel (counting sample). The activity of the Ra-226 radionuclide is determined from the radionuclide Pb-214 (351.93 keV with a quantum yield of 35.60%) and Bi-214 (609.32 keV with a quantum yield of 45.49%, 1120.29 keV with a quantum yield of 14.92%, 1764.49 keV yield with a quantum yield of 15.3%).

Calculation methods

The radon emanation coefficient can be determined by two methods: gamma-spectrometric and radiometric (emanation) methods. The gamma spectrometric method was selected for the present research. The method consists of measuring the gamma activity of samples at various intervals after they are placed in a hermetically sealed container. We used a Marinelli plastic container sealed with a thick layer of sealant. According to our experimental data (Yakovlev et al. 2021), this method of sealing allows minimizing radon leakage from the container. In this experiment, counting samples were prepared in the form of a crushed sample with a grain size of less than

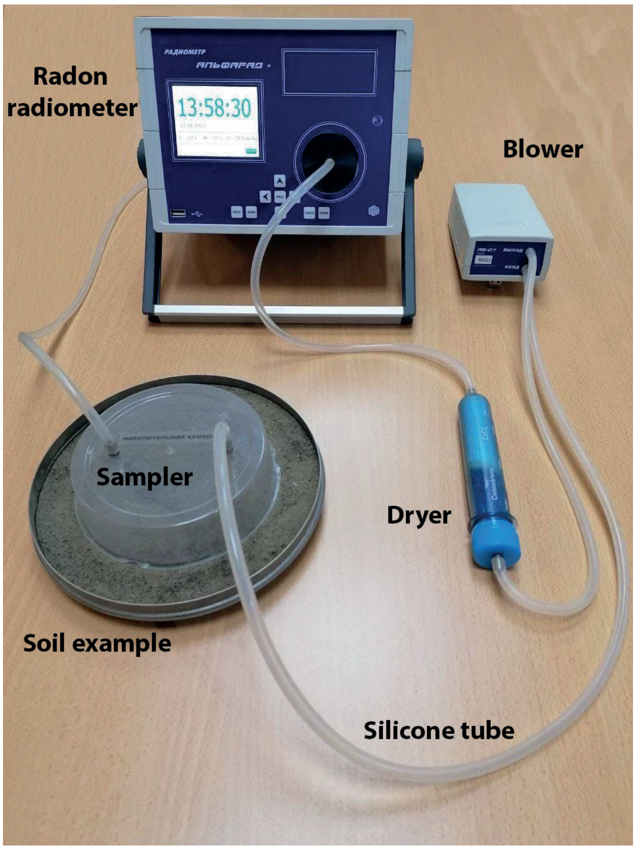

Fig. 2. The radon radiometer «Alpharad plus»

0.5 mm in a 1-L Marinelli vessel. Samples were measured daily for 21 days after they were sealed. Based on the results of these measurements, the following were determined: the activity of ^{226}Ra without taking into account the accumulation of its decay products; the activity of ^{226}Ra taking into account the accumulation of its decay products; the emanation coefficient; and the period during which the daughter products of ^{226}Ra decay enter a state of radioactive equilibrium. The counting sample was depressurized after the experiment and after 1–2 days for the activity of ^{226}Ra to be measured again. Based on the results of the experiment, the radon emanation coefficient (its free state) was determined using the following equation (1):

$$KRn = \left(1 - \frac{A_{226_{Ra}}(non-equilibrium)}{A_{226_{Ra}}(equilibium)}\right) \times 100 \quad (1)$$

where A_{226Ra} (*non-equilibrium*) is the activity of ^{226}Ra (in a nonequilibrium state) determined as the average value of the results of the first and last measurements (unsealed) in Bq·kg^{-1}; and A_{226Ra} (*equilibrium*) is the specific activity of ^{226}Ra (in an equilibrium state) determined as the average value of the results of the last 5 measurements in a sealed state, in Bq·kg^{-1}.

The radon production rate, P (Bq·m^{-3}·h^{-1}), was calculated using the following equation (2) (IAEA 2013, Pereira et al. 2017):

$$P = \lambda K_{Rn} A_{226_{Ra}} \rho_b \quad (2)$$

where λ is the decay constant for radon (2.1·10^{-6} s^{-1}) and ρb is the bulk density, in kg·m^{-3}.

The average density of the rock sample was determined by paraffin-coated method. This last physical parameter was calculated to assess the level of radon production. A detailed method and algorithm for calculating the average density are given in Yakovlev (2021) in which the average density of rock made of kimberlite was estimated.

RESULTS AND DISCUSSION

Radiation and physical parameters of soils and the radium source zone on the site

Table 1 shows the general characteristics of the samples under study. The studied soils are represented by the following: (1) technogenically altered loams, (2) gley-podzolic soils, (3) loams, (4) overlying soils (mixed gley-podzolic soils and loams) and (5) red clay (radium source zone). The background measurement points are represented by soils (1) – (3). The measurement reference points are represented by the overlying soils (4) and the radium source zone (5).

Despite the overlying soils above the radium source zone have a mass of about 400 kg and a total activity of ^{226}Ra of about 4200 Bq, the low levels of emanation coefficient and radon production rate do not allow them to create high values of the RFD. This can be seen as the background point, i.e. at which the highest value of the RFD does not exceed 45 mBq·m^{-2}·s^{-1} (see Fig. 3). From table 1, it can be noted that the radium source zone has the highest values of the activity of ^{226}Ra, the coefficient of emanation and the radon production rate.

Table 1. Radiation and physical parameters of soils and the radium source zone

Type of soils	Radiation and physical parameters			
	^{226}Ra concentration, Bq·kg^{-1}	Emanation coefficient, %	Radon production rate, Bq·m^{-3}·h^{-1}	Bulk density, g·cm^{-3}
Technogenically altered loams	10,9	10,3	12,7	1,5
Gley-podzolic soils	8,8	15,7	12,5	1,2
Loams	11,3	9,5	13,0	1,6
Overlying soils	10,4	12,2	14,4	1,5
Red clay (radium source zone)	103,8	25,7	322,7	1,6

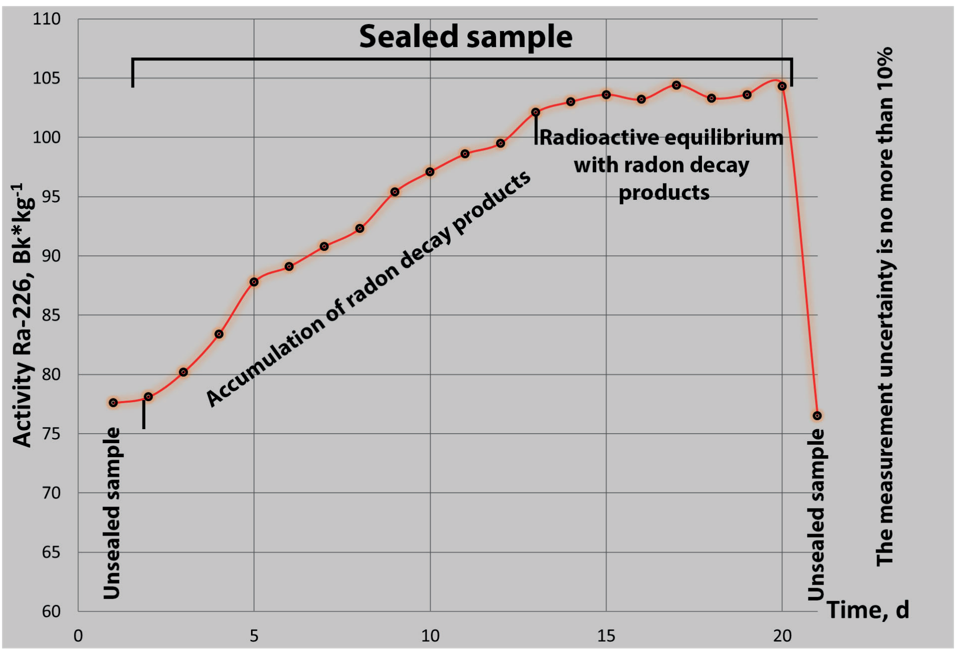

Fig. 3. The accumulation of radon decay products after sealing sample – red clay

The Fig. 3 shows an example of a curve for the accumulation of radon decay products after sealing sample – red clay. It can be noted that the state of radioactive equilibrium occurs in two weeks. The measurement uncertainty of ^{226}Ra from its decay products was no more than 10%.

Seasonal changes in RFD

Changes in the RFD at the control and background points along with air and soil temperatures at different depths are shown in Fig. 4. From March 1 to July 11, an increase in the RFD occurred 4 times. The first time, the RFD increased slightly at the beginning of April, both at the control and background points. This is due to an increase in air temperature above 0°C and the beginning of thawing of the upper soil layers. In early May, when the air temperature sharply increased to 10-25 °C, the depth of soil thawing was up to 1 m. During this period, there was a second increase in the RFD. At the same time, the temperature of the radium source zone remained below 0°C. In this regard, the nature of the increase in the RFD was the same both for the control point and the background point. During this period, the depth of soil thawing continued to gradually increase. As soon as the surface temperature of the radium source zone increased to 0 °C and above, there was a sharp increase in the RFD at the control point. At the same time, at the background point, the radon activity did not change. From the moment the radium source zone began to thaw until its complete thawing, the RFD increased by about 7-8 times, reaching a maximum value of about 240 $mBq \cdot m^{-2} \cdot s^{-1}$. Further, the radon activity did not change and the experiment was stopped afterward. Fluctuations in the RFD after complete thawing of the radium source zone were associated with weather events (rainfall) and changes in soil characteristics (moisture).

Statistical and factor analysis of changes in RFD under experimental conditions

Despite the dependence of the RFD on air and soil temperatures, a statistical analysis of the measured data was carried out and a correlation matrix was built. The statistical characteristics and the correlation matrix were divided into two large blocks (spring and summer) for convenience. Each block was divided into separate months. The results of the calculated statistical characteristics and the correlation matrices are given in Appendix A.

There was a good correlation between air and soil temperature (R=0.73-0.89) as well as between RFD in control and background points (R=0.81) in March. In May, high relationships between air temperature and soil temperature at 0 meter (R=0.85) as well as between soil temperature at 0 m and 1 m (R=0.72) were observed. In April, there were no significant correlations in the measured parameters. This is due to the fact that the RFD varied only at the beginning of April and then the radon activity remained constant.

In spring, RFD changes were insignificant and were associated with thawing of soil up to 1.3 m deep. The RFD values at the control and background points during this period were the same, which means that there was no influence of the radium source zone. A significant correlation between RFDs in the control and background points were observed only in March (R=0.81) and in May (R=0.87) for the whole experiment.

The summer period (June) was characterized by a very good correlation between RFD at the control point and soil temperature at different depths (R=0.75 for 0 m, R=0.79 for 0.5 m, R=0.83 for 1.0 m, R=0.97 for 1.5 m). This is due to the fact that the radium source zone was intensely melting and contributed to an increase in RFD at the surface. At the same time, RFD at the background point remained at a constant level and no dependence on soil temperature was found.

Fig.s 5 and 6 show linear regressions for RFD and soil temperature at 1 m (for spring) and for RFD and soil temperature at 1.5 m (for summer). There is a good correlation (R=0.9) between radon flux density and soil temperature at 1 m depth in spring (Fig. 5) and at 1.5-m depth in summer (Fig. 6) at the control point. RFD increased by a factor of 26.7 and 22.2 in spring and in summer. This corresponds when soil temperature at 1-1.5-meter depth increased by 1 °C.

The calculated correlation matrices were approved by the construction of the frequency diagrams. Frequency distribution of RFDs in the control and background points (Fig. 7) is similar in March (up to 90% of RFDs in the range of 0.5-9 mBq/m^2s and 0.5-5.5 mBq/m^2s in the control and background points respectively) and in April (up to 90% of RFDs in the range of 12-18.5 mBq/m^2s and 12-16.5 mBq/m^2s in the control and background points respectively).

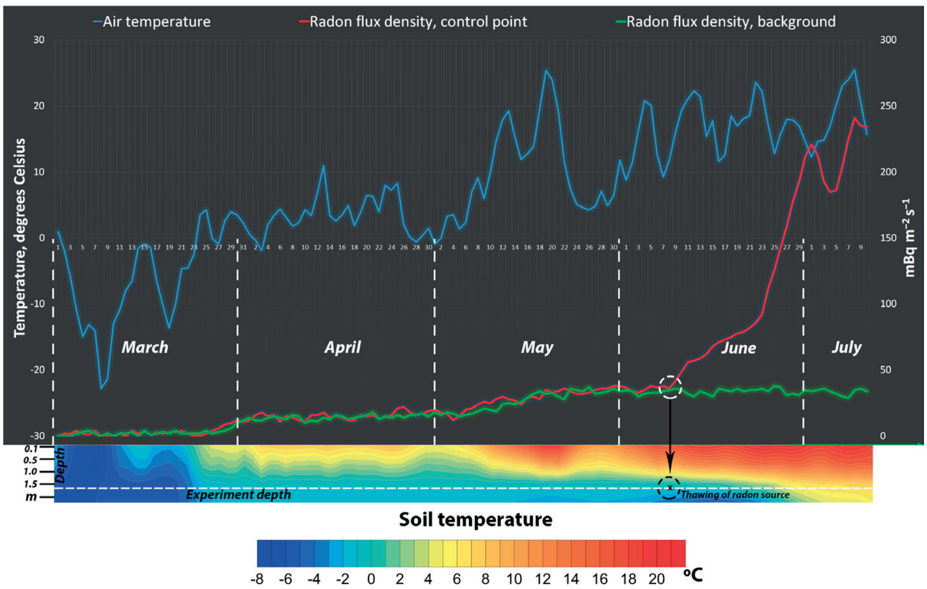

Fig. 4. Temporal changes in the RFD at the control and background points

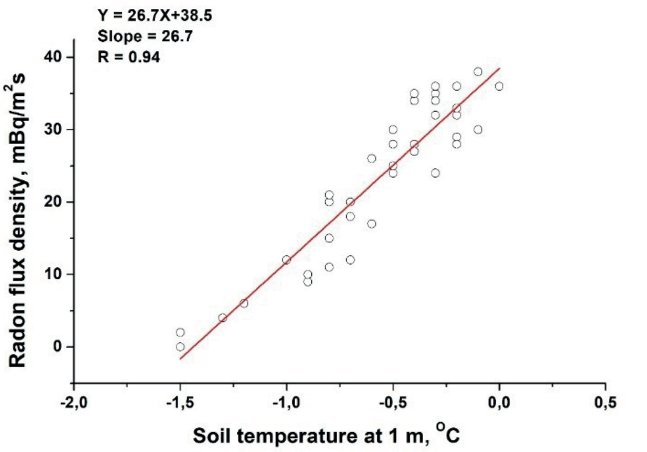

Fig. 5. Linear regression fits for RFD to soil temperature at 1 m depth from spring measurements in the control point

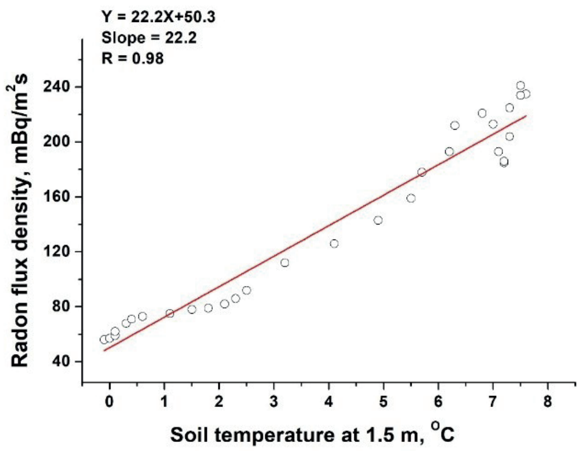

Fig. 6. Linear regression fits for RFD to soil temperature at 1.5 m depth in summer

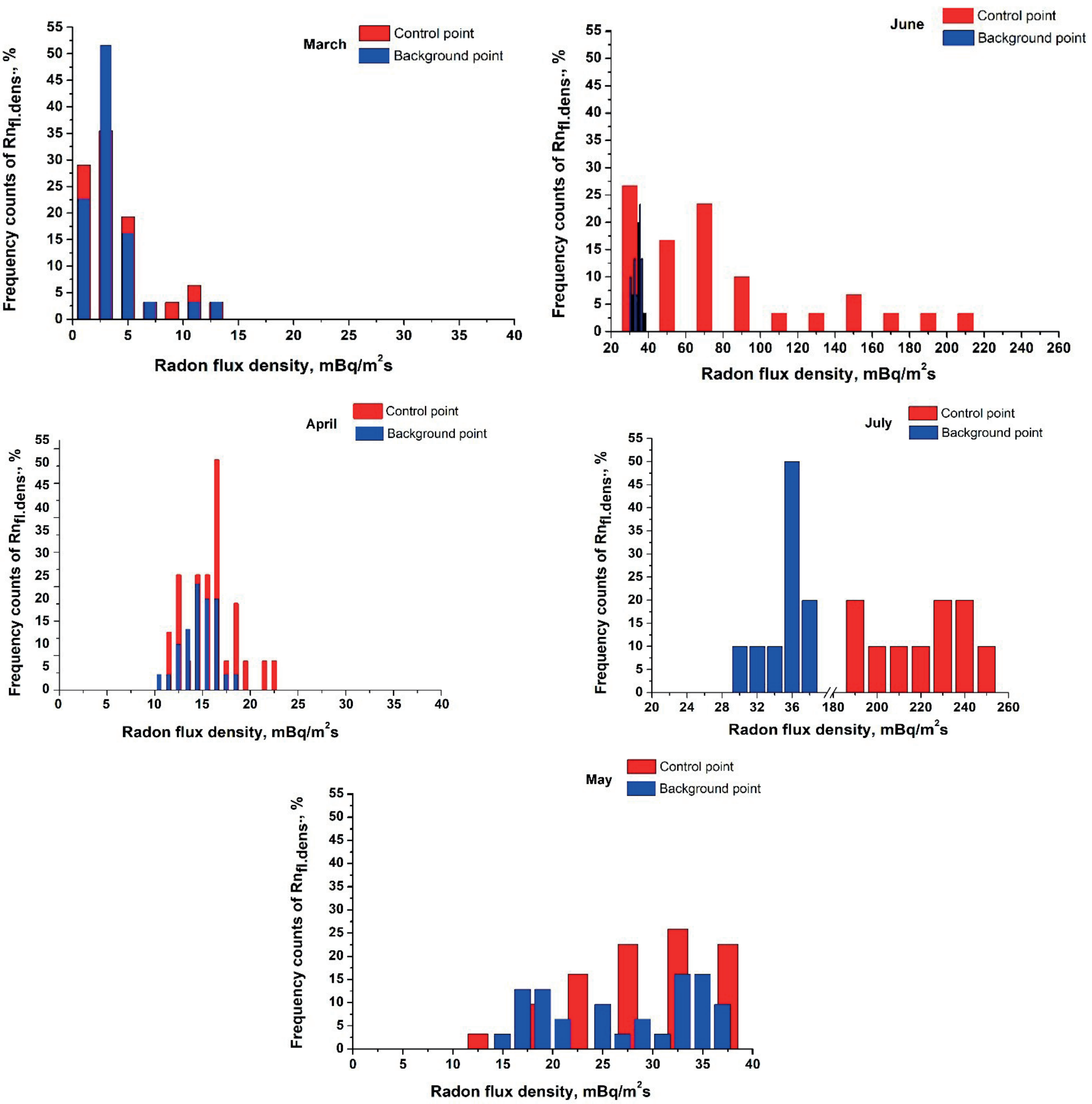

Fig. 7. Frequency counts (in %) of RFD for control (red) and background (blue) points

In May, RFDs in control and background points are about 2 times higher than in April.

In June and July, the significant difference (2-4 times) in RFDs between measurement points was observed. RFD in July in the control point reaches 238 mBq/m^{2}s (90-th percentile) while RFD in the background point is 36 mBq/m^{2}s (90-th percentile).

The factor analysis was used to select the main factor loadings separately for spring (Table 2) and summer (Table 3).

In spring, two factors were enough (Table 2 and Fig. 5). The first factor (Factor 1) is related to the temperature change in air and soil at 0 and 1 m. The second factor (Factor 2) determines the strongness of the relationships between RFDs in control and background points and near-surface soil temperature. In spring, there is no significant difference in RFDs between disturbed (control point) and undisturbed (background point) soil layers.

The factor analysis for the summer data (Table 3 and Fig. 6) shows SS loadings > 1 only for Factor 1. Those points of the Factor 1 are the main ones determining RFD in the control point and are caused by temperature change at different soil depths particularly at 0.5 and 1.5 m.

What does the diffusion equation show?

Based on the results of the experiment and its statistical analysis, it was demonstrated that a change in the radon situation can occur when the permafrost conditions in the geological environment change. In the present experiment, this fact was noticed immediately when the radium source zone thawed. We assume that this is due to the physical properties of ice and permafrost. First of all, it is necessary to take into account the porosity of the ice. This porosity will influence the emanation of the rock. In this case, radon atoms are emanated from the solid phase into the pore space of the soil (production of «free» radon) due to the recoil energy arising from the alpha decay of the parent ^{226}Ra. It can be assumed that the emanation of rock in its frozen state will be much lower than in the thawed state.

We hypothesized that some hypothetical area is composed of rocks similar to a radium source zone. Distribution of radon concentration in the frozen state and thawed state was calculated up to 10 m deep. The following picture is obtained (Fig. 8).

The following diffusion equation (3) was used to calculate distribution of radon concentration [Marenniy A.M. 2016]:

$$C(x) = C_{Ra} \bullet K_{ЭМ} \bullet \rho \bullet (1 - e^{-\sqrt{\frac{\lambda}{D}} \bullet x}) \qquad (3)$$

where:

C(x) – distribution function along the vertical profile of the radiation of «free» radon in the rock, Bq•m^{-3};

C_{Ra} – concentration of ^{226}Ra in the rock, Bq•kg^{-1};

$K_{эм}$ – coefficient of radon emanation in soil, stand. units;

ρ – soil density, kg•m^{-3};

λ – radon decay constant, 1•s^{-1};

D – diffusion coefficient of radon in soil, m^2•s^{-1}.

Table 2. Factor analysis from spring data

Parameters	Uniquenesses	
Air temp. °C	0.130	
Soil temp. at 0 m, °C	0.005	
Soil temp., at 0.5 m, °C	0.186	
Soil temp., at 1 m, °C	0.195	
Soil temp., at 1.5 m, °C		
Radon flux density, control point, mBq m^{-2} s^{-1}	0.055	
Radon flux density, background, mBq m^{-2} s^{-1}	0.006	
	Loadings	
	Factor1	Factor2
Air temp. °C	0.841	0.402
Soil temp. at 0 m, °C	0.833	0.549
Soil temp., at 0.5 m, °C	0.618	0.657
Soil temp., at 1 m, °C	0.778	0.446
Soil temp., at 1.5 m, °C		
Radon flux density, control point, mBq m^{-2} s^{-1}	0.500	0.834
Radon flux density, background, mBq m^{-2} s^{-1}	0.449	0.890
SS loadings	2.841	2.582
Proportion Var	0.474	0.430
Cumulative Var	0.474	0.904

Notes: Test of the hypothesis that 2 factors are sufficient. The chi square statistic is 57.95 on 4 degrees of freedom. The p-value is 7.8e-12

Table 3. Factor analysis from summer data

Parameters	Uniquenesses	
Air temp. °C	0.718	
Soil temp. at 0 m, °C	0.005	
Soil temp., at 0.5 m, °C	0.129	
Soil temp., at 1 m, °C	0.264	
Soil temp., at 1.5 m, °C	0.005	
Radon flux density, control point, mBq m^{-2} s^{-1}	0.028	
Radon flux density, background, mBq m^{-2} s^{-1}	0.994	
	Loadings	
	Factor1	Factor2
Air temp. °C		0.529
Soil temp. at 0 m, °C	0.783	0.619
Soil temp., at 0.5 m, °C	0.925	0.128
Soil temp., at 1 m, °C	0.816	0.266
Soil temp., at 1.5 m, °C	0.998	
Radon flux density, control point, mBq m^{-2} s^{-1}	0.979	-0.117
Radon flux density, background, mBq m^{-2} s^{-1}	-	-
SS loadings	4.088	0.770
Proportion Var	0.584	0.110
Cumulative Var	0.584	0.694

Notes: Test of the hypothesis that 2 factors are sufficient. The chi square statistic is 38.87 on 8 degrees of freedom. The p-value is 5.2e-06

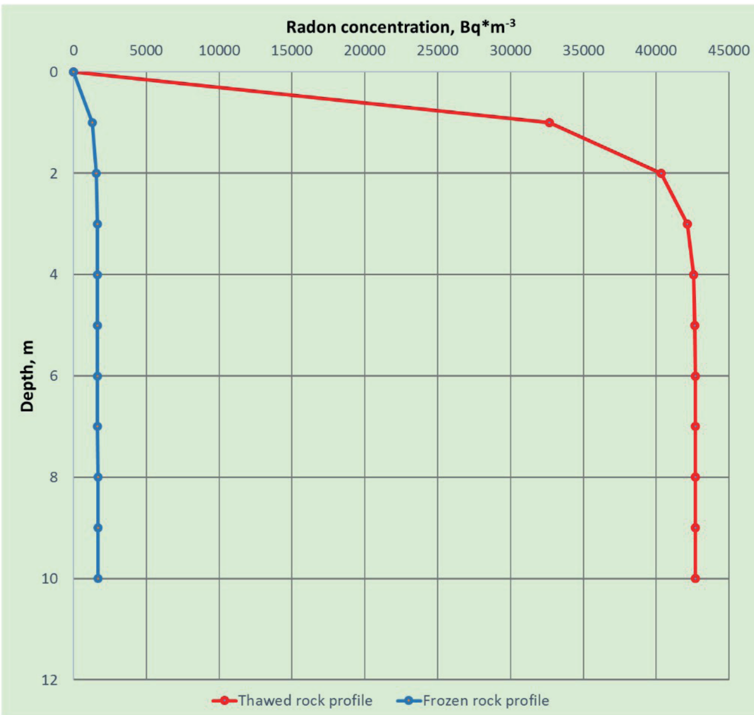

Fig. 8. Distribution of radon concentration in frozen and thawed rocks

The obtained radiation and physical parameters of the radium source zone were used to calculate this diffusion equation. At the same time, for the frozen state, an emanation coefficient equal to 1% was used. This value of the emanation coefficient assumes the absence of radon in a «free» state and its presence in the crystal lattice of ice. Fig. 8 shows that in frozen conditions, the concentration of radon can reach no more than 2000 Bq•m^{-3}. With the complete thawing of such rocks, the concentration of radon will increase 20 times and can reach 43000 Bq•m^{-3}. The actual environment and conditions may be completely different. This calculation is shown as a simple example to understand that the condition of permafrost, frozen state of soils and rocks can play a barrier role for radon flux, reducing them by 10-20 times, depending on the characteristics of the frozen rocks (density, porosity). Another fact proving the barrier function of permafrost may be the isotopic ratios in the soil and rock profile up to 20 m deep. For the isotopic ratio, ^{226}Ra and ^{210}Pb can be used. The ratio of these isotopes around 1 would indicate the absence of «movement» of radon, which is most likely in a bound state in the permafrost. This will be included in a future contribution to study the behavior of radon in conditions of frozen ground, permafrost or ice.

Future health risks if the hypothesis is confirmed

The negative impact of radiation exposure on human health is a known fact. The degree of the negative effect of this radiation is determined by the magnitude of the dose regardless if it is caused by natural or artificial source of ionizing radiation (Karabanov 2013, Radon: An Overview of Health Effects 2015). Back in 1988, the Congress of the World Health Organization and the International Agency for Research on Cancer reviewed the available data and recognized that the intake of radon in the body leads to the development of lung cancer in humans (Nenakhova 2006). In 2009, UNSCEAR, based on a detailed scientific assessment of epidemiological data, made a statement at the UN General Assembly that there is direct evidence to support a detectable risk of lung cancer for the population from radon in dwellings. The statement concluded that there is no effective lower threshold of radon concentration below which radon exposure poses no danger. Strong scientific evidence demonstrates that radon-induced lung cancer is a significant public health risk with children at greater risk than adults (as is often the case with exposure to toxic substances/radiation) (Radon indoor air, Canada 2014).

In the case of a hypothesis about the barrier function of permafrost for radon flux, there are theoretical studies with the construction of a mathematical model of radon intake into residential buildings (Glover 2006, Glover 2007, Glover 2022). In these studies, the authors estimated the radon concentration in a residential building in the event of an instantaneous melting of permafrost 13 m thick. According to their calculations, the radon concentration can increase 100 times, which will lead to an excess of the permissible values of the radon concentration (criteria of 100-300 Bq·m-3 for many countries). According to the model constructed by the authors, this level can persist for several years and will then gradually decrease. The authors believed this fact is extremely relevant considering the extremely negative effect of radon on the incidence of cancer. Our studies confirm the barrier function of permafrost for radon flux. Based on our measurements, an increase in RFD at the surface up to 20 times is observed.

We assume that residential buildings built without an air layer in permafrost areas may be affected by radon in a warming climate. This will lead to an increase exposure to radon for the people living in such buildings. When confirming this assumption, it will be necessary to provide additional protective actions for such buildings. In addition, it will be necessary to take into account the effect of permafrost thawing when assessing the potential radon hazard of the territory before starting the construction of the new buildings. In Russia, a similar coefficient exists in assessing the potential radon hazard (Klimshin et al. 2010). But the value of that coefficient does not exceed 2. The coefficient takes into account only the layer of seasonal freezing and not the degradation of permafrost. Therefore, it will be necessary to take into account the predictor presented in this work when calling for (amend) existing laws. Such changes in the legislation will prevent a possible negative effect on human health associated with an increase exposure to radon for the population of the Arctic countries. This is especially true for the territories of the central and northern parts of Canada, Russia, the northern part of the Scandinavian (Sweden, Norway, Finland) countries and the United States (Alaska) (Puchkov et al. 2021).

CONCLUSIONS

In this paper, an experiment with a frozen source of radon (red clay with a high content of ^{226}Ra) and its gradual thawing in natural conditions was described. The experiment was carried on a 5-month period with radon and temperature measurements in soil every day. In total, 132 measurements of RFD and soil temperature at different depths were made. These results show a strong relationship between radon flux density and soil temperature profiles at different depths. The calculations of radon sourced from frozen and thawed zones show how temperature phase of substrate (e.g. clays) control the barrier influence of radon migration. From March 1 to July 11, RFD increased 4 times. From the moment the radium source zone began to thaw until its complete thawing, RFD increased by about 7-8 times reaching a maximum value of about 240 mBq•m^{-2}•s^{-1}. Fluctuations in RFD after complete thawing of the radium source zone were associated with weather events (rainfalls) and changes in soil characteristics (moisture).

A statistical and factor analysis of the measured values was carried out. There was a good correlation between air and soil temperature (R=0.73-0.89) as well as between RFD in control and background points (R=0.81) in March. In May, air temperature and soil temperature at 0 meter (R=0.85) were correlated as well as soil temperature at 0 and at 1 meter (0.72). In April, there was no significant correlation in the measured parameters. This is because the RFD variation was only at the beginning of April. After this variation period, the radon activity remained at a constant level. During summer (June), a strong correlation was observedbetween RFD at the control point and soil temperature at different depths (R=0.75 at 0 m, R=0.79 at 0.5 m, R=0.83 at 1.0 m, R=0.97 at 1.5 m). This is because the radium source zone was intensely melting and contributed to an increase in RFD at the surface. Simultaneously, RFD at the background point remained at a constant level and no dependence on soil temperature was found. An increase of 26.7 and 22.2 mBq•m^{-2}•s^{-1} on RFD during spring and summer corresponds to an increase of 1 °C of the soil temperature at 1-1.5 m depth.

The factor analysis showed that, in spring, RFD change was mainly caused by air and soil (at 0 and 1 m) temperature changes. There was a high relationship between RFDs in control and background points and near-surface soil temperatures. In spring, there was no significant difference in RFDs between the soil layers in control and background points. During summer, RFD change was caused by temperature variation at different soil depths, particularly at 0.5 and 1.5 m in the control point.

The calculation of distribution of radon concentration in frozen and in thawed state based on the diffusion equation showed that frozen soils and rocks played a barrier role for radon flux, reducing them by 10-20 times depending on the characteristics of frozen rocks (density, porosity). We assume that the barrier function of permafrost may be demonstrated further by the study of isotopic ratios of ^{226}Ra and ^{210}Pb in the soil and rock profiles up to 20 m deep. The ratio of these isotopes around 1 would indicate the absence of «movement» of radon, which is most likely in a bound state in the permafrost. This will be the next step in studying the behavior of radon in conditions of frozen ground, permafrost or ice.

The results of the presented experiment confirm the assumption about the barrier function of permafrost for the flow of radioactive radon gas.

REFERENCES

Afonin A., & Korchunov A. (2013). Optimizing block parameters measurements for monitoring radon, thoron and their daughter products in various environments. ANRI, 1, 9-11. (in Russian).

Aparin B.F., & Sukhacheva E.Yu. (2015). Urban soil classification in the system of Russian and international soil classification. Bulletin of the Soil Institute named after V.V. Dokuchaev, (79), 53-72. (in Russian).

Arenson L., Colgan W., & Marshall H.P. (2021). Physical, thermal, and mechanical properties of snow, ice, and permafrost. In Snow and ice-related hazards, risks, and disasters, 35-71, DOI: 10.1016/B978-0-12-817129-5.00007-X.

Baskaran M. (2016). Radon: A tracer for geological, geophysical and geochemical studies (Vol. 367). Basel: Springer.

Biskaborn B.K., Smith S.L., Noetzli J., Matthes H., Vieira G., Streletskiy D.A., ... & Lantuit H. (2019). Permafrost is warming at a global scale. Nature communications, 10(1), 1-11, DOI: 10.1038/s41467-018-08240-4.

Buldovicz S.N., Khilimonyuk V.Z., Bychkov A.Y., Ospennikov E.N., Vorobyev S.A., Gunar A.Y., … & Amanzhurov R.M. (2018). Cryovolcanism on the earth: Origin of a spectacular crater in the Yamal Peninsula (Russia). Scientific reports, 8(1), 1-6, DOI: 10.1038/s41598-018-31858-9.

Canadian Environmental Law Association. (2014). Radon in indoor air: A review of policy and law in Canada.

Daraktchieva Z., Wasikiewicz J.M., Howarth C.B., & Miller C.A. (2021). Study of baseline radon levels in the context of a shale gas development. Science of The Total Environment, 753, 141952, DOI: 10.1016/j.scitotenv.2020.141952.

Egorov V.V., Ivanova E.N., Friedland V.M., & Rozov N.I. (1977). Classification and diagnosis of soils of the USSR. (in Russian).

Farquharson L.M., Romanovsky V.E., Cable W.L, Walker D.A., Kokelj S.V., Nicolsky D. (2019) Climate Change Drives Widespread and Rapid Thermokarst Development in Very Cold Permafrost in the Canadian High Arctic. Geophysical Research Letters, 46, 12, DOI: 10.1029/2019GL082187.

Field R.W. (2019). Radon: an overview of health effects.

Giustini F., Ciotoli G., Rinaldini A., Ruggiero L., & Voltaggio M. (2019). Mapping the geogenic radon potential and radon risk by using Empirical Bayesian Kriging regression: A case study from a volcanic area of central Italy. Science of the Total Environment, 661, 449-464, DOI: 10.1016/j.scitotenv.2019.01.146.

Glover P.W.J. (2006). Increased domestic radon exposure caused by permafrost thawing due to global climate change, EGU General Assembly, Vienna, Austria, 2–7 April. EGU06-A-01439.

Glover P.W.J., Blouin M. (2022). Increased Radon Exposure from Thawing of Permafrost Due to Climate Change. Earth's Future, 10, 2, DOI: 10.1029/2021EF002598.

Glover P.W., & Blouin M. (2007). Modelling increased soil radon emanation caused by instantaneous and gradual permafrost thawing due to global climate warming.

International atomic energy agency (IAEA) (2013). Measurement and Calculation of Radon Releases from NORM Residues. Technical Reports Series, 474. IAEA, Austria.

Jensen M.A., Demidov I.N., Larsen E., & Lyså A. (2009). Quaternary palaeoenvironments and multi-storey valley fill architecture along the Mezen and Severnaya Dvina river valleys, Arkhangelsk region, NW Russia. Quaternary Science Reviews, 28(23-24), 2489-2506, DOI: 10.1016/j.quascirev.2009.05.009.

Ji M., Kong W., Liang C., Zhou T., Jia H., & Dong X. (2020). Permafrost thawing exhibits a greater influence on bacterial richness and community structure than permafrost age in Arctic permafrost soils. The Cryosphere, 14(11), 3907-3916, DOI: 10.5194/tc-14-3907-2020.

Karabanov A., Zhuk I., Yaroshevich O., Konopelko M., Lukashevich J., & Vasilevsky L. (2013). Radon: health, danger, and protective measures. Science and Innovation, 4(122). (in Russian).

Klimshin A.V., Kozlova I.A., Rybakov E.N., Lukovskoy M.Yu. (2010). Effect of freezing the surface layer of soil on the radon transport. Vestnik Kamchatskoy regional'noy assotsiatsii «Uchebno-nauchnyy tsentr». Seriya: Nauki o Zemle, 16(2), 146-151. (in Russian with English summary).

Koptev D.P. (2020). Norilsk spill: lessons and consequences. Drilling and Oil, (7-8), 3-9. (in Russian with English summary).

Lorenzo-Gonzalez M., Ruano-Ravina A., Torres-Duran M., Kelsey K.T., Provencio M., Parente-Lamelas I., ... & Barros-Dios J.M. (2020). Lung cancer risk and residential radon exposure: A pooling of case-control studies in northwestern Spain. Environmental Research, 189, 109968, DOI: 10.1016/j.envres.2020.109968

Maier A., Wiedemann J., Rapp F., Papenfuß F., Rödel F., Hehlgans S., ... & Frey B. (2021). Radon Exposure—Therapeutic Effect and Cancer Risk. International Journal of Molecular Sciences, 22(1), 316, DOI: 10.3390/ijms22010316.

Marenniy A.M., Tsapalov A.A., Miklyaev P.S., Petrova T.B. (2016) Regularities Formation of a Radon Field in the Geological Environment. Pero Publishing House. (in Russian).

Melnichenko N.A., Tyuveev A.V., Lazaryuk A.Yu, Kustova E.V., & Abramov A.S. (2021). Porosity, permeability and structure of sea ice in Novik Bay (Russkiy Island) according to hydrological measurements, MRI and CT. Bulletin of the Far Eastern Branch of the Russian Academy of Sciences, 1(215), 49-57. (in Russian with English summary).

Miklyaev P.S., Petrova T.B. (2011) Studies of radon emanation from clays. Water Resources, 38, 868-875, DOI: 10.1134/S0097807811070116.

Nazintsev Y.L., Panov V.V. (2000). Phase composition and thermophysical characteristics of sea ice. St. Petersburg: Gidrometeoizdat. (in Russian).

Nenakhova E.V., & Makarov O.A. (2006). Radon and the health of the population. Acta Biomedica Scientifica, (6). (in Russian with English summary).

Obu J., Westermann S., Bartsch A., Berdnikov N., Christiansen H.H., Dashtseren A., ... & Zou D. (2019). Northern Hemisphere permafrost map based on TTOP modelling for 2000–2016 at 1 km2 scale. Earth-Science Reviews, 193, 299-316, DOI: 10.1016/j.earscirev.2019.04.023.

Payandi-Rolland D., Shirokova L.S., Labonne F., Bénézeth P., & Pokrovsky O.S. (2021). Impact of freeze-thaw cycles on organic carbon and metals in waters of permafrost peatlands. Chemosphere, 279, 130510, DOI: 10.1016/j.chemosphere.2021.130510.

Pereira A., Lamas R., Miranda M., Domingos F., Neves L., Ferreira N., & Costa L. (2017). Estimation of the radon production rate in granite rocks and evaluation of the implications for geogenic radon potential maps: A case study in Central Portugal. Journal of environmental radioactivity, 166, 270-277, DOI: 10.1016/j.jenvrad.2016.08.022.

Petrova T., & Miklyaev P. (2020). Variations of Indoor Radon Concentration in Traditional Russian Rural Wooden Houses. Radiation Protection Dosimetry, 191(2), 219-222, DOI: 10.1093/rpd/ncaa156.

Pokrovsky O.S., Manasypov R.M., Pavlova O.A., Shirokova L.S., & Vorobyev S.N. (2022). Carbon, nutrient and metal controls on phytoplankton concentration and biodiversity in thermokarst lakes of latitudinal gradient from isolated to continuous permafrost. Science of The Total Environment, 806, 151250, DOI: 10.1016/j.scitotenv.2021.151250.

Puchkov A.V., Yakovlev E.Y., Hasson N., Sobrinho G.A., Tsykareva Y.V., Tyshov A.S., ... & Ushakova E.V. (2021). Radon hazard in permafrost conditions: Current state of research. Geogr. Environ. Sustain, DOI: 10.24057/2071-9388-2021-037.

Rodríguez-Martínez Á., Torres-Duran M., Barros-Dios J.M., & Ruano-Ravina A. (2018). Residential radon and small cell lung cancer. A systematic review. Cancer letters, 426, 57-62, DOI: 10.1016/j.canlet.2018.04.003.

Rosenberger A., Hung R.J., Christiani D.C., Caporaso N.E., Liu G., Bojesen S.E., ... & Gomolka M. (2018). Genetic modifiers of radon-induced lung cancer risk: a genome-wide interaction study in former uranium miners. International archives of occupational and environmental health, 91(8), 937-950, DOI:10.1007/s00420-018-1334-3.

Rossiter D.G. (2007). Classification of urban and industrial soils in the world reference base for soil resources (5 pp). Journal of Soils and Sediments, 7(2), 96-100, DOI: 10.1065/jss2007.02.208.

Sabbarese C., Ambrosino F., D'Onofrio A., Pugliese M., La Verde G., D'Avino V., & Roca V. (2021). The first radon potential map of the Campania region (southern Italy). Applied Geochemistry, 126, 104890, DOI: 10.1016/j.apgeochem.2021.104890.

Selvam S., Muthukumar P., Sajeev S., Venkatramanan S., Chung S.Y., Brindha K., ... & Murugan R. (2021). Quantification of submarine groundwater discharge (SGD) using radon, radium tracers and nutrient inputs in Punnakayal, south coast of India. Geoscience Frontiers, 12(1), 29-38 DOI: 10.1016/j.gsf.2020.06.012.

Shirokova L.S., Chupakov A.V., Ivanova I.S., Moreva O.Y., Zabelina S.A., Shutskiy N.A., ... & Pokrovsky O.S. (2021). Lichen, moss and peat control of C, nutrient and trace metal regime in lakes of permafrost peatlands. Science of the Total Environment, 782, 146737, DOI: 10.1016/j.scitotenv.2021.146737.

Syam N.S., Lim S., Lee H.Y., & Lee S.H. (2020). Determination of radon leakage from sample container for gamma spectrometry measurement of 226Ra. Journal of environmental radioactivity, 220, 106275, DOI: 10.1016/j.jenvrad.2020.106275.

Walter Anthony K., Schneider von Deimling T., Nitze I., Frolking S., Emond A., Daanen R., Anthony P., Lindgren P., Jones B., & Grosse G. (2018). 21st-century modeled permafrost carbon emissions accelerated by abrupt thaw beneath lakes. Nature Communications, 9, 3262, DOI: 10.1038/s41467-018-05738-9.

Yakovlev E., & Puchkov A. (2021). Radon over Kimberlite Pipes: Estimation of the Emanation Properties of Rocks (Lomonosov Diamond Deposit, NW Russia). Applied Sciences, 11(13), 6065, DOI: 10.3390/app112411765.

Zhang Z.Q., Wu Q.B., Hou M.T., Tai B.W., & An Y.K. (2021). Permafrost change in Northeast China in the 1950s–2010s. Advances in Climate Change Research, 12(1), 18-28, DOI: 10.1016/j.accre.2021.01.006.

Zolkos S., Fiske G., Windholz T., Duran G., Yang Z., Olenchenko V., ... & Natali S.M. (2021). Detecting and Mapping Gas Emission Craters on the Yamal and Gydan Peninsulas, Western Siberia. Geosciences, 11(1), 21, DOI: 10.3390/geosciences11010021.

APPENDICES

APPENDIX A. STATISTICAL CHARACTERISTICS OF THE OBSERVED PARAMETERS AND CORRELATION MATRICES

Parameter	Air temp. °C	Soil temp. at 0 m, °C	Soil temp., at 0.5 m, °C	Soil temp., at 1 m, °C	Radon flux density at control point, mBq m^{-2} s^{-1}	Radon flux density at background, mBq m^{-2} s^{-1}
March						
Air temp. °C	1.00	0.89	0.81	0.73	0.48	0.38
Soil temp. at 0 m, °C	0.89	1.00	0.96	0.92	0.61	0.52
Soil temp., at 0.5 m, °C	0.81	0.96	1.00	0.96	0.66	0.60
Soil temp., at 1 m, °C	0.73	0.92	0.96	1.00	0.65	0.61
Radon flux density, control point, mBq m^{-2} s^{-1}	0.48	0.61	0.66	0.65	1.00	0.81
Radon flux density, background, mBq m^{-2} s^{-1}	0.38	0.52	0.60	0.61	0.81	1.00
April						
Air temp. °C	1.00	0.46	0.16	0.23	0.02	0.02
Soil temp. at 0 m, °C	0.46	1.00	0.00	0.47	0.20	-0.14
Soil temp., at 0.5 m, °C	0.16	0.00	1.00	0.19	-0.16	-0.28
Soil temp., at 1 m, °C	0.23	0.47	0.19	1.00	0.37	0.07
Radon flux density, control point, mBq m^{-2} s^{-1}	0.02	0.20	-0.16	0.37	1.00	0.25
Radon flux density, background, mBq m^{-2} s^{-1}	0.02	-0.14	-0.28	0.07	0.25	1.00
May						
Air temp. °C	1.00	0.85	-0.10	0.43	0.42	0.32
Soil temp. at 0 m, °C	0.85	1.00	0.30	0.72	0.68	0.68
Soil temp., at 0.5 m, °C	-0.10	0.30	1.00	0.64	0.78	0.82
Soil temp., at 1 m, °C	0.43	0.72	0.64	1.00	0.83	0.90
Radon flux density, control point, mBq m^{-2} s^{-1}	0.42	0.68	0.78	0.83	1.00	0.87
Radon flux density, background, mBq m^{-2} s^{-1}	0.32	0.68	0.82	0.90	0.87	1.00

Table A2. Correlation matrix of parameters in summer

Parameter	Air temp. °C	Soil temp. at 0 m, °C	Soil temp., at 0.5 m, °C	Soil temp., at 1 m, °C	Soil temp., at 1.5 m, °C	Radon flux density, control point, mBq m^{-2} s^{-1}	Radon flux density, background, mBq m^{-2} s^{-1}
June							
Air temp. °C	1.00	0.47	0.27	0.27	-0.21	0.09	-0.29
Soil temp. at 0 m, °C	0.47	1.00	0.94	0.92	0.83	0.75	0.11
Soil temp., at 0.5 m, °C	0.27	0.94	1.00	0.98	0.82	0.79	0.25
Soil temp., at 1 m, °C	0.27	0.92	0.98	1.00	0.86	0.83	0.22
Soil temp., at 1.5 m, °C	-0.21	0.83	0.82	0.86	1.00	0.97	0.11
Radon flux density, control point, mBq m^{-2} s^{-1}	0.09	0.75	0.79	0.83	0.97	1.00	0.04
Radon flux density, background, mBq m^{-2} s^{-1}	-0.29	0.11	0.25	0.22	0.11	0.04	1.00
July							
Air temp. °C	1.00	0.78	0.70	-0.06	0.66	0.27	-0.49
Soil temp. at 0 m, °C	0.78	1.00	0.80	-0.04	0.80	0.08	-0.42
Soil temp., at 0.5 m, °C	0.70	0.80	1.00	0.12	0.92	0.24	-0.11
Soil temp., at 1 m, °C	-0.06	-0.04	0.12	1.00	0.40	0.88	0.39
Soil temp., at 1.5 m, °C	0.66	0.80	0.92	0.40	1.00	0.48	0.01
Radon flux density, control point, mBq m^{-2} s^{-1}	0.27	0.08	0.24	0.88	0.48	1.00	0.14
Radon flux density, background, mBq m^{-2} s^{-1}	-0.49	-0.42	-0.11	0.39	0.01	0.14	1.00

Table A3. Statistical characteristics of the observed parameters

Parameter	N total	Mean	Stand. Dev.	Min	Med	Max	P10	P90
March								
Air temp. °C	31	-5.76	7.40	-22.80	-4.60	4.30	-14.00	3.50
Soil temp. at 0 m, °C	31	-2.63	3.41	-8.30	-3.30	3.40	-6.80	2.40
Soil temp., at 0.5 m, °C	31	-3.80	2.25	-6.80	-4.50	-0.10	-6.10	-0.20
Soil temp., at 1 m, °C	31	-4.45	2.08	-6.80	-5.40	-0.80	-6.20	-1.00
Soil temp., at 1.5 m, °C	-	-	-	-	-	-	-	-
Radon flux density, control point, mBq m^{-2} s^{-1}	31	3.19	3.28	0.00	2.00	12.00	0.00	9.00
Radon flux density, background, mBq m^{-2} s^{-1}	31	2.74	2.66	0.00	2.00	12.00	0.00	4.00
April								
Air temp. °C	30	3.50	2.95	-1.90	3.40	11.00	-0.10	7.65
Soil temp. at 0 m, °C	30	3.91	0.90	1.20	4.05	5.30	2.85	5.10
Soil temp., at 0.5 m, °C	30	-0.43	0.13	-0.70	-0.40	-0.10	-0.60	-0.30
Soil temp., at 1 m, °C	30	-0.72	0.09	-0.90	-0.70	-0.60	-0.80	-0.60
Soil temp., at 1.5 m, °C	-	-	-	-	-	-	-	-
Radon flux density, control point, mBq m^{-2} s^{-1}	30	15.33	2.71	11.00	15.50	22.00	12.00	18.50
Radon flux density, background, mBq m^{-2} s^{-1}	30	14.27	1.80	10.00	14.00	18.00	12.00	16.00
May								
Air temp. °C	31	9.80	7.02	-0.90	7.30	25.40	2.30	19.30
Soil temp. at 0 m, °C	31	7.11	3.10	2.40	7.00	13.40	3.10	11.50
Soil temp., at 0.5 m, °C	31	1.29	1.99	-0.60	-0.10	4.50	-0.40	4.20
Soil temp., at 1 m, °C	31	-0.40	0.23	-0.80	-0.40	0.00	-0.70	-0.10
Soil temp., at 1.5 m, °C	-	-	-	-	-	-	-	-
Radon flux density, control point, mBq m^{-2} s^{-1}	31	28.19	7.12	12.00	29.00	38.00	18.00	36.00
Radon flux density, background, mBq m^{-2} s^{-1}	31	26.58	7.44	15.00	28.00	37.00	17.00	35.00
June								
Air temp. °C	30	16.67	3.95	8.80	17.00	23.60	11.50	21.85
Soil temp. at 0 m, °C	30	13.31	2.25	8.60	13.55	16.30	9.70	15.80
Soil temp., at 0.5 m, °C	30	8.87	2.68	4.00	9.75	12.00	4.40	11.65
Soil temp., at 1 m, °C	30	4.98	3.42	0.00	5.25	9.30	0.40	8.90
Soil temp., at 1.5 m, °C	20	2.43	2.26	-0.10	1.95	6.30	0.05	5.95
Radon flux density, control point, mBq m^{-2} s^{-1}	30	81.33	50.30	33.00	69.50	212.00	35.50	168.50
Radon flux density, background, mBq m^{-2} s^{-1}	30	33.80	2.12	30.00	34.00	38.00	30.50	36.00
July								
Air temp. °C	10	18.76	4.53	12.30	18.50	25.50	13.45	24.75
Soil temp. at 0 m, °C	10	15.73	0.84	14.20	16.10	16.40	14.25	16.40
Soil temp., at 0.5 m, °C	10	13.16	0.46	12.10	13.25	13.80	12.45	13.65
Soil temp., at 1 m, °C	10	8.69	0.52	8.00	8.50	9.50	8.10	9.40
Soil temp., at 1.5 m, °C	10	7.25	0.25	6.80	7.25	7.60	6.90	7.55
Radon flux density, control point, mBq m^{-2} s^{-1}	10	213.70	20.83	185.00	217.00	241.00	185.50	238.00
Radon flux density, background, mBq m^{-2} s^{-1}	10	33.50	2.42	29.00	34.00	36.00	29.50	36.00

RESEARCH PAPER

ANIMALS ON REGIONAL COATS OF ARMS IN RUSSIA: GEOGRAPHICAL ASPECTS

Dmitry A. Ruban[1,2*], Natalia N. Yashalova[3]
[1]Southern Federal University, 23-ja Linija Street 43, Rostov-on-Don 344019, Russia
[2]K.G. Razumovsky Moscow State University of Technologies and Management (the First Cossack University), Zemlyanoy Val Street 73, Moscow 109004, Russia
[3]Cherepovets State University, Sovetskiy Avenue 10, Cherepovets, Vologda Region 162600, Russia
***Corresponding author:** ruban-d@mail.ru
Received: February 3rd, 2022 / Accepted: August 8th, 2022 / Published: October 01st, 2022
https://DOI-10.24057/2071-9388-2022-014

ABSTRACT. The broadly-used official regional symbols allow increasing awareness of animals, which is essential to their effective conservation and ecotourism development. The presence of animals on the coats of arms of the Russian regions was evaluated. It was found that 49% of them show animal figures, and these regions constitute 76.3% of the country's territory. About twenty animals are shown on the analyzed coats of arms, of which 63% are mammals. The most common are bears (including polar), eagles, and martens. Some rare and endangered species like Amur (Siberian) tiger and Caucasian leopard are also shown. The majority of the regional coats of arms depict only one animal, while two or three animal figures appear together only in a few cases. The geographical distribution of the animals depicted on the regional coats of arms coincides only partly with the true zoogeographical patterns. This is an expected finding because coats of arms are elements of the cultural space, even if they represent natural features. Although the regional coats of arms reflect a small portion of the entity of Russian animals and the choice of animals does not always match the true conservation needs, this auxiliary 'channel' of promotion of the knowledge of animals appears to be valuable.

KEYWORDS: endangered species, geography of Russia, place branding

CITATION: Ruban D. A., Yashalova N. N. (2022). Animals On Regional Coats Of Arms In Russia: Geographical Aspects. 3(15), 19-26
https://DOI-10.24057/2071-9388-2022-014

ACKNOWLEDGEMENTS: The authors thank the editors and the reviewers for their support and helpful suggestions.

Conflict of interests: The authors reported no potential conflict of interest.

INTRODUCTION

Effective biodiversity conservation depends strongly on the broad public awareness of natural heritage values, vulnerability, endangered species, and other related issues. Various aspects of this topic were addressed by numerous experts, including Kassas (2002), Martín-López et al. (2009), Clements (2013), Lee and Iwasa (2014), Opermanis et al. (2015), Lundberg et al. (2019), and Dimopoulos and Kokkoris (2020). Additionally, the rich biodiversity of a given territory is an important ecotourism resource, rational exploitation of which also requires the increased awareness of visitors (Meletis and Harrison 2010; Olmsted et al. 2020; Abidin et al. 2021). Because of this, it appears to be highly important to actively promote the knowledge of territorial biodiversity through various 'channels' and with various approaches. Particularly, place branding techniques can become helpful (Jones et al. 2009; Hassan and Rahman 2015; Tam 2019). Linking key elements of biodiversity, including genera and species of animals and plants, to names and images of regions, cities, and other localities seems to be really helpful for increasing the public awareness of the wildlife heritage of a given territory. A good example can be found in Brazil where it is recommended to use flagship species for nature conservation needs (Wosnick et al. 2021).

Russia and its numerous territories can boast outstanding biodiversity, which is effectively conserved in nature (and biosphere) reserves, national parks, and other protected areas with federal and regional status. Their quantity reaches 12000 (with >100 nature reserves), and they occupy up to 14% of the country's territory (Marcot et al. 1997; Spetich et al. 2009; Bukvareva et al. 2015; Grebennikov 2016; Romanov et al. 2017). An increase in public awareness of particular elements of this biodiversity, including animal species, can positively influence further improvement in nature conservation practices. For instance, the public awareness campaign facilitated the conservation of saiga antelope (Howe et al. 2012). Another task is ecotourism development, which remains in low demand on the national scale (Ruban and Yashalova 2020), and the usage of place branding techniques for biodiversity promotion seems to be promising for its successful solution.

The Russian Federation consists of 85 administrative units, which include republics, regions, national districts, and cities of federal importance. Each of them has official symbols, including flags, songs, and coats of arms. The latter are complex and usually serve to reflect the regional identity, i.e., the specific features of the regional nature, culture, economy, achievements, and heritage. The coats of arms are designated officially by special regional legal acts. Their present versions were adopted in the post-Soviet times (after 1991), but some of them use elements from the symbols used in the Soviet period (1917–1991) and even earlier, during Tsarist times (before 1917). Regardless, these new symbols reflect the modern identity of the Russian regions. The regional coats of arms are actively used in official documents, at various meetings and exhibits, on house facades, on product labels, in mass media, etc. It is among their purposes to make the region well-identifiable and to stimulate regional pride. In other words, coats of arms contribute to a better awareness of the regional distinctive features by both locals and visitors. The presence of animals on coats of arms is common. Although their figuring sometimes follows heraldic traditions, which is typical of the national coats of arms (Wrona 2005), the marketing-related role of such symbols (Droulers 2016) makes them very useful to promote the knowledge of the regional wildlife, i.e., to link the key elements of biodiversity to regional brands. In Russia, such a heraldic tradition is strong, as a two-headed eagle has been depicted in its national coat of arms for centuries.

The main objective of the present study was to analyze the representation of animals on the coats of arms of the Russian regions as important biodiversity elements, addressing their geographical distribution and examining the potential of this specific, but promising and novel 'channel' of biodiversity promotion. This study only included animals for three reasons. First, animals can be identified with more precision than plants. Second, animals are more recognizable by the broad public. Third, such animals as bears are stereotypically associated with the image of Russia. More generally, this contribution was aimed at exploring the very possibility of using official regional symbols for increasing the public awareness of biodiversity. This possibility is linked to the information, which can be deduced from the official regional coats of arms. Notably, their general importance as brands that are well-visible to the local population and visitors is undisputable as the active use of the regional coats of arms in Russia is very common. This work specifically focused on the information about animals provided by these official symbols to the people (both locals and visitors).

MATERIALS AND METHODS

The officially designated coats of arms of all 85 Russian regions were checked for the presence of animal figures (the coats of arms can be found easily on the Internet, including web portals of regional administrations). Only real animals were considered in the study, mythic creatures were excluded as they cannot inform about biodiversity. All real animals were identified by their common names and actual Latin names. The majority of animals were identified to the level of genus, although species and even subspecies identification are also possible in several cases (official descriptions of the coats of arms facilitate such identification). There were also few animal figures, which could be identified only too generally (e.g., birds, fishes. etc.). All this information (Table 1) served as material for the present analysis.

Table 1. Animals in the coats of arms of the Russian regions (numbers are used on subsequent figures)

Regions (area, 10^3 km^2)	Animal	
	Common name	Latin name
1. Bashkortostan (142.9)	Horse	*Equus*
2. Belgorod (27.1)	Lion, Eagle	*Panthera leo, Aquila*
3. Chukotka (721.5)	Polar bear	*Ursus maritimus*
4. Chelyabinsk (88.5)	Camel	*Camelus*
5. Dagestan (50.3)	Eagle	*Aquila*
6. Evreyskaya (36.3)	Tiger	*Panthera tigris altaica*
7. Ingushetia (3.6)	Eagle	*Aquila*
8. Irkutsk (774.8)	Sable	*Martes zibellina*
9. Ivanovo (21.4)	Lion, Eagle	*Panthera leo, Aquila*
10. Kabardino-Balkaria (12.5)	Eagle	*Aquila*
11. Karelia (108.5)	Bear	*Ursus*
12. Khabarovsk (787.6)	Two bears, Tiger	*Ursus, Panthera tigris altaica*
13. Komi (416.8)	Wild bird, Six mooses	---, *Alces*
14. Krasnoyarsk (2366.8)	Lion	*Panthera leo*
15. Kurgan (71.5)	Marten	*Martes*
16. Kursk (30.0)	Three partridges	*Perdix*
17. Magadan (462.5)	Three fishes	---
18. Mordovia (26.1)	Fox	*Vulpes*
19. Nizhniy Novgorod (76.6)	Deer	*Cervus*

20. Novgorod (54.5)	Two bears, Two fishes	*Ursus*, ---
21. Novosibirsk (177.8)	Two sables	*Martes zibellina*
22. Orenburg (123.7)	Marten	*Martes*
23. Perm (160.2)	Bear	*Ursus*
24. Primorye (164.7)	Tiger	*Panthera tigris altaica*
25. Pskov (55.4)	Leopard	*Panthera pardus*
26. Ryazan (39.6)	Two horses	*Equus*
27. Sakha (Yakutia) (3103.3)	Horse	*Equus*
28. Samara (53.6)	Wild goat	*Capra*
29. Saratov (101.2)	Three sterlets	*Acipenser ruthenus*
30. Severnaya Ossetia – Alania (8.0)	Caucasian leopard	*Panthera pardus ciscaucasica*
31. Sverdlovsk (194.3)	Sable	*Martes zibellina*
32. Tambov (34.5)	Three bees	*Apis mellifera*
33. Tomsk (316.9)	Horse	*Equus*
34. Tyumen (1464.2)	Two sables	*Martes zibellina*
35. Tyva (168.6)	Horse	*Equus*
36. Vladimir (29.1)	Lion	*Panthera leo*
37. Voronezh (52.2)	Two eagles	*Aquila*
38. Udmurtia (42.1)	Swan	*Cygnus*
39. Ulyanovsk (37.2)	Two lions	*Panthera leo*
40. Yamalo-Nenets (769.3)	Two polar bears, Reindeer	*Ursus maritimus, Rangifer tarandus*
41. Yaroslavl (36.2)	Bear, Deer	*Ursus, Cervus*
42. Zabaykalye (431.9)	Eagle, Buffalo	*Aquila, Bubalus*

The analytical procedures were as follows (their simplicity is explained by the pioneering nature of this study). First, the share of the regional coats of arms reflecting animals was calculated. Second, the numbers of animal taxa and specimens on the coats of arms were addressed. Third, the abundance of animals on the regional coats of arms was assessed. For each animal, the number of regions with the relevant coats of arms, the presence in a given region and the entire country, and the status were established. The presence was registered with the overview by Litvinov et al. (2018) supplemented by various sources of biological information available online. As for the status, domesticated animals were distinguished from wild animals, and rare and endangered species of special concern were identified with the information from the World Wide Fund for Nature (Russia) (WWF (Russia) 2021). The noted indicators of abundance were measured for the entity of the considered regions, i.e., where animals appear on the coats of arms. These procedures formed the basis for further qualitative interpretation of the potential efficacy of the coats of arms for increasing the public awareness of biodiversity.

RESULTS

Of all 85 Russian regions, as many as 42 regions have coats of arms with figures of real animals (Table 1), i.e., the share of these regions is 49%. Importantly, they represent all main geographical domains of the country, including European Russia, the Russian South, the Urals, the Russian Arctic, Siberia, and the Russian Far East (Fig. 1). 81% of these regions have coats of arms with one animal, and the remaining 19% of the regions have coats of arms with two kinds of animals (Table 1). When two animals are shown, the most common combination is a bird and a mammal (Table 1). As for the number of animal specimens, one specimen of each animal is shown in the majority of cases. However, there are coats of arms showing two, three, and more specimens (Table 1). As many as six moose heads coupled with the wild bird figure symbolize the Republic of Komi, whereas two bears and two fishes symbolize the Novgorod Region.

The animals shown on the coats of arms of the Russian regions are quite numerous (Table 2). More common are mammals (63%), and less common are birds (21%), fishes (11%), and insects (5 %). Of the identified animals, the most typical are bears, including polar bears (17% of the regions), eagles (17% of the regions), and martens, including sables (14% of the regions). Horses and, surprisingly, lions (the latter do not occur in Russia) are also quite common on the coats of arms (12% of the regions each).

The regional coats of arms with bears are found in the western (European) part of Russia, the Russian Arctic, and the Russian Far East (Fig. 2). Bears really populate these territories and are widely known as a symbol of Russia. Eagles are typically represented on the coats of arms in

Fig. 1. Geographical distribution of the regional coats of arms with animal figures (regions with such coats of arms are marked as circles, with numbers explained in Table 1)

Table 2. Abundance of animals in the coats of arms of the Russian regions

Animal	Number of regions	Regional presence	National presence	Status notes
Bear (including polar)	7	Yes	Yes	Polar bear – WWF(R) (rare)
Bee	1	Yes	Yes	
Buffalo	1	Yes	Yes	Domesticated
Camel	1	Yes	Yes	Domesticated
Deer (including reindeer)	3	Yes	Yes	Reindeer – domesticated
Eagle	7	Yes	Yes	
Fish (unspecified)	2	Yes	Yes	
Fox	1	Yes	Yes	
Horse	5	Yes	Yes	Domesticated
Leopard (including Caucasian)	2	Yes (1 region)/No (1 region)	Yes	Caucasian – WWF(R) (rare)
Lion	5	No	No	
Marten / sable	6	Yes	Yes	
Moose	1	Yes	Yes	
Partridge	1	Yes	Yes	
Sterlet	1	Yes	Yes	WWF(R) (rare)
Swan	1	Yes	Yes	
Tiger	3	Yes	Yes	WWF(R) (rare)
Wild bird (unspecified)	1	Yes	Yes	
Wild goat	1	No	Yes	

Note: WWF(R) (rare) – rare species according to the World Wide Fund for Nature (Russia).

the southwest of the country (Fig. 2), although their actual distribution is much broader and embraces a significant part of Russia. Notably, eagles are often shown on the coats of arms of the mountainous republics of the Russian South (Dagestan, Ingushetia, and Kabardino-Balkaria), and are stereotypically associated with mountain environments. Martens are often found on the coats of arms from the Urals and West Siberia (Fig. 2). Although this animal populates these territories, it is also common in other parts of the country, mainly in East Siberia. Of the other animals of interest, tigers are typical to the southern part of the Russian Far East (Fig. 2), where they actually live.

Many animals from the regional coats of arms are actually present in the relevant regions (Fi. 3). Two regions employ animals (leopard in Pskov and wild goat in Samara), which do not occur in their territories but are known from

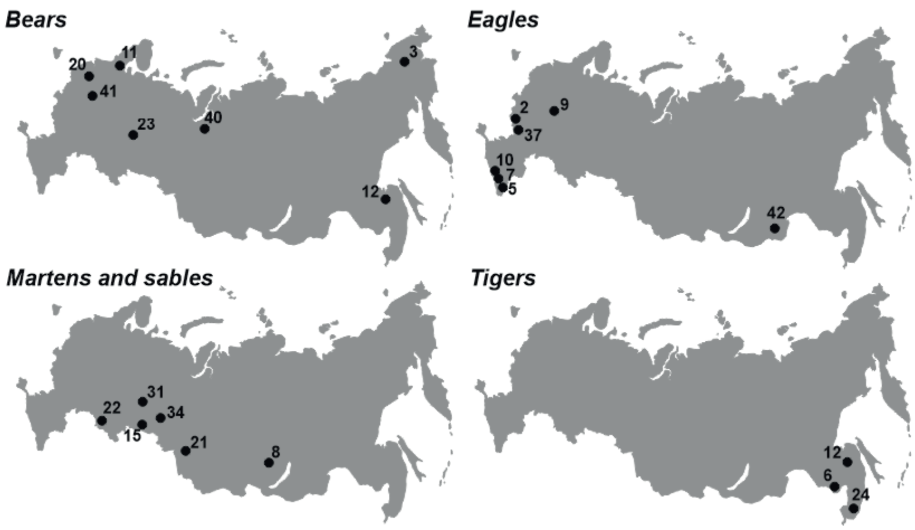

Fig. 2. Geographical distribution of the regional coats of arms with common animal figures (marked as circles, with numbers explained in Table 1)

other parts of the country. The animal, which is shown on many coats of arms, but does not occur either regionally or nationally, is a lion. Most probably, the use of this animal follows a very common heraldic tradition more typical for Western Europe (Wrona 2005). Four animals, including the popular horse, are domesticated, but the majority (84%) are wild. Four of them are recognized by the World Wide Fund for Nature (Russia) as rare and requiring conservation (WWF (Russia), 2021) (Table 2). Of them, Amur (Siberian) tigers and Caucasian leopards are subjects of special national conservation programs implemented in the Russian Far East (Miquelle 2015; Poddubnaya et al. 2021) and the Northern Caucasus (Kharchenko et al. 2019), respectively.

The regions considered in the present study are all official administrative units of the Russian Federation of the same level. Nonetheless, their difference in size is evident (Table 1). Some of them cover the area measured by millions of square kilometers, whereas the others cover only thousands of square kilometers, i.e., their size may differ by 1000 times. This factor also needs to be taken into account (Table 3).

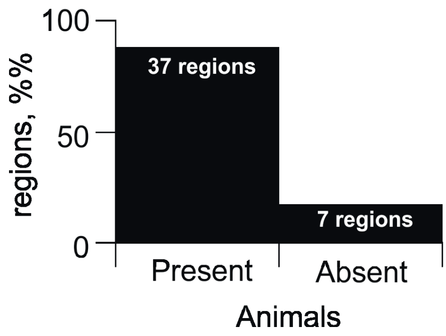

Fig. 3. The presence of the animals shown on the coats of arms in the respective region

Table 3. Abundance of animals in the coats of arms of the Russian regions

Animal	Number of regions	Total area of regions, 10^3 km^2	%% of the country's area
All	42	13074.5	76.3
Bear (including polar)	7	2637.8	15.4
Bee	1	34.5	0.2
Buffalo	1	431.9	2.5
Camel	1	88.5	0.5
Deer (including reindeer)	3	882.1	5.2
Eagle	7	599.0	3.5
Fish (unspecified)	2	517.0	3.0
Fox	1	26.1	0.2
Horse	5	3771.3	22.0
Leopard (including Caucasian)	2	63.4	0.4
Lion	5	2481.6	14.5
Marten / sable	6	2806.3	16.4
Moose	1	416.8	2.4

Partridge	1	30.0	0.2
Sterlet	1	101.2	0.6
Swan	1	42.1	0.2
Tiger	3	988.6	5.8
Wild bird (unspecified)	1	416.8	2.4
Wild goat	1	53.6	0.3

It can be seen that the regions showing animals on their coats of arms constitute more than three quarters of the total territory of Russia. Of wild animals from the coats of arms, martens and bears correspond to the largest territories, whereas eagles are 'less important' due to the small area of the regions showing them on their coats of arms (Table 3). Ironically, although bears are stereotypically associated with the image of Russia, it appears that martens deserve this 'status' a bit more. One should also note the very big territory of the regions depicting a horse on their coats of arms. This animal is not wild and does not need conservation as a biodiversity element. Lions, which do not occur in Russia, but are shown due to heraldic traditions, also represent large area (Table 3).

DISCUSSION AND CONCLUSION

The frequent placement of wild animals onto the regional coats of arms (taking into account the regional presence of these animals, as well as their abundance or rare status) means that the premises for such an important 'channel' of biodiversity promotion are already formed in Russia. Many coats of arms show wild animals representing the regional fauna. Often these are either symbolic mammals (for instance, bears stereotypically associated with Russia) or endangered species (for instance, Amur tigers and Caucasian leopards). The passive functioning of this 'channel' is supposed to be as follows. The regional coats of arms do not need any special promotion and governmental efforts – they already exist and are widely used in numerous official documents, at various meetings and exhibits, on house facades, on product labels, in mass media, etc. Their abundance in the socio-economic and information environment of each region is outstanding, and, thus, they are exceptionally well-visible to both the local population and visitors. The presence of animal figures on them makes these figures also well-visible and increases the awareness. Although special studies are necessary to analyze the actual people's perception of these symbols, it is logical to hypothesize a very significant contribution of the regional coats of arms to the awareness of the figured animals. This broad awareness is the first step towards wildlife conservation and its public support. There can also be active functioning of this 'channel' when a regional coat of arms is specially emphasized to draw the people's attention to the biodiversity awareness and conservation needs.

The preliminary analysis of Internet resources allowed us to find two examples of animals depicted on the regional coats being used for increasing biodiversity awareness in Russia. In the first case, the presence of a bear on the coat of arms of the Republic of Karelia has motivated a project at the local primary school aimed to study the natural and cultural-historical aspects of bears and their habitats (https://ppt-online.org/908629). In the second case, the coat of arms of the Primorye Region is considered as an important tool to stress the importance of tigers for regional heritage and identity (https://otvprim.tv/society/primorskij-kraj_15.09.2017_55785_proekt-tigrinaja-istorija-startuet-v-primorje.html?printr).

The validity of the proposed and similar 'channels' of biodiversity promotion linked to branding and labeling of goods and places is confirmed by other studies (Courchamp et al. 2018; Hooykaas et al. 2020; Good et al. 2021). The limitations of this 'channel' are as follows. First, some coats of arms depict animals that do not occur in the given regions or even entire Russia and, thus, are not suitable for promoting conservation on the regional scale, for example, leopards from Novgorod and lions from Ulyanovsk (Table 1). Second, the reflected biodiversity is biased (with too much focus on a few mammals, a part of which are domesticated) and incomplete. The number of regions and the possibility to show animal figures on coats of arms is too limited in comparison to the outstanding richness of the Russian biodiversity (e.g., Marcot et al. 1997; Spetich et al. 2009; Bukvareva et al. 2015; Grebennikov 2016; Romanov et al. 2017; Litvinov et al. 2018). Moreover, some regions prefer to be associated with domesticated, not wild animals. Third, the efficacy of the discussed 'channel' is restricted by the ability of the broad public to identify the animals correctly. While the figures of bears and tigers are easily recognizable, this may not be the case for moose heads, partridges, or sterlets. However, all three limitations are almost unavoidable, and the place (region) branding techniques are always auxiliary to other approaches (first of all, environmental education initiatives) aimed at increasing the biodiversity awareness of the broad public.

An important question is whether the wildlife representation by the regional coats of arms satisfies the present conservation needs in Russia. It should be noted that many animals represented in the analyzed coats of arms are quite common. Rare and endangered species (e.g., Litvinov et al., 2018) are also represented, but not so frequently (Table 2), despite the decline in some mammal species that is registered in Russia (Howe et al. 2012; Bragina et al. 2015), not speaking of birds, insects, invertebrates, etc. Moreover, the coats of arms seem to be more suitable for increasing the public awareness of animals, not plants. As explained above, the latter are difficult to identify, which contrasts with the urgent need for the conservation of many plant species in Russia (Nabieva and Elisafenko 2017; Chugunov and Khapugin 2020). Moreover, coat of arms can reflect only particular elements of biodiversity, not the entire biodiversity of a region. In fact, many areas need holistic conservation approaches (Marcot et al. 1997; Griffin 1999; Romanov et al. 2017; Shchelchkova and Boeskorov 2018). This means that the regional coats of arms can serve the needs of biodiversity conservation in Russia only partly. Nonetheless, their significant focus on animals (Table 1) makes them suitable to attract the attention of the broad public to the national wildlife, which itself is very important. This results from the abundant use of the regional coats of arms and, thus, their exceptional exposure to the public.

It is reasonable to add that the present study somewhat echoes the work by Wosnick et al. (2021) who analyzed flagship species in the Brazilian states. These approaches, differing in many details and applied to very different geographical domains, were developed independently, and their co-appearance signifies the international urgency of the studies of the regional animal symbols. One can even presume the emergence of a new research field at the intersection of zoogeography and place branding.

Conclusively, the coats of arms of the Russian regions should be considered as a valuable auxiliary instrument contributing to the public awareness of biodiversity and, particularly, animals as its key element. The finding of such potential is of general importance because it links the ideas of biodiversity conservation and place branding. The present study has also evident practical implications. First, new coats of arms of administrative units and settlements (where they did not exist previously) can be designed specially to include elements stimulating the public awareness of biodiversity if this issue is urgent in a given place. These procedures are controlled by the regional/local governments, and they can specify the pro-conservation requirements when they order a coat of arms. Second, the environmental and ecotourism initiatives in Russia should pay attention to the regional coats of arms and use this instrument for their own needs. Governmental support seems to be essential in this case, particularly in the context of the already launched 'Ecology' (Egorchenkov and Egorchenkov 2020; Semenova 2020) and the planned 'Tourism and Hospitality Industry' national projects. Third, the stakeholders responsible for the development of place branding strategies and/or eco-branding need to consider the potential of the regional coats of arms. In other words, the present findings can be important for improving and also integrating regional and environmental governance in Russia and beyond.

The present tentative study indicates the potential of the official regional symbols to increase the public awareness of biodiversity, which is important for nature conservation and ecotourism development. The perspectives of future research are linked to sociological surveys aimed at investigating the public perception of the regional coats of arms, i.e., their actual contribution to biodiversity awareness. This research should clarify whether the local population and visitors perceive the animals from the regional coats of arms as biodiversity elements and targets of conservation. Of interest is also whether these animals can be detected correctly by the broad public. However, even without these in-depth analyses, it is evident that future researchers should pay significant attention to conceptual developments concerning the relationship between regional branding, conservation needs and their geographical aspects. ■

REFERENCES

Abidin Z., Setiawan B., Muhaimin A.W. and Shinta, A. (2021). The role of coastal biodiversity conservation on sustainability and environmental awareness in mangrove ecosystem of southern Malang, Indonesia. Biodiversitas, 22, 648-658, DOI: 10.13057/biodiv/d220217.

Bragina E.V., Ives A.R., Pidgeon A.M., Kuemmerle T., Baskin L.M., Gubar Y.P., Piquer-Rodríguez M., Keuler N.S., Petrosyan V.G. and Radeloff V.C. (2015). Rapid declines of large mammal populations after the collapse of the Soviet Union. Conservation Biology, 29, 844-853, DOI: 10.1111/cobi.12450.

Bukvareva E.N., Grunewald K., Bobylev S.N., Zamolodchikov D.G., Zimenko A.V. and Bastian O. (2015). The current state of knowledge of ecosystems and ecosystem services in Russia: A status report. Ambio, 44, 491-507, DOI: 10.1007/s13280-015-0674-4.

Chugunov G.G. and Khapugin A.A. (2020). Population status of Bupleurum aureum (Apiaceae), a Critically Endangered plant species in a region of European Russia. Ecological Questions, 31, 45-56, DOI: 10.12775/EQ.2020.006.

Clements C.F. (2013). Public interest in the extinction of a species may lead to an increase in donations to a large conservation charity. Biodiversity and Conservation, 22, 2695-2699, DOI: 10.1007/s10531-013-0535-z.

Courchamp F., Jaric I., Albert C., Meinard Y., Ripple W.J. and Chapron G. (2018). The paradoxical extinction of the most charismatic animals. PLoS Biology, 16, e2003997, DOI: 10.1371/journal.pbio.2003997.

Dimopoulos P. and Kokkoris I.P. (2020). Protection and management of species, habitats, ecosystems and landscapes: Current trends and global needs. Forests, 11, 1244, DOI: 10.3390/f11121244.

Droulers O. (2016). Heraldry and brand logotypes: 800 years of color combinations. Journal of Historical Research in Marketing, 8, 507–523, DOI: 10.1108/JHRM-12-2014-0037.

Egorchenkov A.V. and Egorchenkov D.A. (2020). Social aspects of environmental issues in the context of the national project «Ecology». IOP Conference Series: Earth and Environmental Science, 579, 012099, DOI: 10.1088/1755-1315/579/1/012099.

Good C., Burnham D., Moorhouse T.P. and Macdonald D.W. (2021). Connecting the spots: Leopard print fashion and Panthera pardus conservation. Journal for Nature Conservation, 61, 125976, DOI: 10.1016/j.jnc.2021.125976.

Grebennikov K.A. (2016). Study of biodiversity of nature reserves of the Russia in the digital age: Experience and perspectives. Nature Conservation Research, 1, 1-10.

Griffin P.C. (1999). Endangered species diversity 'hot spots' in Russia and centers of endemism. Biodiversity and Conservation, 8, 497-511, DOI: 10.1023/A:1008837023242.

Hassan A. and Rahman M. (2015). World Heritage site as a label in branding a place. Journal of Cultural Heritage Management and Sustainable Development, 5, 210-223, DOI: 10.1108/JCHMSD-01-2014-0002.

Hooykaas M.J.D., Schilthuizen M. and Smeets I. (2020). Expanding the role of biodiversity in laypeople's lives: The view of communicators. Sustainability, 12, 2768, DOI: 10.3390/su12072768.

Howe C., Obgenova O. and Milner-Gulland E.J. (2012). Evaluating the effectiveness of a public awareness campaign as a conservation intervention: The saiga antelope Saiga tatarica in Kalmykia, Russia. Oryx, 46, 269-277, DOI: 10.1017/S0030605311001025.

Jones T., Nagata S., Nakajima M. and Masuyama K. (2009). Prefectural branding in Japan - Tourism, national parks and the Shinshu brand. Place Branding and Public Diplomacy, 5, 192-201, DOI: 10.1057/pb.2009.13.

Kassas M. (2002). Environmental education: Biodiversity. Environmentalist, 22, 345–351, DOI: 10.1023/A:1020766914456.

Kharchenko N., Voronin N. and Semenov U. (2019). Preliminary assessment of Chvizhepse and Sochi complex for potential recovery of Persian leopards. IOP Conference Series: Earth and Environmental Science, 226, 012005, DOI: 10.1088/1755-1315/226/1/012005.

Lee J.H. and Iwasa Y. (2014). Modeling socio-economic aspects of ecosystem management and biodiversity conservation. Population Ecology, 56, 27-40, DOI: 10.1007/s10144-013-0423-0.

Litvinov L.I., Litvinova E.A. and Litvinov M.B. 2018. Zoogeography. Vladivostok: Apelsin. (in Russian).

Lundberg P., Vainio A., Ojala A. and Arponen A. (2019). Materialism, awareness of environmental consequences and environmental philanthropic behaviour among potential donors. Environmental Values, 28, 741-762, DOI: 10.3197/096327119X15579936382527.

Marcot B.G., Ganzei S.S., Zhang T. and Voronov B.A. (1997). A sustainable plan for conserving forest biodiversity in Far East Russia and northeast China. Forestry Chronicle, 73, 565–571, DOI: 10.5558/tfc73565-5.

Martín-López B., Montes C., Ramírez L. and Benayas J. (2009). What drives policy decision-making related to species conservation? Biological Conservation, 142, 1370-1380, DOI: 10.1016/j.biocon.2009.01.030.

Meletis Z.A. and Harrison E.C. (2010). Tourists and turtles: Searching for a balance in Tortuguero, Costa Rica. Conservation and Society, 8, 26-43, DOI: 10.4103/0972-4923.62678.

Miquelle D.G. (2015). The Amur tiger in Northeast Asia: Conservation and ecology of an endangered subspecies. Integrative Zoology, 10, 311-314, DOI: 10.1111/1749-4877.12144.

Nabieva A.Yu. and Elisafenko T.V. (2017). Approaches to the conservation of Iris tigridia bunge – The endangered species of flora in Russia. Plant Cell Biotechnology and Molecular Biology, 18, 356-365.

Olmsted P., Honey-Rosés J., Satterfield T. and Chan K.M.A. (2020). Leveraging support for conservation from ecotourists: can relational values play a role? Journal of Sustainable Tourism, 28, 497-514, DOI: 10.1080/09669582.2019.1683184.

Opermanis O., Kalnins S.N. and Aunins, A. (2015). Merging science and arts to communicate nature conservation. Journal for Nature Conservation, 28, 67-77, DOI: 10.1016/j.jnc.2015.09.005.

Poddubnaya, N.Y., Salkina, G.P., Eltsova, L.S., Ivanova, E.S., Oleynikov, A.Yu., Pavlov, D.D., Kryukov, V.K. and Rumyantseva, O.Y. (2021). Mercury content in the Siberian tiger (Panthera tigris altaica Temminck, 1844) from the coastal and inland areas of the Russia. Scientific Reports, 11, 6923, DOI: 10.1038/s41598-021-86411-y.

Romanov A.A., Koroleva E.G. and Dikareva T.V. (2017). Integration of species and ecosystem monitoring for selecting priority areas for biodiversity conservation: Case studies from the Palearctic of Russia. Nature Conservation, 22, 191-218, DOI: 10.3897/natureconservation.22.10711.

Ruban D.A. and Yashalova N.N. (2020). Russian Ecotourism in International Research: Limited Literature Contrasts Rich Resources. e-Review of Tourism Research, 18, 22-44.

Semenova G. (2020). Global environmental problems in Russia. E3S Web of Conferences, 157, 02023, DOI: 10.1051/e3sconf/202015702023.

Shchelchkova M.V. and Boeskorov G.G. (2018). The relic steppes of Yakutia (Eastern Siberia, Russia)-unique ecosystems of the past (productivity, biological activity, protection). International Multidisciplinary Scientific GeoConference Surveying Geology and Mining Ecology Management, SGEM, 18, 949-956, DOI: 10.5593/sgem2018/5.1/S20.122.

Spetich M.A., Kvashnina A.E., Nukhimovskya Y.D. and Rhodes O.E., Jr. (2009). History, administration, goals, value, and long-term data of Russia's strictly protected scientific nature reserves. Natural Areas Journal, 29, 71-78, DOI: 10.3375/043.029.0109.

Tam C.-L. (2019). Branding Wakatobi: Marine development and legitimation by science. Ecology and Society, 24, 23, DOI: 10.5751/ES-11095-240323.

Wosnick, N., Leite, R.D., Giareta, E.P., Nunes, A.R.O.P., Charvet, P. and Monteiro-Filho, E.L.A. (2021). Evaluating conservation status and governmental efforts towards regional flagship species in Brazil. Journal of Environmental Management, 292, 112732, DOI: 10.1016/j.jenvman.2021.112732.

Wrona J. (2005). Regional similarities between national flags and coat of arms in the contemporary world. Czasopismo Geograficzne, 76, 201-213.

WWF (Russia). Rare species. URL: https://wwf.ru/species/ (Accessed on February 1, 2022).

RESEARCH PAPER

MEASURING TRAFFIC-RELATED AIR POLLUTION USING SMART SENSORS IN SRI LANKA: BEFORE AND DURING A NEW TRAFFIC PLAN

Mahesh Senarathna[1,2], Sajith Priyankara[3], Rohan Jayaratne[4], Rohan Weerasooriya[2], Lidia Morawska[4] and Gayan Bowatte[2,5,6*]

[1]Postgraduate Institute of Science, University of Peradeniya, Peradeniya 20400, Sri Lanka.
[2]National Institute of Fundamental Studies, Hantana Road, Kandy 20000, Sri Lanka.
[3]Department of Mathematics & Statistics, Texas Tech University, Lubbock, TX 79409, USA.
[4]International Laboratory for Air Quality and Health, Queensland University of Technology, Brisbane, QLD 4000, Australia.
[5]Allergy and Lung Health Unit, Melbourne School of Population and Global Health, University of Melbourne, Melbourne, VIC 3053, Australia
[6]Department of Basic Sciences, Faculty of Allied Health Sciences, University of Peradeniya, Peradeniya 20400, Sri Lanka.
***Corresponding author:** gayan.bowatte@ahs.pdn.ac.lk

Received: January 21st, 2021 / Accepted: August 8st, 2022 / Published: October 1st, 2022
https://DOI-10.24057/2071-9388-2022-011

ABSTRACT. Motor vehicle emissions are the primary air pollution source in cities worldwide. Changes in traffic flow in a city can drastically change overall levels of air pollution. The level of air pollution may vary significantly in some street segments compared to others, and a small number of stationary ambient air pollution monitors may not capture this variation. This study aimed to evaluate air pollution before and during a new traffic plan established in March 2019 in the city of Kandy, Sri Lanka, using smart sensor technology. Street level air pollution data ($PM_{2.5}$ and NO_2) was acquired using a mobile air quality sensor unit before and during the implementation of the new traffic plan. The sensor unit was mounted on a police traffic motorcycle that travelled through the city four times per day. Air pollution in selected road segments was compared before and during the new traffic plan, and the trends at different times of the day were compared using data from a stationary smart sensor. Both $PM_{2.5}$ and NO_2 levels were well above the World Health Organization (WHO) 24-hour guidelines during the monitoring period, regardless of the traffic plan period. Most of the road segments had comparatively higher air pollution levels during compared to before the new traffic plan. For any given time (morning, midday, afternoon, evening), day of the week, and period (before or during the new traffic plan), the highest $PM_{2.5}$ and NO_2 concentrations were observed at the road segment from Girls High School to Kandy Railway Station. The mobile air pollution monitoring data provided evidence that the mean concentration of $PM_{2.5}$ during the new traffic plan (116.7 μg m^{-3}) was significantly higher than before the new traffic plan (92.3 μg m^{-3}) ($p < 0.007$). Increasing spatial coverage can provide much better information on human exposure to air pollutants, which is essential to control traffic related air pollution. Before implementing a new traffic plan, careful planning and improvement of road network infrastructure could reduce air pollution in urban areas.

KEYWORDS: air quality, mobile air quality sensors, particulate matter, road traffic

CITATION: Senarathna M., Priyankara S., Jayaratne R., Weerasooriya R., Morawska L. and Bowatte G. (2022). Measuring Traffic-Related Air Pollution Using Smart Sensors In Sri Lanka: Before And During A New Traffic Plan. Geography, Environment, Sustainability, 3(15), 27-36
https://DOI-10.24057/2071-9388-2022-011

ACKNOWLEDGEMENTS: We acknowledged the Sri Lanka National Science Foundation for providing funds (grant number: RG/2019/BS/01). This study was partially supported by a seed grant from the Australian National Health and Medical Research Council's Centre for Air pollution, energy, and health Research (CRE-CAR). We gratefully acknowledge the support of the National Institute of Fundamental Studies (NIFS) and participation of the traffic unit of Kandy Police Station.

Conflict of interests: The authors reported no potential conflict of interest.

INTRODUCTION

Air pollution is a major global public health issue. According to the World Health Organization (WHO), approximately 7 million people die annually from air pollution exposure (World Health Organization (WHO), 2014), and it is the leading environmental risk factor associated with the global burden of disease. In addition, exposure to polluted air leads to the development and exacerbations of respiratory and cardiovascular diseases

(Pope III et al. 2002), lung cancer (Vineis et al. 2006) and multiple additional diseases. The majority of deaths related to outdoor air pollution occur in South and South-East Asia (HEI International Scientific Oversight Committee, 2010). Despite this, regular mandatory air monitoring in urban environments in South Asian countries is sparse.

In cities and towns across the globe, Traffic-Related Air Pollution (TRAP) is the primary source of air pollution (Matz et al. 2019). Traffic plans have often been changed to ease road congestion in urban areas. These changes in traffic flow can impact air pollution levels, either increasing or decreasing them or making no change at all. Previous research has evaluated ambient air pollution levels using stationary monitors in a limited number of selected areas before and after establishing new traffic plans (Atkinson et al. 2009). However, most of these studies did not evaluate air pollution in different street segments. Air pollution levels may vary significantly in some street segments compared to others. Measuring average ambient air pollution using a low number of stationary monitors may not capture the actual spatial variation of air pollution in the study area. The standard air pollution monitors are expensive, and developing countries like Sri Lanka do not have the funds to establish the required number of monitoring stations to measure air pollution. The development of small sensor technology offers an attractive alternative solution where air pollution can be monitored at a low cost. These sensors have several advantages over standard monitoring stations, such as; they are versatile and can be customized to suit different requirements, including mobile air pollution monitoring. Previous studies have reported the implementation of smart sensors in a mobile air pollution framework. A vehicular wireless sensor network architecture was implemented at the National Chiao-Tung University in Taiwan (Hu et al. 2009), and researchers in Seoul, South Korea, mapped urban air quality using mobile sampling with low-cost sensors and machine learning (Lim et al. 2019). The public buses in Sharjah city, United Arab Emirates, were also used to test an air pollution sensing network (Al-Ali et al. 2010) while in New Jersey and New York, the United States, a fine-grained vehicular-based mobile air pollution measuring technique using solid-state carbon monoxide (CO) sensors and optical analysers (PM) was used to measure 'on road' pollution (Devarakonda et al. 2013). In the city centre of Uppsala, Sweden, an experimental study was conducted on real-time air pollution monitoring using wireless sensors on public vehicles (Kaivonen and C-H Ngai, 2020).

Evaluation of air pollutants in cities along the roads provides the true levels of emissions generated by vehicles as well as the exposure levels to commuters, pedestrians, and individuals who live or work close to these roads. To the best of our knowledge, there has been no traffic-related mobile air pollution monitoring study published in Sri Lanka to date. This study aimed to monitor and evaluate traffic-related air pollution on the roads of Kandy city, Sri Lanka, before and during a new traffic plan.

MATERIALS AND METHODS

Study area

In this study, we focused on measuring, monitoring, and comparing air pollution levels on the roads of Kandy city before and during a new traffic plan was installed. On average, air pollution in and around the city of Kandy is known to be higher compared to other cities in Sri Lanka (Seneviratne et al. 2017) due to it being located in a basin and surrounded by mountains. We measured air pollution on the main roads (where the main traffic flow occurs) of the city of Kandy, including the three main traffic access routes to the Kandy Municipal area (total area of 28.53 Km^2) (Fig. 1.).

The new traffic plan in the city of Kandy

The new traffic plan converted two previously two-way roads, both of which took traffic towards and away from the city (Figure 1, Old Peradeniya Road and William Gopallawa Mawatha), into one-way roads. The new traffic plan meant that all vehicles travelling to Kandy from Peradeniya had to enter William Gopallawa Mawatha, and all vehicles leaving Kandy towards Peradeniya had to use the Old Peradeniya Road. The new traffic planed commenced on 2nd March 2019 for six days,

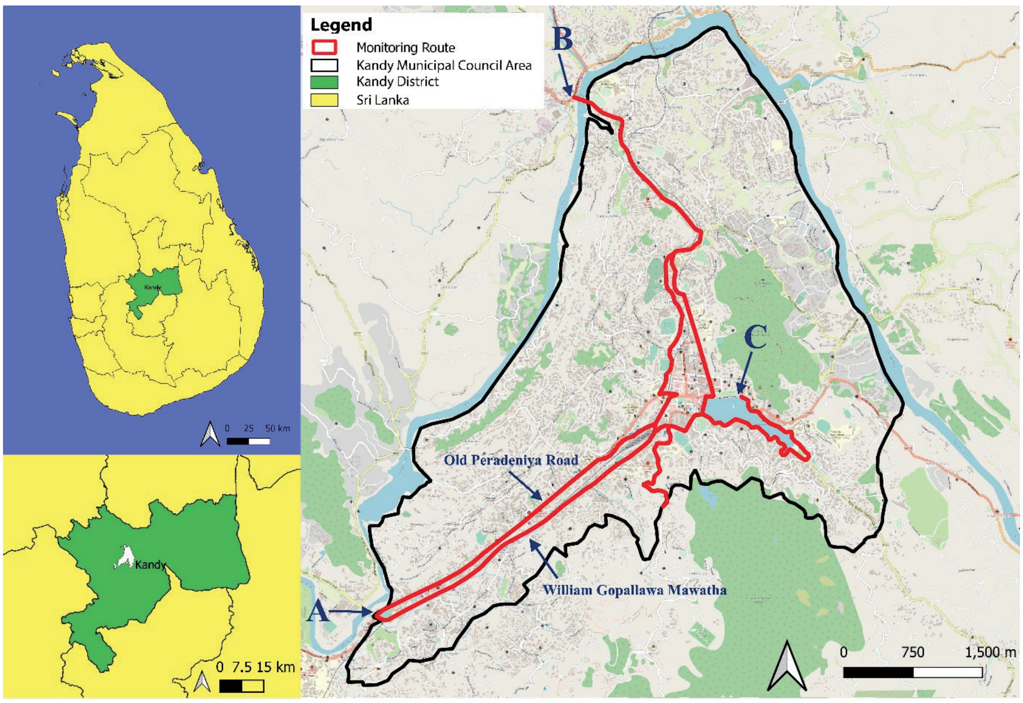

Fig. 1. Study Area; Study area was in and around the Kandy city roads. A- via Peradeniya, B – via Katugastota, and C- via Tennekumbura: three main traffic access to Kandy city

ending on 7th March 2019. Here we defined the period "Before" the new traffic plan as 23rd February 2019 to 28th February 2019, and "During" as 2nd March 2019 to 07th March 2019. Although the change was only made to two roads, the traffic flow of the entire city was affected.

Mobile air pollution monitoring

This study used a small, low-cost mobile air quality measurement device called «Sniffer4D». Sniffer4D (Soarability Technologies Co. Ltd) is used for high-end air quality mapping based on aerial and ground vehicles. It provides real-time operational information such as 2D grid air pollution distribution heat maps, 3D points cloud pollutant distribution heat maps, automated operation report generation, and readable comma-separated value file exports of raw data. The device can be carried by moving vehicles and has an anti-electromagnetic interference carbon fibre casing, an internal suspension mechanism, and an active ventilation system. It transfers geotagged and timestamped air pollution data to analytic software in real-time. The device is integrated with an inhalable particulate matter (PM) sensing module, which detects particles by the laser scattering method, while a high-resolution Nitrogen Dioxide (NO_2) sensing module detects particles up to 5ppb (Specifications of Sniffer4D Mobile Air Quality Mapping System (2019 . 08 . 05), 2019). Each sensing module was calibrated according to its intrinsic properties, and Sniffer4D's performance has been evaluated by a Chinese national-level metrology institute (Sniffer4D – Sniffer4D – Mobile Air Poluttant Mapping System, n.d.).

In this study, we measured Particulate Matter < 2.5 µm in diameter ($PM_{2.5}$) and NO_2. Data were collected by attaching the Sniffer4D device to a police traffic motorcycle before and during the new traffic plan was in effect. Data were collected before and during the new traffic plan. Monitoring was conducted at regular time intervals – morning (7.00 am – 10.00 am), midday (10.00 am – 1.00 pm), afternoon (1.00 pm – 4.00 pm) and evening (4.00 pm – 7.00 pm). The sensor unit was mounted vertically on the motorcycle's handlebars (Fig. 2.) so that the exhaust plume of the bike did not influence the readings.

Fig. 2. Sniffer 4D sensor mounted on a police traffic motorcycle

The motorcycle's speed was maintained at less than 20 km per hour at all times. When moving along the roads, sniffer4D provides a geographic location (longitude, latitude, and elevation), temperature, humidity, $PM_{2.5}$, and NO_2 concentration at each point at intervals of 1 second.

Stationary air pollution monitoring

The background ambient $PM_{2.5}$ concentration was monitored before and during the new traffic plan with the "Knowing Our Ambient Local Air-quality" (KOALA) air quality device located at the National Institute of Fundamental Studies (NIFS), Kandy (Sri Lanka). KOALA is a low-cost small air quality sensor unit developed by the Queensland University of Technology, Australia. The KOALA sensors unit have already been tested against standard air quality instruments (Liu, Jayaratne, et al. 2020) and successfully used in previous research on air pollution in several countries (Jayaratne et al. 2020; Liu, Zhao, et al. 2020), including in Sri Lanka (Priyankara et al. 2021; Senarathna et al. 2021).

Statistical analysis

Roads were selected based on the main traffic flow. All roads where the main traffic flow was toward the city was included, and the selected roads were divided into 17 road segments (Fig. 3 and Table 1) based on road length, geographic features, and road traffic conditions using ArcGIS (version 10.5. Redlands, CA: Environmental Systems Research Institute, Inc. 2010).

Fig. 3. Categorization of road segments in Kandy city

Point data values of air pollutants ($PM_{2.5}$, NO_2) on each road segment were averaged for each time interval (morning, midday, afternoon and evening) using the ArcGIS software to evaluate the variation of pollutants during the study period. Due to the non-normality of meteorology data, the non-parametric Mann-Whitney U test was performed to evaluate the difference between before and during the new traffic plan was implemented.

To identify air pollution variations in the before and during periods, graphs were plotted by averaging the concentrations of pollutants in each road segment. The paired t-test was used to compare air pollution levels obtained from a mobile air pollution sensor device (Sniffer 4D) before and during the new traffic plan. Further, patterns and trends of air pollution were evaluated. Pollutant data obtained from the KOALA stationary monitor unit were not normally distributed. Therefore, the non-parametric Wilcoxon Signed Rank test was performed to compare the pollutant concentrations before and during the new traffic plan. All statistical tests were conducted using R studio software (RStudio Team, 2020) (version 1.3.1056).

Table 1. Road segments identified in Kandy city

Buffer ID	Details of the road segment
1	Getambe Junction- Mulgampola Junction (Old Peradeniya Road)
2	Getambe Junction – Mulgampola Junction (New Kandy Road)
3	Mulgampola Junction – Kandy Railway Station
4	Mulgampola Junction – Girls' High School
5	Girls' High School – Kandy Railway Station
6	Hantana Road
7	Baladaksha Mawatha + Keppetipola Road
8	Kandy Railway Station – Clock Tower
9	Bogambara Road
10	Clock Tower – Kandy Police Station
11	Lake Round – EL Senanayake Children's Park
12	EL Senanayake Children's Park – Dalada Maligawa
13	Dalada Maligawa – Lake Round
14	Kandy Jaffna Road – Welikanda Railway Station
15	Kandy Police Station – Welikanda Railway Station
16	Welikanda Railway Station – St. Anthony's Boys College
17	St. Anthony's Boys College – Katugasthota

RESULTS

The average $PM_{2.5}$ and NO_2 concentrations of the 17 road segments before the new traffic plan is shown in Fig. 4(A). The highest average $PM_{2.5}$ concentration before the new traffic plan was implemented was at road segment ID 5 (Girls' High School to Kandy Railway Station), and the lowest was at road segment ID 15 (Kandy Police Station to Welikanda Railway Station). The highest and the lowest average NO_2 concentration before the new traffic plan was in road segment ID 5 (Girls' High School to Kandy Railway Station) and road segment ID 2 (Getambe Junction to Mulgampola New Kandy Road), respectively. Average $PM_{2.5}$ and NO_2 concentrations during the new traffic plan by road segment ID are provided in Fig. 4(B). For any given day/any time session, the highest average $PM_{2.5}$ concentration during the new traffic plan was at road segment ID 5 (Girls' High School to Kandy Railway Station) and lowest at road segment ID 6 (Hantana Road). During the new traffic plan, the highest average NO_2 concentration was at road segment ID 5 (Girls High School to Railway Station) and the lowest at road segment ID 15 (Kandy Police Station to Welikanda Railway Station).

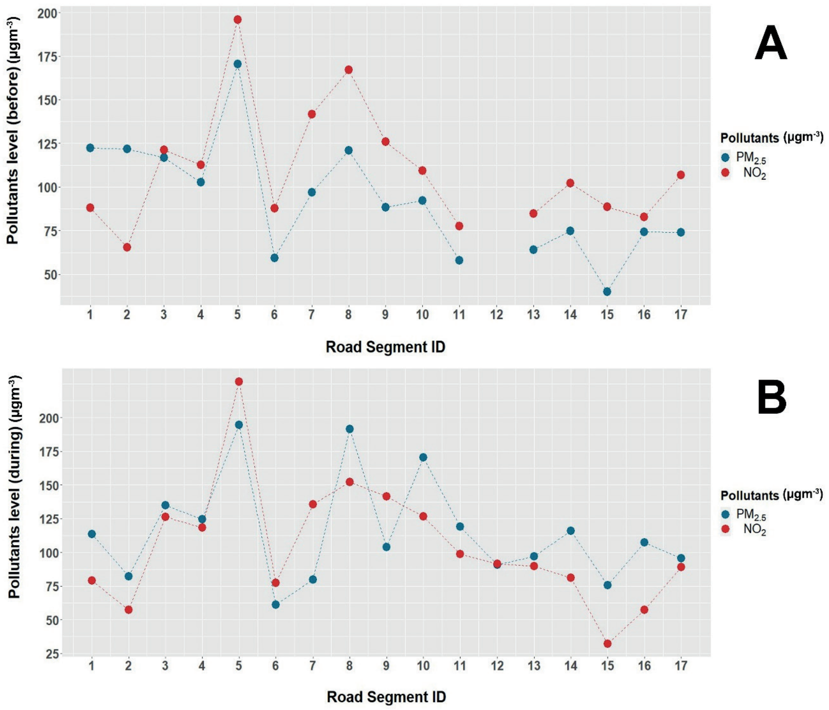

Fig. 4. Temporal changes in the RFD at the control and background points

Fig. 5. shows the average $PM_{2.5}$ variations on each time interval during the new traffic plan. For example, the Morning average indicates the morning average pollution concentration of all days during the new traffic plan by each road segment ID. During the new traffic plan, the average $PM_{2.5}$ was the highest in the morning (131.24 µg m^{-3}), followed by evening (111.67 µgm^{-3}), afternoon (110.27 µg m^{-3}) and midday (106.28 µg m^{-3}).

Average $PM_{2.5}$ and NO_2 levels before and during the new traffic plan by road segment ID is shown in Fig. 6. The results showed a significant increase in PM2.5 concentration during (M = 116.71 µg m^{-3}, SD = 9.86) compared to before (M = 92.32 µg m^{-3}, SD = 8.22), t (15) = -3.14, $p < 0.007$ (two-tailed) the new traffic plan. The mean increase of PM2.5 concentration was 24.39 µgm^{-3} (95% CI: 7.84 to 40.94). The eta square statistic of 0.39 indicated a large effect size. For NO_2, there was no significant difference during (M = 105.58 µg m^{-3}, SD = 46.76) compared to before (M = 109.87 µg m^{-3}, SD = 34.61), t (15) = 0.806, p = 0.433 (two-tailed) the new traffic plan. The average $PM_{2.5}$ and NO_2 at each road segment is shown in Table S1. For stationary air pollution, the Wilcoxon Signed Rank test revealed a statistically significant increment of $PM_{2.5}$ concentration during compared to before the new traffic plan, z = -6.689, p = 0.001, with a small effect size (0.127).

There was no significant difference in total rain between the traffic plan periods (z= -0.408, p = 0.689) and, similarly, there was no significant difference for relative humidity (z = -1.41 p = 0.159). Fig. S1. shows the variation of meteorology data (relative humidity, temperature, wind speed) before and during the new traffic plan. A comparison of average ambient $PM_{2.5}$ variations before and during the new traffic plan for each day is shown in Fig.S2. Fig. S3 shows a comparison of the daily variation of the average ambient $PM_{2.5}$ for the monitoring period; comparatively high levels of $PM_{2.5}$ were recorded during the new traffic plan in the evening times. Summary statistics of KOALA data are shown in Table S2. Fig. 7. shows a scatter plot of average $PM_{2.5}$ variation at 17 road segments before and during the new traffic plan. The background $PM_{2.5}$ concentration measured by the KOALA increased by 13.6% during the new traffic plan period compared to before, the corresponding average $PM_{2.5}$ concentration on the roads increased by 21%. There was a high correlation between $PM_{2.5}$ in each road segment before and during the new traffic plan $R^2 = 0.93$ (Figure 7).

DISCUSSION

We found that $PM_{2.5}$ levels were consistently well above the WHO standard in the city of Kandy during both traffic plan periods. For any given time period (morning, midday, afternoon, evening), day of the week, or period (before or during new traffic plan), the highest $PM_{2.5}$ and NO_2 concentrations were observed at the road from Girls' High School to Kandy Railway station (Road Segment ID 5). We found the lowest $PM_{2.5}$ concentrations at Hantana road (Road Segment ID 6) and the Kandy Police station to Welikanda Railway Station (Road Segment ID 15) both before and during the traffic plan.

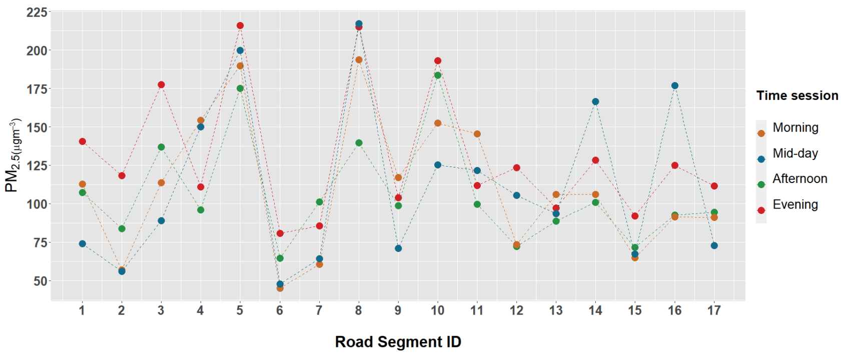

Fig. 5. Average $PM_{2.5}$ variations in each time period during the new traffic plan

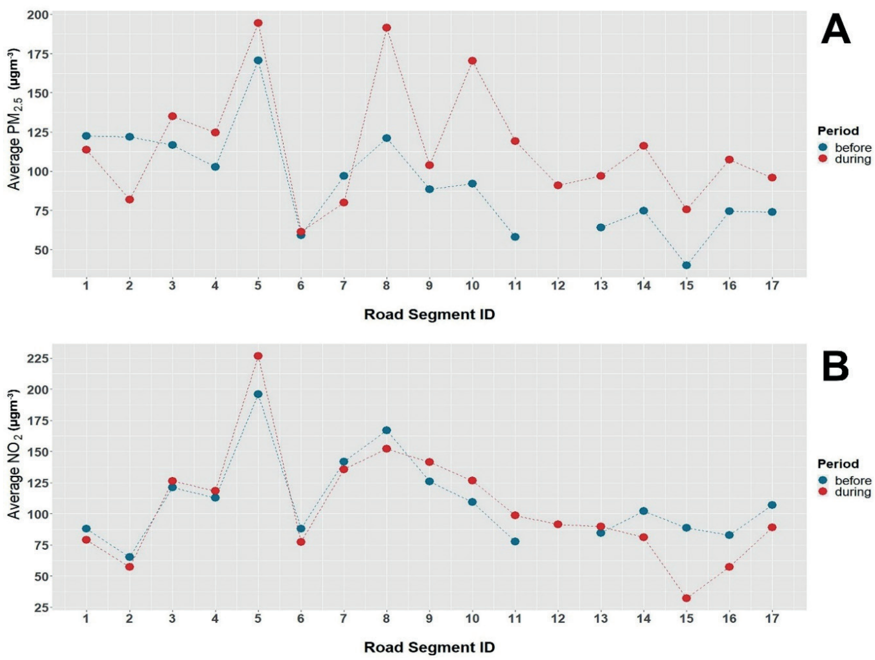

Fig. 6. $PM_{2.5}$ (A) and B) NO_2 (B) level by Road Segment ID before and during the new traffic plan

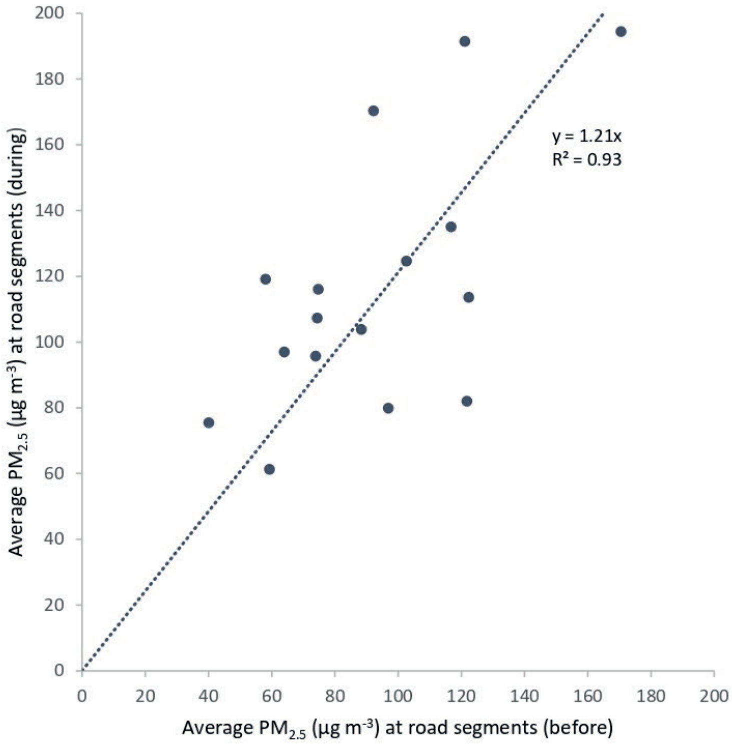

Fig. 7. Scatter plot of average $PM_{2.5}$ variation at 17 road segments, before and during the new traffic plan

Heavy traffic conditions are usually present on the road from Girls' High School to the Kandy Railway Station) as the main bus stop in Kandy is located there. The road segments where we observed comparatively low pollution levels have a smooth traffic flow. Previous studies revealed that the morning and evening times, associated with the two rush-hour periods, had the highest $PM_{2.5}$ concentrations compared to midday and afternoon in Kandy (Senarathna et al. 2019). The KOALA stationary monitor captured this, where diurnal $PM_{2.5}$ average concentration showed two similar spikes in $PM_{2.5}$ levels, one in the morning and the other in the evening rush hours.

The majority of roads had comparatively higher pollution concentrations during the new traffic plan period than before the traffic plan was implemented. Average $PM_{2.5}$ values from the KOALA stationary monitors showed higher air pollution during the new traffic plan than before. Before implementing the new traffic plan, traffic jams were created mainly in the city centre and immediate surroundings. However, during the new traffic plan, substantial traffic congestion was observed on the roads beyond the city centre as well. When comparing the effect of the new traffic plan on levels of ambient $PM_{2.5}$ in Kandy, we observed an increase of approximately 6 μgm^{-3} (13.6%). However, this increase was approximately 24 µgm-3 (21%) at the street level, indicating a more significant detrimental impact in terms of $PM_{2.5}$ air pollution. The increased $PM_{2.5}$ in the street and ambient levels may have been due to increased vehicle exhaust with slow-moving traffic. Overall, there was a slight increase in NO_2 at the street level before and during the new traffic plan, but this was not statistically significant.

The influence of the precipitation and $PM_{2.5}$ concentration in the atmosphere has been discussed elsewhere (Z. Liu et al. 2020). When considering the region's meteorological conditions, the average temperature in Sri Lanka is higher in March and April. Total precipitation was also lower during that time. This study was conducted only for two weeks in March, and the influence of the mereological conditions was assumed to be the same during the study period.

Over the last decade, smart low-cost sensors have been rapidly adopted for air quality monitoring. Different types of wireless sensor network-based air pollution monitoring systems and their advantages disadvantages have been extensively discussed elsewhere (Khedo and Chikhooreeah 2017). The most significant advantage of vehicular sensor networks over traditional static sensor networks is their ability to conduct measurements over large areas with a small number of sensor nodes. One sensor node can achieve sufficient sizeable geographic coverage by utilizing low-cost portable ambient sensors and the mobility of vehicles(Gaglio and Lo Re 2014). In 2009 Wong et al. (Wong et al. 2009) discussed the advantages of mobile sensing by mounting sensor nodes onto vehicles and several studies have suggested that vehicles could be used to create large-scale air quality monitoring systems. For example, the Mobile Air Quality Monitoring Network (MAQUMON) is a system made up of solid-state sensor nodes mounted on cars that measure CO, NO_2, and O_3. An onboard GPS is used to tag air pollution with precise location and time data. The data is uploaded to a server via a Wi-Fi connection regularly (Völgyesi et al. 2008). Although the vehicle sensor network system for air quality monitoring is very cost-effective with high geographical and coverage technology, there has been no such air quality monitoring study in Sri Lanka to date. Our mobile air quality data can be used by city planners, population health professionals, education leaders, and transportation managers to inform policy and influence decision-making. Although there are many strengths, we also acknowledge some limitations to our study. For example, some data point locations were missed as a result of weak GPS signal strength and only a single mobile sensor unit was used throughout the monitoring period. Having more sensor units would have allowed us to take measurements more frequently and cover additional road segments throughout the city.

CONCLUSIONS

This study showed the spatial characteristics of $PM_{2.5}$ pollution variation before and during a new traffic plan in Kandy, Sri Lanka. Overall, the levels of $PM_{2.5}$ in the city of Kandy were consistently much higher than WHO standards, and changes in traffic plans comparatively increased $PM_{2.5}$ levels on many road segments. Prior to implementing a new traffic plan, careful planning and improvement of road infrastructure should be considered to potentially reduce air pollution in urban areas. Extensive spatial coverage of air quality monitoring by mobile sensor networks enables to determine the level of population air pollution exposure and consider that in traffic planning. Good traffic plans make day-to-day tasks easier while also enhancing the health benefits of its citizens by improving air quality.

REFERENCES

Al-Ali A.R., Zualkernan I. and Aloul F. (2010). A mobile GPRS-sensors array for air pollution monitoring. IEEE Sensors Journal, 10(10), 1666-1671, DOI: 10.1109/JSEN.2010.2045890.

Atkinson R.W., Barratt B., Armstrong B., Anderson H.R., Beevers S.D., Mudway I.S., Green D., Derwent R.G., Wilkinson P. and Tonne C. (2009). The impact of the congestion charging scheme on ambient air pollution concentrations in London. Atmospheric Environment, 43(34), 5493-5500, DOI: 10.1016/j.atmosenv.2009.07.023

Devarakonda S., Sevusu P., Liu H., Liu R., Iftode L. and Nath B. (2013). Real-time Air Quality Monitoring Through Mobile Sensing in Metropolitan Areas. January.

Gaglio S. and Lo Re G. (2014). Urban Air Quality Monitoring Using Vehicular Sensor Networks. Advances in Intelligent Systems and Computing, 260, 311-323, DOI: 10.1007/978-3-319-03992-3

HEI International Scientific Oversight Committee. (2010). Outdoor air pollution and health in the developing countries of Asia: a comprehensive review. Special report 18. Health Effects Institute, Boston, November.

Hu S.C., Wang Y.C., Huang C.Y. and Tseng Y.C. (2009). A vehicular wireless sensor network for CO^2 monitoring. Proceedings of IEEE Sensors, 1498-1501, DOI: 10.1109/ICSENS.2009.5398461

Jayaratne R., Kuhn T., Christensen B., Liu X., Zing I., Lamont R., Dunbabin M., Maddox J., Fisher G. and Morawska L. (2020). Using a Network of Low-cost Particle Sensors to Assess the Impact of Ship Emissions on a Residential Community. Aerosol Air Qual. Res, 20(12), 2754-2764, DOI: 10.4209/aaqr.2020.06.0280

Kaivonen S. and C-H Ngai E. (2020). Real-time air pollution monitoring with sensors on city bus, DOI: 10.1016/j.dcan.2019.03.003

Khedo K.K. and Chikhooreeah V. (2017). Low-Cost Energy-Efficient Air Quality Monitoring System Using Wireless Sensor Network. Wireless Sensor Networks – Insights and Innovations, DOI: 10.5772/intechopen.70138

Lim C.C., Kim H., Vilcassim M.J.R., Thurston G.D., Gordon T., Chen L.C., Lee K., Heimbinder M. and Kim S.Y. (2019). Mapping urban air quality using mobile sampling with low-cost sensors and machine learning in Seoul, South Korea. Environment International, 131(March), 105022, DOI: 10.1016/j.envint.2019.105022

Liu X., Jayaratne R., Thai P., Kuhn T., Zing I., Christensen B., Lamont R., Dunbabin M., Zhu S., Gao J., Wainwright D., Neale D., Kan R., Kirkwood J. and Morawska L. (2020). Low-cost sensors as an alternative for long-term air quality monitoring. Environmental Research, 185, 109438, DOI: 10.1016/j.envres.2020.109438

Liu X., Zhao Q., Zhu S., Peng W. and Yu L. (2020). An experimental application of laser-scattering sensor to estimate the traffic-induced PM2.5 in Beijing. Environ. Monit. Assess, 192(7), DOI: 10.1007/s10661-020-08398-9

Liu Z., Shen L., Yan C., Du J., Li Y. and Zhao H. (2020). Analysis of the Influence of Precipitation and Wind on $PM_{2.5}$ and PM_{10} in the Atmosphere. Advances in Meteorology, 2020, 5039613, DOI: 10.1155/2020/5039613

Matz C.J., Egyed M., Hocking R., Seenundun S., Charman N. and Edmonds N. (2019). Human health effects of traffic-related air pollution (TRAP): a scoping review protocol. Systematic Reviews, 8(1), 223, DOI: 10.1186/s13643-019-1106-5

Pope III C.A., Burnett R.T., Thun M.J., Calle E.E., Krewski D. and Thurston G.D. (2002). to Fine Particulate Air Pollution. The Journal of the American Medical Association, 287(9), 1132–1141, DOI: 10.1001/jama.287.9.1132

Priyankara S., Senarathna M., Jayaratne R., Morawska L., Abeysundara S., Weerasooriya R., Knibbs L.D., Dharmage S.C., Yasaratne D. and Bowatte G. (2021). Ambient $PM_{2.5}$ and PM_{10} Exposure and Respiratory Disease Hospitalization in Kandy, Sri Lanka. In: International Journal of Environmental Research and Public Health , Vol. 18, Issue 18, DOI: 10.3390/ijerph18189617

RStudio Team. (2020). RStudio: Integrated Development Environment for R. http://www.rstudio.com/

Senarathna M., Jayaratne R., Morawska L., Guo Y., Knibbs L.D., Abeysundara S., Weerasooriya R. and Bowatte G. (2021). Impact of COVID-19 lockdown on air quality of Sri Lankan cities. International Journal of Environmental Pollution and Remediation, 9, 12-21.

Senarathna M., Priyankara S., Jayaratne R., Morawska L. and Gayan B. (2019). Monitoring the air quality in Kandy using smart sensor technology. NIFS-Young Scientists' Symposium on Multidisciplinary Research.

Seneviratne S., Handagiripathira L., Sanjeevani S., Madusha D., Waduge V.A.A., Attanayake T., Bandara D. and Hopke P.K. (2017). Identification of sources of fine particulate matter in Kandy, Sri Lanka. Aerosol and Air Quality Research, 17(2), 476–484, DOI: 10.4209/aaqr.2016.03.0123

Sniffer4D – Sniffer4D – Mobile Air Poluttant Mapping System. (n.d.). http://sniffer4d.eu/sniffer4d/

Specifications of Sniffer4D Mobile Air Quality Mapping System (2019 . 08 . 05), 4 (2019).

Vineis P., Hoek G., Krzyzanowski M., Vigna-Taglianti F., Veglia F., Airoldi L., Autrup H., Dunning A., Garte S., Hainaut P., Malaveille C., Matullo G., Overvad K., Raaschou-Nielsen O., Clavel-Chapelon F., Linseisen J., Boeing H., Trichopoulou A., Palli D., … Riboli E. (2006). Air pollution and risk of lung cancer in a prospective study in Europe. International Journal of Cancer, 119(1), 169-174, DOI: 10.1002/ijc.21801

Völgyesi P., Nádas A., Koutsoukos X. and Lédeczi Á. (2008). Air quality monitoring with SensorMap. Proceedings – 2008 International Conference on Information Processing in Sensor Networks, IPSN 2008, 529-530, DOI: 10.1109/IPSN.2008.50

Wong K.J., Chua C.C. and Li Q. (2009). Environmental monitoring using wireless vehicular sensor networks. Proceedings – 5th International Conference on Wireless Communications, Networking and Mobile Computing, WiCOM 2009, 9-12, DOI: 10.1109/WICOM.2009.5303846

World Health Organization (WHO). (2014). 7 million deaths linked to air pollution annually NIEHS : Public Health, Environmental and Social Determinants of Health (PHE), 63. https://www.who.int/phe/eNews_63.pdf

APPENDICES

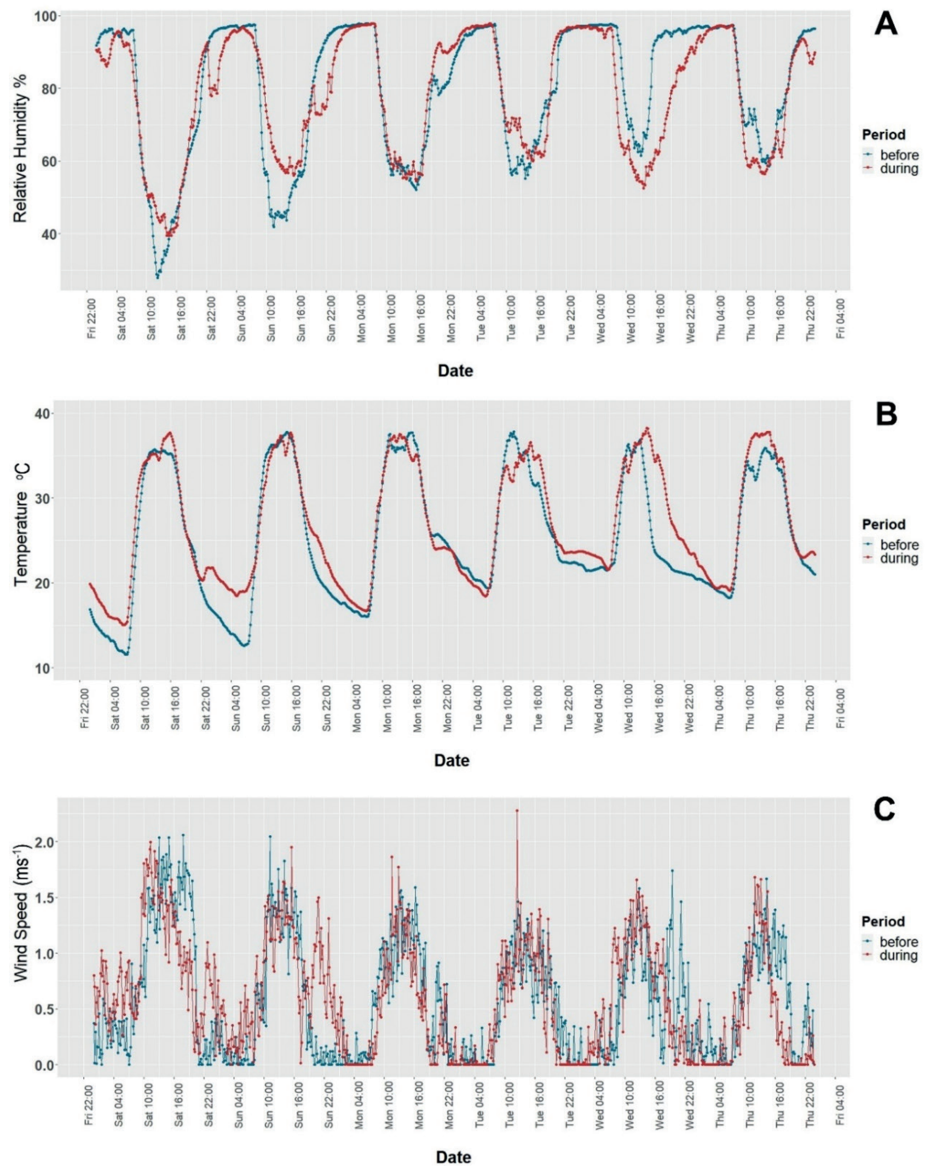

Fig. S1. Comparison of meteorology data variations before (2019-02-23 to 2019-02-28) and during the new traffic plan (2019-03-02 to 2019-03-07) on Relative Humidity (A), Temperature (B) and Wind speed (C)

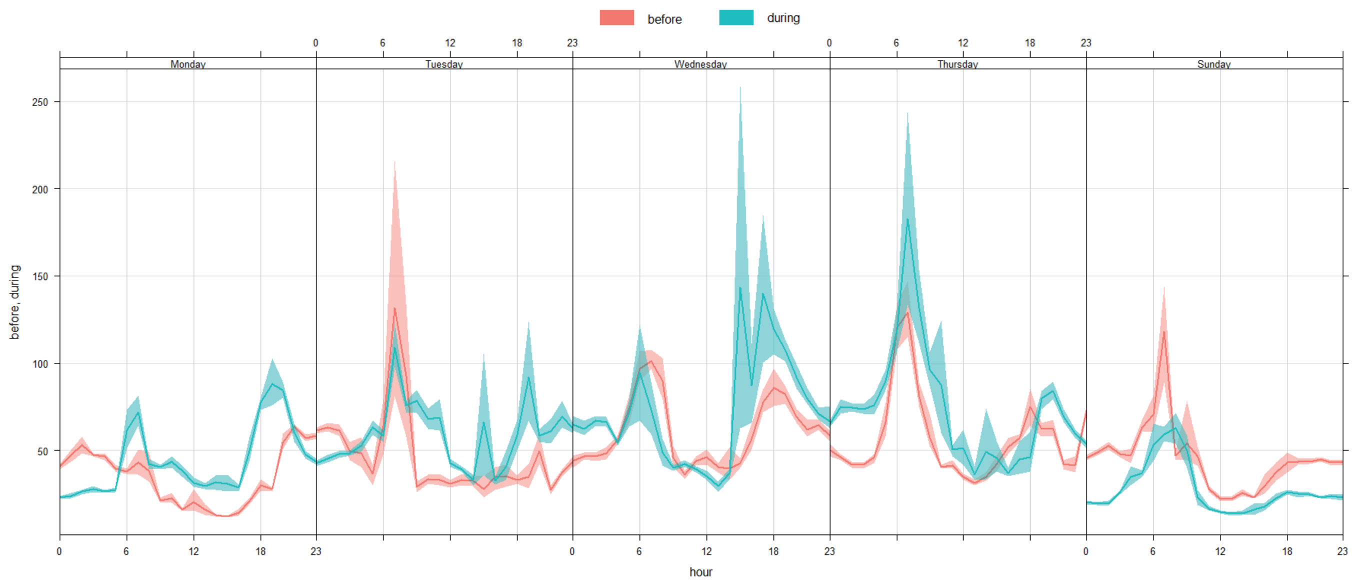

Fig. S2. Comparison of average $PM_{2.5}$ variations before and during the new traffic plan for each day of the study period

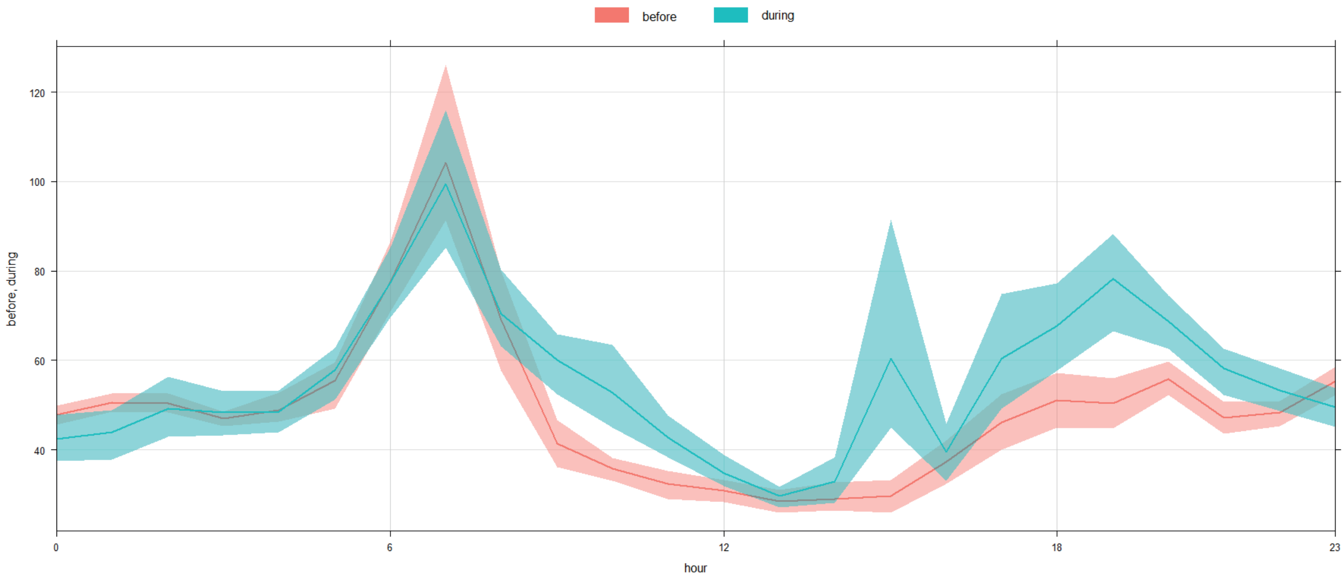

Fig. S3. Comparison of average daily PM2.5 representations before and during the new traffic plan

Table S1. Average pollutant levels at each road segment before and during the new traffic plan

	$PM_{2.5}$ (μgm^{-3})		NO_2 (μgm^{-3})	
Road Segment ID	before	during	before	during
1	122.34	113.65	88.01	79.12
2	121.79	81.99	65.42	57.18
3	116.79	135.02	121.24	126.40
4	102.61	124.63	112.72	118.26
5	170.52	194.47	195.88	226.69
6	59.29	61.26	87.91	77.23
7	96.90	79.86	141.73	135.63
8	121.07	191.45	167.14	152.19
9	88.36	103.86	125.95	141.66
10	92.17	170.38	109.36	126.57
11	58.07	119.13	77.53	98.56
12		90.85		91.32
13	64.00	96.96	84.66	89.89
14	74.73	116.06	102.23	81.12
15	40.06	75.47	88.60	32.22
16	74.40	107.32	82.71	57.39
17	73.93	95.76	106.89	89.11

Table S2. Summary statistics of KOALA data on PM2.5 before and during the new traffic plan

	Traffic plan period	
	Before	During
Mean	48.62	55.23
Standard Deviation	28.525	39.000
Percentile 25	34.00	31.00
Percentile 50	44.00	47.00
Percentile 75	57.00	70.00

RESEARCH PAPER

H/A/α POLARIMETRIC DECOMPOSITION OF DUAL POLARIZED ALOS PALSAR FOR EFFICIENT LAND FEATURE DETECTION AND BIOMASS ESTIMATION OVER TROPICAL DECIDUOUS FOREST

Suman Sinha[1]
[1]Department of Geography, Amity University Kolkata, Newtown, Kolkata, West Bengal, India.
***Corresponding author:** sumanrumpa.sinha@gmail.com
Received: August 13th, 2021 / Accepted: August 8th, 2022 / Published: October 01st, 2022
https://DOI-10.24057/2071-9388-2021-095

ABSTRACT. Information regarding land use and land cover is an important for formulating decision making for land information system. The easiest and most effective way to gather such information is via using Earth observation remote sensing satellites supported by ground data. Synthetic Aperture Radar (SAR), due to its additional unique intrinsic characteristics is favoured over the optical systems for procuring land information. An innovative and effective technique for land feature detection is the use of polarimetric capabilities of SAR. Generally applicable for quad polarized data, this study investigates the polarimetric capabilities of a dual polarized data obtained from ALOS PALSAR, which is not a general notion. The approach applied in the study shows accurate results for detection of land features using polarimetric decomposition of dual polarized ALOS PALSAR data over an area of Munger in the state of Bihar, India. Twelve distinct land cover features are identified in the study area using this approach. The polarimetric products are also investigated for deriving the biomass information for the vegetation cover in the study area. The relation between in-situ biomass generated from floral species-specific volumetric equations and SAR polarimetric products showed a moderate correlation of 0.56 with RMSE=29.13 t/ha and data agreement of 0.62 based on exponential regression model for predicting biomass. The decomposition parameters revealed more evidences for forest structure and feature identification rather than biomass information. The method adopted in the study can be well utilized for land resource information and mapping; hence, natural and man-made resource monitoring and management.

KEYWORDS: SAR, ALOS PALSAR, polarimetric decomposition, LULC, biomass

CITATION: S. Suman (2022). H/A/α Polarimetric Decomposition Of Dual Polarized Alos Palsar For Efficient Land Feature Detection And Biomass Estimation Over Tropical Deciduous Forest. Geography, Environment, Sustainability, 3(15), 37-46
https://DOI-10.24057/2071-9388-2021-095

ACKNOWLEDGEMENTS: The author sincerely thanks JAXA (Japan Aerospace Exploration Agency, Japan) for providing the ALOS PALSAR data and SAC (Space Application Centre, ISRO, Ahmedabad, India) for providing facilities to process the PALSAR data.

Conflict of interests: The authors reported no potential conflict of interest.

INTRODUCTION

Forest is an important component of the carbon cycle that reflects the state and health of our environment (Usoltsev et al. 2019). The emerging climate change concept of reducing emissions from deforestation and forest degradation (REDD) comprises of the temporal change in the assessment of forest biomass/carbon stock (Sharma et al. 2013). Above ground biomass (AGB) serves as the major carbon pool (Englhart et al. 2012). Successful implementation of REDD targets in the precise and accurate enumeration of biomass/carbon estimates (Sinha and Santra 2019). Development of forest inventories with field-generated measurements provides the most accurate means for AGB estimation using allometric equations (Sinha et al. 2021).

In-spite of its high quality, the field-based method is arduous, time consuming, and difficult to apply in inaccessible areas with limited spatial information, which are prominent drawbacks in the assessment (Lu 2006). In contrary, the ability of satellite remote sensing to cover extensive and remote areas made this technique a better approach for AGB estimation, however with lesser accuracy in the assessment in comparison to forest inventorization (Lu et al. 2016).

The use of optical sensors for the forest structure (Chopping et al. 2012), and biomass assessment (Kumar et al. 2013), involves early saturation in the estimates, specifically for mature forests (Lu et al. 2012: JFR). Thermal sensors too have limited use though relationship do exist between the surface temperature and biomass (Sinha and Sharma 2013). Microwave synthetic aperture radar (SAR) sensor has the potential to give better estimates of biomass in comparison to optical sensors, due to its unique capability of canopy penetration leading to volumetric scattering and its interaction to surface roughness and moisture content even during adverse climatic conditions (Sinha et al. 2015a). Recent studies reveal the importance of L-band SAR for forest biomass estimation due to its interaction with larger components of vegetation (Sinha et al. 2019a, 2020a).

The range of retrievable AGB from L-band ALOS PALSAR data is 40–150 t/ha (Englhart et al. 2011; Sinha et al. 2016). Integrated use of multi-frequency SAR data have shown even better results (Sinha et al. 2019b). Inability of the interferometric coherence information has led to the exploration of polarimetric decomposition analyses for forest biomass assessment (Sinha et al. 2015b). Multi-polarized SAR data has great utility in land cover feature detection (Sinha et al. 2020b). Polarimetry helps in image coherence decomposition to different scattering mechanisms and removes the azimuth slopes induced by the orientation angle (Sinha 2016).

The distinct property of polarimetry adds to the potentiality of SAR that deals with the polarization state of the electromagnetic field. Polarimetric Synthetic Aperture Radar (PolSAR) advanced instrument used in remote sensing that plays an important role in understanding the electromagnetic phenomenology related to the complex targets and also the respective SAR image interpretation using the scattering mechanism of these complex targets (Gomathi et al. 2021). Several coherent and incoherent target decomposition methods have been developed to understand these target-specific scattering mechanisms. H/A/α decomposition proposed by Cloude-Pottier helps in understanding the dichotomies of different targets (Kumar and Raghav 2018). H/A/α decomposition of dual-pol SAR data simplifies the complex multi-parameter depolarization of quad-pol SAR data and reduces the high data processing requirement and storage issues. The improved Cloude-Pottier decomposition is widely used for segmentation and classification purposes (Ji and Wu 2015). Dual polarized SAR data has wide ranged application (Abimanyu et al. 2021), specially in land feature extractions (Sinha et al. 2018a). The relatively easy data availability from spaceborne dual polarimetric SAR missions, like ASAR, Sentinel-1 and PALSAR with wider swath and greater temporal availability has more applicability (Potin et al. 2014).

The use of models developed with polarimetric decompositions is mainly limited to image classification (Avtar et al. 2011), rather than vegetation studies (Maity et al. 2011) and biomass assessment (Tanase et al. 2013). New SAR projects, for instance, NISAR (a collaborative project of NASA and ISRO) have been planned to explore the polarimetric capabilities, with a prime target of ecosystem-related studies including forest biomass estimation. Taking into consideration the urgency and importance of such technique, the objective of this study is to investigate potential relationship between forest biomass with certain polarimetric scattering parameters (PSP) products generated from polarimetric target decomposition techniques and explore its capability to predict biomass.

MATERIALS AND METHODS

Study area and datasets

The study area of Munger forests is situated in the state of Bihar, India having geographic extent of 25º19'30"N–24º56'50"N latitudes and 86º33'33"E–86º11'51"E longitude as illustrated in Figure 1. Land use and land cover (LULC) analysis shows that nearly 89% of the area is covered under forest out of which the dominant forest types are mixed; Shorea robusta (Sal), Acacia catechu (Khair) and *Dendrocalamus* sp. (Bamboo) forests. Munger forest division comprises reserved and protected forests of nearly 257.50 km^2 and 424.40 km^2 respectively; henceforth, the area under investigation comprises nearly 672.5 km^2 and the detailed LULC study of the area is performed (Sinha et al. 2013). Along with the survey of India (SOI) toposheets, ALOS PALSAR L-band dual HH/HV (FBD) polarized imagery dated 27th July, 2010 was used in the study.

METHODOLOGY

Field Measurements

Field investigation was carried out to collect the training data during the same period of the SAR image acquisition.

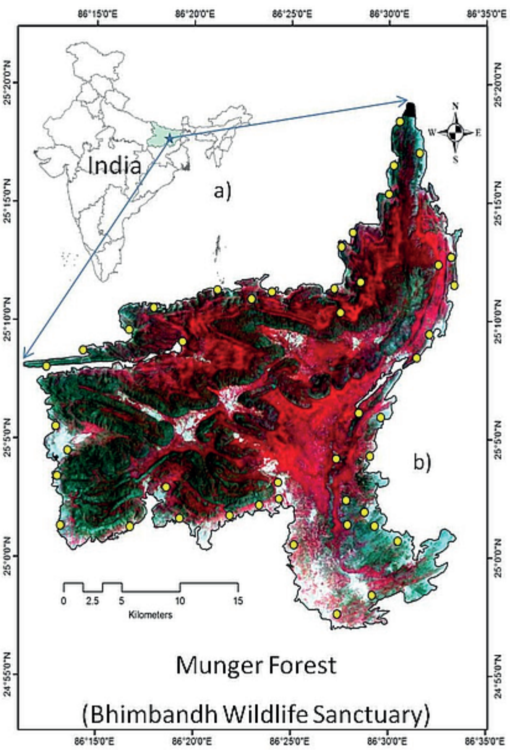

Fig. 1. Location of the study area

The training field data were used to establish the models for biomass estimation and serves as reference for SAR derived estimated biomass. Topographic sheets of 1:50,000 scale formed the base map for field inventory where a total of 45 square plots of 0.1 ha were laid from which primary data related to tree species name, height, girth at breast height (GBH), diameter at breast height (DBH), etc. for all trees above 10 cm DBH were carried out. Out of the total 45 sample plots, 36 plots were randomly selected for model development whereas the remaining nine plots were used for model validation. Information regarding the geographic location (latitude/longitude) of the sample plots was recorded using global positioning system (GPS) and imported in GIS mode.

Field Estimation of Biomass

Standard procedure for biomass estimation using volumetric equation was followed (Sinha et al. 2018b; Malik et al. 2020). For estimation of tree volume in the sample plots, local and general equations reported by forest survey of India were used. Tree GBH (converted to DBH) and tree height values were fed to the species-specific volumetric equations. The volume was then multiplied with specific gravity of the corresponding species to obtain biomass of individual trees. Individual tree biomass of all species in a plot was summed up to get biomass of the plot. This was done for all the 45 sample plots. The regional volumetric equation and specific gravity of major vegetation species type has been listed in Table 1. Here, V is the volume under bark (m^3), D is the diameter over bark at breast height (m), and H is the tree height (m); all measured in SI units.

SAR Polarimetric Decomposition

Polarimetric decompositions characterize the image in terms of its scattering mechanism. The two forms of decompositions: the coherent decomposition dealing with decomposition of the scattering matrix, and the incoherent decomposition dealing with decomposition of coherency or covariance matrices. In coherent decomposition, like Pauli decomposition, a single discrete scatterer produces a fully polarized wave.

The incoherent decomposition, H/A/α (entropy, anisotropy, alpha) decomposition uses coherency matrix, and coherent decomposition, Pauli decomposition technique uses scattering matrix expressed in Pauli basis were used in the study. Span gives the total power received from all the polarimetric channels. Hence, the following major steps were undertaken:

- Scattering matrix,
- Covariance and coherency matrices,
- Polarimetric decomposition (Pauli and H/A/α decomposition), and
- Geocoding.

H/A/α decomposition was developed by Cloude and Pottier using the second-order statistic-based smoothing algorithm (Gomathi et al. 2021). Eigenvector analysis of the coherency matrix [T] involving the eigenvalues distribution and the characterization of the scattering mechanism, is used. Each feature on ground behaves as an unique scatterer and the process of scattering is analyzed through the decomposition using eigenvectors and their respective relative magnitudes using eigenvalues (Pottier et al. 2008). The basics of polarimetric scattering mechanisms developed on a quad-pol data (Yonezawa et al. 2012) needs to be modified for dual-pol data.

L-band is sensitive to the small surface variations as well as show penetration in the canopy layer (Sinha et al. 2015a). Pauli images are in fact RGB images constructed from Pauli decomposition that necessitates the use of an orthogonal set of polarization data. Although, HH/HV is not an orthogonal set of data hence does not represent Pauli elements. Under monostatic conditions, the coherent decomposition of the scattering mechanisms is assessed by the Pauli decomposition. In this case, the PolSARPro software has been instructed and forced to generate polarimetric decompositions in order to visualize, investigate and interpret the outputs from the dual polarized data. Hence, the term 'PSRFBD False RGB composite' is used for Pauli RGB generated, simultaneously, the terms 'PSRFBD H/A/α and 'PSRFBD Span' is used for H/A/α decompositions and span respectively.

The general elements of the scattering matrix [S] for fully polarized SAR data are defined as

$$[S]=\begin{bmatrix} S_{HH} & S_{HV} \\ S_{VH} & S_{VV} \end{bmatrix} \tag{1}$$

Table 1. Volumetric equations and specific gravity for calculating biomass (FSI 1996)

Botanical Name	Volume Equation	Specific Gravity (ρ)
Acacia catechu	$V=0.21612-4.16597*D+24.50948*D^2-29.6773*D^3$	0.97
Adina cordifolia	$V=0.0052355+0.55615*D^2H$	0.62
Anogeissus latifolia	$V=0.020760+0.447658*D^2H$	0.89
Boswellia serrata	$V=2.091911*D+0.18818*D^2H-0.200382$	0.57
Buchanania lanzan	$V=0.017+0.381*D^2H$	0.56
Dendrocalamus strictus#	$\ln(AGB)=2.487+0.414*(\ln(\rho D^2H))$	1.1
Diospyros melanoxylon	$V=0.400004*D^2H-0.007336$	1.1
Madhuca latifolia	$V=0.275*D^2H-0.014$	0.94
Semecarpus anacardium	$V=(1.67477+14.83747*D-9.43386*\sqrt{D})^2$	0.62
Shorea robusta	$V=0.375132*D^2H-0.004092$	0.74
Sterculia urens	$V=0.27909-3.26515*D+13.46829*D^2$	0.57
Terminalia tomentosa	$V=0.42823*D^2H-0.002149$	0.84

where, V=Volume under bark (m3), D=Diameter at breast height (m), H= Tree height (m).

The scattering matrix [S] for the HH/HV dual polarized (FBD) L-band ALOS PALSAR data is modified accordingly and expressed as

$$[S]=\begin{bmatrix} S_{HH} & S_{HV} \\ 0 & 0 \end{bmatrix} \quad (2)$$

The dual polarimetric mode has horizontal transmission and horizontal received in HH polarization, while horizontal transmission and vertical received in HV polarization. Hence, the corresponding scattering vector for the HH/HV dual polarimetric data can be expressed as

$$[S_{HH} 2S_{HV}]^T \quad (3)$$

T in eq. 3 refers to the transpose of matrix. Thereafter, the coherency matrix derived, and its decomposition can be represented in eqs. 4 and 5 respectively.

$$\langle T\rangle=\frac{1}{L}\sum_{i-1}^{L}k_i k_i^H \quad (4)$$

$$\langle T\rangle=\sum_{i-1}^{q}\lambda_i u_i u_i^H \quad (5)$$

where, L is the number of looks, ki is the i th look of sample k (i =1, 2), H is the complex conjugate transpose, q is the number of polarized channels, λi is the eigen value of <T>, ui is the eigen vector and <.> is the assembly average. The averaged polarimetric scattering mechanism described by entropy H, alpha angle (α) and probabilities obtained from eigenvalues (anisotropy, A) is derived via POLSARPro based on the HH/HV dual polarized L-band SAR data.

'Span' gives the total power received from the four polarimetric channels. Span of [S] is expressed as $|S_{HH}|^2+|S_{VV}|^2+2|S_{HV}|^2$ which is converted to $|S_{HH}|^2+|S_{HV}|^2$ for HH/HV dual polarized data.

Biomass and PSP relationships

Figure 2 depicts the overall methodology for estimating AGB using SAR polarimetric decomposition using the ALOS PALSAR dataset. Remote sensing image processing software is used to extract the values of the polarimetric decomposition parameters and establish a relation between the polarimetric scattering parameters (PSPs) and the field-based plot AGB.

Regression Modeling

The model is generated from the 36 sample plot field-based data. The equation is used for calculating the biomass with information of Span as generated from the L-band ALOS PALSAR data and equated with the estimated 09 sample plot field-based data that are kept for evaluation of the model. The model is statistically validated with the nine additional field AGB data and the corresponding statistical measures that include coefficient of determination (R2), root mean square error (RMSE), mean absolute deviation (MAD), mean bias error (MBE), non-dimensional RMSE (NDRMSE), non-dimensional MAD (NDMAD), non-dimensional MBE (NDMBE), average absolute accuracy (ς) and Willmott's index of agreement (d) are executed (Santra et al. 2021, Sinha et al. 2016).

RESULTS

Field Measurements for AGB Estimation

Field-based AGB estimations showed the highest biomass accumulation for the Shorea robusta (sal) mixed forests of 172.07 t/ha (t/ha equivalent to Mg/ha) and thereafter for the mixed Acacia catechu (khair) forests with high density canopy cover. The minimum value of 11.35 t/ha occurred for the low density canopy cover of the Acacia catechu (khair), Dendrocalamus sp. (bamboo) mixed forests. The average and standard deviation (SD) of the AGB estimation value for all the plots was observed to be 72.94 and 41.15 t/ha respectively. The high SD indicates that the data points are spread out over a large range of values and the sample has large variation of data.

Polarimetric Analysis for LULC

The polarimetric decomposition analysis is used to identify the land cover features so as to separate the forest areas from the non-forested regions efficiently. The different scattering mechanisms occurring over the test study area shown by the PSRFBD False RGB composite is represented in Figure 3 and is specific for distinct features on ground. The figure shows an area marked in red that is zoomed in Figure 4 showing distinct land features. The following land features are identified: road, river, forest/vegetation, bare soil, built-up, man-made structures and agricultural fields. The Google Earth images of the features are shown in Figure 5 so as to visually compare the feature on ground as seen from high resolution satellite image to that obtained as signatures from PSRFBD False RGB composite image. On the other hand, Figure 6 shows the PSP products generated in the area. Most of the forested areas show that α values, depicting the dominant

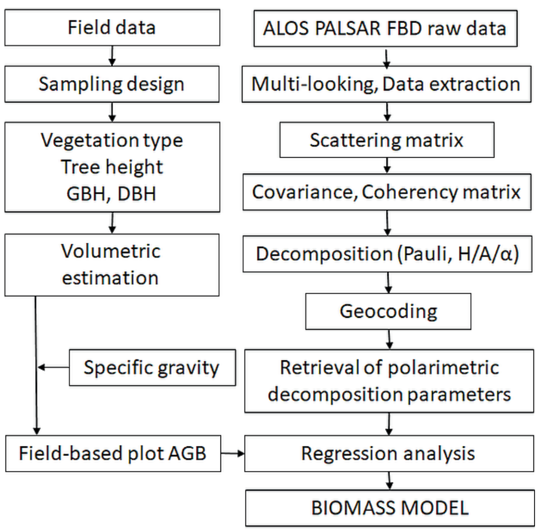

Fig. 2. Approach of the study

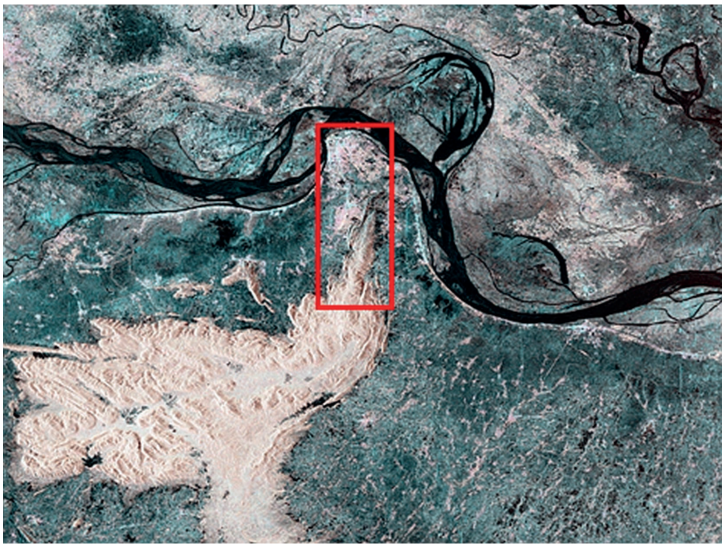

Fig. 3. PSRFBD False RGB composite of the study area

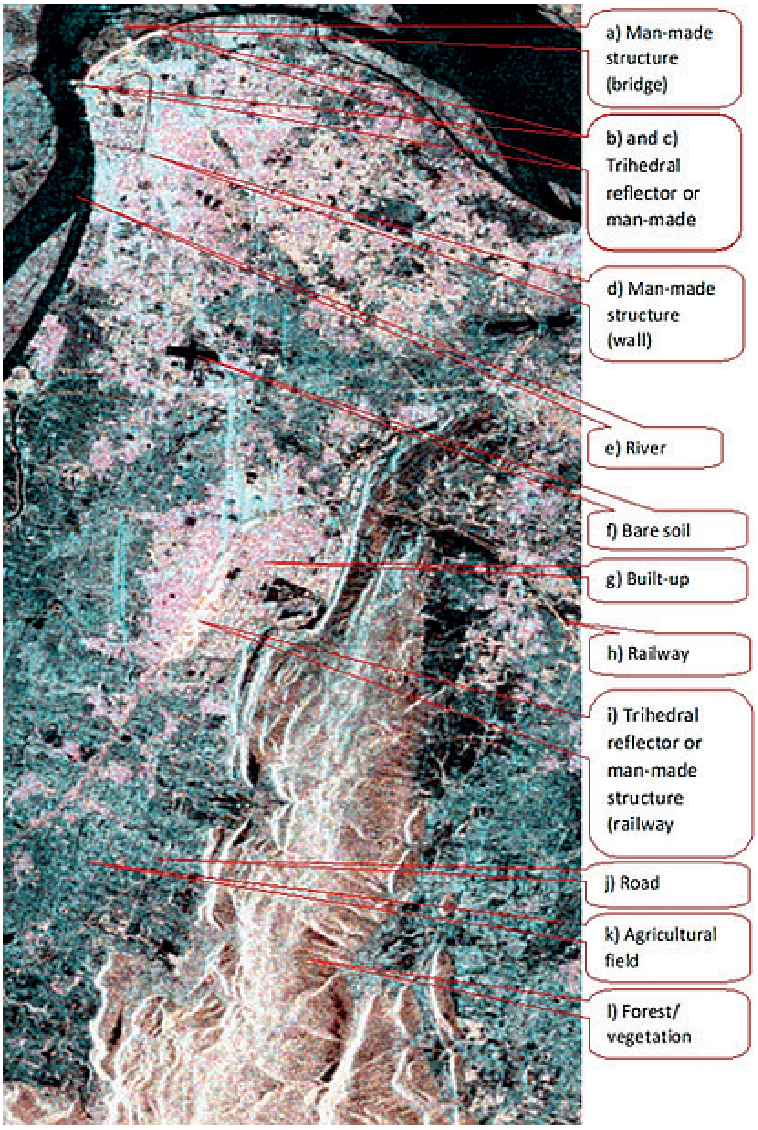

Fig. 4. Zoomed portion of PSRFBD False RGB composite

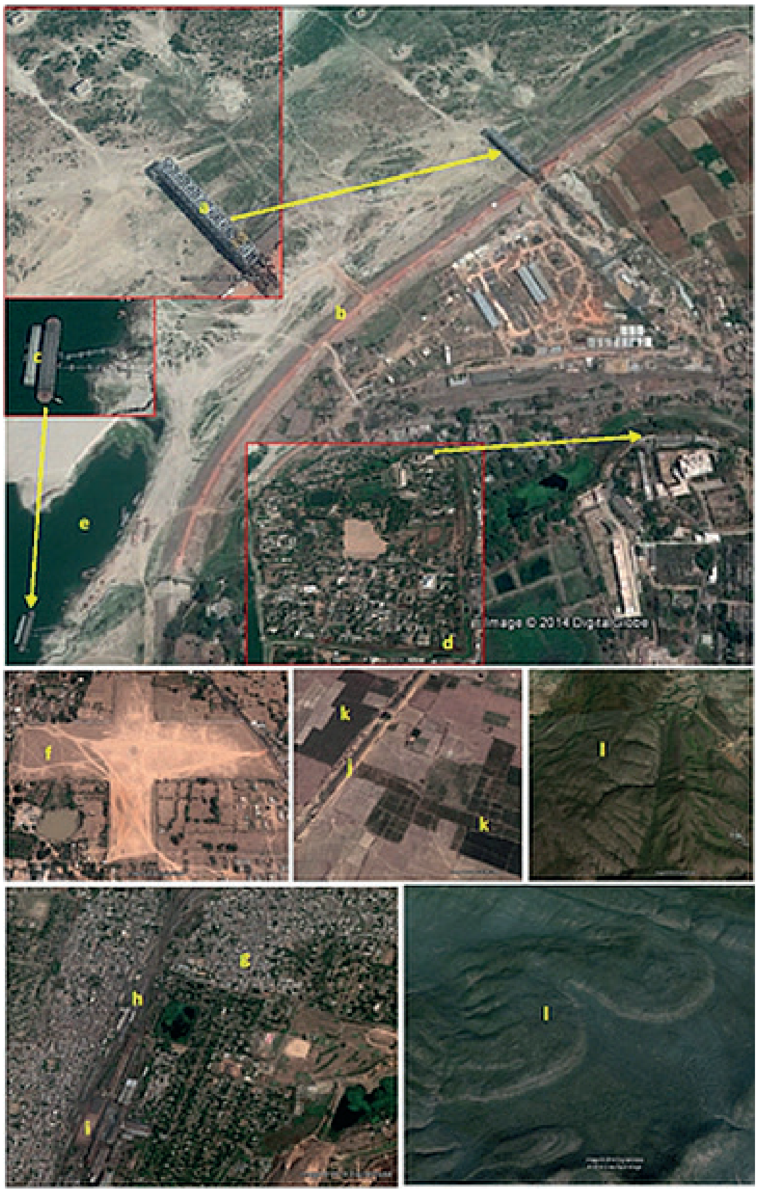

Fig. 5. Google Earth images identifying features from the zoomed portion mentioned in Fig. 4

scattering mechanism, lie within the range of 0 to 45°. The values show a very weak correlation with the plot AGB (Figure 7). The figure also shows that the value ranges within 10–30° for the selected sample plots. The value of H ranges from 0.5 to 0.9 for the selected sample plots which indicates depolarizing system of scatterers and scattering is from the mixture of point scatterers. However, there exist a very poor relationship between the plot AGB and the H as illustrated in Figure 7. Polarimetric scattering anisotropy (A) is the parameter complementary to H. It shows poor correlation with the plot AGB, however, at H>0.7, it shows better correlation (Figure 7). Span, which is a measure of total scattered power, shows the best relationship. Eq. (6) is developed from the relation between plot AGB with:

$$AGB = 120.5 * e^{(0.063 * Span)} \quad (6)$$

AGB Estimation

The Eq. (6) is generated from the 36 sample plot field-based data used for developing the biomass model. The model is statistically validated with nine additional field AGB data and evaluated. Table 2 documents the results of model evaluation and Figure 8 represents the graph between the predicted and estimated AGB values. Results showed the agreement for model validation is 0.622, with R^2 of 0.565 and RMSE 29.136 t/ha. This reveals the potential of polarimetric span in the estimation of AGB. The biomass map developed from Eq. (6) is shown in Figure 9, which shows the spatial extent of the distribution of AGB over the study area.

DISCUSSION

Polarized decomposition for LULC

Scattering mechanisms vary with different land features. Referring to figures 3 and 4, in this study area, dominated by open sparse and degraded forests, the brownish-red color represents double-bounce scattering from tree trunk-ground interactions. Pink color of the built-up areas results from a mixture of double-bounce and odd-bounce scattering. River is demarcated in dark-

Table 2. Model Evaluation Statistical Parameters

R^2	RMSE (t/ha)	NDRMSE	MAD	NDMAD	MBE	NDMBE	Slope	Av. Abs. Accuracy	Willmott's Index (d)
0.565	29.136	1.489	25.316	0.763	16.326	0.683	0.323	23.692	0.622

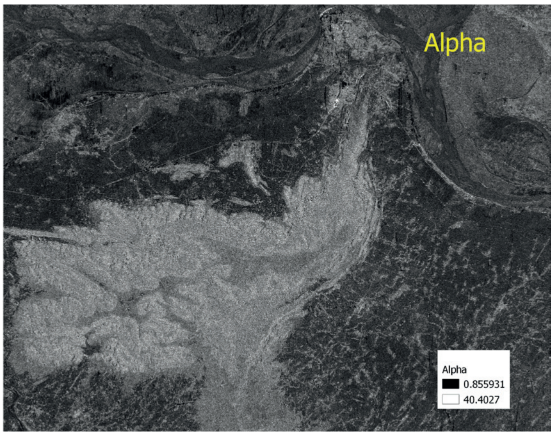

(A)

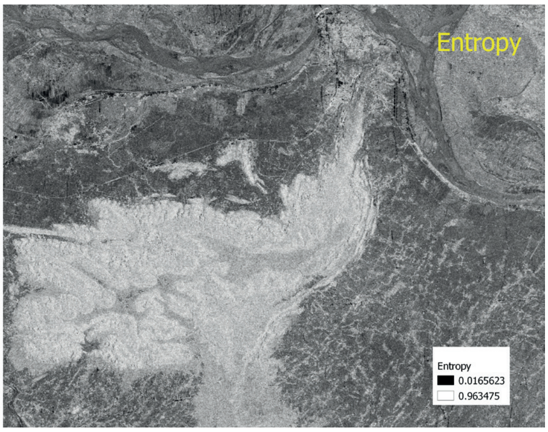

(B)

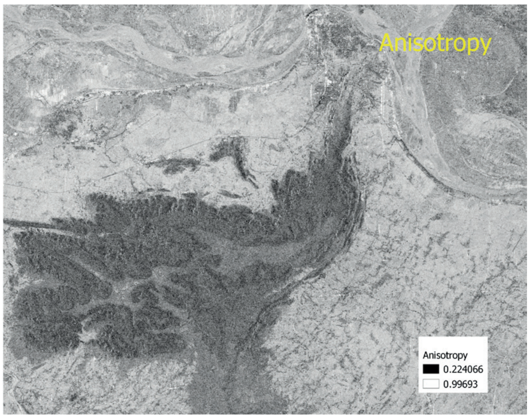

(C)

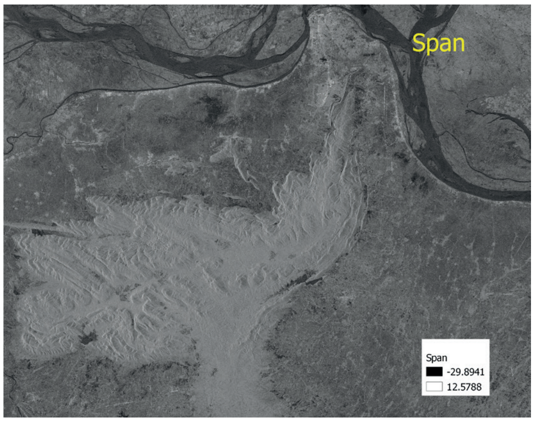

(D)

Fig. 6. PSP parameters

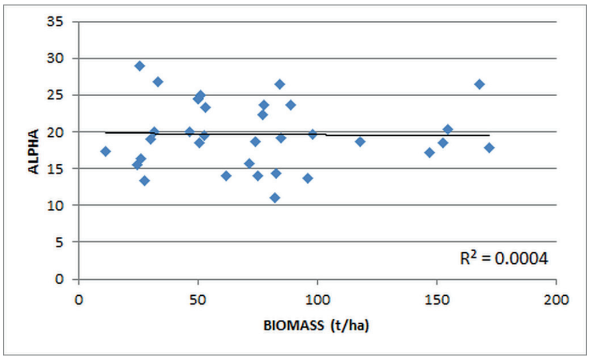

(A)

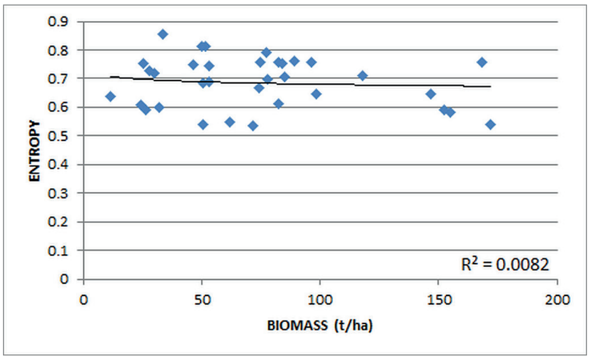

(B)

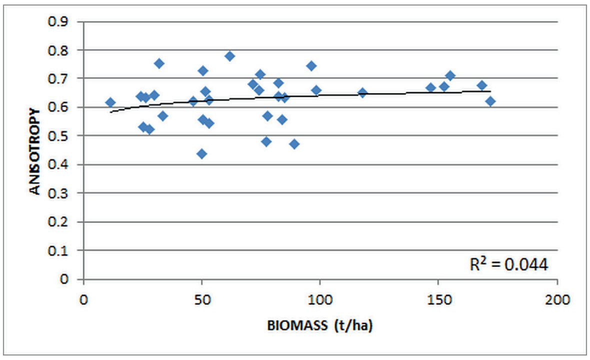

(C)

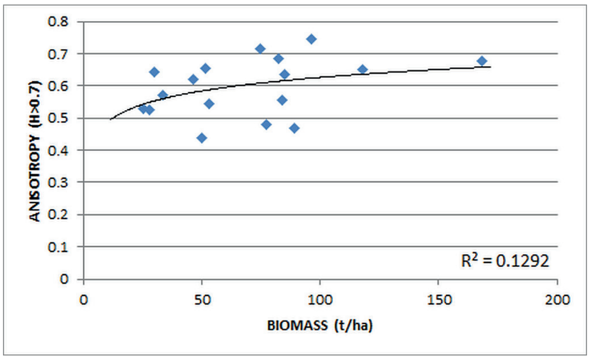

(D)

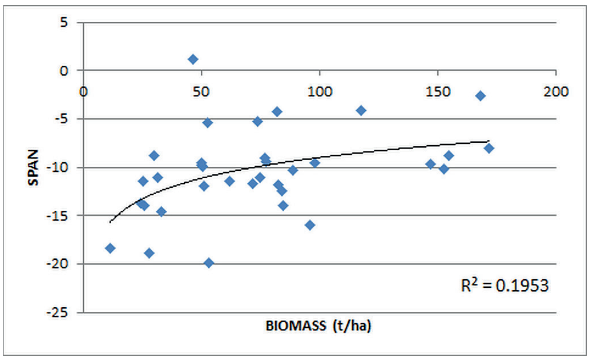

(E)

Fig. 7. Relationship between Plot AGB and PSPs

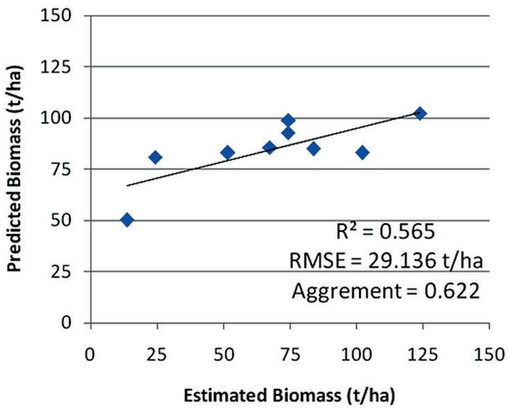

Fig. 8. Predicted vs estimated values

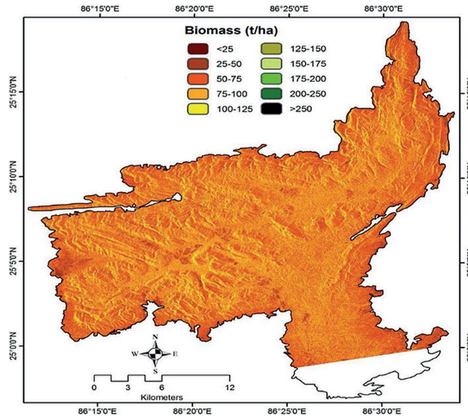

Fig. 9. Above-ground biomass map

blue represents surface (odd-bounce) scattering. Cyan color represents a mixture from odd-bounce and volume scattering from the agricultural fields; however, odd-bounce scattering seems to have more contribution. Bare soil is symbolized in black color due to lack of any scattering and L-band with high penetration power penetrates the ground. The linear features like road, wall, bridge, etc. are clear from the figure. The figure shows high backscatter from the trihedral reflector caused by the odd bounce scattering, mostly observed at the railway junctions. The Google Earth images of the features are shown in Figure 5 so as to visually compare the feature on ground as seen from high resolution satellite image to that obtained as signatures from PSRFBD False RGB composite image. This reveals that there exist specific signatures for every land features depending upon the scattering mechanisms that the features undergo. Hence, the signatures should also vary depending on the tree structure and orientation in a forest. After clearly demarcating every pixel under forest or non-forest class, investigation for forest above-ground biomass is done on the forest pixels.

Polarimetric Scattering Parameters

Alpha (α) is the roll invariant parameter, depicting the dominant scattering mechanism is associated with the physics behind the scattering process involved (Agashe 2013). The value ranges between 0 and 90°. α value represents the following mechanisms:

1. α=0° represents isotropic odd bounce scattering or surface scattering where the surface roughness variation is larger than the wavelength of incident wave.
2. 0°≤α≤45° represents anisotropic odd bounce scattering or surface where the surface roughness variation is smaller than the wavelength of incident wave.
3. α=45° represents Bragg surface model, like the dipole or volume scattering by cloud of anisotropic particles.
4. 45°≤α≤90° represents anisotropic even or multiple bounce scattering, like scattering from two perpendicular dielectric surfaces.
5. α=90° represents isotropic even or multiple bounce scattering, like the reflection from two perpendicular metallic surfaces.

Polarimetric scattering entropy (H) is a roll invariant parameter measuring the statistical disorder of each different scatterer within the group. The value of H indicates the type of scatterers.

1. H=0 indicates a single scattering mechanism.
2. A low value of H (H<0.3) indicates scattering from a dominant scatterer and the system is considered to be weakly depolarizing.
3. A high value of H (H>0.3) indicates depolarizing system of scatterers and scattering is from the mixture of point scatterers.
4. H=1 indicates random target scattering process representing completely depolarizing system.

Polarimetric scattering anisotropy (A) is the parameter complementary to H. It becomes a valuable parameter particularly when H attains a high value. Low H values give noisy anisotropy. As the value of H increases (H>0.7), it becomes difficult to distinguish between different types of scattering processes involved. At this point, anisotropy becomes useful for identification of the number of distinguishable scattering processes (Agashe 2013). PSPs imparted more information regarding forest structure rather than providing information on biomass; yet the PSPs showed potential in enumerating the forest biomass; specifically, the 'Span' component.

CONCLUSIONS

Polarimetry in SAR provides new opportunity in the field of remote sensing of forestry. Of all the wave polarizations, HH and HV polarizations provide maximum information regarding tree biomass. The choice of ALOS PALSAR (FBD) HH/HV dual polarization dataset is hence accurate for the study. Relationship between ground biomass and corresponding PSP products is investigated and a biomass estimation model is developed based on linear regression analysis of the maximally correlated PSP, which is span, as observed in this study. The model developed on 36 sample points and validated on additional nine points showed R^2=0.565 with RMSE=29.13 t/ha and Willmott's index of agreement of 0.62. PSPs imparted more information regarding forest structure rather than providing information on biomass; yet the PSPs showed potential in enumerating the forest biomass. The performance of the model can potentially improve by developing more sophisticated models involving ground topography, soil moisture and forest structure and using fully polarized SAR data. Hence, the study can augment forestry, climate change and REDD research, simultaneously overcoming the limitations offered by traditional field-based and conventional optical sensor-based biomass estimation approaches.

REFERENCES

Abimanyu A., Pranowo W.S., Faizal I., Afandi N.K.A., and Purba N.P. (2021). Reconstruction Of Oil Spill Trajectory In The Java Sea, Indonesia Using Sar Imagery. Geography, Environment, Sustainability, 14 (1), 177-184, DOI: 10.24057/2071-9388-2020-21.

Agashe S. (2013). Polarimetric Decomposition of SAR Data for Forest Structure Assessment. M.S. Dissertation, Dept. Earth and Space Sciences, Chalmers University of Technology, Göteborg, Sweden.

Avtar R., Takeuchi W., and Sawada H. (2011). Full polarimetric PALSAR-based land cover monitoring in Cambodia for implementation of REDD policies. International Journal of Digital Earth, 6 (3), 255-275, DOI: 10.1080/17538947.2011.620639.

Chaturvedi R.K., Raghubanshi A.S. and Singh J.S. (2012). Biomass estimation of dry tropical woody species at juvenile stage. The Scientific World Journal, 2012, 1-5, DOI: 10.1100/2012/790219.

Chopping M., North M., Chen J., Schaaf C.B., Blair J.B., Martonchik J.V. and Bull M.A. (2012). Forest canopy cover and height from MISR in topographically complex Southwestern US landscapes assessed with high quality reference data. IEEE Journal of Selected Topics in Applied Earth Observations and Remote Sensing, 5(1), 44-58, DOI: 10.1109/JSTARS.2012.2184270.

Englhart S., Keuck V. and Siegert F. (2011). Aboveground biomass retrieval in tropical forests – the potential of combined X- and L-band SAR data. Remote Sensing of Environment, 115, 1260-1271. DOI:10.1016/j.rse.2011.01.008.

Englhart S., Keuck V. and Siegert F. (2012). Modeling aboveground biomass in tropical forests using multi-frequency SAR data – a comparison of methods. IEEE Journal of Selected Topics in Applied Earth Observations and Remote Sensing, 5, 298-306. DOI:10.1109/JSTARS.2011.2176720.

FSI (1996). Volume Equations for Forests of India, Nepal and Bhutan. Forest Survey of India, Ministry of Environment and Forests, Government of India, Dehradun. India.

Gomathi M., Geetha Priya M., Chandre Gowda C. and Krishnaveni D. (2021). Flood damage assessment using H-A-Alpha dual polarimetric decomposition for Godavari Flood-2019. In: Komanapalli, V. et al. (eds.), Advances in Automation, Signal Processing, Instrumentation, and Control, Lecture Notes in Electrical Engineering, 700, 1199-1208, DOI: 10.1007/978-981-15-8221-9_113.

Ji K. and Wu Y. (2015). Scattering mechanism extraction by a modified Cloude-Pottier decomposition for dual polarization SAR. Remote Sensing, 7 (6), 7447–7470, DOI: 10.3390/rs70607447.

Kumar A.R. and Raghav A.A. (2018). A case study on the flood situation of Assam state. International Research Journal of Engineering and Technology, 5(5), 4192-4194.

Kumar P., Sharma L.K., Pandey P.C., Sinha S. and Nathawat M.S. (2013). Geospatial strategy for tropical forest-wildlife reserve biomass estimation. IEEE Journal of Selected Topics in Applied Earth Observations and Remote Sensing, 6(2), 917-923, DOI: 10.1109/JSTARS.2012.2221123.

Lu D. (2006). The potential and challenge of remote sensing-based biomass estimation. International Journal of Remote Sensing, 27(7), 1297-1328, DOI: 10.1080/01431160500486732.

Lu D., Chen Q., Wang G., Liu L., Li G. and Moran E. (2016). A survey of remote sensing-based aboveground biomass estimation methods in forest ecosystems. International Journal of Digital Earth, 9(1), 63-105, DOI: 10.1080/17538947.2014.990526.

Maity S., Patnaik C., Parihar J. S., Panigrahy, S. and Reddy K.A. (2011). Study of physical phenomena of vegetation using polarimetric scattering indices and entropy. IEEE Journal of Selected Topics in Applied Earth Observations and Remote Sensing, 4(2), 432-438, DOI: 10.1109/JSTARS.2010.2076272.

Malik A., Jalil Abd. R., Arifuddin A., and Syahmuddin A. (2020). Biomass Carbon Stocks In The Mangrove Rehabilitated Area Of Sinjai District, South Sulawesi, Indonesia. Geography, Environment, Sustainability, 13(3), 32-38, DOI: 10.24057/2071-9388-2019-131.

Potin P., Rosich B., Roeder J., and Bargellini P. (2014). Sentinel-1 Mission operations concept. In: IEEE Geoscience and Remote Sensing Symposium, 13-18 July 2014, Quebec City, QC, Canada, 1465-1468, DOI:10.1109/IGARSS.2014.6946713.

Pottier E., Lee J.S. and Ferro-Famil L. (2008). Advanced concepts, PolSARpro v3.0 – Lecture Notes.

Santra A., Mitra S.S. and Sinha S. (2021). Estimation and counter- validation of LISS-III derived leaf area index in Deltaic vegetation. Caspian Journal of Environmental Sciences, 19(2), 239-249, DOI: 10.22124/CJES.2021.4741.

Sharma L.K., Nathawat M.S. and Sinha S. (2013). Top-down and bottom-up approach for above ground forest biomass and carbon monitoring in REDD framework using multi-resolution satellite data. Environmental Monitoring and Assessment, 185 (10), 8621-8637, DOI: 10.1007/s10661-013-3199-y.

Sinha S. (2016). Polarimetric Scattering Parameter products of ALOS PALSAR for forest biomass assessment. Research & Reviews: Journal of Space Science & Technology, 5(1), 1-9.

Sinha S. and Santra A. (2019). An estimation of change in forest above ground carbon in Bhimbandh Wildlife Sanctuary between 2007 and 2016. Current Science, 117(6), 1090-1094, DOI: 10.18520/cs/v117/i6/1090-1094.

Sinha S. and Sharma L.K. (2013). Investigations on potential relationship between biomass and surface temperature using thermal remote sensing over tropical deciduous forests. Research & Reviews: Journal of Space Science & Technology, 2(3), 13-18.

Sinha S., Jeganathan C., Sharma L.K. and Nathawat M.S. (2015a). A review of radar remote sensing for biomass estimation. International Journal of Environmental Science and Technology, 12, 1779-1792, DOI: 10.1007/s13762-015-0750-0.

Sinha S., Jeganathan C., Sharma L.K., Nathawat M.S., Das A.K. and Mohan S. (2016). Developing synergy regression models with space-borne ALOS PALSAR and Landsat TM sensors for retrieving tropical forest biomass. Journal of Earth System Science, 125(4), 725-735, DOI: 10.1007/s12040-016-0692-z.

Sinha S., Mohan S., Das A.K., Sharma L.K., Jeganathan C., Santra A., Mitra S.S. and Nathawat, M.S. (2020a). Multi-sensor approach integrating optical and multi-frequency synthetic aperture radar for carbon stock estimation over a tropical deciduous forest in India. Carbon Management, 11(1), 39-55, DOI:10.1080/17583004.2019.1686931.

Sinha S., Santra A. and Mitra S.S. (2020b). Semi-automated impervious feature extraction using built-up indices developed from space-borne optical and SAR remotely sensed sensors. Advances in Space Research, 66 (6), 1372-1385, DOI: 10.1016/j.asr.2020.05.040.

Sinha S., Santra A. and Mitra S.S. (2018a). A method for built-up area extraction using dual polarimetric ALOS PALSAR. ISPRS Annals of the Photogrammetry, Remote Sensing and Spatial Information Sciences, IV-5, 455-458, DOI: 10.5194/isprs-annals-IV-5-455-2018.

Sinha S., Santra A., Das A.K., Sharma L.K., Mohan S., Nathawat M.S., Mitra S.S. and Jeganathan C. (2019a). Accounting tropical forest carbon stock with synergistic use of space-borne ALOS PALSAR and COSMO-Skymed SAR sensors. Tropical Ecology, 60, 83-93, DOI: 10.1007/s42965-019-00011-6.

Sinha S., Santra A., Das A.K., Sharma L.K., Mohan S., Nathawat M.S., Mitra S.S. and Jeganathan, C. (2019b). Regression-based integrated bi-sensor SAR data model to estimate forest carbon stock. Journal of the Indian Society of Remote Sensing, 47, 1599-1608, DOI: 10.1007/s12524-019-01004-7.

Sinha S., Santra A., Sharma L.K., Das A.K., Jeganathan C., Mohan S. and Mitra, S.S. (2021). Responses of Multi-Frequency Remote Sensing to Forest Biomass. In: Pandey P.C., Sharma L.K. (eds) Advances in Remote Sensing for Natural Resource Monitoring. John Wiley & Sons, UK, 58-80, DOI: 10.1002/9781119616016.ch5.

Sinha S., Santra A., Sharma L.K., Jeganathan C., Nathawat M.S., Das A.K. and Mohan, S. (2018b). Multi-polarized Radarsat-2 satellite sensor in assessing forest vigor from above ground biomass. Journal of Forestry Research, 29 (4), 1139-1145, DOI: 10.1007/s11676-017-0511-7.

Sinha S., Sharma L.K. and Nathawat M.S. (2013). Integrated geospatial techniques for land-use/land-cover and forest mapping of deciduous Munger forests (India). Universal Journal of Environmental Research and Technology, 3(2), 190-198.

Sinha S., Sharma L.K., Jeganathan C., Nathawat M.S., Das A.K. and Mohan, S. (2015b). Efficacy of InSAR coherence in tropical forest remote sensing in context of REDD. International Journal of Advancement in Remote Sensing, GIS & Geography, 3 (1a), 38-46.

Tanase M.A., Panciera R., Lowell K., Hacker J. and Walker J.P. (2013). Estimation of forest biomass from L-band polarimetric decomposition components. In Proc. IEEE Geoscience and Remote Sensing Symposium (IGARSS), 2013, Melbourne, VIC, 949-952, DOI: 10.1109/IGARSS.2013.6721318.

Usoltsev V.A., Danilin I.M., Tsogt Z., Osmirko A.A., Tsepordey I.S., and Chasovskikh V.P. (2019). Aboveground Biomass Of Mongolian Larch (Larix Sibirica Ledeb.) Forests In The Eurasian Region. Geography, Environment, Sustainability, 12 (3), 117-132, DOI: 10.24057/2071-9388-2018-70.

Yonezawa C., Watanabe M. and Saito G. (2012). Polarimetric decomposition analysis of ALOS PALSAR observation data before and after a landslide event, Remote Sensing 4, 2314-2328, DOI: 10.3390/rs4082314.

RESEARCH PAPER

THE EFFECT OF URBAN GREEN SPACES IN REDUCING URBAN FLOODING IN LAHORE, PAKISTAN, USING GEOSPATIAL TECHNIQUES

Sahar Zia[1], Muhammad Nasar-u-Minallah[2,3*], Nikhat Zahra[1], Aysha Hanif[1]
[1]Department of Geography, Lahore College for Women University, Lahore, Pakistan
[2]Institute of Geography, Humboldt University Berlin, Germany
[3]Department of Geography, Govt. Postgraduate College Gojra, Pakistan
*Corresponding author: Nasarbhalli@gmail.com
Received: December 4th, 2021 / Accepted: August 8th, 2022 / Published: October 01st, 2022
https://DOI-10.24057/2071-9388-2021-135

ABSTRACT. Urban Green Spaces (UGS) curtails all environmental issues and ensure an eco-friendly locale. Similarly, the emergence of UGS is very helpful to cope with emerging urban flooding in cities by setting up the world standard of green space ratio (20 to 25 percent of the area) and green per capita ($9m^2$) in a geographical area. Therefore, the present study is conducted to evaluate the causal effect relation of UGS with the frequency of urban flooding. For this purpose, 69 selected union councils are taken as a study area in District Lahore, Pakistan. The relation between UGS and the occurrence of floods is evaluated using geo-statistical and geospatial analysis techniques during the monsoon rainfalls from 2013 to 2019. Furthermore, the data sets of sore points (inundated areas), occurrences of urban flooding (number of event occurrences), green per capita, and green ratio are used. Results revealed that selected union councils in Lahore don't have enough urban green spaces. There is only a 51 sq km area with adequate UGS that accounts for only 18 percent of the study area. The rest of the area does not meet the world standards of green area. There are some areas including Ravi town, Gulberg town, and Samanabad town with green per capita more than 4 green per capita. On the other hand, there are only 02 union councils including Race Course and Model Town that are comprised of a 20 percent green area. The findings of the study will be helpful for proper urban planning and strategies i.e. with greener structures.

KEYWORDS: hydro-meteorological disasters, nature-based solutions, green space, flooding mitigation, Lahore

CITATION: Zia S., Nasar-u-Minallah M., Zahra N., Hanif A. (2022). The Effect Of Urban Green Spaces In Reducing Urban Flooding In Lahore, Pakistan, Using Geospatial Techniques. Geography, Environment, Sustainability, 3(15), 47-55
https://DOI-10.24057/2071-9388-2021-135

ACKNOWLEDGEMENTS: This study was made possible only by the government organization Water and Sanitation Agency (WASA) as they provided me data on ponding points/flooded areas of Lahore District and all necessary support in the completion of the study work.

Conflict of interests: The authors reported no potential conflict of interest.

INTRODUCTION

Rapid urban expansion has produced massive changes in the urban and regional environment (Kim 2021; Nasar-u-Minallah et al. 2021). Specifically, in high-density urban centers, there are a large number of impervious surfaces made by roads, parking lots, and large-scale architecture because of the new developments (Foster et al. 2011). As a result, unexpected events may be triggered, which may drastically affect human habitation (Meerow and Newell 2017). Whenever the impervious surface increases, it can affect the store-ability of flowing water, causing greater flooding at hazardous sites (Liu and Jensen 2018). Urban flooding is a key issue in the cities of the developing world and is mainly caused by natural hazards such as riverine floods, coastal storm surges, sea-level rise, poor absorptivity, and urban management. These challenges were faced by city planners while dealing with the mitigation of flood disasters. Pakistan is inclined to many geological and hydro-meteorological disasters mainly due to climate change and environmental degradation (Mahmood and Rahman 2019) including floods which have severe impacts on human losses and destruction of built-up areas and property. It is mainly caused due to inability of city drainage and sewage systems to deplete rainfall water during the period of excessive rainfall. Due to climate change, increasing precipitation by 40-45% flood zones will develop at the end of the 21st century. However, infrastructure is not designed to adapt mitigation to predict urban flooding hazards and eventually make cities vulnerable (Gimenez-Maranges et al. 2020; Mohtar et al. 2020).

Urban development raises the risk of floods in cities because of hydrogeological and meteorological conditions caused by increased flood hazards, vulnerability, and the association between runoff and flooding has seemed through variations in rainfall patterns and climate change. Rising populations in urban areas are mostly initiated in developing countries which may be due to the conversion of rural areas into big cities and the migration of rural people to cities to improve their lifestyles. Urban flooding is a persistently repeating regular danger as far as the number of lives lost and the general expense of harm to property, public works foundation, and normal assets (Shuster et al. 2005). The rate of urban flooding is increased with the growing population and change in climate (Hammond et al. 2015). The condition will worsen due to the migration of people from rural to urban areas which result in an increase in impervious surfaces which causes serious effects on the water cycle and an increase in flood hazards.

The benefits of urban green space include reduction of rainfall-runoff primarily for affected cities from intense flooding and hazards (Gordon 2007). However, its efficiency in mitigating its effects is not fully determined (Duffy et al. 2008; Wong and Brown 2009). To protect and manage the urban environment from severe flood events, a common method is a green infrastructure (Ballard et al. 2015; Bowen and Lynch 2017) which mainly includes ponds, swales, rainwater tanks, vegetated filter strips, wetlands to gather a certain quantity of rain, with the help of either storage devices or groundwater recharge (Afriyanie et al. 2020) including green roofs, rainwater capture or harvesting and permeable paving/surfaces (Zia et al 2021a). Therefore, the objective of this study is to correlate the existing green space ratio and frequency of urban flooding at the union council's level of Lahore from 2013 to 2019. Correlative analysis was based on the frequency of urban flooding and its hotspots. This research study is conducted to find the exact ratio of green space that is triggering urban flooding and hazardous environmental conditions. This study will help to trace the actual situation and to conclude in which areas green spaces are needed to curtail urban flooding.

MATERIALS AND METHODS

Study Area

The strategic political and administrative role of the study area is Lahore, comprised is the second largest metropolitan city after Karachi in terms of population (GOP 2017). The latitudinal and longitudinal extent of the Lahore district lies between 31° 15′0″ N to 31°43′0″ N and 74° 10′0″ E to 74°39′0″ E in the Punjab province of Pakistan (Figure 1). The total area of district Lahore is 1772 km^2 (GOP 2000). It is bounded on the north and west by the Sheikhupura District, on the east by Wagah, and on the south by Kasur. The total population of Lahore has increased from 6.31 million in 1998 to 11.12 million in 2017 (GOP 2017; Nasar-u-Minallah 2020). The current population density is 6300 persons per km^2 which are projected to be increased to 16.88 million by 2030 (United Nations 2018). Lahore ranked 26th among the most densely populated cities in the world (United Nations, 2018) with a total population of 11.12 million (GOP 2017). District Lahore is governed through 151 UCs and one Cantonment area out of which 69 UCs are selected which are influenced by urban flooding.

Data and its Sources

Digitization of urban green spaces (UGS) of 69 Union Councils of district Lahore acquired by using Google earth explorer (https://explorer.earthengine.google.com) which permits scientists

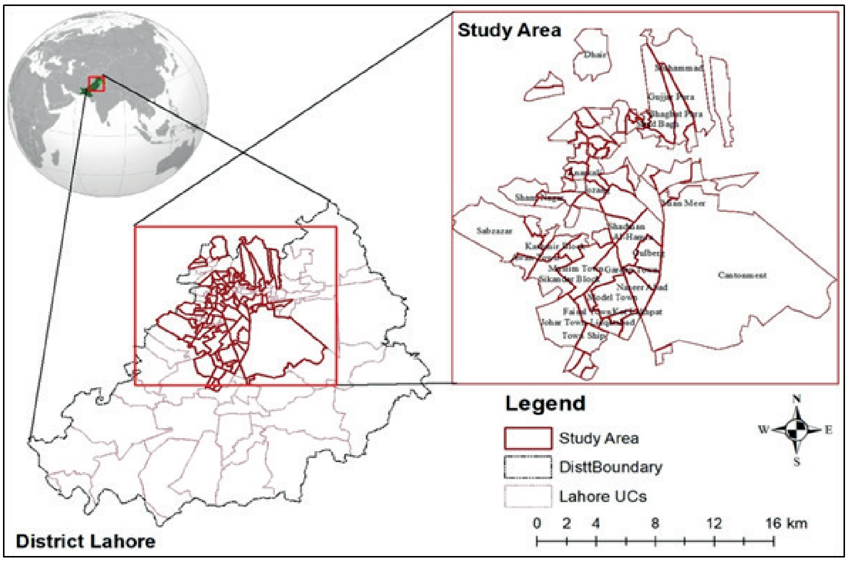

Fig. 1. Map showing the study area (Union councils of Lahore)

Table 1. Characteristics of the Landsat-8 OLI image used in this study

Date of Acquisition	Sensor	Bands	Wavelength (um)	Spatial Resolution	Thermal Resolution	Path/Row
08-05-2021	OLI	Band 1—Ultra Blue	0.435–0.451	30m	-	149/38
		Band 2—Blue (B)	0.452–0.512			
		Band 3—Green (G)	0.533–0.590			
		Band 4—Red (R)	0.636–0.673			
		Band 5—Near Infrared (NIR)	0.851–0.879			
		Band 6—Shortwave Infrared (SWIR) 1	1.566–1.651			
		Band 7—Shortwave Infrared (SWIR) 2	2.107–2.294			
	TIRs	Band 10—Thermal Infrared (TIR)	10.60–11.19	-	100m	
		Band 11—Thermal Infrared (TIR)		-	100m	

Source: http://earthexplorer.usgs.gov/

everywhere in the world to interconnect their data and examine research verdicts in an instinctive three-dimensional (3D) universal outlook (Yu & Gong 2012). The satellite imagery of Landsat-8 for the year 2021 (Table 1) is acquired from the USGS website (https://earthexplorer.usgs.gov/) obtained for path 149 and row 38.

The population data were obtained from Punjab development statistics (PDS) which is an authorized report issued by an agency named Pakistan Bureau of statistics. It is selected due to uneven census practices and the database is the only source that offers efficient projected population data at UC and town levels. The categorization of population data is in urban and rural union councils. While considering the current study, the estimated population of urban-rural union councils wise was obtained for analytical purposes (GOP 2016). The ponding point's data from the year from 2013 to 2019 was acquired from the government organization Water and Sanitation Agency (WASA). The data contains flood depth in inches and ponding points of union councils of Lahore. Considering the aim and objectives of this paper, the qualitative approach is selected to conduct explanatory research (Figure 2).

Tabulation and organization of data

Three datasets were required to achieve the objective of the current study including the area of green spaces to calculate the green ratio, population to calculate green per capita concerning available green area, and ponding points that are frequently inundated during Monsoon. For this purpose, the urban green spaces of 69 union councils of Lahore were digitized in Google earth and were converted from kml (Keyhole Markup Language) format to shp (Shape file) format which is a compatible model for calculating the green ratio as shown in the table. The selection of union councils is done on basis of those areas only where flood inundation is observed in previous years every time after a rainfall episode.

Besides, the area of green space is also retrieved from satellite imagery and details are mentioned in the 3.4 section. Moreover, the population data were obtained from Punjab Development Statistics of Lahore Union Councils. Likewise, the ponding points and their frequencies of flooding events were obtained from Water and Sanitation

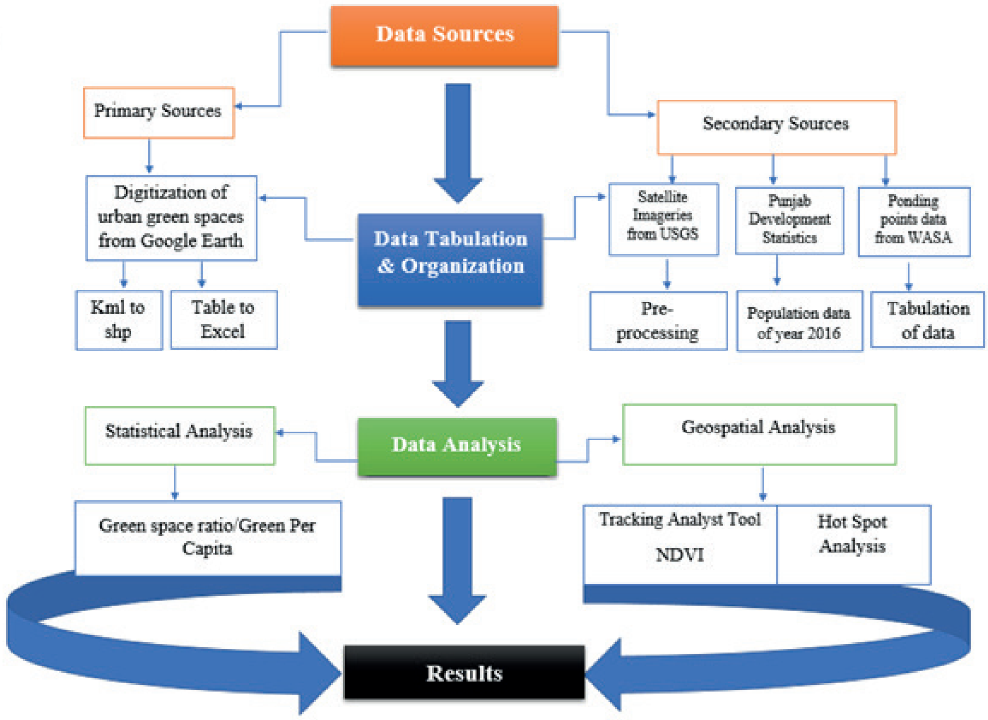

Fig. 2. Methodological Framework of the study

Table 2. Selected Union councils in each town in District Lahore

Town Name	Number of selected Union councils
Aziz Bhatti Town	2
Cantonment	1
Data Gunj Baksh Town	12
Gulberg Town	13
Iqbal Town	6
Nistar Town	4
Ravi Town	12
Samanabad Town	10
Shalamar Town	7
Wagha Town	2

Agency (WASA) and tabulated in an Excel spreadsheet for 69 union councils of District Lahore. The frequency of urban flooding is defined as the occurrence of an urban flood at one point after any rainfall event.

Image preprocessing

The satellite imagery acquired from Landsat 8 of 2021 for the Lahore District was further processed for the classification of the Normalized Difference Vegetation Index (NDVI). While the investigation of NDVI can deliver observation of vegetation fluctuations in contrast to other vegetation indices by using Landsat imageries based on variations in absorption and reflectivity of energy resulting from vegetative cover in the red and near-infrared bands (Fung and Siu 2000). This technique hires the Multi-Spectral Remote Sensing data method to discover Vegetation Index, land cover organization, vegetation, water bodies, open area, undergrown area, mountainous areas, agrarian areas, and forests with limited band fusions of the remote sensed data, particularly to interpret exterior structures of the noticeable areas which are significant for policymakers while making strategies by using formula as (NIR-RED)/(NIR +RED) whereabouts NIR denotes reflectivity which discharges in the near-infrared frequency band of satellite (Gandhi et al. 2015) to access the vegetative area in union councils.

Geo-statistical Analysis

Statistical data analysis mainly includes various statistical formulas and functions. The current study involves the use of the statistical technique for calculating Green per capita using a formula stated as the total area of green space (sq. m)/ Total Population of the city as green per capita common quantifiable measure to evaluate urban green infrastructure.

Geospatial Analysis

The geospatial analysis includes various Geographic Information System tools and techniques. Keeping in view the objectives of this study, the Tracking Analyst tool (Data Clock Manager) in ArcGIS was used to monitor and associate spatiotemporal variable data from several sources which use path evidence to access the positions of time-enabled and spatially variable scatter data via an amalgamation of trajectory alteration and spatial interpolation (Gad et al. 2018). Hotspot statistical analysis in ArcGIS was used as recognition of present hotspots is considered as one of the primary steps for developing policy to alleviate urban flooding which uses Getis-Ord Gi statistic to discover spatial variations (Zia and Shirazi 2019; Zia et al. 2021).

RESULTS AND DISCUSSION

Green space per capita

The current study involves the use of the statistical technique explained in the previous section for calculating green per capita. According to World Health Organization (WHO), the availability of 9 m^2 value to 50 m^2 per capita of green space per person is an ideal urban green space (UGS) that plays a pivotal role in maintaining a healthy urban environment. This is considered standard because the rate of urbanization is increasing and causing severe impacts on the urban environment by contaminating the biosphere and consequently harm to biodiversity making the city an urban heat island.

Observing the data, it is revealed that a higher proportion of urban towns and respective union councils that falls in extremely low green per capita on average include all towns of District Lahore shown in Table 3. Values shown in Table 3 are derived by excluding the outliers that exist in the area of Model town, Racecourse, and Al-Hamra of Lahore. These are three areas where green per capita is 27, 20, and 14 sq. meters per person respectively. The data is further categorized into three groups to evaluate the situation in each union council of Towns in District Lahore including (a) Extremely low (0.080 to 2.464), (b) Moderate (3.256 to 9.310), and (c) High (14.083 to 27.866).

Observing the data reveals a higher proportion of Urban Towns and Union Councils that falls in extremely low green per capita including 58 union councils out of 69. This result shows that 224 sq. km out of 285 sq. km selected study area comprising 78 percent of the area is deprived of green spaces. The second criteria of moderate values range from 2.464 to 14.083 which includes only 8 union councils in the study area comprising only 15 percent of the study area.

Likewise, the class showing high green per capita range from 14.083 to 27.866 sq. m includes only three union

Table 3. Green Per capita in the study area

Town Name	Green Per Capita (World standard 9m^2 to 50m^2 per person)
Cantonment	0.10
Nistar Town	0.37
Data Gunj Baksh Town	0.70
Wagha Town	0.75
Samanabad Town	0.80
Shalamar Town	0.86
Ravi Town	1.11
Aziz Bhatti Town	1.15
Iqbal Town	1.97
Gulberg Town	2.20

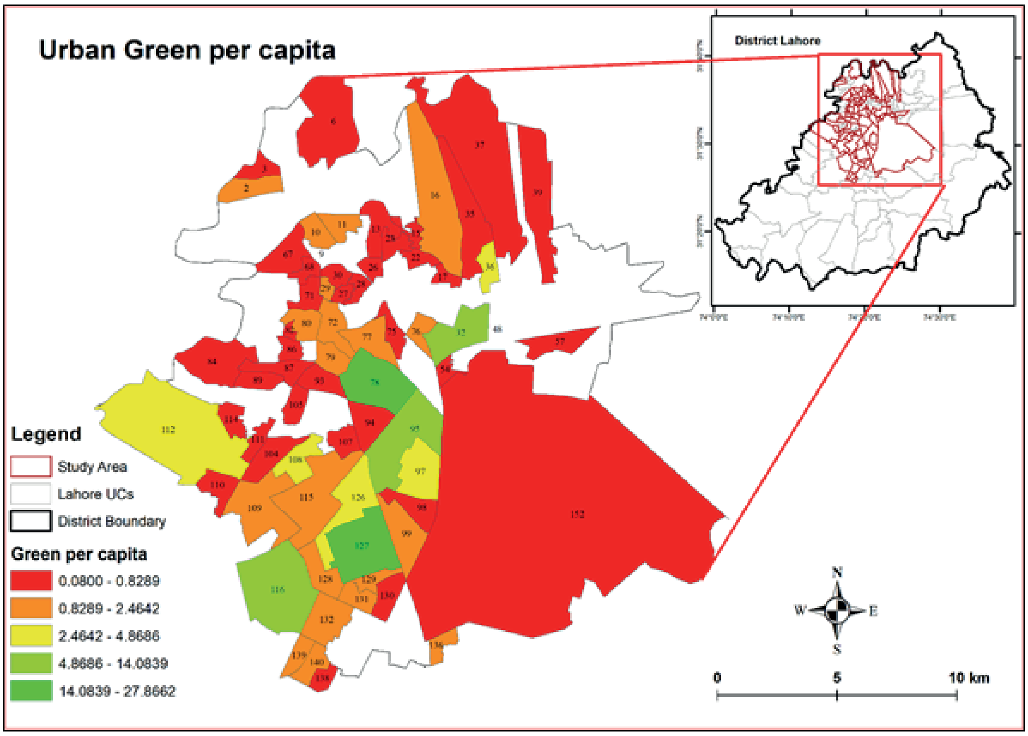

Fig. 3. Green per capita in the study area

councils. However, this range approximately covers 18 percent of the study area. The spatial distribution of green per capita is shown in Fig 3. In past studies, green spaces played a significant role in maintaining a healthy urban environment because the rate of urbanization is increasing and causing severe impacts on the urban environment by contaminating the biosphere and consequently harm to biodiversity making the city an urban heat island (Alam et al. 2014; Hanif et al. 2022).

The Green Area Ratio (GAR)

The Green Area Ratio (GAR) score narrates to rise in the amount and value of ecological presentation of the urban site. Data is categorized into five categories to evaluate the green area ration includes: (a) Very Low (0.03-0.85), (b) Low (1.08-1.99), (c) Moderate (2.00-5.79) (d) High (7.54-15.25), (e) Very High (20.0-23.74) shown in Fig 4. The world standard recommended a minimum of 25 to 30 percent of green open space in an urban locality. However, results reveal that only two Union Councils lie in the Very High category including Model Town of Data Gunj Baksh Town and Racecourse of Shalamar Town ranging from 20.0-23.74 shown by green color. On the other hand, the union councils lie in a very low category including union council Muhammad of Data Gunj Baksh Town Rehmatpura of Shalamar Town ranging from 0.03-0.85.

Ong (2003) provided a piece of evidence that for the sustainability of cities the application and preservation of green areas in the urban setting have been preferred as plants are not just ecological but also recreational and appealing.

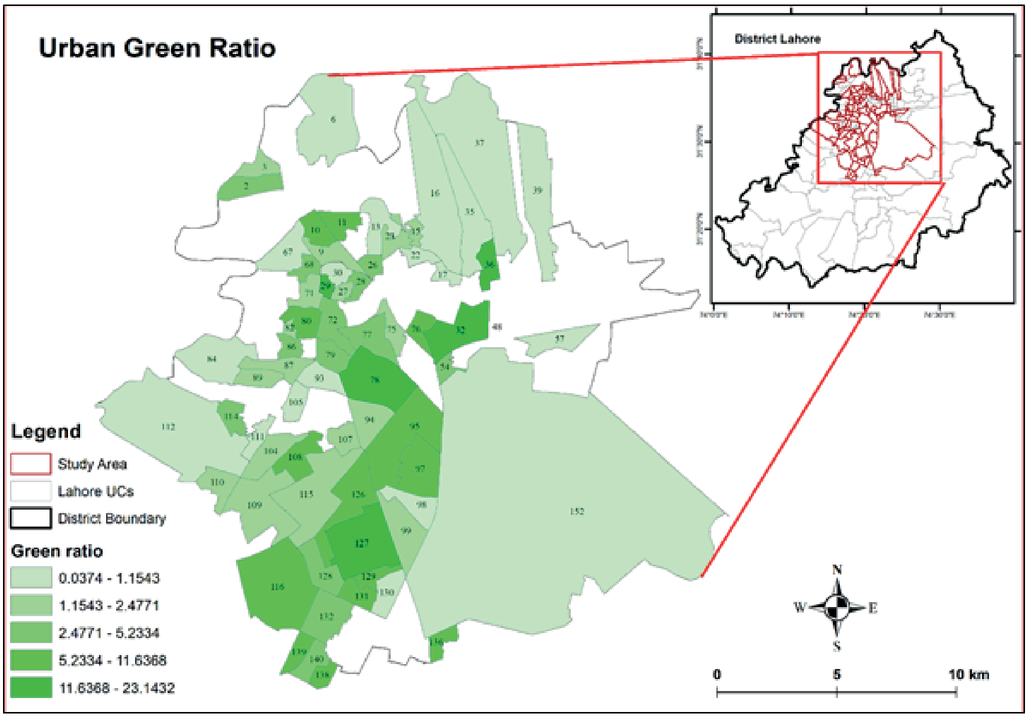

Fig. 4. Urban green area ratio in the study area

Normalized Vegetation Difference Index (NDVI)

To illustrate the current scenario of vegetation (Figure 5) in the study area Normalized Vegetation Difference Index (NDVI) in selected 69 urban union councils of district Lahore was used. Land Assets are effectively interpreted by processing their standardized difference vegetation for land cover arrangement by Gandhi et al. (2015). The names of union councils are shown by different numbers assigned to 69 union councils such as 1 to Mughalpura, 2 to Rehmanpura, and so on, and are grouped into three categories: Low (0.1 or less), Moderate (0.2-0.5), High (0.6-0.9) designated with different colors. The urban union councils which lie in the low category constitute 100 union councils and 66% of Lahore shown by the color red, moderate constitutes 30% and 46 union councils shown by yellow color The third category high constitutes 3% with designated color green includes only 5 union councils. The analysis showed that the situation of NDVI in Lahore does not meet the standard of vegetation (Figure 5).

Occurrences of urban flooding

Temporal analyses were used to quantify incidents of rainwater that couldn't be drained due to poor sewage systems during the spell of heavy rainfall and the least reported events of urban flooding are in the years 2013 and 2019. For this purpose, the Data Management Tool in ArcGIS which offers a data clock chart, which is circularly alienated into cells by the grouping of concentrically circles and radiated lines was used to show the annual average depth and trend of water during the monsoon period from June to September in 2013–2019-time span. The study years are shown by rings, while each wing is showing monthly data. The average depth of urban flooding is observed from 1 to 485 inches (0.08 to 40.08 feet) in the study period classified into 6 classes based on no concentration of rainwater to more stationary/stagnant water up to 40.08 feet depth of urban flooding. The data management tool is used to reveal the situation of urban flooding for the monsoon period which uses a novel Direction based Trajectory Tracking Analyst (TTA) that can track and connect spatiotemporally factor information from different sources using multiple sensors (Gad et al. 2018).

Different colors are designated to show the intensity of urban flooding temporally. Orange to blue color is showing highest to lowest averages in inches of urban flooding correspondingly. Though grey color is depicting omitted months from this study as the monsoon period was not practiced during these months. Results of the study indicate that urban flooding in Lahore occurred throughout the monsoon period from 2013-to 2019 with variable intensities and incidences such as fewer events reported in June, and July can be considered as an intense month for urban flooding events, August showing consistency in the occurrence of flood events. However, September is considered as least intense month in the recording of flood events because it is the last month of the monsoon period (Figure 6).

Spatial hotspots of urban flooding

Spatial hotspots of urban flooding events were identified in the study area of 69 Union Councils in the Lahore District. For this purpose, values are categorized into three confidence levels shown by different colors such as red for the hot spot with +3 and 3 Gi-Bin value through 99% confidence level, blue for a cold spot with +2 and -2 Gi-Bin value with 95% confidence level and yellow for clustering of features with no significant value based on the susceptibility of flood events by Dilley (2005) state hotspots as topographical areas where the dangers

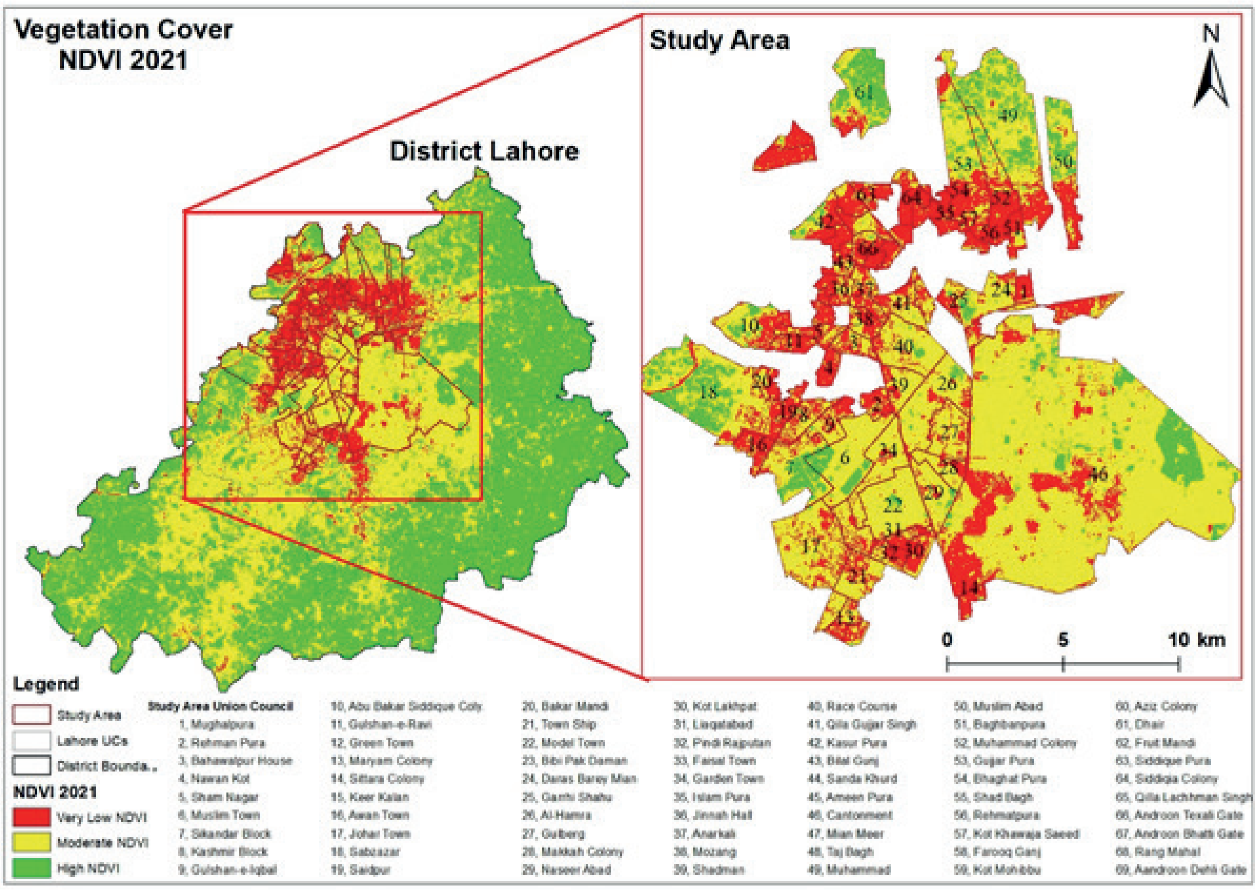

Fig. 5. The vegetation cover of the study area

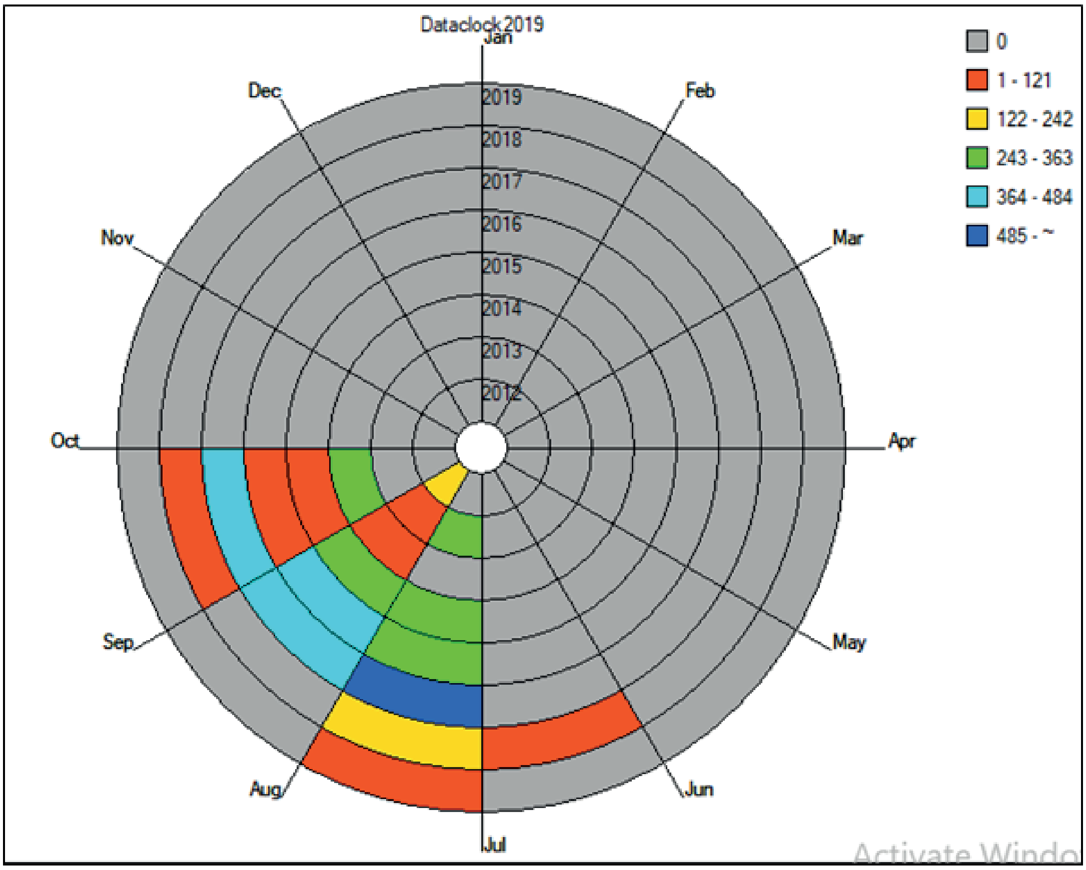

Fig. 6. The peak time of urban flooding in the study area during the monsoon period (2013–2019)

of natural calamities are mainly high or the zones that are comparatively more expected to be visible to flooding as the demarcation of the hotspots is considered as a productive means for recognizing the regions for comprehensive risk evaluation. The density of the graduated circle represents the intensity of urban flooding i.e., the largest circle is depicting more occurrences of flood events in the study area. The name of union councils is shown by different numbers such as 1 to Mughalpura, 152 to Cantonment, and so on. The results of the hotspot analysis indicate 4 hotspot zones including number 72(Anarkali), 77(Qilla Gujjar Singh), 29(Androon Bhatti Gate), and 79(Mozang), and 2 cold spots including number 36(Baghbanpura) and 128(Faisal Town). The reference number of each union council is mentioned in Figure 5. As half of the world's population lives in urban areas, the identification of hotspots is significant in developing policies for eradicating urban flooding from megacities as it is an evolving problem due to the rapid increase in urbanization and devise different methods such as more urban green spaces in cities to overcome urban flooding to an extent (Figure 7).

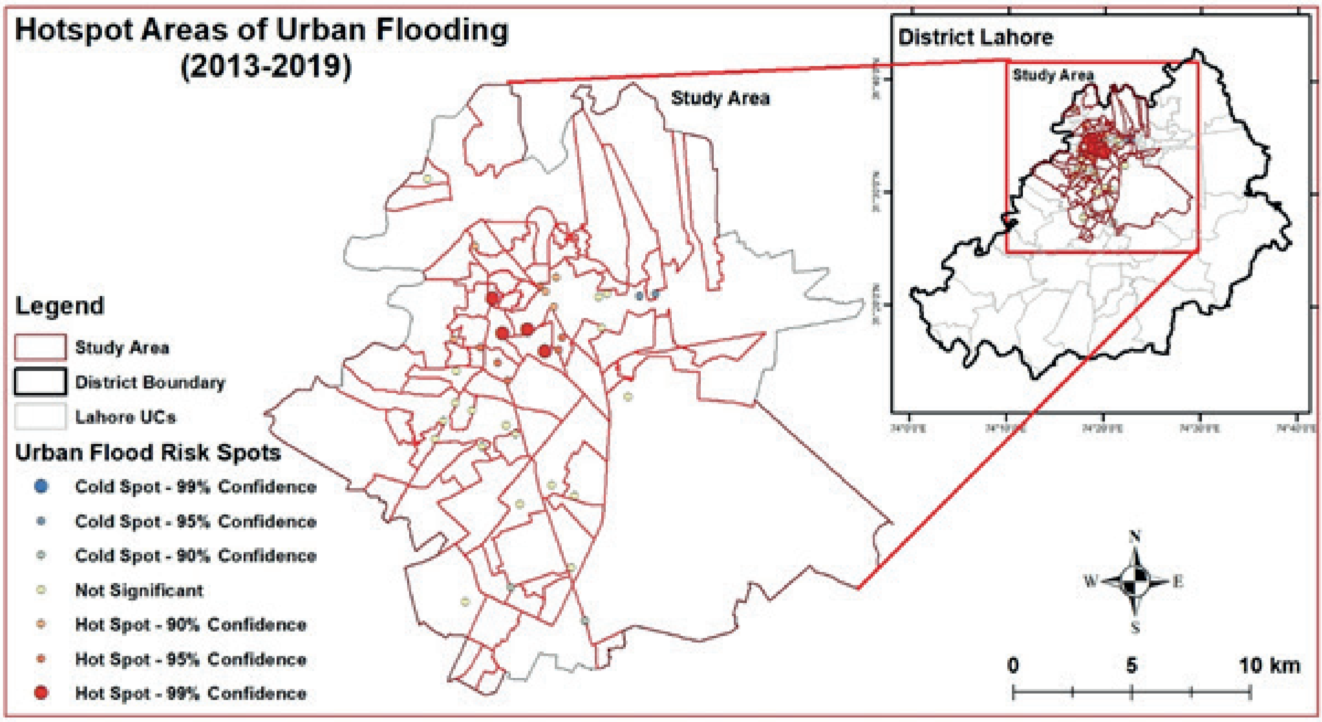

Fig. 7. Hotspot analysis incidents; 2013–2019

Correlative analysis of urban green spaces and occurrences of urban flooding

Figure 8 shows the situation or correlation between the urban green spaces and hotspots of urban flooding in 69 Union Councils of Lahore District. For this purpose, a hotspot analysis tool is used for assessing high-risk zones, and the green per capita and green space ratio is calculated for depicting green space situations in the study area. Based on the results of the analysis, four hot spots are detected including Gawalmandi, Anarkali, Qilla Gujjar Singh, and Androon Bhati gate.

Table 4 depicts that areas with very low green ration and green per capita are more prone to urban flooding as compared to areas with higher values. The condition of green per capita and green ratio in four hotspots is 1.08% green per capita and 2.80% green ratio in union council Anarkali, 2.46% green per capita and 5.23% green ratio in Qilla Gujjar Singh, 0.968% green per capita and 14.30% green ratio in Androon Bhatti Gate, 1.05% green per capita and 5.16% green ratio in union council.

However, cold spots comprise comparatively high values of green per capita and green ratio. On the other hand, cold spots include 3.5% green per capita and 15% green ratio in Baghpanpura and 1.80% green per capita and 4.2% green ratio in Faisal Town. The correlation between urban green spaces and the frequency of urban flooding reveals that the situation is not favorable because very few union councils meet the standard requirement of urban green spaces due to which situation is worse in union councils of Lahore District.

CONCLUSION

The present study examined the effect of urban green spaces on the frequency of urban flooding in 69 union councils of Lahore District. The result shows that the union councils that lack green spaces have experienced more frequent events of a flood than those union councils that meet the standard ratio of urban green spaces as per the area. In past studies, it is evident that green spaces are playing a significant role in maintaining a healthy urban environment because the rate of urbanization is increasing and causing severe impacts on the urban environment. This research contributes to the literature from different perspectives. Firstly, this research examines the frequency of urban flooding events. For this purpose, data were collected from 22 sore points from a governmental body Water and Sanitation Agency with information on ponding points and flood depth in inches to perform hotspot analysis for identification of urban hotspots and cold spots in the study area. Secondly, statistical analysis is performed to calculate green per capita and green ratio to govern the situation in the study area which reveals that most union councils fall in the extremely low category of green spaces and no one meets the standard value of 9m2. Therefore, it is a timely need to see the actual situation and either structured or unstructured ways to create green spaces may introduce to cope with the situation. City planners should pay more attention to the role of urban green spaces in rainwater regulation and the scientific management of urban green spaces.

Table 4. Correlative assessment of urban flooding and green spaces on detected hotspots

UC Name	Events	UC area sq. meter	Park area sq. meter	Population	Green ratio (%)	Green capita per person
Androon Bhatti Gate	28	441095.51	63100	65120	14.305	0.969
Qilla Gujar Singh	29	2411458.19	126201	51212	5.233	2.464
Anarkali	46	2043795.17	57364	55167	2.807	1.04
Gawalmandi	34	877979.3595	0	66356	0	0

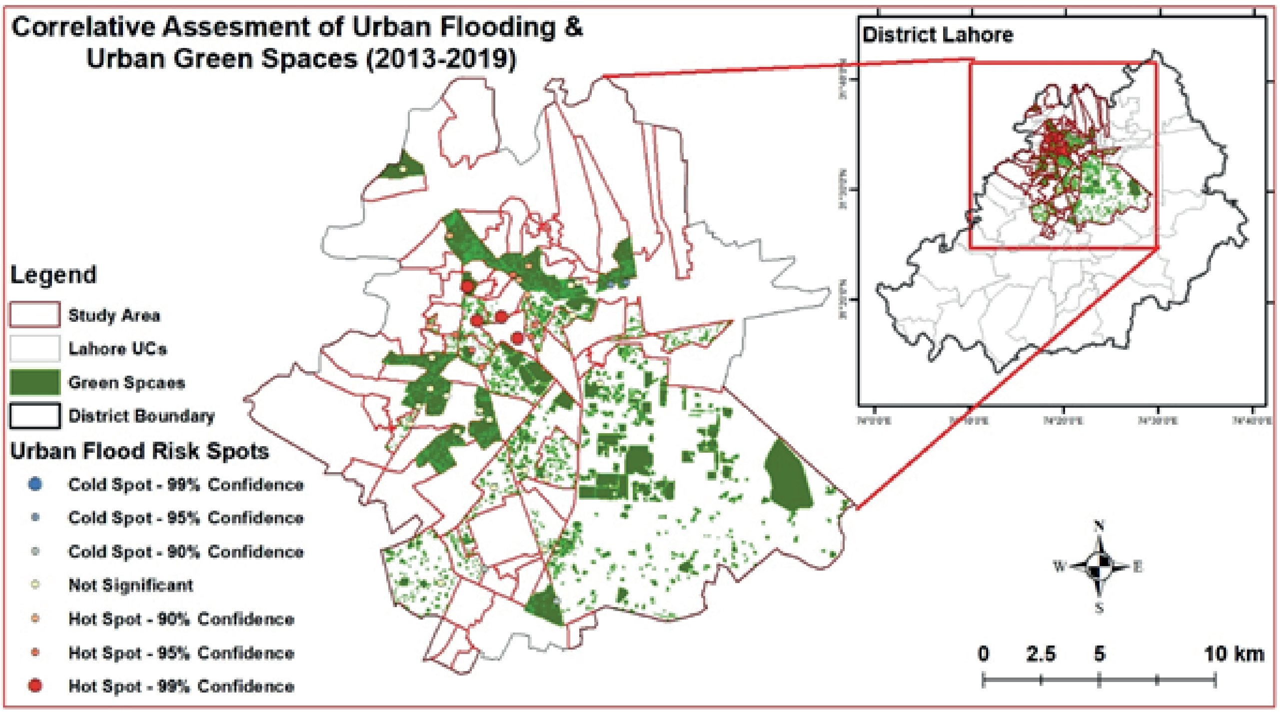

Fig. 8. Correlation between frequency of urban flooding and urban green spaces

REFERENCES

Afriyanie D., Julian M.M., Riqqi A., Akbar R., Suroso D.S.A. and Kustiwan I. (2020). Re-framing urban green spaces planning for flood protection through socio-ecological resilience in Bandung City, Indonesia. Cities, 101, 102710, DOI: 10.1016/j.cities.2020.102710.

Alam R., Shirazi S.A., Zia S. and Bhalli M.N. (2014). Spatial distribution of urban green spaces in Lahore, Pakistan: A case study of Gulberg Town. Pakistan Journal of Science, 66(3), 277-281.

Ballard B.W., Wilson S., Udale-Clarke H., Illman S., Scott T., Ashley R., and Kellagher R. (2015). The SUDS manual. CIRIA: London, UK.

Bowen K.J. and Lynch Y. (2017). The public health benefits of green infrastructure: the potential of economic framing for enhanced decision-making. Current Opinion in Environmental Sustainability, 25, 90-95.

Duffy A., Jefferies C., Waddell G., Shanks G., Blackwood D. and Watkins A. (2008). A cost comparison of traditional drainage and SUDS in Scotland. Water Science and Technology, 57(9), 1451-1459.

Dilley M. (2005). Natural disaster hotspots: a global risk analysis (Vol. 5): World Bank Publications.

Foster J., Lowe A., and Winkelman S. (2011). The value of green space for urban climate adaptation. Center for Clean Air Policy, February.

Fung T., and Siu W. (2000). Environmental quality and its changes, an analysis using NDVI. International Journal of Remote Sensing, 21(5), 1011-1024.

Gad M.A., Elshehaly, M.H., Gračanin, D., and Elmongui, H.G. (2018). A Tracking Analyst for large 3D spatiotemporal data from multiple sources (case study: Tracking volcanic eruptions in the atmosphere). Computers & Geosciences, 111, 283-293, DOI: 10.1016/j.cageo.2017.10.003.

Gandhi G.M., Parthiban S., Thummalu N. and Christy A. (2015). NDVI: Vegetation Change Detection Using Remote Sensing and GIS – A Case Study of Vellore District. Procedia Computer Science, 57, 1199-1210, DOI: 10.1016/j.procs.2015.07.415.

Gimenez-Maranges M., Pappalardo V., La Rosa D., Breuste J., and Hof A. (2020). The transition to adaptive storm-water management: Learning from existing experiences in Italy and Southern France. Sustainable Cities and Society, 55, 102061.

GOP (2000). District Census Report of Lahore 1998. Population Census Organization, Statistics Division Islamabad: Govt. of Pakistan. Retrieved from http://www.pbscensus.gov.pk

GOP. (2016). Punjab Development Statistics (PDS) 2016. Bureau of Statistics Lahore. Government of Punjab. Pakistan.

GOP. (2017). Provisional Summary Results of 6th Population and Housing Census 2017, Population Census Organization, Statistics Division Islamabad: Govt. of Pakistan, Retrieved from https://www.pbs.gov.pk/content/brief-census-2017.

Gordon W.S., Harle T. and Naismith I. (2007). Cost-benefit of SUDS retrofit in urban areas: Environment Agency.

Hammond M.J., Chen A.S., Djordjević S., Butler D. and Mark O. (2015). Urban flood impact assessment: A state-of-the-art review. Urban Water Journal, 12(1), 14-29, DOI: 10.1080/1573062x.2013.857421.

Hanif A., Nasar-u-Minallah M., Zia S., Ashraf, I. (2022) Mapping and Analyzing the Park Cooling Intensity in Mitigation of Urban Heat Island Effect in Lahore, Pakistan. Korean Journal of Remote Sensing, 38(1), 127-137, DOI: 10.7780/kjrs.2022.38.1.10

Kim H.Y. (2021). Analyzing green space as a flooding mitigation–storm Chaba case in South Korea, Geomatics, Natural Hazards and Risk, 12:1, 1181-1194, DOI: 10.1080/19475705.2021.1920478.

Liu L, Jensen M.B. (2018). Green space for sustainable urban water management: Practices of five forerunner cities. Cities, 74, 126-133.

Mahmood S. and Rahman A. U. (2019). Flash flood susceptibility modeling using geo-morphometric and hydrological approaches in Panjkora Basin, Eastern Hindu Kush, Pakistan. Environmental Earth Sciences, 78(1), 43.

Meerow S., and Newell J.P. (2017). Spatial planning for multifunctional green space: Growing resilience in Detroit. Landscape Urban Plan, 159, 62-75.

Mohtar W.H.M.W., Abdullah J., Maulud K.N.A. and Muhammad N. S. (2020). Urban flash flood index based on historical rainfall events. Sustainable Cities and Society, 56, 102088.

Nasar-u-Minallah M. (2020) Exploring the Relationship between Land Surface Temperature and Land use change in Lahore using Landsat Data. Pakistan Journal of Scientific & Industrial Research Series A: Physical Sciences, 63A (3), 188-200.

Nasar-u-Minallah, M. Zia S., Rahman A., Riaz O. (2021) Spatio-Temporal Analysis of Urban Expansion and Future Growth Patterns of Lahore, Pakistan. Geography, Environment, Sustainability, 14(3):41-53, DOI: 10.24057/2071-9388-2020-215

Ong B. L. (2003). Green plot ratio: an ecological measure for architecture and urban planning. Landscape and urban planning, 63(4), 197-211, DOI: 10.1016/S0169-2046(02)00191-3.

Shuster W.D., Bonta J., Thurston H., Warnemuende E. and Smith D. (2005). Impacts of impervious surface on watershed hydrology: A review. Urban Water Journal, 2(4), 263-275.

United Nations (2018). The World's Cities in 2018. In The World's Cities in 2018-Data Booklet (ST/ESA/ SER.A/417).

Wong T. H. and Brown R. R. (2009). The water sensitive city: principles for practice. Water Science and Technology, 60(3), 673-682.

Yu L., and Gong P. (2012). Google Earth as a virtual globe tool for Earth science applications at the global scale: progress and perspectives. International Journal of Remote Sensing, 33(12), 3966-3986.

Zia S. and Shirazi, S.A. (2019). Spatio-Temporal Analysis of Areas Vulnerable to Urban Flooding: A Case Study of Lahore, Pakistan. International Journal of Economic and Environmental Geology, 10(3), 85-89.

Zia S., Shirazi, S.A., and Nasar-u-Minallah M. (2021) Vulnerability Assessment of Urban Floods in Lahore, Pakistan using GIS based integrated Analytical Hierarchy Approach. Proceedings of the Pakistan Academy of Sciences: A. Physical and Computational Sciences, 58(1), 85-96.

Zia S., Shirazi, S.A., Nasar-u-Minallah M., and Batool M. (2021a) Urban Floods and Suitability Analysis of Rainwater Harvesting Potential Areas in Lahore City, Pakistan. International Journal of Economic and Environmental Geology, 12(2), 13-20.

RESEARCH PAPER

EVALUATING ZINC NUTRITION IN PERENNIAL RYEGRASS GROWN IN AN ANDISOL

Jason W. Stuckey[1], José Verdejo[2], Sebastián García[2], Dante Pinochet[2], Carolina Yáñez[3], Yu. A. Krutyakov[4,5], Alexander Neaman[6*]
[1]Natural Sciences Department and Environmental Science Program, Multnomah University, Portland, OR, USA
[2]Instituto de Ingeniería Agraria y Suelos, Facultad de Ciencias Agrarias y Alimentarias, Universidad Austral de Chile, Valdivia, Chile
[3]Instituto de Biología, Pontificia Universidad Católica de Valparaíso, Valparaíso, Chile
[4]National Research Centre «Kurchatov Institute», Moscow, Russia
[5]Laboratory of Functional Materials for Agriculture, Department of Chemistry, Lomonosov Moscow State University, Moscow, Russia
[6]Departamento de Recursos Ambientales, Facultad de Ciencias Agronómicas, Universidad de Tarapacá, Arica, Chile
***Corresponding author:** alexander.neaman@gmail.com
Received: April 8th, 2022 / Accepted: August 8th, 2022 / Published: October 01st, 2022
https://DOI-10.24057/2071-9388-2022-041

ABSTRACT. Zinc is an essential nutrient for humans, animals, and plants. Zinc uptake by crops is dictated by zinc availability in the soil, which in turn may be dictated, at least in part, by soil mineralogy. Little is known about the phytoavailability of Zn in Andisols, which are important agricultural soils in volcanic regions, such as Japan, New Zealand, and southern Chile. In this study, we assessed the vegetative growth response of perennial ryegrass (*Lolium perenne*, L.) to Zn fertilization in an Andisol from southern Chile. Ryegrass was grown in a greenhouse pot experiment with twelve rates of Zn application from 0 to 6075 mg Zn/kg soil. After 63 days, shoot length, specific leaf area, and biomass were measured. Foliar Zn concentrations were measured and correlated with plant-available Zn as measured by a diethylenetriaminepentaacetic acid (DTPA)-soil extraction (DTPA-Zn hereafter). Zinc toxicity to ryegrass was assessed using the Toxicity Relationship Analysis Program. This study demonstrated that a DTPA-Zn level of 1 mg Zn/kg soil was not limiting for ryegrass growth. Although Zn fertilization did not improve ryegrass growth in the studied Andisol, this study still has practical implications. Zinc deficiency in humans is a global problem and increasing Zn in staple food and forage crops may require Zn fertilization. This study suggests that Andisols can be fertilized with high doses of Zn without a risk of causing Zn toxicity to crops. However, a DTPA-Zn level of >489 mg Zn/kg soil decreased shoot length, indicating a toxicity response.

KEYWORDS: Zinc, ryegrass, soil, Andisols, DTPA

CITATION: Stuckey J. W., Verdejo J., García S., Pinochet D., Yáñez C., Krutyakov Yu. A., Neaman A. (2022). Evaluating Zinc Nutrition In Perennial Ryegrass Grown In An Andisol. Geography, Environment, Sustainability. 3(15), 56-60
https://DOI-10.24057/2071-9388-2022-041

ACKNOWLEDGEMENTS: The experimental study was partially funded by the FONDECYT 1200048 project (granted to Alexander Neaman). We wish to thank anonymous reviewers for their helpful comments and Andrei Tchourakov for editing this article.

Conflict of interests: The authors reported no potential conflict of interest.

INTRODUCTION

Zinc is an essential nutrient for humans, animals, and plants. Specifically, Zn is a vital component of many enzymes involved in the metabolic growth and development of plant tissue. Zinc is particularly important for nitrogen metabolism and protein synthesis (Brown et al. 1993).

Assessing the potential for Zn deficiency in crops rests on correlating method-dependent extractable Zn levels to plant growth responses in various soils. The critical limit for Zn is the soil-extractable Zn level below which a particular crop will respond to Zn application. For instance, DTPA-extractable Zn (hereafter, DTPA-Zn) was correlated with corn yields in 77 near-neutral and calcareous soils from Colorado, USA (Lindsay and Norvell 1978). The critical level for corn was 0.8 mg/kg DTPA-Zn (Alley et al. 1972, Lindsay and Norvell 1978). Similarly, the critical level for corn was 0.9 mg/kg NH_4HCO_3-DTPA-extractable Zn in 44 Colorado soils (Havlin and Soltanpour 1981). In soils of the Atlantic Coastal Plain, Midwest, and California (USA), the critical levels for soybean and corn were in the range of 0.5-0.6 mg/kg DTPA-Zn (Brown et al. 1971, Makarim and Cox 1983). The critical level of Zn was 0.69 mg/kg DTPA-Zn for peas grown in Indian paddy soils (Indira Sarangthem et al. 2018), and is generally between 0.6 and 1.0 mg/kg in Indian soils depending on the crop (Katyal 1993, Katyal and Sharma 1991).

Salazar et al. (2021) developed a model for recommending the application of Zn fertilizer in the Mediterranean region of central Chile. However, little is known about Zn phytoavailability in Andisols (i.e., soils derived from volcanic ash) (Hue 2004). Andisols contain a preponderance of short-range order minerals, such as allophone and imogolite, which are known to limit phosphorus availability to plants (Velásquez et al. 2016, Vistoso et al. 2020). Andisols are geographically prominent in agricultural regions of southern Chile, Colombia, Iceland, Indonesia, Japan, central Mexico, New Zealand, and the pacific northwest of the United States. Andisols are important for cereal crops and livestock grazing in southern Chile.

In this study, we hypothesized that Zn may be a crop-limiting nutrient in Andisols. Accordingly, the objective of this research was to evaluate the vegetative growth response of perennial ryegrass *(Lolium Perenne*, L.) to Zn fertilization in an Andisol of southern Chile. Perennial ryegrass was chosen for its global use as a forage crop.

MATERIALS AND METHODS

Ryegrass growth bioassay

Soil from a 2 m^2 area was excavated completely from the land surface to a depth of 20 cm from a permanent grassland field at the Austral Farming Experimental Station (EEAA) of the Universidad Austral de Chile (39° 47' S, 73° 14' W). The soil is classified as a Duric Hapludand (Bravo et al. 2020). The sample was sieved though a 5 mm mesh, homogenized and dried at 40°C for 48 hours. In order to determine the general physicochemical characteristics of the soil (Table 1), a 1 kg subsample was taken and sieved through a 2 mm mesh. Soil texture and total metal concentrations were determined by standard methods (Sadzawka et al. 2015).

Perennial ryegrass (*Lolium perenne* L.), variety Nui, was used for the Zn nutrition assessment bioassay. Twelve different Zn^{2+} application rates with four replicates were used: 0 mg kg^{-1}, 12 mg kg^{-1}, 28 mg kg^{-1}, 40 mg kg^{-1}, 61 mg kg^{-1}, 121 mg kg^{-1}, 202 mg kg^{-1}, 405 mg kg^{-1}, 810 mg kg^{-1}, 2025 mg kg^{-1}, 4050 mg kg^{-1}, and 6075 mg kg^{-1} (Supplementary Table 1). One week prior to the bioassay, the different Zn dose treatments were fertilized using $ZnSO_4$, then incubated at field capacity and room temperature, and homogenized daily.

A mass of 450 g of soil was placed in a plastic container measuring 9 cm x 9 cm x 9.5 cm (width x length x height; 770 cm^3) for each replicate. The containers were placed in the greenhouse using a fully randomized design. Fifty seeds were sown per container and were thinned out on day 7 to leave 25 plants in each container. The total length of the test period was 63 days, including the germination period. Plant-available Zn was determined for the initial soil and at the end of the 63-day greenhouse experiment for each treatment using a DTPA extracting solution (0.005 M DTPA + 0.005 M $CaCl_2$ + 0.1 M TEA, pH 7.3) (Lindsay and Norvell 1978).

Each container was watered and fertilized with a Hoagland nutrient solution without Zn and diluted 5 times more than the standard nutrient solution: 1.40 mM K^+; 3.80 mM NO_3^-; 0.40 mM PO_4^{3-}; 0.011 mM Na^+; 1.40 mM Ca^{2+}; 0.40 mM Mg^{2+}; 0.41 mM SO_4^{2-}; 0.0056 mM Fe^{2+}; 0.0018 mM Mn^{2+}; 0.0091 mM BO_3^{3-}; 0.0001 mM Cu^{2+}; 2.73 x 10^{-5} mM MoO_4^{2-}.

Plant responses

Upon completion of the biotesting period, the shoot length of five representative plants was recorded. Shoot lengths were measured from the root neck to the distal ends of the last leaf. The biomass of shoots was determined with a precision balance (Radwag WTC 2000, Radom, Poland) after drying the shoots in an oven at 70°C for 48 hours. In order to compare with field conditions, shoot dry biomass is expressed in ton ha^{-1}, calculated by projecting the surface of the container used in the bioassay (63.6 cm^2). Specific leaf area in each container was measured using an electronic leaf area meter (LI 3100, Licor Inc., Lincoln NE, USA). Specific leaf area is expressed in m^2 kg^{-1} dry weight. Foliar concentrations of Zn were measured at the end of the testing period using standard methods (Kalra 1998).

Statistical analysis

Simple linear and non-linear regressions were carried out between the biological responses and DTPA-Zn and foliar Zn concentrations. Normal distribution and homogeneity of residuals were verified (Kutner et al. 2004). Linear and polynomial regressions between plant and soil variables were performed using the software GraphPad Prism 8. Statistical analyses were carried out using Statgraphics Centurion 18. DTPA-Zn effective concentrations (EC_x) were determined by the Toxicity Relationship Analysis Program (TRAP) version 1.22 (US EPA 2013). For the determination of the EC_x values, the 0 mg Zn kg^{-1} rate was used as a control (i.e., the unamended soil that contained 1.0 DTPA-Zn).

RESULTS AND DISCUSSION

Zinc availability and uptake response to Zn application

The DTPA-Zn level of 1 mg/kg in the studied Andisol falls within the typical range of 0.5-1.5 mg/kg for soils of southern Chile (Table 1; Figure 1). Similarly, DTPA-Zn levels in agricultural Andisols of the Ethiopian Rift Valley were in the range of 0.9-3.5 mg/kg (Baissa et al. 2007). Our results showed that applying additional Zn to the studied Andisol increased the plant available Zn (DTPA-Zn) and foliar uptake of Zn in ryegrass. Specifically, foliar Zn increased linearly up to 1.6 x 10^3 mg/kg with increasing Zn application rate up to 2.0 x 10^3 mg/kg and increased exponentially up to 3.3 x 10^4 mg/kg with a further increase in Zn application rate up to 6.1 x 10^3 mg/kg (Figure 2). DTPA-Zn increased up to 4.9 x 10^2 mg/kg with increasing Zn application rate up to 2.0 x 10^3 mg/kg (Figure 3). Foliar Zn increased linearly to 1.8 x 10^2 mg/kg as DTPA-Zn increased up to 4.9 x 10^1 mg/kg, and then tapered with increasing DTPA-Zn levels up to 2.5 x 10^2 mg/kg (Figure 4). As DTPA-Zn increased to 4.9 x 10^2 mg/kg and beyond, foliar Zn increased exponentially (Figure 4; Supplementary Figure 1). Similarly, DTPA-Zn strongly correlated with Zn uptake by ryegrass in Zn-contaminated soils with a range of DTPA-Zn of 10-3500 mg/kg (Singh et al. 1996).

Plant growth response to Zn availability and uptake

DTPA-Zn level in the range of 0-5 x 10^2 mg/kg did not impact shoot dry biomass, specific leaf area, and shoot length for ryegrass (Figure 5). Similarly, shoot dry biomass, specific leaf area, and shoot length for ryegrass were independent of foliar Zn concentrations (Figure 6). Thus, a DTPA-Zn level of 1 mg/kg was sufficient for growth of ryegrass in an Andisol of southern Chile. This is the first assessment of Zn nutrition for ryegrass grown in Andisols of which we are aware.

Perennial ryegrass is sensitive to excessive Zn levels (Grigorita et al. 2020). As DTPA-Zn levels increased above 5 x 10^2 mg/kg, shoot length in ryegrass decreased,

Fig. 1. General physicochemical properties of the studied soil

Soil property	Unit	Value
Organic matter	%	15
Texture		Silt loam
Total Cu	mg kg^{-1}	53
Total Zn	mg kg^{-1}	86
Total Pb	mg kg^{-1}	28
Total Cd	mg kg^{-1}	1.4
Total Cr	mg kg^{-1}	15
DTPA-Zn	mg kg^{-1}	1.0

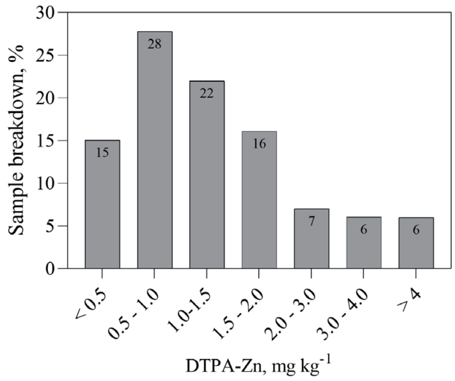

Fig. 1. Frequency histogram for the sample breakdown of DTPA-extractable Zn (DTPA-Zn) in soils from southern Chile. The data were obtained from the soil service laboratory of the Instituto de Ingeniería Agraria y Suelos, Universidad Austral de Chile (n = 1714)

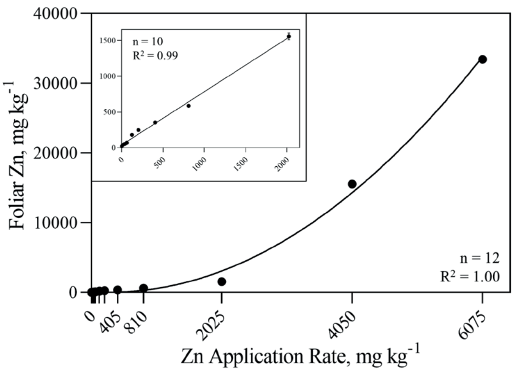

Fig. 2. Foliar Zn concentration as a function of the Zn application rate (n = 12). A third order polynomial function is fitted to this relationship. The inserted figure shows a linear regression model when we used the first 10 of 12 Zn dose treatments

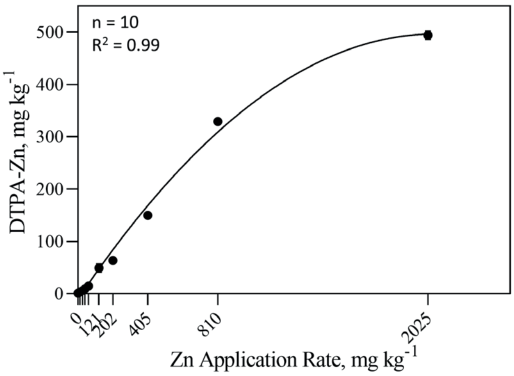

Fig. 3. DTPA-extractable Zn (DTPA-Zn) concentration as a function of the Zn application rate (n = 10). A second order polynomial function is fitted to this relationship

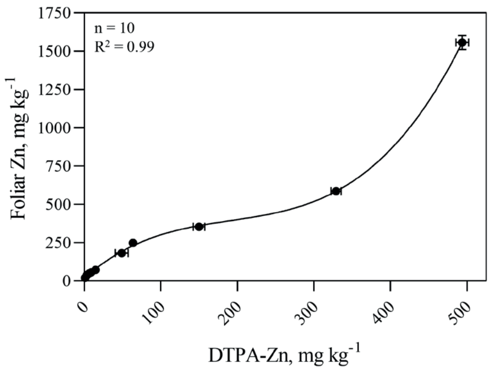

Fig. 4. Foliar Zn concentration as a function of DTPA-extractable Zn (DTPA-Zn) concentration (n = 10). A third order polynomial function is fitted to this relationship. Bars show the standard error of the means

exhibiting a toxicity response (Figure 7). For instance, at a DTPA-Zn level of 6.2 x 10^2 mg/kg, the shoot length of ryegrass decreased by 50% relative to control treatments (Figure 7; Supplementary Table 2). Thus, Zn application rates of 810 mg/kg Zn^{2+} (2000 mg/kg $ZnSO_4$) induced toxicity in ryegrass.

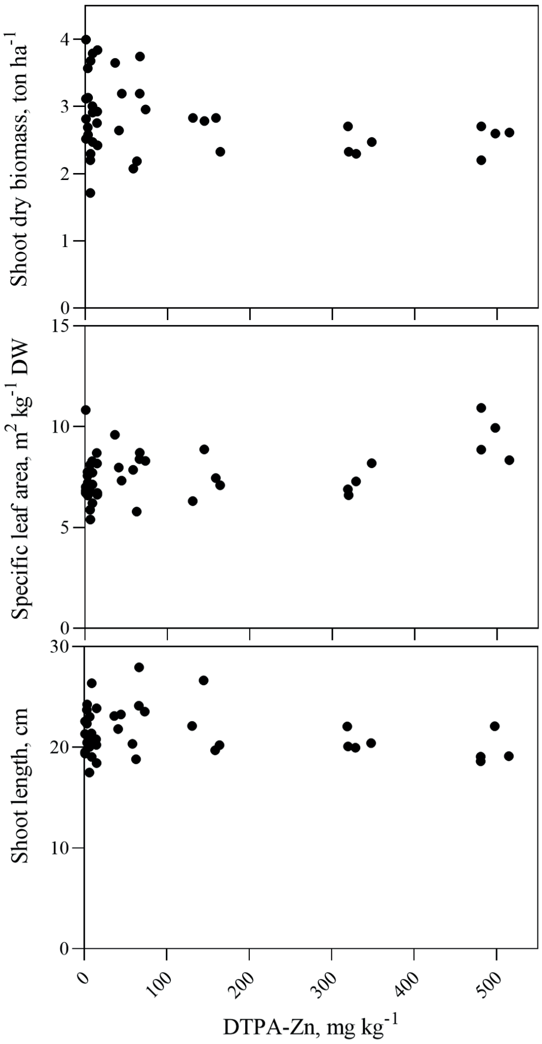

Fig. 5. Ryegrass responses as a function of DTPA-extractable Zn (DTPA-Zn) concentration (n = 10). Biological responses were independent of DTPA-Zn concentration not showing a linear or non-linear regression model

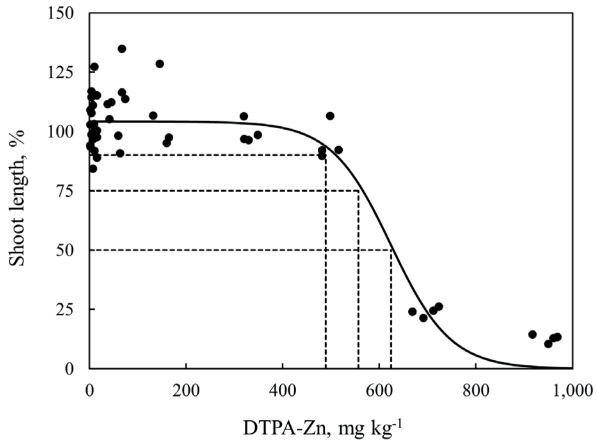

Fig. 7. Ryegrass shoot length as a function of DTPA-extractable Zn (DTPA-Zn) concentration. The y-axis represents shoot length expressed as a percentage respect to the control experiments. A logistic sigmoid regression analysis was used to fit the data (Toxicity Relationship Analysis Program, US Environmental Protection Agency). EC_{10}, EC_{25}, and EC_{50} are indicated

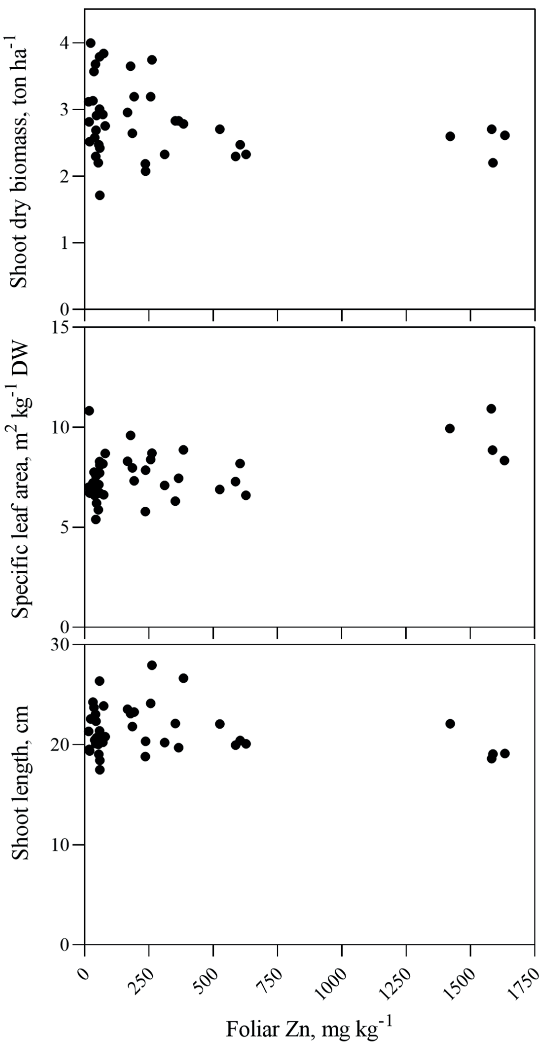

Fig. 6. Ryegrass responses as a function of foliar Zn concentration (n = 10). Biological responses were independent of foliar Zn concentration not showing a linear or non-linear regression model

CONCLUSION, PRACTICAL IMPLICATION AND FUTURE STUDY NEEDS

In this study, we hypothesized that zinc may be a crop-limiting nutrient in Andisols. However, a DTPA-Zn level of 1 mg Zn/kg soil was not limiting for ryegrass growth.

Although zinc fertilization did not improve ryegrass growth in the studied Andisol, this study still has practical implications because zinc deficiency in humans is a global problem. Indeed, approximately one-fifth to one-third of the world's human population has insufficient dietary Zn (Hotz and Brown 2004, Stein 2010). Thus, increasing Zn in staple food and forage crops may require Zn fertilization (Cakmak et al. 2017). This study suggests that Andisols can be fertilized with high doses of Zn without a risk of causing Zn toxicity to crops. However, a very high dose of Zn fertilization (>2000 mg Zn/kg soil, equal to a DTPA-Zn level of >489 mg Zn/kg soil) decreased shoot length, indicating a toxicity response.

Zinc fertilization should be studied in Andisols with DTPA-Zn levels lower than 1 mg Zn/kg soil. Likewise, studies involving other crops are warranted.

REFERENCES

Alley M., Martens D., Schnappinger Jr M., and Hawkins G. (1972). Field calibration of soil tests for available zinc. Soil Science Society of America Journal 36, 621-624, DOI: 10.2136/sssaj1972.03615995003600040034x.

Baissa T., Suwanarit A., Osotsapar Y., and Sarobol E. (2007). Status of Mn, Fe, Cu, Zn, B and Mo in Rift Valley Soils of Ethiopia: Laboratory Assessment. Agriculture and Natural Resources 41, 84-95.

Bravo S., González-Chang M., Dec D., Valle S., Wendroth O., Zúñiga F., and Dörner J. (2020). Using wavelet analyses to identify temporal coherence in soil physical properties in a volcanic ash-derived soil. Agricultural and Forest Meteorology 285, 107909, DOI: 10.1016/j.agrformet.2020.107909.

Brown A., Quick J., and Eddings J. (1971). A comparison of analytical methods for soil zinc. Soil Science Society of America Journal 35, 105-107, DOI: 10.2136/sssaj1971.03615995003500010031x.

Brown P.H., Cakmak I., and Zhang Q. (1993). Form and Function of Zinc Plants, In: Robson A. D., editor Zinc in Soils and Plants. Dordrecht: Springer, 93-106, DOI: 10.1007/978-94-011-0878-2_7.

Cakmak I., McLaughlin M.J., and White P.J. (2017). Zinc for better crop production and human health. Plant and Soil 411, 1-4, DOI: 10.1007/s11104-016-3166-9.

Grigorita G., Neaman A., Brykova R., Brykov V.A., Morev D.V., Ginocchio R., Paltseva A.A., Vidal K., Navarro-Villarroel C., and Dovletyarova E.A. (2020). Use of Zinc Carbonate Spiking to Obtain Phytotoxicity Thresholds Comparable to Those in Field-Collected Soils. Environmental Toxicology and Chemistry 39, 1790-1796, DOI: 10.1002/etc.4809.

Havlin J., and Soltanpour P. (1981). Evaluation of the NH4HCO3-DTPA soil test for iron and zinc. Soil Science Society of America Journal 45, 70-75, DOI: 10.2136/sssaj1981.03615995004500010016x.

Hotz C., and Brown K.H. (2004). Assessment of the risk of zinc deficiency in populations and options for its control. . Food and Nutrition Bulletin 25, S94-S203.

Hue N. (2004). Responses of coffee seedlings to calcium and zinc amendments to two Hawaiian acid soils. Journal of Plant Nutrition 27, 261-274, DOI: 10.1081/PLN-120027653.

Indira Sarangthem L., Sharma D., Oinam N., and Punilkumar L. (2018). Evaluation of Critical Limit of Zinc in Soil and Plant. International Journal of Current Research in Life Sciences 7, 2584-2586.

Kalra Y.P. (1998). Handbook of Reference Methods for Plant Analysis. Boca Raton, FL, USA: Soil and Plant Analysis Council, CRC Press.

Katyal J. (1993). Distribution of zinc in Indian soils. Fertilizer News 38, 15.

Katyal J.C., and Sharma B.D. (1991). DTPA-extractable and total Zn, Cu, Mn, and Fe in Indian soils and their association with some soil properties. Geoderma 49, 165-179, DOI: 10.1016/0016-7061(91)90099-f.

Kutner M., Nachtsheim C., and Neter J. (2004). Applied Linear Regression Models. Boston: McGraw-Hill Education.

Lindsay W.L., and Norvell W. (1978). Development of a DTPA soil test for zinc, iron, manganese, and copper. Soil Science Society of America Journal 42, 421-428, DOI: 10.2136/sssaj1978.03615995004200030009x.

Makarim A., and Cox F. (1983). Evaluation of the Need for Copper with Several Soil Extractants. Agronomy Journal 75, 493-496, DOI: 10.2134/agronj1983.00021962007500030018x.

Sadzawka A., Carrasco M.A., Demanet R., Flores H., Mora M.L., Neaman A., Hernández P., and Sandoval M. (2015). Métodos de análisis de lodos y de suelos. Chillán: Sociedad Chilena de la Ciencia del Suelo. Universidad de Concepción.

Salazar O., Manrique A., Tapia Y., Casanova M., Govan J., Covarrubias J.I., Contreras A., and Cabeza R.A. (2021). The Development of a Model for Recommending the Application of Zinc Fertilizer in the Mediterranean Region of Central Chile. Journal of Soil Science and Plant Nutrition 21, 249-257, DOI: 10.1007/s42729-020-00357-0.

Singh S., Tack F., and Verloo M. (1996). Extractability and bioavailability of heavy metals in surface soils derived from dredged sediments. Chemical Speciation & Bioavailability 8, 105-110, DOI: 10.1080/09542299.1996.11083274.

Stein A.J. (2010). Global impacts of human mineral malnutrition. Plant and Soil 335, 133-154, DOI: 10.1007/s11104-009-0228-2.

US EPA (2013). Toxicity Relationship Analysis Program (TRAP) version 1.22 United States Environmental Protection Agency, Mid-Continent Ecology Division, http://www.epa.gov/med/Prods_Pubs/trap.htm.

Velásquez G., Ngo P.-T., Rumpel C., Calabi-Floody M., Redel Y., Turner B.L., Condron L.M., and de la Luz Mora M. (2016). Chemical nature of residual phosphorus in Andisols. Geoderma 271, 27-31, DOI: 10.1016/j.geoderma.2016.01.027.

Vistoso E., Iraira S., and Sandaña P. (2020). Effects of phosphorus fertilizer solubility on pastures yield and quality in Andisols. Journal of Soil Science and Plant Nutrition 20, 637-647, DOI: 10.1007/s42729-019-00152-6.

RESEARCH PAPER

SEDIMENT DYNAMICS IN LACUSTRINE ENVIRONMENTS — NORTHERN AMAZON

Raquel A. Alves[1]*, Luiza C. Beserra Neta[2]
[1]Federal University of Minas Gerais, Avenida Presidente Antônio Carlos, CEP-31270-901, Belo Horizonte, Brazil
[2]Federal University of Roraima, Avenida Ene Garcês, CEP- 69310-970, Boa Vista, Brazil
***Corresponding author:** raquel.ar@yahoo.com
Received: August 12th, 2021 / Accepted: August 8th, 2022 / Published: October 01st, 2022
https://DOI-10.24057/2071-9388-2021-094

ABSTRACT. Lakes are features found in Brazil's northern region, commonly formed in sandy-clay layers of the Plio-Pleistocene, in a setting of the extensive flat surface, and under a high precipitation rate. Our goal in this work is to understand the sediment transport dynamic and its relation to the hydrological behavior of the regional lacustrine system. Two lakes were selected, Lago do Italiano (LIT) and Lago do Bicho (LB), situated in the municipality of Bonfim in the state of Roraima, Brazil. The lakes differ in hydrological regime, depth, and vegetation. The methodology involved bibliographical and remote sensor data and field surveys followed by laboratory processing. The results revealed that the lakes are composed of sandy materials, with layers what reach 95% of sand. The grains is medium to fine texture, with morphology angular (0 a 50%) and subangular (18% a 43%) grains, disposed at different depths. The grains' morphology suggests that their sediment provider source is near and, at the same time, indicates a low energy environment. Concerning the mineralogical attributes, the sediments are of a quartzose nature, which permits their correlation with the arenites of the Boa Vista Formation, a sub-cropping unit. The sediment input is controlled by the seasonal oscillation of the groundwater level and inundation pulses that reach the fluvio-lacustrine plain of the Tacutu River in which the lakes are inserted.

KEYWORDS: aquatic ecosystem, hydrological regime, sediment provenance, Amazonian lakes

CITATION: Alves R.A., Neta L.C.B. (2022). Sediment Dynamics In Lacustrine Environments — Northern Amazon. Geography, Environment, Sustainability, 3(15), 61-69
https://DOI-10.24057/2071-9388-2021-094

Conflict of interests: The authors reported no potential conflict of interest.

INTRODUCTION

The great diversity of formation processes of lake basins, such as the geological phenomena that act jointly or in isolation, causes the lakes to be common to different landscapes on the terrestrial surface. The lacustrine genesis generally links these features to glacial, volcanic, and tectonic environments, and its dynamics are related mainly to the fluvial and coastal processes. The lake basin development is reflected in the sediment compositions, made up of different materials from primary and secondary structures and with great variety in size, shape, and chemical composition.

These materials may come from autochthonous sources, such as those formed from the lake's own debris, originating mainly from herbaceous plants and plankton, deposited after dying, or from allochthonous sources, materials transported beyond their source area and later deposited in the lakes, carrying important information about the drainage basin to which they are integrated (Murdoch and Macknight 1994; Vonk et al. 2016).

The lakes are also considered to be sources of greenhouse gasses, resulting, amongst other factors, from the anaerobic degradation of the vegetal biomass, mediated by microorganisms acting according to the thermal stratification of the water column (Zdorovennova et al. 2016). In this scenario, the sediment-lake interface is of special interest to studies on climate change on different scales, due mainly to anthropic disturbances that have been observed, such as bad soil use, erosion, and siltation problems, reflecting the conditions of use and occupation of the lake (Cardoso et al. 2019).

Throughout the lakes' evolution, sediment layers are formed, containing chemical composts along with biological structures, representing the different phases of the process (Moiseenko et al. 2012). Thus, the sediments' capacity at accumulating composts is also responsible for turning this compartment into one of the most important for analyzing contamination levels of the aquatic environments since most of the fresh, liquid, and surface water on which humans depend is located in only a few lake basins (Meneses et al. 2007; Bootsma 2018).

In this light, understanding the lake sediment attributes is essential, considering that the flow and drainage dynamics interfere directly in the pedogenetic processes. Additionally, these studies help keep regular information about chemical element concentrations that may constitute a source of lake environment pollution, e.g., aluminum used in wastewater treatment and barium coming from insecticides (Maia et al. 2006). A study by Xu et al. (2017) in 110 lakes in China described the pollution of sediments by heavy metals, including cadmium, which is a highly toxic metal used, mainly in the manufacture of batteries.

That said, knowing the properties of lake sediments allows us to identify important historical records of events that occurred in the depositional environment, essential for the evolution and dynamics of the drainage basin, as well as for predicting scenarios for the recovery of these ecosystems. In Amazonia, systematic investigations of lake sediments have focused on the reconstruction of environmental changes in the late Quaternary; for example, the record of sediments dominated by organic material interspersed with debris indicate fluctuations in lake levels related to changes in humidity conditions and levels of precipitation in the region (Costa et al. 2005; Guimarães et al. 2016; Fassoni-Andrade and Paiva 2019).

Studies facing lacustrine environments in Roraima have been directed mainly to the state's eastern portion. Amongst them stand out works emphasizing ecological change (Simões Filho et al.1997); physiographic (Meneses et al. 2007); morphological and morphometrical (Pinheiro and Jardim 2015). Evidence of environmental transformation, pointed out by Santos Neto et al. (2013), promoted mainly by anthropic occupation at the lakes' natural limits, along with the morphogenetic approach of Alves and Beserra Neta (2018).

In this approach, the authors considered that the main responsible morphogenetic principles for the installation of the lakes are intimately linked to the condition of the predominantly plane relief, associated with the humid climatic conditions and the sandy-clay sediment cover of the Boa Vista Formation. In this sense, these lakes' spatial distribution derives from the relationship between the factors mentioned above and the local climatic regime, which affect the groundwater level variations. These factors result in the occurrence of the majority of the lakes in specific locations of which the gradient is concentrated in the inundation areas of the region's main rivers.

So far, the Northern Amazon lakes have been contemplated by studies approaching their diverse natural and anthropic aspects. However, aspects of their sediments in a refined scale remain poorly understood. Thus, the effort of this study is to support future limnological reconstitutions, since these lakes are already showing signs of degradation (Alves and Ribeiro 2018), having as its objective an understanding of the sediment transportation and depositing dynamics and the possible relation with the hydrological behavior of the regional lacustrine system, using as indicators the morphological, granulometric, mineralogical and chemical aspects of the superficial grains.

Two lakes were selected, differing in their hydrological regime, depth, and vegetation that adapts according to the presence of the water sheet. Such factors grant different answers to the characteristics of the sediment transport dynamics. In terms of environmental conditions, these lakes represent the reality of many northern Amazon lakes due to the environmental implications they are subjected to through the increase in urban occupations on their riverbanks.

MATERIALS AND METHODS

Study Area

The study area is located in the Bonfim municipality, east of the Roraima State, north of Brazil. The lakes investigated in this study are situated in this stretch: the *Lago do Italiano* (LIT) and the *Lago do Bicho* (LB), the former representing an intermittent regime, the latter perennial (Fig. 1).

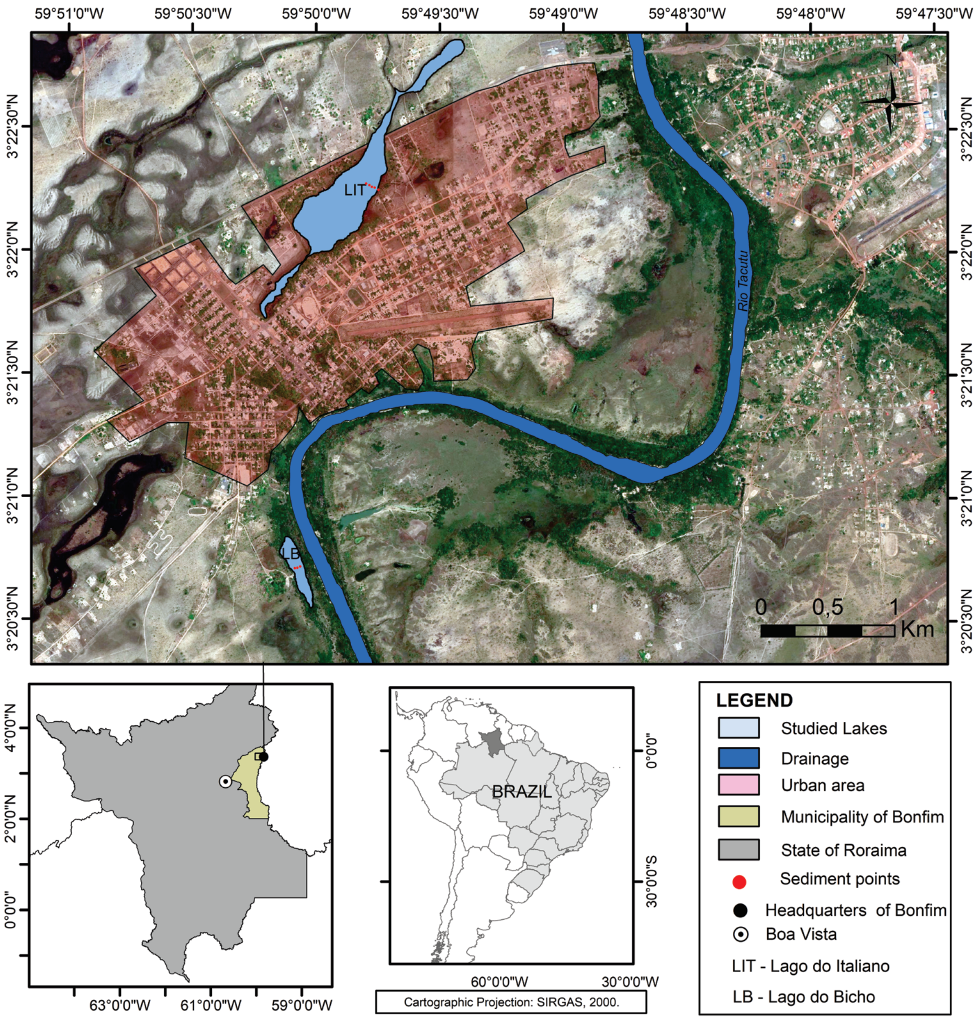

Fig. 1. Location of the study area with the Lago do Italiano (LIT) and the Lago do Bicho (LB), Roraima, Brazil

The geological terrain integrates the Cenozoic covers that comprise the lithotypes conglomeratic and arcosian sandstone and siltstone, grouped in the Boa Vista Formation, of Pliocene age, and recent alluvial deposits constituted of gravel, sand, and semi consolidated and unconsolidated clay (CPRM 2009). The area is inserted in a fluvial-lacustrine plain in the morphostructural domain Pediplano Rio Branco — Rio Negro (Franco, Del'Arco and Rivetti 1975), presenting plane features, gently undulating patterns with low altitudes.

The lithology is closely related to the region's soil types, predominantly oxisols, gleysols, and entisols (quartzipsamments). The first is distributed in the savannah, found on the plains, while the others are more predominant along the valley bottoms and tributaries of the river Tacutu (Melo et al. 2010).

The climate is tropical with dry and wet seasons, type "Aw" of the Köppen classification, having rainfall concentrated in the period May through August, and the dry season from September through April. The mean annual temperature is 27°C, with a rain index varying between 1,400 and 1,700mm yearly (Barbosa 1997).

The landscape is dominated by savannahs, composed of graminoid strata permeated by small arborescent species, spaced out or grouped, consisting of palm trees surrounding the aquatic ecosystems, thus forming the physiognomical mosaic of the region.

Procedure

The present study was guided by a survey of bibliographical, remote sensors, field, and laboratory data. In the field campaign, 23 lake sediment samples were collected in a sequential mode, considering vegetation, slope, and pedological gradient (Fig. 2). Vegetation was identified from field recognition and visual comparison of taxonomic data contained in Amaral et al. (2008) and Lorenzi (2017).

The sediment samples were subjected to granulometric analysis in two stages: the first was the separation of the sand, silt and clay fractions (aqueous method), the second was the separation of the sand fractions (dry sieving method) according to EMBRAPA (2018).

To separate the sand, silt, and clay fractions, 100 g of samples were placed in a beaker and added to 400ml of water, placed in a Unique brand ultrasonic washer, and stirred with the help of a glass rod for 10 minutes. In this process, the washer emits vibrations that allow the heaviest particles to remain at the bottom of the beaker, in this case, the sand, leaving the silt and clay in suspension. The process was repeated a few times until the water in the beaker looked clear and showed only the sand fraction. After disaggregation, the sand was left to dry at ambient air temperature.

The silt and clay were reserved for separation, which was carried out in a CentriBio® benchtop centrifuge. Inside the centrifuge, the samples were placed in test tubes that, when rotating for 2 minutes (Repetition Per Minute/1000), the silt fraction (solid) was deposited at the bottom of the container, while the clay fraction remained in suspension. After separation and drying, the fractions were weighed separately, which allowed the determination of the percentage between the sand, silt, and clay fractions. In each fraction, the values obtained in grams were statistically treated according to Folk and Ward (1957). The distribution of samples in granulometric classes was processed in SysGran 3.1 and demonstrated in triangular diagrams by Shepard (1954).

For sand separation, a set of Tyler series sieves was used with openings of 1.00mm, 500μ, 250μ, 125μ, 63μ,

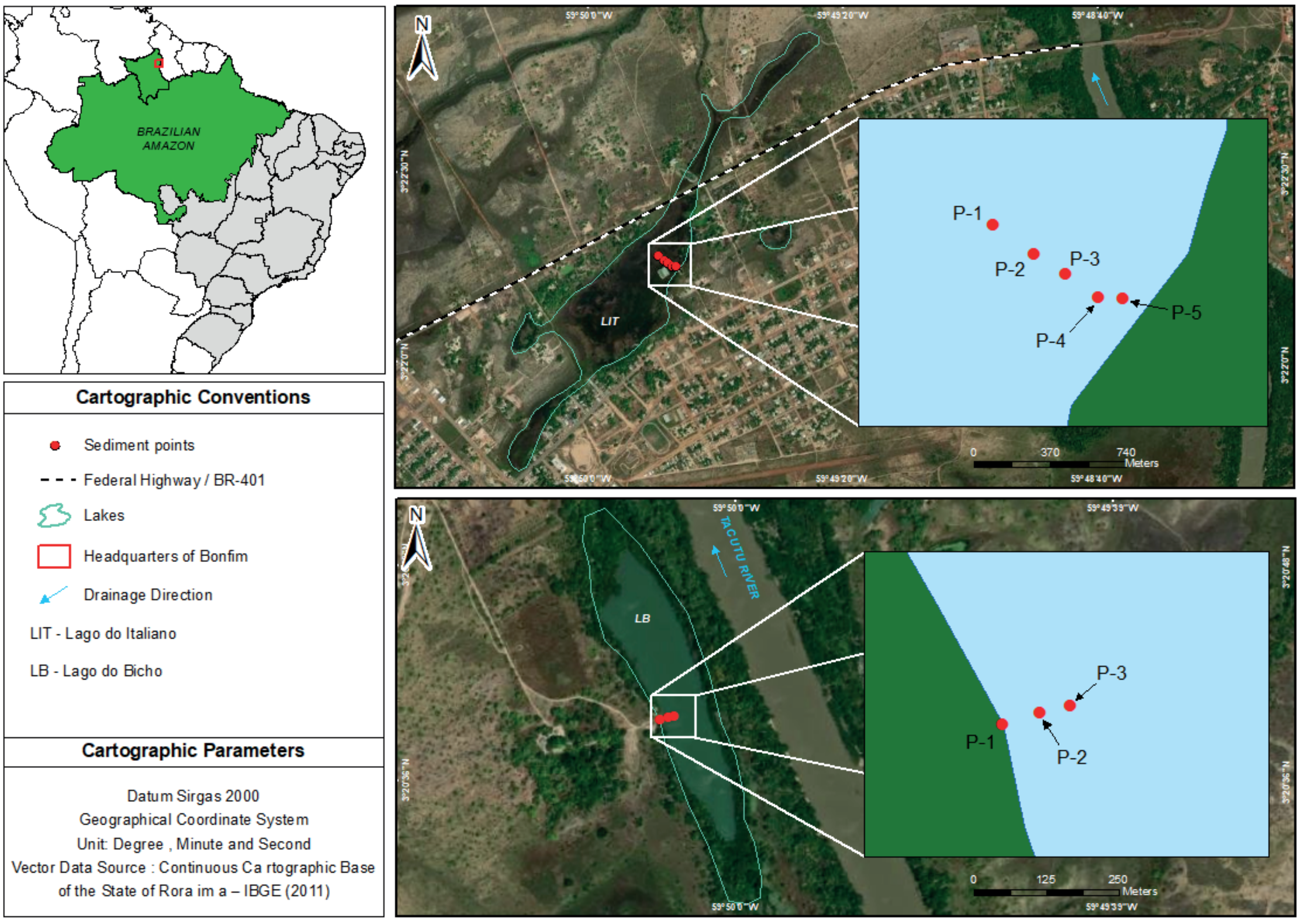

Fig. 2. Collection site in the Italiano (upper quadrant) and Bicho (lower quadrant) lakes

<63μ, superimposed in descending order placed in a mechanical shaker of the Bertel brand for 5 minutes. Upon sieving, the subfractions retained on each sieve were weighed separately, providing the necessary data for the constitution of histograms representative of their distribution in the samples. In the classification of the sediments in coarse, medium, and fine sand, the scale was used A. S. T. M. (American Society for Materials) being represented through of graphic.

The morphological analyzes of the sand grains were performed to determine the degree of roundness and sphericity of the sand grains. For this analysis, samples containing 100 grains of sand were separated and visually compared in a lupa binocular with a table of the degree of roundness mentioned by Suguio (1973). The measure of the degree of roundness for each grain is dependent on the roughness of the outer surface of the grain (perimeter) and gives the result between 0 and 1. The morphological classification being angular (0 - <15), subangular (0.15 - 0.25), rounded (0.25 - 0.40), subrounded (0.40 - 0.60) and well rounded (0.60 - 1.00).

The mineralogical identification was obtained through x-ray diffractometer, whose reading of the sample was analyzed in the scanning range of 5° to 70° 2θ (Theta), lasting 40 minutes (EMBRAPA 2018). The X'PertHighScore software was used to interpret the diffractogram peaks.

For the acquisition of high-resolution images of the sediments, a small number of grains was deposited on a carbon adhesive and inserted into the sample holder of the Scanning Electronic Microscope (SEM) model Hitachi TM3030, the scale varied from 20μm to 1mm, which allowed the detailed analysis of sediment morphology. Subsequently, punctual analyzes of the chemical composition of the grains were carried out by Energy Dispersive Spectrometry (EDS), and the percentage of chemical elements was acquired by linear mapping (single grain method).

RESULTS

Plant physiology of the lake environments

Located in the urban region of Bonfim, the Lago do Italiano, occupying an area of ~3.750m^2, is a system with a drainage flow connection pattern, presenting stretches of different width and elongated morphology. The hydrologic regime is intermittent, while in the driest period of the year, the absence of rain associated with the lowering of the groundwater level favors rapid evapotranspiration, leaving the lake's basin exposed. During the rainy season, the lake becomes intensely colonized by emerging aquatic macrophytes, mainly reed (Juncus effusus), besides colonization of adapted species, occurring in lower numbers, such as fixed nymphaeaceous macrophytes with floating leaves, capable of colonizing both shallow and deeper environments. The landscape surrounding the Lago do Italiano is characterized by an arboreal plant cover, concentrated at the eastern bank of the lake basin and one more herbaceous vegetation concentrated at its western bank.

The Lago do Bicho, in turn, occupying an area of 531m^2, is a lake of lateral accretion, with an elongated shape and NW-SE orientation, formed along the right bank of the river Tacutu.

During the wettest periods, this lake receives large amounts of sediments. Situated in the Tacutu flood plain, the lake undergoes a perennial regime, presenting significant depth as compared to the Lago do Italiano. Because of its depth, vegetation is restricted to the lake's margins. Furthermore, the settlement of species is modified according to the altimetry of the area. In this respect, arboreal densification (Genipa americana) occurs intermingled with isolated palm species (Astrocaryum aculeatum). In the intermediate area, on the other hand, bordering the water sheet, fixed macrophytes with floating stalks appear (Montrichardia arborescens), these in turn being adapted to the ecotone conditions of lacustrine environments and hydromorphic environments at the valley bottoms, influenced mainly by slope and water level variations.

Sediment characterization and its relation with transportation dynamics and lake deposits

According to Shepard Classification, the sediments have a predominance of sand texture, followed by silty sand and clayey sand, with texture variation in the intervals throughout the sampled sequence (Fig. 3). The largest textural changes were observed in the range from 0 to 20 cm of the (P1-LIT) with the occurrence of clayey silt sediments and of (P5-LIT) with the occurrence of silt-clay-sandy sediments.

On the other hand, the granulometric distribution pattern between the layers of Lago do Bicho presented subtle textural variation between the intervals. In this lake, the silty sand texture prevailed, with an increase in the concentration of silt at depth in the (P2-LB) range of 40 to 60 cm. Notably, at point P3-LB, there was a significant increase in clay in the range of 20 to 40 cm, which was reflected in the texture that was classified as clayey sand (Fig. 3).

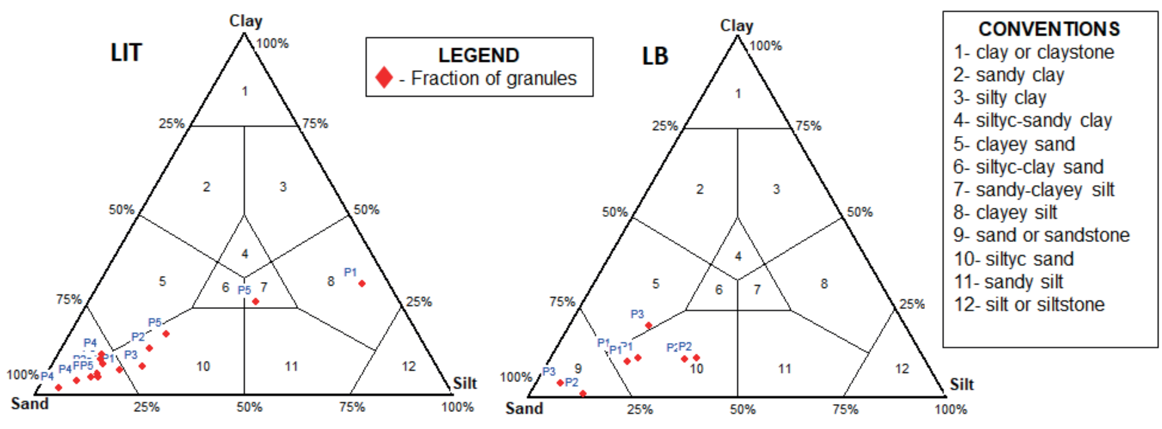

Fig. 3. Textural classification of sediments sampled in lakes. Each point and depth is indicated on Shepard's diagrams with blue letters and red symbol

The granulometric distribution in Lago do Italiano occurs in the order of 8% to 95% of sand in the entire sampled sequence, values of 3% to 61% of silt, and values of clay between 2% to 31%. In the (P1-LIT) range of 0 - 20 cm (center of the lake), there was a high concentration of silt in contrast to the absence of coarser granulometry in this surface layer. In Lago do Bicho, the sediments are dominated by a sand fraction with a content of 54% to 90%, silt with values from 6% to 35%, and clay with values from 4% to 20% (Fig. 4).

For what concerns the morphological analyses, it was evidenced that the lakes are constituted by angular and sub-angular grains. The angular grains varied between 0% and 50% and the sub-angular ones between 18% and 43%. The other grains, sub-rounded, rounded, and well rounded, occur in the order of 3% to 35%. The angular grains are present predominantly at the border of the Lago do Italiano at greater depth. In contrast, the sub-rounded grains prevail increasingly toward the center of the lake, in the more shallow layers with the interval of 0 to 20 cm (Fig. 5). Those grains are disposed of at greater depth and linked to a coarser material.

The largest part of the materials found in this group shows contrasting environmental conditions, such as redox status changes in some cases, with grains appearing crystalline, translucent, or more opaque, while others show yellowish chroma pigments and more brownish tones (Fig. 6).

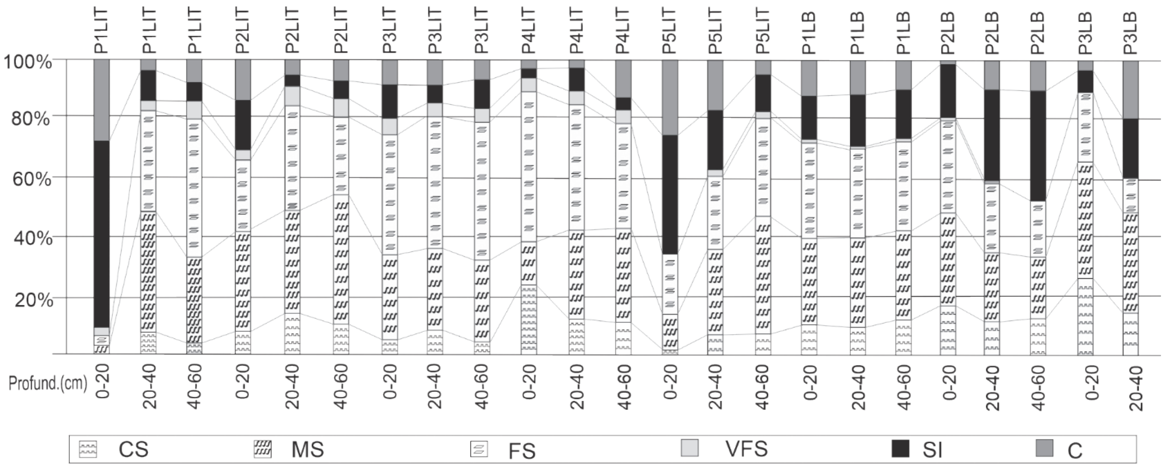

Fig. 4. Textural distribution of sediments along the profiles
Key: CS=coarse sand; MS=medium sand; FS=fine sand; VFS= very fine sand; SI=silt; C=clay.

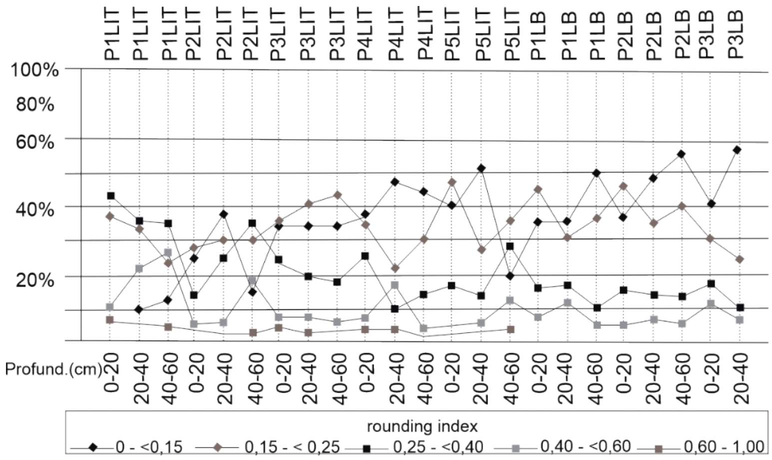

Fig. 5. Morphological sediment distribution at intervals of 0 to 60 cm

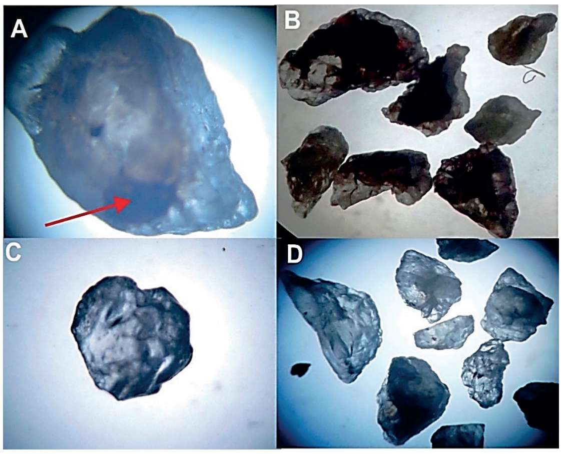

Fig. 6. Node presents zones of depletion and accumulation of Fe, corresponding to changes in the element's oxidation state. (B) Angular translucent grains with interior fabric with brownish pigment. (C) Sub-rounded grain presenting cavities. (D) Angular to sub-angular grains containing edges on the surface

The images generated by SEM showed different degrees of rounding and a variety of superficial features of mechanical origin such as abrasion marked surfaces, fractures, and edges. The sub-rounded grains show an expressive reworking, indicated by dissolution features on their surfaces (Fig. 7).

In order to confirm the visual observations, the minerals were detected through x-ray diffraction, which revealed in their spectra quartz, kaolinite, goethite, and muscovite, being similarly distributed between the intervals, with the exception of sediments at a depth of 0 to 20 cm of (P1), corresponding to the sample of the center of Lago do Italiano. Lower peak values for quartz were obtained in this interval, which may be justified by the concentration of organic matter in the samples of this profile.

Based on these data, the main chemical elements obtained from the total EDS chemical analyses can be distributed (Fig. 8). Such analyses evidenced and reinforced the discussion of the mineralogy found in the sediments where the occurrence of Si (69.1%) prevailed, and secondarily, Al_2O_3 contents (28.89%), reflecting the predominance of quartz and the significant participation of accessories such as kaolinite and muscovite. Despite low levels, the occurrence of FeO (0.87%) was also detected, associated with goethite, and TiO_2 (0.56%), which may be associated with Zircon (Fig. 7D), a mineral that was not identified at the x-ray diffraction peaks.

The chemical composition mapping also evidenced traces of SO_3 (0.58%) that has sulphur as its carrier and

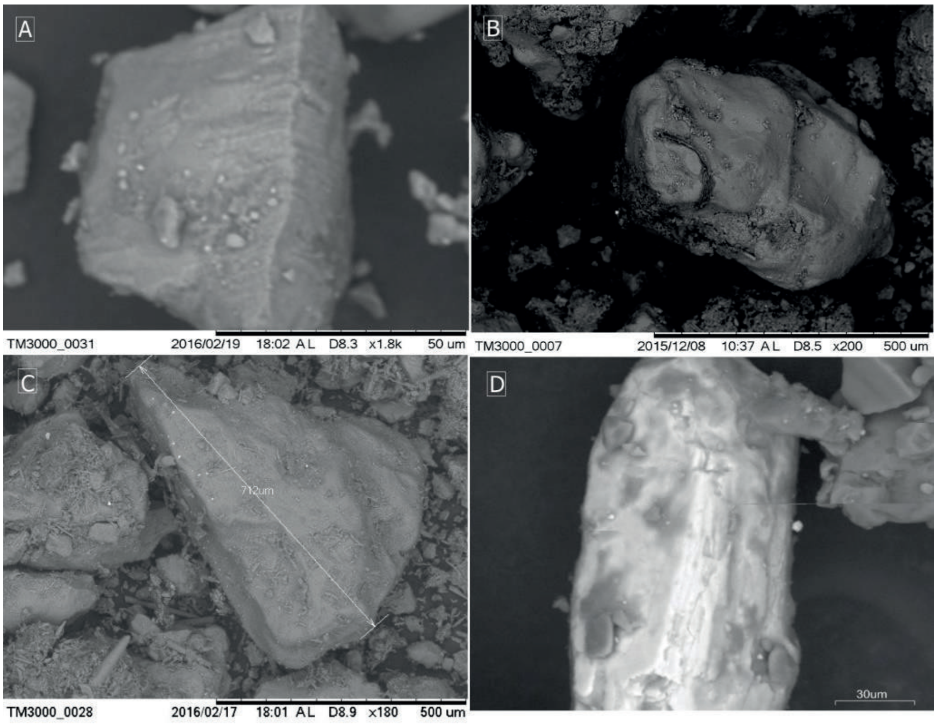

Fig. 7. Photomicrograph of grains obtained by SEM. (A) Detail of lenticular banding in quartz. (B) Grain with fractures and dissolution features on its surface. (C) Features of mechanical origin with abrasion edges in a quartz grain. (D) Zircon with rounded edges

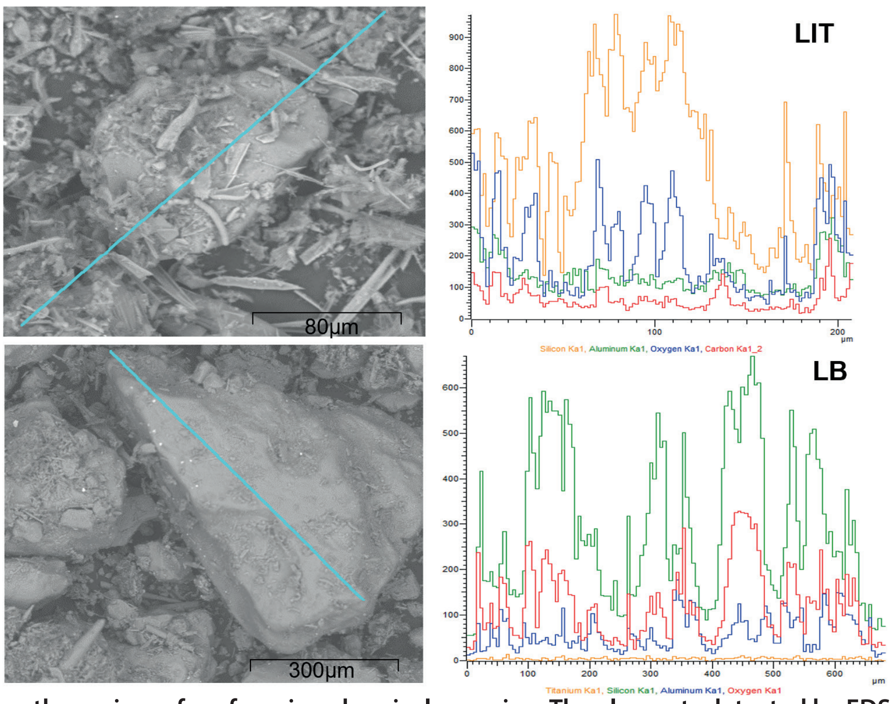

Fig. 8. Linear trace on the grain surface for microchemical mapping. The elements detected by EDS are shown in the graph on the side, where the occurrence of Si prevailed

is related to the in situ production of organic matter, as a consequence of the decomposition processes of macrophytes abundant in the lake. High levels of this chemical compound were found at the 0 - 20 cm interval, this being confirmed by the lower peak of quartz on XRD for this interval.

DISCUSSION

The presence of emerging macrophytes revealed the shallowness of the Lago do Italiano, Pinheiro and Jardim (2015), in analyses about the floristic colonization of lakes of similar shape, registered the occurrence of macrophytes in the horizontal zonation of the northern Amazon lakes: 45.8% of the species occur exclusively in the marginal areas; 12.5% in the intermediate area and 12.5% in the central area of the lakes.

Such results show that macrophytes' presence indicates eutrophication and is associated with abundant nutrient conditions (Ludikova 2021), suggesting a response of the ecosystem to the solar radiation intensity and temperature, these being: therefore, the main regulating factors of propagation. The rarefaction of emerging macrophyte species in the Lago do Bicho, on the other hand, is due to the morphometry of the basin and the constant water input, inhibiting productivity and vegetation settlement. In this regard, no vegetation was found in the central area of the lake. Thus, the plant cover variation surrounding the lakes must respond to the edaphic conditions, followed by the varied textural gradient, influencing the drainage dynamics and conferring vegetation heterogeneity.

Because these lakes possess a direct connection with the drainage network, they are fed seasonally (wet season) by the sediment input, mainly coming from canals of the first order, pointed out here as a possible source of sand for the system. The light textural variation observed in the shallow layers (Fig. 4) corresponds to the depositing pattern described by Thomas and Meybeck (1996). This occurs according to hydrodynamic energy differences, as the water's oscillating movement involves slow-moving currents and influences sediment transportation directions. The coarsest grain size values in the superficial layers of 0 - 20 cm entailed a directly proportional relationship to the silt concentration at this interval (Fig. 4). Generally, lake environments are places formed by sediments that present spatial grain size variation in a way that the coarsest material deposits occur near the borders. In contrast, fine texture materials occur in the central parts of lakes.

In this way, the angularity of the materials found in both lakes indicates that the sediments generally underwent short-distance transportation, evidencing that their source area is proximal. Barros et al. (2007) obtained similar data about sediment provenance in a coastal section stretch drained by the river Timbó in Pernambuco, northeastern Brazil. The predominance of angular and very angular grains (66%) in the sample analyses took these authors to acknowledge the sediment source area as being proximal, next to the river mouth.

The high degree of angularity of the Lago do Bicho sediments must be associated with the influence of the river Tacutu, which overflows during the periods of high precipitation and coalesces into the Lago do Bicho, delivering sediments to the lakes and plain, thus evidencing a strong seasonal control on the sediment transportation offer. Despite the minimal textural variation between the intervals, the granulometric distribution pattern between the layers showed a rise in silt concentration at a depth of (P2) of the Lago do Bicho. This is indicative of the material transportation from the highest point of the slope, that at reaching (P3), the contact with the water favors an energy reduction and, consequently, the precipitation of the finest materials near the river bed, while the coarsest fractions tend to concentrate at the borders of the lake. In this sense, the absence of coarser grain sizes in the shallow level of 0 - 20% in (P1, center of the Lago do Italiano) and high silt concentration at this interval may be observed (Figs. 3 and 4).

The nature of grains in the layers suggests an environment with low energy during the depositing process. The angular grains present sharp, well-preserved edges, pointing to source area proximity, causing little reworking during its transport, thus providing less opportunity for more rounding of the grains. Despite the sediments possessing quartz sand characteristics, they are not free of redoximorphic features that accumulate on the grains under the form of dark shaded nodes and stains, associated with saturation and desaturation of the water through groundwater level oscillation, resulting in a reduction of Fe compound precipitation (Fig. 6A).

Since we are dealing with lentic environments, the accumulation of organic matter is favored by the low hydrological energy and nutrition of organisms that influence the aspect of acidification of the medium, causing better preservation of the deposited organic matter (Fig. 6B). For example, grain size and carbon-nitrogen analyses of black water lakes, studied by Amorim et al. (2009), present organic matter as a consequence of in situ and marginal production processes, mainly by phytoplankton by the aquatic macrophytes. Furthermore, these studies provided evidence that these lakes possess more elevated levels of organic matter in the sediments for having more acidic waters that tend to better preserve it, beyond the fact that these lakes are characterized by low levels of suspended mineral matter that could dilute the organic content of the sediment.

The x-ray diffraction results (XRD) indicate the concentration of primary minerals such as quartz, followed by secondary phyllosilicates such as kaolinite, and secondary non-silicate minerals such as iron oxides, mainly goethite. These mineralogical; constituents encountered agree with the results obtained from SEM analysis. Furthermore, the presence of iron oxides usually favors the pigmenting action of the goethite, providing the sediment layers with the yellowish coloration, common to the inter-tropical regions, owing to the more pronounced weathering action in these areas.

Despite the mineralogy remaining quartzose, the occurrence of lithogenic metals as $ZrSiO_4$ is added (Fig. 7D). This occurrence is characteristic of granite rocks, made up essentially of quartz and feldspar, frequently registered among the coarse fractions of the detrital minerals in most of the sedimentary deposits, as they offer resistance to the natural wear caused by crustal processes (Machado et al. 2012). Furthermore, the adsorptive capacity of the fine-grained materials produces a directly proportional relationship with the occurrence of heavy metals and with the accumulation of organic matter in the superficial layers of the lake environments. The concentration of SO3 traces (0.58%) is related to the in situ production of organic matter, as a consequence of decomposition processes of macrophytes that are abundant in the lake, seeing that the organic matter is an important provider of sulphuric compounds for the sediments. The accumulation of organic matter in the Lago do Italiano is related to the proper sedimentation dynamics of the environment, where the greatest content changes occur after sedimentation. Due to the anaerobic conditions of these environments, the production processes of organic matter are intensified to the detriment of the decomposition processes, thus permitting its accumulation (Drabkova 1983). The decomposition of plant residues, on the other hand, produces fine organic matter that appears under the form of pigments that are incorporated into the grains as dark or reddish-brown stains (Fig. 6A and B).

The most abundant element identified by EDX analysis, Si, presents the highest concentrations reflected in the mineralogy of the sand fractions. Thus, such results are in consonance with those found by Benedetti et al. (2011), corresponding to the same constituents encountered by the author in the rocks of the Boa Vista Formation. In this way, it can be inferred that the Boa Vista Formation is the probable provider of the analyzed lake sediments, arriving at these lakes through the seasonal oscillation of the groundwater level and the flooding pulses to which the plain of the river Tacutu is subjected. Being a tropical environment, with the incidence of high temperatures and precipitation, allied to the geological formation with predominantly sedimentary rock, there are rapid changes in the evolutionary patterns of the drainage network, triggering severe erosive processes that provoke filling in and siltation of these lakes (Santos et al. 2020).

The results, however, present extremely fragile lake environments due to their texture, predominantly sandy, indicating a low water retention capacity. With the fluctuation of the groundwater level, water retention is much less due to a strong seasonality, leaving the lake basin exposed and subjected to anthropic actions.

CONCLUSIONS

The lakes encountered in the studied area reflect the diversity of climatic and geomorphological conditions of the Amazon region. They present themselves in a variety of shapes and sizes, differing in the perennial or intermittent regimes, reflected mainly in the distribution of aquatic plant colonization and sediment transportation dynamics. While the Lago do Italiano is fed by sediments coming from first-order canals, a consequence of its direct connection with the drainage network, the Lago do Bicho receives a seasonal input of sediments coming from flood pulses of the river Tacutu.

Despite the differences in the transportation modalities that feed these lakes, the sediments concentrate on angular sandy grains, varying from medium to fine texture, with colors characteristic of redoximorphic processes. Such attributes were interpreted as resulting from hydrological behavior, marked by depositional successions of a low energy environment.

REFERENCES

Alves R. and Beserra Neta L. (2018). Geomorphological compartmentation and morphological classification of lacustrine environmentsin the savannahsof the northeastern region of Roraima. Journal Acta Geographic, Boa Vista: UFRR, 12(29), 1-18, DOI: 10.5654/acta.v12i29.3669. (in Portuguese with English summary)

Alves R. and Ribeiro S. (2018). Changes in the lake landscape result from the anthropogenic activity in Lago do Italiano in Bonfim – Roraima. Annals: XV National Congress of the Environment. [online]. Availlable at: http://www.meioambientepocos.com.br/Anais2018 [Acessed 27 Mar. 2021]. (in Portuguese with English summary)

Amaral M., Bittrich V., Faria A., Anderson L. and Aona L. (2008). Field guide for aquatic and marshland plants of the state of São Paulo. Ribeirão Preto: Holos, p. 452.

Amorim M., Moreira-Turcq P., Turcq B. and Cordeiro R. (2009). Origin and dynamics of superficial sediment deposits in varzea do large lake of Curuai, Pará, Brasil. Journal Acta Amazônica, 39(1), 165-172, DOI: 10.1590/S0044-59672009000100016.

Benedetti U., Vale Júnior J., Schaefer C., Melo V. and Uchôa S. (2011). Genesis, chemistry and mineralogy of soils derived from plio-pleistocene sediments and basic volcanic rocks in Roraima, northern Amazon. Brazilian Journal of Soil Science, 35(2), 299-312, (in Portuguese with English summary), DOI: 10.1590/S0100-06832011000200002.

Barbosa R. (1997). Distribution of rains in Roraima. In: R. Barbosa, E. Ferreira and E. Castellon, eds., Man, Environment and Ecology in the State of Roraima. Manaus, INPA, (in Portuguese with English summary), 325-335.

Barros L., Valença L., Manso V., Madruga Filho J. and Oliveira, J. (2007). Texture, composition and rounding of sediments of the internal continental platform, adjacent to the river mouth south of the Santa Cruz Canal and the river Timbó, north of the state of Pernambuco. Geological Studies, 17(1), (in Portuguese with English summary), 58-70.

Bootsma H.A. (2018). Oceans, Lakes, and Inland Seas: A Virtual Issue on the Large Lakes of the World. Limnology and Oceanography Bulletin, 27, 87-88, DOI: 10.1002/lob.10230.

Cardoso S., Quadra G., Resende N. and Roland F. (2019). The role of sediments in the carbon and pollutant cycles in aquatic ecosystems. Acta Limnologica Brasiliensia, 31(201), DOI: 10.1590/s2179-975x8918.

Costa M.L., Carmo M.S. and Behling H. (2005). Mineralogy and geochemistry of lake sediments with lateritic substrate in the Brazilian Amazon. Brazilian Journal of Geosciences, 35(2), (in Portuguese with English summary), 165-176.

CPRM . Geological Service of Brazil — Basic Geological Surveys Programme Brazil. (2009). Geological Map State of Roraima Scale 1:500.000, (in Portuguese with English summary), Manaus: CPRM.

Drabkova V.G. (1983). Bacterial decomposition of organic matter in lacustrine sediments. Hydrobiology, 99-102, DOI: 10.1007/BF00028435.

EMBRAPA. Brazilian Agricultural Research Corporation. (2018). Manual of soil analysis methods. 3rd ed., (in Portuguese with English summary), Rio de Janeiro.

Esteves F.A. (2011). Fundamentals of Limnology. 3rd ed. Rio de Janeiro: Interciência. (in Portuguese with English summary), 826.

Fassoni-Andrade A.C. and Paiva R.C.D. (2019). Mapping of the spatio-temporal sedimentary dynamics of river floodplains in the Amazon. Remote Sensing of the Environment, 221, 94-107, (in Portuguese with English summary), DOI: 10.1016/j.rse.2018.10.038

Folk R. and Ward W. (1957). Brazos River bar: A study in the significance of grainsize parameters. Journal of Sedimentary Research, 27(1), 3-26, DOI: 10.1306/74D70646-2B21-11D7-8648000102C1865D.

Franco E., Del'Arco J. and Rivetti M. (1975). Geomorphology. In: BRASIL. Projeto Radam Brasil. Survey of Natural Resources. Pages NA 20 Boa Vista and part of Pages NA 21 Tumucumaque, NB20 Roraima and NB21, Rio de Janeiro: IBGE.

Ludikova A.V. (2021). Long-Term Studies of Surface-Sediment Diatom Assemblages In Assessing the Ecological State of Lake Ladoga, The Largest European Lake. Geography, Environment, Sustainability, 14(1), 251-262, DOI: 10.24057/2071-9388-2020-174.

Guimarães J.T.F., Sahoo P.K., Souza-Filho P.W.M., Maurity C.W., Silva Júnior R.O., Costa F.R. and Dall'Agnol R. (2016). Late Quaternary environmental and climate changes registered in lacustrine sediments of the Serra Sul de Carajás, south-east Amazonia. Journal of Quaternary Science, 31(2), 61-74, DOI: 10.1002/jqs.2839.

Lorenzi H. (2017). Brazilian trees: manual for identification and cultivation of arboreal plants arbóreas native of Brasil. Plantarum Institute of Flora Studies Ltd.. 5th ed. São Paulo: Nova Odessa, 2, (in Portuguese with English summary), 384.

Machado D.A.M, Fernandes L.A., Góes A.M., Mesquita M.J. and Lima F.M. (2012). Origin of sediments from the Curitiba Basin by studies of heavy minerals. Brazilian Journal of Geosciences, 42(3), 563-572, (in Portuguese with English summary), DOI: 10.25249/0375-7536.2012423563572.

Maia P., Boaventura G. and Pires A. (2006). Spatial distribution of trace elements in the sediments of Lake Paranoá – DF, Brazil. Journal of Geochemistry Brasiliensis, 20(2), 158-174, DOI: 10.21715/gb.v20i2.242.

Melo V., Vale Júnior J. and Uchôa S. (2010). Use and maintenance of soil under Savannah. In: J. Vale Junior and C. Schaefer, eds., Soils under savannahs of Roraima: genesis, classification and environmental relations. Boa Vista: Gráfica Ioris, 219.

Meneses M., Costa M. and Costa J. (2007). The Lakes of the Lavrado of BoaVista — Roraima: physical-chemical physiographyof the water, mineralogy and chemistry of the sediments. Brazilian Journal of Geosciences, 37(3), 478-489, DOI:10.25249/0375-7536.2007373478489.

Moiseenko T., Sharov A., Voinov A. and Shalabodov A. (2012). Long-term changes in the large lake ecosystems under pollution: the case of the north-east European lakes. Geography, Environment, Sustainability, 5(1), 67-83, DOI: 10.24057/2071-9388-2012-5-1-67-83.

Murdoch A. and Macknight A. (1994). Handbook of Techniques for Aquatic Sediments Sampling. 2nd ed. Boca Roton, Florida: Lewis.

Pinheiro M. and Jardim M. (2015). Floristic composition and biological forms of aquatic macrophytes in lakes of the western Amazon, Roraima, Brazil. Journal Biota Amazônia, 5(3), 23-27, DOI: 10.18561/2179-5746.

Santos W., Silva P. and Moreira J. (2020). Hydro-sedimentological dynamics in fluvial lentic environment, Rio Branco, Acre: Initial investigation of silting process in fluvial canal. Journal GEOgrafias, 28(2), 135-156.

Santos Neto A., Tavares Junior S. and Souza V. (2013). Lacustrine Landscapes and Urban Expansion in the Municipality of Bonfim-RR. In: A. Filho and L. Beserra Neta, eds., Bonfim: A Geographical Vision. Boa Vista: Editora UFRR, (in Portuguese with English summary), 260

Shepard F. (1954). Nomenclature based on sand-silt-clay ratios. Journal of Sediment Research, 24(23), 151-158, DOI: 10.1306/D4269774-2B26-11D7-8648000102C1865D.

Simões Filho F., et al. (1997). Sedimentary registers of lakes and marshlands in the fields of Roraima: Paleo-environmental implications along the holocene In: R. Barbosa, E. Ferreira and E. Castellon, eds., Man, Environment and Ecology in the State of Roraima. Manaus, INPA, (in Portuguese with English summary), 295-302.

Suguio K. (1973). Introduction to Sedimentology. São Paulo: Edgard Blucher, 342.

Thomas R. and Meybeck M. (1996). The use of particulate material. In: D. Chapman, ed., Water Quality Assessments: a guide to the use of biota, sediments and water in environmental Monitoring, 2nd ed., UNESCO/WHO/UNEP.

Vonk J.E., Dickens A.F., Giosan L., Hussain Z.A., Kim B., Zipper S.C., Holmes R.M., Montlucon D.B., Galy V. and Eglinton T.I. (2016). Arctic Deltaic Lake Sediments As Recorders of Fluvial Organic Matter Deposition. Frontiers in Earth Science, 4(77), 1-24, DOI: 10.3389/feart.2016.00077.

Xu Y., Wu Y., Han J. and Li P. (2017). The current status of heavy metal in lake sediments from China: Pollution and ecological risk assessment. Ecology and Evolution, 7(14), 5454-5466, DOI: 10.1002/ece3.3124.

Zdorovennova G., Palshin N., Zdorovennov R., Golosov S., Efremova T., Gavrilenko G. and Terzhevik A. (2016). The Oxygen Regime of a Shallow Lake. Geography, Environment, Sustainability, 9(2), 47-57, DOI: 10.15356/2071-9388_02v09_2016_04.

RESEARCH PAPER

USING SUPPORT VECTOR MACHINE TO IDENTIFY LAND COVER CHANGE DURING COVID-19 PANDEMIC IN KOMODO NATIONAL PARK, INDONESIA

Laode Muhammad Golok Jaya[1*], Rizal Adi Saputra[1], Sitti Hairani Idrus[2]
[1]Department of Informatics Engineering, Halu Oleo University, Jl. HEA Mokodompit Kampus Hijau UHO Bumi Tridharma Anduonohu, Kendari, Sulawesi Tenggara (93232), Indonesia.
[2]Department of Business Administration, Halu Oleo University, Jl. HEA Mokodompit Kampus Hijau UHO Bumi Tridharma Anduonohu, Kendari, Sulawesi Tenggara (93232), Indonesia.
***Corresponding author:** laodemgj@uho.ac.id
Received: March 27th, 2022 / Accepted: August 8th, 2022 / Published: October 01st, 2022
https://DOI-10.24057/2071-9388-2022-030

ABSTRACT. The Covid-19 pandemic affects many areas of life, including the tourism sector. Furthermore, it significantly reduced the number of people visiting tourist destinations, and the reduction has helped to improve the environment in the National Park. Therefore, this study aims to present a satellite image classification method using Support Vector Machine to identify changes in the vegetation area of Komodo National Park. The satellite image used was created with Google Earth Pro with a resolution of 1920 x 1280 pixels using data collected in 2019 and 2020 before and during the pandemic. This study focuses on six tourist destinations in Komodo National Park: Loh Liang, Loh Buaya, Padar Island, Kanawa Island, Pink Beach, and Loh Sebita. The image was pre-processed using radiometric calibration, atmospheric correction, and contrast enhancement. The results of the pre-processing showed that segmentation will be performed to distinguish the area between one class and another. Furthermore, the image will be classified into five classes using the Support Vector Machine, including Soil, Vegetation, Built-Up Area, Deep Water, and Shallow Water. The measurement of the area of vegetation from 2019 and 2020 using Otsu's thresholding showed environmental changes. Meanwhile, environmental improvements occurred in seven areas in the vegetation area category, with a 31.86% rise from 2019 to 2020. The increase in the area of green areas in the Komodo National Park all because tourist restriction and there is no climate fluctuations during the time of study.

KEYWORDS: Vegetation Area Change, Environmental Recovery, Machine Learning, Support Vector Machine, Komodo National Park

CITATION: Jaya L.M.G., Saputra R.A., Idrus S.H. (2022). Using Support Vector Machine To Identify Land Cover Change During Covid-19 Pandemic In Komodo National Park, Indonesia. Geography, Environment, Sustainability. 3(15), 70-79
https://DOI-10.24057/2071-9388-2022-030

Conflict of interests: The authors reported no potential conflict of interest.

INTRODUCTION

The coronavirus (Covid-19) first hit the world in December 2019 in Wuhan, China. It then continued to spread around the world, with more than 236 million confirmed cases and 4.8 million deaths in 223 countries (WHO 2021). With around 4.2 million confirmed cases by the end of September 2021, Indonesia is one of the countries with the most infections in the world (Worldometer 2021). According to WHO, the group of cases affected have mild to severe respiratory symptoms and will recover without additional treatment. However, with limited healthcare facilities, many cases end in death. The Ministry of Health reported 141.743 overall death cases by the end of September 2021 (Health Ministry of Indonesia 2021).

The Government has taken several measures in response to the Covid-19 pandemic, including travel restrictions. On 31 March, the Ministry of Law and Human Rights issued Regulation Number 11 of 2020 Concerning Temporary Prohibition for Foreigners to Enter Indonesia (Regulation 11/2020). Currently, Covid-19 Task Force has continued to temporarily ban the entry of all foreign visitors except for people with work permits, business visas, permanent residence, diplomatic visas, as well as those who traveling under special corridor arrangements (Medina 2021). For domestic travelers, different guidelines have been introduced to help to contain the Covid-19 virus. It started with the cancellation of all international and domestic commercial flights from April 24th, 2020, until May 31st, 2020. However, Indonesian can travel under some circumstances such as negatives PCR Test results and evidence of being vaccinated (minimum one dozes) (Kemenlu RI 2021).

Travel bans, strict travel rules, and Covid-19 itself have all impacted the domestic and global tourism sectors at the national level. Badan Pusat Statistics (BPS), the statistical center of Indonesia, reported that the number of international tourists fell 47.02% from April to December 2020 compared to the first quarter of 2020. The decline continued until 2021 since only 937,747 visited in July 2021, and the number dropped by 71.42% from the same period last year (BP, 2021a). This outbreak has affected all tourist destinations, including Komodo National Park (Veyadi Purba et al. 2021).

Komodo National Park is located between the islands of Sumbawa and Flores in the middle of the Indonesian archipelago. The Park was founded in 1980 with the primary objective of protecting the endangered Komodo dragon (Varanus komodoensis) and its environment. However, it has evolved through time to include the protection of its entire terrestrial and marine diversities (UNESCO 2020). In 1986, the Park was designated as a World Heritage Site and a Man and Biosphere Reserve by UNESCO, emphasizing its biological importance.

Komodo National Park is home to several other significant terrestrial species, including the orange-footed scrub fowl, a unique rat, and the Timor deer. The rising demand for forest cover and water resources as more tourists visit Komodo National Park poses a threat to terrestrial biodiversity (Ariefiandy et al. 2021). During the incidence of Covid-19 in 2020, only 51618 tourists visited the park. The number fell drastically compared to the previous year which reached 221708 people (BPS 2021b). In addition, to influence the decline in foreign exchange from the tourism sector, there is a positive impact from the decrease of tourist number, such as the improvement of the vegetation and ecosystem of the Komodo National Park.

Several studies related to area changes in national parks have also been carried out by several researchers, such as the Oni Gambari reserve, Ibadan, Nigeria (Khadijat et al. 2021); Lake Malombe, Southern Malawi (Makwinja et al. 2021); and Sikkim Himalayas, India (Mishra et al., 2020). According to the studies, a satellite image classification can determine the change of area on some period of time. Although in this study only using two (2) years data image, but some preprocessing method and a detailed object classification using Support Vector Machine could bring a good result to this study (Talukdar et al. 2020). By using SVM, it is expected to be able to separate vegetated and non-vegetated areas and be able to prove the hypothesis that there is an additional vegetation area in Komodo National Park during the COVID-19 pandemic.

MATERIAL AND METHODS

The primary focus is to offer a reliable satellite classification system using SVM method that uses image pre-processing, segmentation, classification phases, and land cover and use change analyses. This study will classified the area of Komodo National Park into vegetation or non vegetation area based on image satellite. The processed image can be used to acquire information on the total area of vegetation in Komodo National Park during pandemic Covid-19. The stages of this research include data acquisition using images from google earth followed by pre-processing using radiometric calibration and atmospheric correction which then improves contrast by means of histogram equalization. The pre-processed image will then be subjected to an object detection process to separate the vegetation and non-vegetation objects. From objects that have been detected, MultiSVM will then be used to classify objects into previously prepared labels. The final stage of this research is to calculate the area of vegetation and non-vegetation based on images in different years using LULC digital image processing with several stages to obtain the area of vegetation before and after the pandemic. Figure 1 shows framework from this study.

Study Area

Komodo National Park has three large islands: Komodo, Rinca, and Padar, as well as several smaller islands, totaling 1817 km^2 (marine and land), with proposed extensions that can bring the total surface area up to 2321 km^2

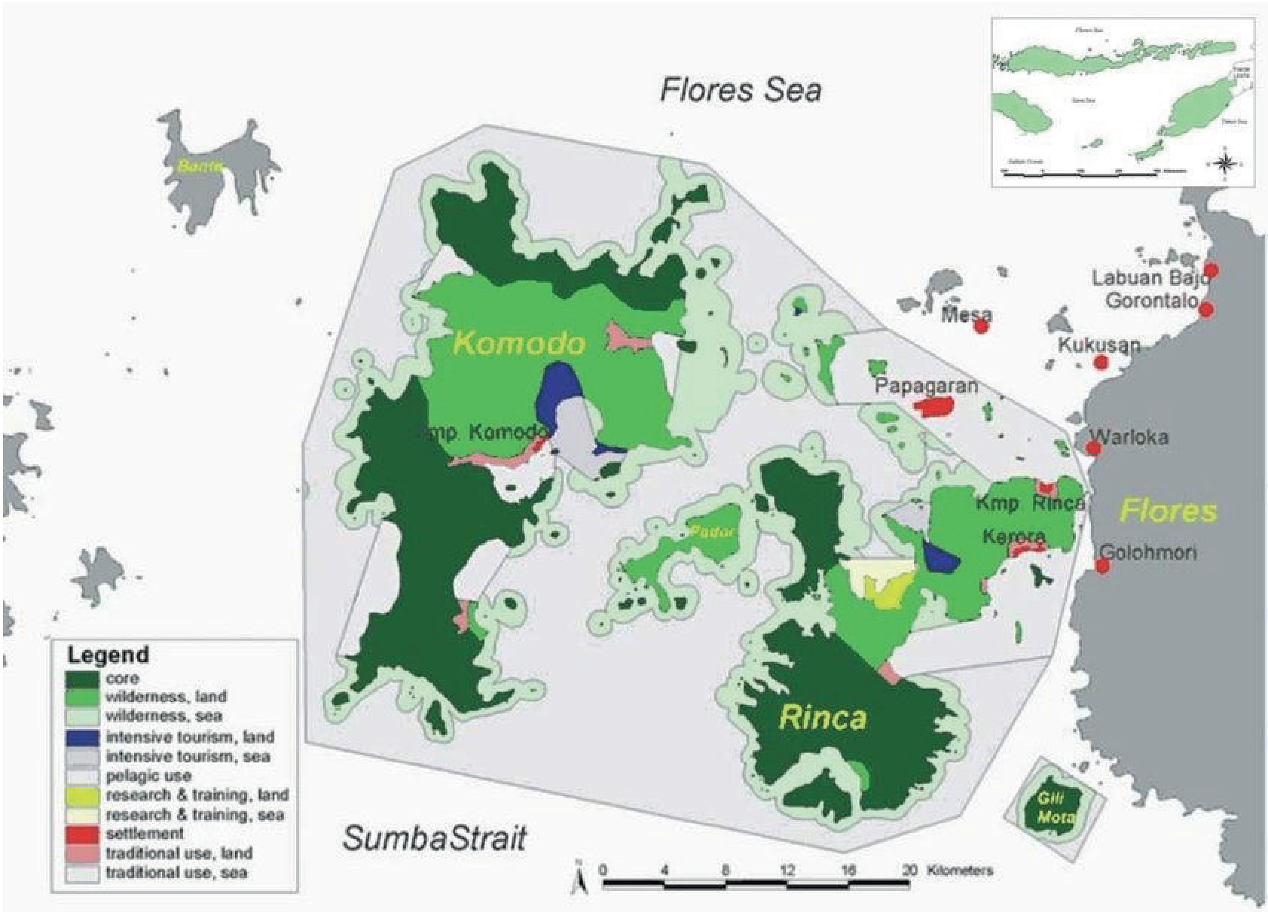

Fig. 1. Zoning Komodo National Park Area (www.komodonationalpark.org, n.d.)

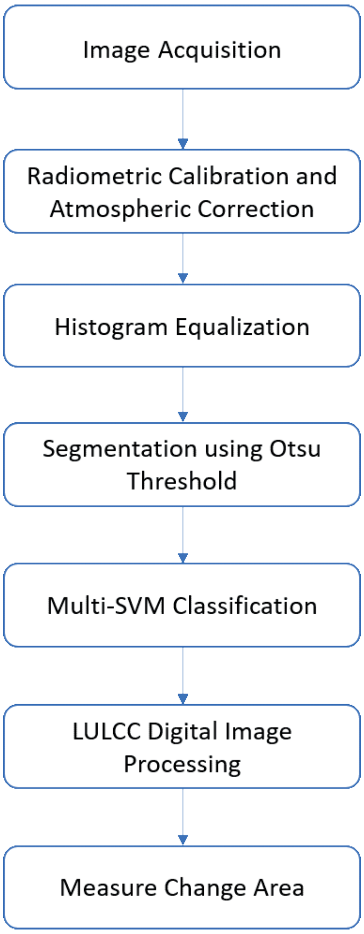

Fig. 2. Framework of research

(Komodo National Park 2017). There are presently almost 4,000 people living within the park spread out over four settlements (Komodo, Rinca, Kerora, and Papa Garang) and only Komodo and Papa Garang have a habitant. All villages existed before 1980 when the area was declared a national park. At the 2020 Census, Komodo Village had 1,845 inhabitants and Papagaran Village had 1,493 inhabitants. The total population currently living in the park is 3,338 people with 16,816 people live in the area immediately surrounding the park (Harum 2021). This study focuses on six tourist destinations in Komodo National Park: Loh Liang, Loh Buaya, Padar Island, Kanawa Island, Pink Beach, and Loh Sebita. In the focuses study area there are none villagers building, there is only office building for entrance and some bungalow.

Data Used

The data downloaded using Google Earth Pro with the original size is 1920 x 1080 pixels and a resolution of 96 dpi. Furthermore, there are 22 images from 11 tourist spot locations in Komodo National Park, and the tourist spots are used by following the map in Figure 1. The intensive tourism land region include Loh Buaya, Loh Liang, Loh Sebita, Pink Beach, Kanawa Island, and Padar Island. In addition, the satellite image used were acquired in 2019 and 2020 in the same season and taken in the morning at 08.00 (GMT+8) to compare the area of vegetation change during the Covid-19 pandemic. Table 1 showed the precise parameters and the acquired data.

Preprocessing

Image pre-processing is also known as a satellite image data pre-analysis, and it is used to enhance digital geospatial information into a presentation that is more meaningful to users. Furthermore, it offers quantifiable information about an item and can solve issues. In pre-processing, the image captured by the sensor will be normalized to process the image at the feature separation stage. The quality of the features produced in the separation process is highly dependent on the results of pre-processing. In this study, radiometric calibration and atmospheric correction were used for image preprocessing (Talukdar et al. 2020).

Radiometric Calibration

Radiometric calibration, also known as radiometric correction converts raw digital image data from satellites or aerial sensors to a regularly occurring scale based on verified reflectance measurements from ground surface objects. When working with satellite image data, the first step is to conduct radiometric calibration. The primary goal is to transform image data recorded as a Digital Number (DN) into radiance and/or reflectance, as well as brightness temperature for Thermal Infrared channels (Thome et al. 1997). Furthermore, Score Spectral radians are used for processing related to the surface temperature. The value of reflectance is the ratio of the reflected energy (and received by the sensor) with the object. The unit does not exist (dimensionless) since reflectance is widely used for processing indexes. The vegetation index, for example, produces the best results when processed using reflectance measurements. Meanwhile, atmospheric correction should be conducted which corrects the sun position, recording angle, and topography of the area to obtain a good reflectance value.

Table 1. Satellite Image of Tourism Area in Komodo National Park

No	Name	Picture 2019	Picture 2020	Source Data
1	Loh Liang		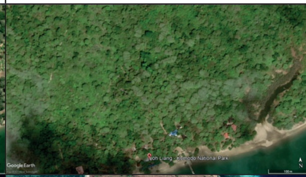	Google Earth Pro application was used to get the data. The images for 2019 were taken on December 19th, while the images for 2020 were taken on December 16th, 2020. Both photos were shot around 8 a.m.
2	Kanawa Island			
3	Loh Buaya			
4	Pink Beach			
5	Padar Island Entrance			
6	Padar Island Tracking Area			
7	Loh Sebita			

Convert Digital Number (DN) to Top of Atmosphere (TOA) Radiance

To obtain the spectral radian value, pixel rescaling should be conducted using the same value listed in the metadata (Jaelani 2015). The equation used is:

$$L_\lambda = M_L Q_{cal} + A_L \quad (1)$$

with
L_λ= TOA spectral radiance (*watss/(m²*srad*µm)*)
M_L= A multiplicative rescaling factor for each band from metadata
A_L= A band-specific additive rescaling factor from the metadata
Q_{cal}= Quantized and calibrated standard product pixel values (DN)

Convert Digital Number (DN) to Top of Atmosphere (TOA) Reflectance

For the thermal band, the correction level is only at conversion into spectral radian values since it is not a reflecting band but thermal infrared energy (Jaelani 2014). The correction on Landsat-8 does not use the value spectral radian (Lλ) but rescaling pixels value (Qcal). Reflectance correction was obtained by the equation:

$$\rho_\lambda = M_\rho Q_{cal} + A_\rho \quad (2)$$

with
ρλ'= TOA planetary reflectance, without any adjustment for the angle of the sun It should be noted that ρλ' does not include an adjustment for the sun angle
M_ρ= A multiplicative rescaling factor for each band from metadata
A_ρ= A band-specific additive rescaling factor from the metadata
Q_{cal}= Quantized and calibrated standard product pixel values (DN)

Atmospheric Correction

This adjustment was conducted by considering a variety of atmospheric characteristics, such as seasonal variables and environmental circumstances at the picture recording site (e.g., tropical, sub-tropical, etc.). The advantages are in the ability to correct atmospheric disturbances such as haze, smoke, and others (Yuniar 2018). The primary goal is to transform sensor data (at sensor reflectance or Top of

Atmosphere reflectance) into surface reflectance (Bottom of Atmosphere reflectance) using the basic schema correction atmosphere algorithm as follows:

$$\rho_{toa}(\lambda) = \rho_r(\lambda) + \left[\rho_a(\lambda) + \rho_{ra}(\lambda)\right] + t(\lambda)\rho_w(\lambda) \quad (3)$$

with

$\rho_{toa}(\lambda)$ = satellite sensor captured reflectance

$\rho_r(\lambda)$ = Rayleigh scattering reflectance

$\rho_a(\lambda)+\rho_{ra}(\lambda)$ = total reflectance due to aerosol scattering, as well as the interplay between Rayleigh and aerosol scattering

$t(\lambda)$ = diffuse transmittances of atmospheric column

$\rho_w(\lambda)$ = water leaving reflectance (surface reflectance, Bottom of Atmosphere reflectance)

Contras Enhancement Using Histogram Equalization

Histogram Equalization is a computer-assisted image processing approach for enhancing picture contrast (Rao 2020). This is accomplished by spreading out some of the most frequent intensity values, i.e., broadening the intensity range of the image. When such usable data is processed by near contrast values, this method improves the global contrast (X. Wu et al. 2017), and this permits areas with poor local contrast to gain more contrast. Furthermore, the method enhances the general contrast of numerous pictures, specifically when the image is represented by a narrow range of intensity values. By making use of the varying intensities evenly, it may be better dispersed on the histogram with this change, and this enables areas with poor local contrast to gain more contrast. Histogram equalization is conducted by efficiently distributing the highly dense intensity values required to reduce image contrast (Voronin 2019). The Bi-Histogram Equalization was used to spread the pixel of the satellite image and also to differentiate between various colors of objects.

Object Detection

Object detection in digital image processing is a process used to determine the existence of certain objects in a digital image (Naiemi et al. 2021). The detection process can be conducted by various methods which generally read the features of all objects in the input image. The features of the object in the input images will be compared to the reference or template's features. Meanwhile, the comparison results can be used to determine whether an object is detected as the intended template or not. Image segmentation was used in this study because it provides pixel-by-pixel detail of an object, making it distinct from object classification and detection. The image is split into homogenous object primitives during image segmentation, and it is a preparatory step in object-oriented image classification. Multi-resolution segmentation was used to segment the study area, which decreases the average heterogeneity of image objects at a given resolution. The scale parameter is an arbitrary integer that determines the amount of heterogeneity tolerated in the image objects. A higher scale value results in bigger things, and vice versa. In addition, it is good when the image items are smaller than the real things since larger objects are more prone to errors. The three factors that can characterize an object's heterogeneity are color, smoothness, and compactness (C. F. Wu et al. 2016).

The compactness of an item is defined by its perimeter and the boundary of the object's enclosing box. Meanwhile, the smoothness is determined by its boundary and the number of pixels within it, and these criteria describe the object's shape. The shape and color together define the object's homogeneity, and manual analysis is widely regarded as the most accurate method. The diversity of values for each variable and the combinations were tested to analyze the affected segmentation performance (Wang et al. 2021). The variables of the multi-resolution segmentation process were determined through trial and error to ensure the final segmentation matched the graphical illustration. Initially, a correlation analysis was performed to decrease the redundancy of the bands included in the segmentation. Due to the general high correlations among bands, this study performs multiple segmentation by using the Otsu Thresholding method to gain each feature required. It is used to recognize "large" items such as land, water, forests, building, etc. The Otsu technique divides the histogram of a gray level image into two regions without the need for a threshold value to be entered by the user (Otsu 1979). It employs discriminant analysis, which entails identifying a variable that can differentiate between two or more groups (Saputra 2021). The thresholds value that should find examples expressed by k which value ranges from 1-255 since the value of k chosen is the maximum of the equation by using formula:

$$\sigma_B^2(k^*) = \max_{1 \le k \le L} \sigma_B^2(k) \quad (4)$$

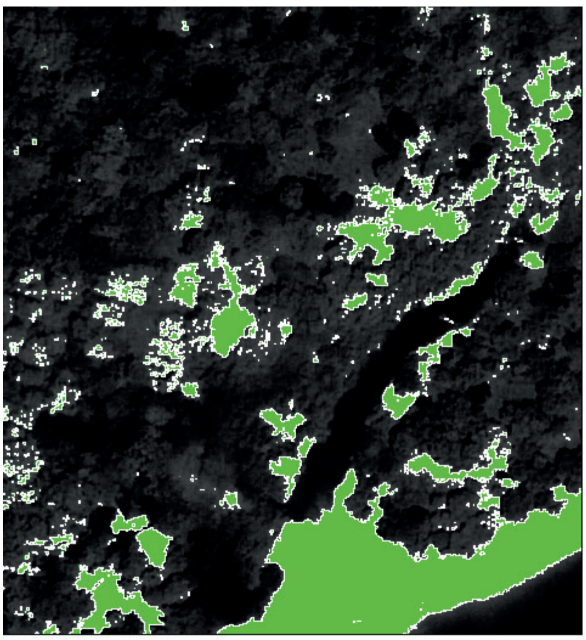
(a)


(b)

Fig. 3. (a) Segmentation using Otsu Threshold (b) Masking area with Original Image

For a better object classification, original image was divided into 60 smaller of the as shown in figure 3. Figure 3 showed that soil and building area was the first segmentation to be distinguished from forest and waters. The second segmentation will be used to differentiate between soil and structure, as well as forest and water. A total of 5 classes were extracted from this study, and they are soil, forests, buildings, deep water, and shallow water.

Classification Using Support Vector Machine (SVM)

SVM is a supervised classification method used to categorize items by establishing a boundary between them, and binary SVM is not practical for tasks with many categories (López-Serrano et al. 2016). Multiple continuous and categorical variables, as well as linear and non-linear samples in various class memberships, can also be supported by SVM (Shih et al. 2019). Unlike the neural network approach, which seeks a separating hyperplane across classes, this classification obtains the optimal hyperplane in the input space. It was created as a linear classifier but was later improved to cope with non-linear problems by incorporating the kernel notion into a high-dimensional workspace. Furthermore, it identifies the optimum hyperplane separator between two classes by maximizing the margin between each class's nearest points (Anantrasirichai et al. 2018).

Multiclass SVM includes five different classes of soil, vegetation, built-up area, shallow water, and deep water. Support vectors are the training or bordering samples that define the margin or hyper-plane of SVM. This study uses n(n-1) classifiers to distinguish between classes, and the final decisions are considered. Finally, the areas are categorized according to the maximum-voting policy, and all the distinct classes are processed at the same time by calculating the equation below. The slack variable is sv, the bias is b, and both appear to be normal to the hyperplane., $i = 1,2, \ldots r$ is the number of classes, and y is the number of training samples. The following equation is used to make a final decision:

$$decn = \max \tag{5}$$

$$y(wyp\beta(xi) + by) \tag{6}$$

this study's kernel function was a linear function with a formula:

$$k(x, y) = x, y \tag{7}$$

Where x and y are two data pairs of all training sections. In this method, each pair of classes is subjected to all the classifiers. Consider an object that should be classified into one of three categories (say x,y,z), and this is achieved by applying all the classifiers to an image. When a classifier defines an item as belonging to class x, the value is increased by one, and the maximum votes are used to make the final classification decision (Farda 2017). This method gives accurate results in a fair amount of time (Pelletier et al. 2017).

The second binary image was created by combining the land (rock, vegetation) and water characteristics from the coastal-surface categorization map. Meanwhile, the second coastline was recovered from the improved second binary picture by choosing the boundary between the detected land and water features. Then morphological filtering was used to refine the border between the land and water features in the second binary image. The checkpoints were used to assess the accuracy of both produced shorelines to choose the best technique for the shoreline mapping assignment. Figure 4 showed the result of sample classification using SVM on Loh Liang and Kanawa Island.

Land Use and Land Cover Change (LULCC) Analysis

Land-use change refers to alterations in how a single piece of land is exploited or maintained by people. Meanwhile, land-cover change is an alteration in the continuous characteristics of the land, such as the type of plant and soil quality (Majumdar 2020). This involves the natural landscape being altered because of population expansion (Verma et al. 2020). It should be noted that this alteration can cause a slew of local and global effects, including biodiversity loss and its implications for human health, as well as ecosystem damage (Patel et al. 2019). In recent studies on sustainable development, planning, and management, monitoring and mapping LULCC has become increasingly essential (Mishra et al. 2020). In this study, LULCC analysis used the following digital image processing.

Color Threshold

The Color Threshold is used to eliminate picture portions within a certain color range. This method is useful for detecting items with constant color values (Al Mamun et al. 2021), and the interface showed the histograms in red, green, and blue. The histogram contains the value and number of each pixel (0-255 and 0-image size) with that color value. It is used to remove pixels with the values from the picture, leaving only the desired object visible. All the green colors from vegetation were set to white pixels, which were disregarded by the histogram in the image.

Table 2. Description of the land use/land cover LULLC classes identified

Class Name	Class Description	Clas Description Example
Soil Area	Area without vegetation	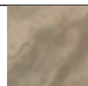
Vegetation Area	Area covered by trees, forest, sparse. etc.	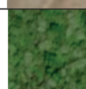
Built-Up Areas	This are include all of structure made by human example building, dock, ship,etc	
Deep Water	Area covered by water	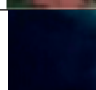
Shallow Water	Area covered by water but with the turquoise blue color (beach)	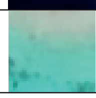

This enables images to have a useful histogram even when dark or bright. Furthermore, these values can be re-added, but they have no impact on the threshold operation.

Convert Image RGB to Grayscale 8-bit

When converting a picture from RGB to 8-bit grayscale, down-sampling occurs when 24-bit information is squeezed into the range. The simplest method is to use a straight translation that averages the red, green, and blue values for each pixel. To estimate the human luminance viewpoint, a conversion with color-specific weights is appropriate to estimate the human luminance viewpoint (Putra 2010). Therefore, this study aims to RGB's image to 8-bit grayscale using formula:

$$Grayscale = 0.299R + 0.587G + 0.114B \tag{8}$$

When the RGB image is transformed into grayscale, the value of each pixel is reduced from three to one. This defines the regional boundaries between one area class and another. In this study, the vegetation area will remain white, while others will be gray to black.

Invert to LUT Threshold

LUT is an acronym for Look-Up Table, and it converts one color range in an image to another. For 8-bit pictures, the value (v) of each table item is substituted with 255-v (Lee et al. 2018), and the pixels with a value of zero are white.

Meanwhile, the pixels with a value of 255 are black when using inverted LUTs. The vegetations used were white and were inverted into black and other areas were inverted to white.

Measure Area

In the next step, the area of vegetation is measured by counting all pixels that represent the area. Black pixels were measured from an inverted threshold image of a region in Komodo National Park for this investigation. The area that has more vegetation was darker than those with less vegetation. Figure 5 showed all the digital image processing used to analyze the land cover change of Komodo National Park.

Classification results using SVM are then calculated using a confusion matrix for accuracy assessment of LULCC classifcation of the years 2019 and 2020. The result of confusion matrix shown in Table 3 and Table 4. With Kappa coefciency of 90% and 88% in 2019 and 2020, the confusion matrix produced overall very good accuracies for the five classifcation points and the defned LULCC classes. Both class-specifc user accuracies and producer's accuracies were at least 81%, suggesting that a considerable percentage of pixels were correctly classifed.

RESULTS AND DISCUSSION

The areas measure in seven tourist sites of Komodo National Park discovered a significant change of land cover specifically the vegetation that increased between

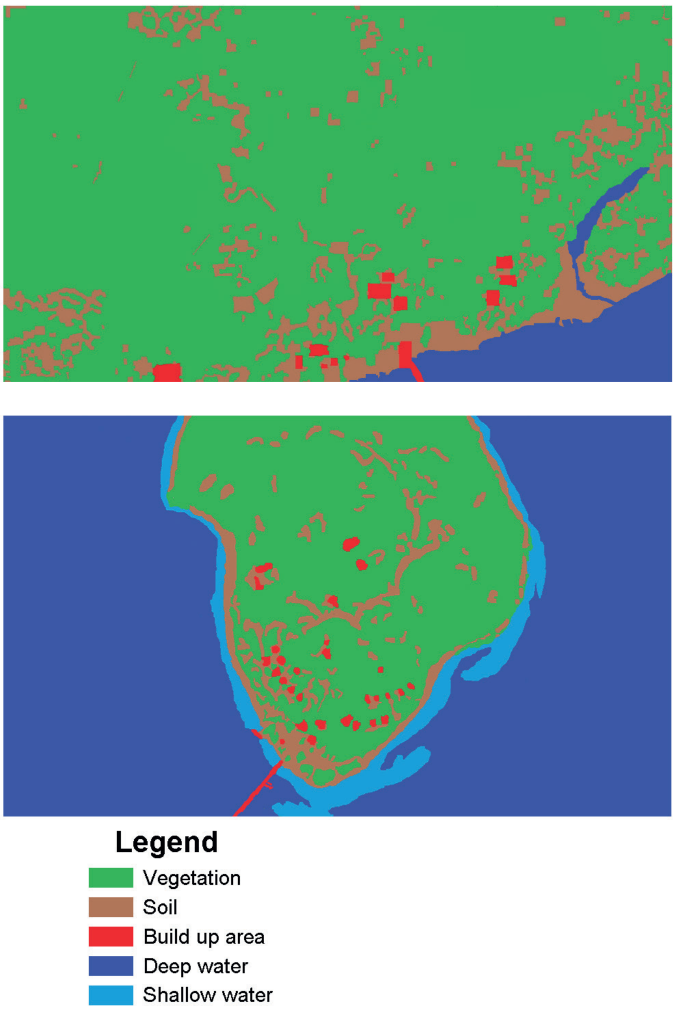

Fig. 4. Classification using SVM on Loh Liang and Kanawa Island

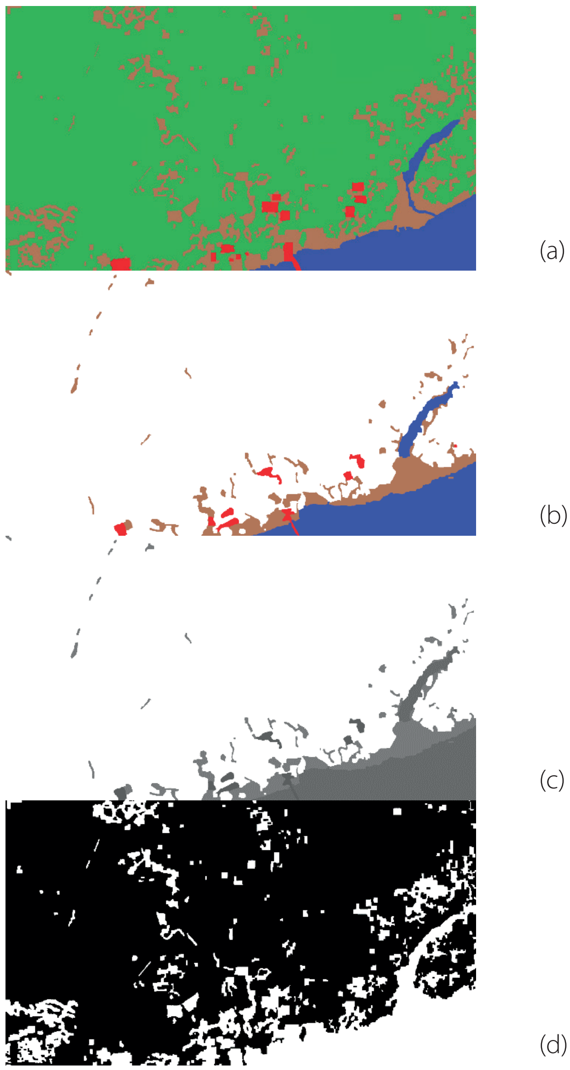

Fig. 5. (a) Original RGB Image, (b) Colour Threshold, (c) Grayscale Image 8-bit, and (d) Inverted LUT Image

Table 3. Confusion matrix of classification accuracies for the year 2019

LULC	Vegetation	Soil	Built Up	Deep Water	Shallow Water	User Accuracy
Vegetation	97.10	5.25	2.89	1.02	0	92.04
Soil	2.72	92.24	3.57	0.81	8.19	89.24
Built Up area	0.18	3.48	93.74	0	0	91.43
Deep Water	0	0.03	0	94.10	9.31	93.37
Shallow Water	0	0	0	4.07	82.50	80.42
	100	100	100	100	100	
Producer Acc	97.81	92.22	94.76	93.23	81.34	
Overall Accuracy = 92.18						
Kappa Coefficent = 0.90						

Table 4. Confusion matrix of classification accuracies for the year 2020

LULC	Vegetation	Soil	Built Up	Deep Water	Shallow Water	User Accuracy
Vegetation	98.81	3.45	3.72	1.02	0	95.34
Soil	1.19	95.10	3.43	0	6.42	93.27
Built Up area	0	1.45	90.23	0	0	89.85
Deep Water	0	0.0	2.62	90.75	5.83	91.53
Shallow Water	0	0	0	8.23	87.75	90.18
	100	100	100	100	100	
Producer Acc	98.21	96.23	90.25	93.12	88.92	
Overall Accuracy = 90.24						
Kappa Coefficent = 0.88						

2019 and 2020 as shown in Table 5. There was a 10.18% increase in vegetation area at Loh Liang, which is the main entrance of Komodo National Park. Furthermore, there was a 41.17% increase in vegetation area at Kanawa Island, which has many resorts. There was an 18.42% increase in vegetation area at Loh Buaya, which is the future site for the construction of Komodo Geopark. Meanwhile, Pink Beach as the most renowned beach tourist item in the park has a 21.32% increase.

The entry region to Padar Island has a 60.94% increase in vegetation area. The largest rise, 69.52% occurred in the Padar Island Tracking Area, while the smallest increase of 1.43%, occurred in Loh Sebita which is the Mangrove area. From 2019 to 2020, the vegetation in Komodo National Park increased by 31.86% on average from 7 tourism spots. The results showed that the decrease in the number of tourists during Covid-19 aided in the improvement of vegetation. The island area that was not covered with vegetation in 2019 due to tourism activities such as hiking, camping, and tracking was mostly covered with

Table 5. Total Vegetation Area

Area	Vegetation Area (Pixel)		Pixel Addition	Percentage (%)
	2019	2020		
Loh Liang	1632495	1817455	184960	10.18%
Kanawa Island	503765	856375	352610	41.17%
Loh Buaya	735921	902110	166189	18.42%
Pink Beach	246732	313590	66858	21.32%
Padar Island Entrance	135035	345683	210648	60.94%
Padar Island Tracking Area	176349	578642	402293	69.52%
Loh Sebita	1019742	1034584	14842	1.43%
Average				31.86%

vegetation in 2020. This result showed a positive impact on environmental change during pandemic Covid-19. Although there could be other factors at play that may have a link as well to increase vegetation area and it is need more work to do. But according to a recent study, Covid-19 lockdowns resulted a better environment such as significant reductions in air and water pollutants (Zambrano-Monserrate et al. 2020; Chakraborty et al. 2021), noise pollution (Mandal & Pal 2020), and land cover change (Khadijat et al. 2021). Furthermore, the world's changing environmental quality has acquired a favorable shift toward sustainable environmental-friendly circumstances as a result of the imposition of a lockdown. It is also reported India's megacities positive move toward sustainable environment-friendly during the pandemic such as changes of the vegetation index. According to (Firozjaei et al. 2021), Covid-19 lockdown had an impact on the proportion and health of the vegetation. Furthermore, it positively affected plant health because of the considerable reduction in air and water pollutants.

The results showed that the environmental condition of Komodo National Park, particularly the vegetation, has improved from previous years. The study also showed the increase in the area of green areas in the Komodo National Park According to the data from Badan Pusat Statistik Manggarai Barat during 2019 – 2021 number of precipitation, number of rainy days, and duration of sunshine in Komodo National Park there just slightly different and there is no climatic fluctuations affect. Regardless of the deadly pandemic scenario, the promoting sign gives Komodo some reason to chance for a better and more recovered environmental state.

CONCLUSION

The study aims to identify environmental changes in Komodo National Park by using a support vector machine to classify area categories. The results showed that there is a change in the vegetation area and a drop in the number of tourists due to Covid-19. The most changes in vegetation occurred in the tracking area of Padar Island. It is one of Komodo National Park's most famous tourist attractions, and it accounts for up to 69.52 %. Generally, there was a 31.86% growth in vegetation area from 7 location points that became the subject of study by comparing satellite imagery in 2019 and 2020. In the future, this research can be developed when the pandemic has been declared over by WHO by adding data in the year after 2020 to be able to clearly see the changes in LULCC. This research can also be developed by comparing other machine learning classification methods

REFERENCES

Al Mamun A., Hossain M.S., Em P.P., Tahabilder A., Sultana R., & Islam M.A. (2021). Small intestine bleeding detection using color threshold and morphological operation in WCE images. International Journal of Electrical and Computer Engineering, 11(4), 3040-3048, DOI: 10.11591/ijece.v11i4.pp3040-3048.

Anantrasirichai N., Biggs J., Albino F., Hill P., & Bull D. (2018). Application of Machine Learning to Classification of Volcanic Deformation in Routinely Generated InSAR Data. Journal of Geophysical Research: Solid Earth, 123(8), 6592-6606, DOI: 10.1029/2018JB015911.

Ariefiandy A., Purwandana D., Azmi M., Nasu S.A., Mardani J., Ciofi C., & Jessop, T. S. (2021). Human activities associated with reduced Komodo dragon habitat use and range loss on Flores. Biodiversity and Conservation, 30(2), 461-479, DOI: 10.1007/s10531-020-02100-8

BPS. (2021a). Kunjungan Wisatawan Mancanegara per bulan Menurut Kebangsaan (Kunjungan), 2021. https://www.bps.go.id/indicator/16/1470/1/kunjungan-wisatawan-mancanegara-per-bulan-menurut-kebangsaan.html

BPS. (2021b). Pengunjung Taman Nasional Komodo Turun 76 persen pada 2020. https://databoks.katadata.co.id/datapublish/2021/08/03/pengunjung-taman-nasional-komodo-turun-76-persen-pada-2020

Chakraborty T.C., Sarangi C., & Lee X. (2021). Reduction in human activity can enhance the urban heat island: Insights from the COVID-19 lockdown. Environmental Research Letters, 16(5), 1-12, DOI: 10.1088/1748-9326/abef8e

Farda N. M. (2017). Multi-temporal Land Use Mapping of Coastal Wetlands Area using Machine Learning in Google Earth Engine. IOP Conference Series: Earth and Environmental Science, 98(1), 1-12, DOI: 10.1088/1755-1315/98/1/012042.

Firozjaei M.K., Fathololomi S., Kiavarz M., Jokar J., Homaee M., & Alavipinah S.K. (2021). Modeling the impact of the COVID-19 lockdowns on urban S Surface Ecological status: A case study of Milan and Wuhan cities. Journal of Environmental Management, 286(January), 1-10.

Harum P.H. (2021). Kecamatan Komodo Dalam Angka. https://manggaraibaratkab.bps.go.id/publication/2021/09/24/6293f9e0293853e7b252d95c/kecamatan-komodo-dalam-angka-2021.html

Health Ministry of Indonesia (2021). SITUASI COVID-19 di Indonesia (Kumulatif). https://www.kemkes.go.id/index.php?lg=ln02

Jaelani L.M. (2015). Development of a New Atmospheric Correction Algorithm for Turbid Inland Waters. Journal of The Remote Sensing Society of Japan, 35(3), 152-152, DOI: 10.11440/rssj.35.152.

Kemenlu RI. (2021). Update: Indonesia Travel Restrictions. https://kemlu.go.id/losangeles/en/news/11727/indonesia-travel-restrictions

Khadijat A., Anthony T., Ganiyu O., & Bolarinwa S. (2021). Forest cover change in Onigambari reserve, Ibadan, Nigeria: Application of vegetation index and Markov chain techniques. The Egyptian Journal of Remote Sensing and Space Science, xxxx, 1-8, DOI: 10.1016/j.ejrs.2021.08.004.

Komodo National Park (2017). Komodo National Park. http://www.komodonationalpark.org/

Lee, S., Lee, K., & Kim, B. (2018). Binary Image Based Fast DoG Filter Using Zero-Dimensional Convolution and State Machine LUTs. 5(2), 131-138.

López-Serrano P.M., López-Sánchez C.A., Álvarez-González J.G., & García-Gutiérrez J. (2016). A Comparison of Machine Learning Techniques Applied to Landsat-5 TM Spectral Data for Biomass Estimation. Canadian Journal of Remote Sensing, 42(6), 690-705, DOI: 10.1080/07038992.2016.1217485.

Majumdar S. (2020). Assessment and detection of land cover changes in the southern fringe of Kolkata using remotely sensed data. Geography, Environment, Sustainability, 13(4), 121-132, DOI: 10.24057/2071-9388-2020-65.

Makwinja R., Kaunda E., Mengistou S., & Alamirew T. (2021). Impact of land use/land cover dynamics on ecosystem service value—a case from Lake Malombe, Southern Malawi. Environmental Monitoring and Assessment, 193(8), 1-23, DOI: 10.1007/s10661-021-09241-5.

Mandal I., & Pal S. (2020). COVID-19 pandemic persuaded lockdown effects on environment over stone quarrying and crushing areas. Science of The Total Environment, 732, 1-10, DOI: 10.1016/j.scitotenv.2020.139281.

Medina A.F. (2021). What are Indonesia's Latest Guidelines on International Travel? Asean Briefing. https://www.aseanbriefing.com/news/what-are-indonesias-latest-guidelines-on-international-travel/

Mishra P.K., Rai A., & Rai S.C. (2020). Land use and land cover change detection using geospatial techniques in the Sikkim Himalaya, India. Egyptian Journal of Remote Sensing and Space Science, 23(2), 133-143, DOI: 10.1016/j.ejrs.2019.02.001.

Naiemi F., Ghods V., & Khalesi H. (2021). A novel pipeline framework for multi oriented scene text image detection and recognition. Expert Systems with Applications, 170(November 2020), 1-16, DOI: 10.1016/j.eswa.2020.114549.

Otsu N. (1979). A Threshold Selection Method from Gray-Level Histograms. IEEE Transaction on Systems, Man and Cybernetics, 20(1), 62-66.

Patel S.K., Verma P., & Shankar Singh G. (2019). Agricultural growth and land use land cover change in peri-urban India. Environmental Monitoring and Assessment, 191(9), 1-17, DOI: 10.1007/s10661-019-7736-1.

Pelletier C., Valero S., Inglada J., Champion N., Sicre C.M., & Dedieu G. (2017). Effect of training class label noise on classification performances for land cover mapping with satellite image time series. Remote Sensing, 9(2), 1-24, DOI: 10.3390/rs9020173.

Putra D. (2010). Pengolahan Citra Digital (Westriningsih (ed.)). Penerbit Andi.

Rao B.S. (2020). Dynamic Histogram Equalization for contrast enhancement for digital images. Applied Soft Computing Journal, 89, 106-114, DOI: 10.1016/j.asoc.2020.106114.

Saputra R.A. (2021). Comparison of wavelet transform for image recognition system using Learning Vector Quantization. SemanTIK, 7(1), 1-8, DOI: 10.5281/zenodo.5034914.

Shih H., Stow D.A., & Tsai Y.H. (2019). Mapping, Guidance on and comparison of machine learning classifiers for Landsat-based land cover and land use. International Journal of Remote Sensing, 40(4), 1-15, DOI: 10.1080/01431161.2018.1524179.

Talukdar S., Singha P., Mahato S., Shahfahad Pal S., Liou Y. A., & Rahman A. (2020). Land-use land-cover classification by machine learning classifiers for satellite observations-A review. Remote Sensing, 12(7), 1-24, DOI: 10.3390/rs12071135.

Thome K., Markham B., Barker J., Slater P., & Biggar S. (1997). Radiometric calibration of Landsat. Photogrammetric Engineering and Remote Sensing, 63(7), 853-858.

UNESCO. (2020). Komodo National Park. https://whc.unesco.org/en/list/609/

Verma P., Singh R., Singh P., & Raghubanshi A.S. (2020). Urban ecology – current state of research and concepts. Urban Ecology, 3-16, DOI: 10.1016/b978-0-12-820730-7.00001-x.

Veyadi Purba J.H., Fathiah R., & Steven (2021). The Impact of COVID-19 on the Tourism Sector in Indonesia. Riset : Jurnal Aplikasi Ekonomi, 3(1), 389-401.

Voronin V. (2019). Modified Local and Global Contrast Enhancement Algorithm for Color Satellite Image. EPJ Web of Conferences, 224, 1-5, DOI: 10.1051/epjconf/201922404010.

Wang L., Weng L., Xia M., Liu J., & Lin H. (2021). Multi-resolution supervision network with an adaptive weighted loss for desert segmentation. Remote Sensing, 13(11), 1-18, DOI: 10.3390/rs13112054.

WHO (2021). Coronavirus disease (COVID-19) pandemic. https://www.who.int/emergencies/diseases/novel-coronavirus-2019

Worldometers (2021). COVID-19 CORONAVIRUS PANDEMIC. https://www.worldometers.info/coronavirus/

Wu C.F., Deng J.S., Wang K., Ma L.G., & Tahmassebi A.R.S. (2016). Object-based classification approach for greenhouse mapping using Landsat-8 imagery. International Journal of Agricultural and Biological Engineering, 9(1), 79-88, DOI: 10.3965/j.ijabe.20160901.1414.

Wu X., Liu X., Hiramatsu K., & Kashino K. (2017). CONTRAST-ACCUMULATED HISTOGRAM EQUALIZATION FOR IMAGE ENHANCEMENT. typically 256, 3190-3194.

www.komodonationalpark.org. (n.d.). Zoning Komodo National Park. www.komodonationalpark.org

Yuniar E. (2018). Validasi Produk Reflektan Permukaan Landsat-8 Menggunakan Data In-Situ (Studi Kasus : Danau Kasumigaura, Jepang).

Zambrano-Monserrate M.A., Ruano M.A., & Sanchez-Alcalde L. (2020). Indirect effects of COVID-19 on the environment. Science of The Total Environment, 728, 1-4, DOI: 10.1016/j.scitotenv.2020.138813.

RESEARCH PAPER

IDENTIFYING CLIMATE CHANGE IMPACTS ON HYDROLOGICAL BEHAVIOR ON LARGE-SCALE WITH MACHINE LEARNING ALGORITHMS

Aleksander M. Ivanov[1], Artem V. Gorbarenko[1], Maria B. Kireeva[1*], Elena S. Povalishnikova[1]
[1]Lomonosov Moscow State University, Leninskie Gory – ГСП-1, Moscow, 119991, Russia
*Corresponding author: kireeva_mb@mail.ru
Received: May 3rd, 2022 / Accepted: August 8th, 2022 / Published: October 01st, 2022
https://DOI-10.24057/2071-9388-2022-087

ABSTRACT. The article presents the results of study of the application of machine learning methods to the problem of classification and identification of different river water regimes in a large region – the European territory of Russia. An accumulation of hydrological observation data for the 60 – 80 years makes it possible to create an information basis for such studies. The article uses information on the average monthly runoff at 351 hydrological gauges during the period from 1945 to 2018. The most widely used data clustering approaches were used as analysis methods – K-means, EM-method, agglomerative hierarchical clustering, DBSCAN algorithms and the application of gradient boosting methods (CATBUST). Clustering and classification algorithms were given eight parameters as a basis for prediction. It was found that the most distinct and stable clusters are formed with three parameters, and the highest silhouette coefficient (SS = 0,3-0,5) is obtained using the numbers for months of the maximum and minimum runoff and the ratio of the maximum to the minimum water flow. The best result gives DBSCAN (SS = 0,6 – 0,7). Supervised classification models also show high correspondence with the reference classification, with an accuracy of 87%. Both clustering methods and classification methods showed a shift of clusters representing southern water regimes. In the central region these regimes expanded by a 1000 km to the north. Furthermore, results demonstrate that currently available data already makes it possible to apply machine learning methods to the analysis of hydrological data. Clusters corresponding to different types of water regime can be obtained by utilizing contemporary clustering algorithms. The study shows that over the past 40 years, the southern types of water regimes have noticeably shifted to the north.

KEYWORDS: Hydrological behavior, machine learning, climate change, East European Plain

CITATION: Ivanov A. M., Gorbarenko A. V., Kireeva M. B., Povalishnikova E. S. (2022). Identifying Climate Change Impacts On Hydrological Behavior On Large-Scale With Machine Learning Algorithms. Geography, Environment, Sustainability. 3(15), 80-87
https://DOI-10.24057/2071-9388-2022-087

ACKNOWLEDGEMENTS: This study was supported by the Russian Science Foundation, project no. 19-77-10032 in terms of calculations and analyzes. This research has been supported by the Interdisciplinary Scientific and Educational School of M.V.Lomonosov Moscow State University» Future Planet and Global Environmental Change» in methodology and climate change context.

Conflict of interests: The authors reported no potential conflict of interest.

INTRODUCTION

The hydrological regime of a river represents a specific pattern of changes in the state of the water body, unique for each territory (Frolova et al. 2021, 2022; Gelfan et al. 2021). The main characteristics of the hydrological regime of rivers are the character of inflow components, morphodynamic and climatic conditions (Blöschl et al. 2017; 2019; Hall and Blöschl 2018; Frolova et al. 2021; Frolova et al. 2020; Kireeva et al. 2019). The local unevenness of these values has led to the development of various methods for zoning rivers according to the types of water regime (Water regime… 2001; Frolova et al. 2021; Ayzel 2021). The study of geographic dependencies in the formation of the water regime, the analysis of the impact of economic activity – all of this is necessary to improve the existing methods of hydrological calculations. Climate change is also an important factor that affects rivers and leads to transformations and shifts in the water regime types.

One of the most important tasks of modern society is to develop resistance mechanisms and adapt to these changes (Frolova et al. 2021, 2022; Djamalov et al. 2014, 2015). In many regions, climate change has a negative impact on the quality and quantity of water resources, water temperature and the state of related ecosystems, leading to an increase in the scale and frequency of extreme natural events such as floods and droughts (Georgievsky and Shalygin 2012; Long-term fluctuations… 2021). All this, in turn, negatively affects many sectors of the economy, including agriculture, energy, fisheries, tourism and healthcare.

In addition, it is necessary to study the transformation of the water regime due to decreasing performance by currently existing methods and classifications. Most of the systematic studies devoted to the classification of the water regime of the ETR rivers were published decades ago and as of now have undergone significant changes that require a detailed analysis.

The goal of this work is to create a new model for automatic classification of ETR rivers by water regime type and assess the impact of climate change on changes in the water regime and its classes.

The abundance of up-to-date hydrometeorological information, automation of calculations, the development of different technologies and machine learning methods have made it possible to move away from general geographical patterns of classification to more modern quantitative methods. Modern approaches to the analysis of the water regime reduce the possibility of a subjective assessment of the analysis processes and allow to infor accurate numerical indicators of zoning and additional informative visualization.

Over the past 35 years, a lot of work has been done in the context of application of numerical methods to the task of water regime clustering. The pioneering work on the global data scale in this area was a 1988 paper (Haines et al. 1988). The authors set themselves the task of identifying different regions of the water regime and climatic zones algorithmically and exclusively on the basis of data. This work became possible precisely during this period due to accumulation of data on a significant scale and existence of reliable algorithms to process it. In their work, the authors used hierarchical clustering methods, and the Ochiai coefficient was taken as a distance measure. As a result of the work, the authors obtained the first map of water regimes in Western practice based only on the characteristics of the river runoff and made algorithmically. In the 2000s, a lot of new regional works appeared (Harris et al, 2000; Tavassoliet et al. 2014; Olden and Poff 2003; Kingston 2011; Brunner et al. 2018) where the authors have used algorithmic tools for assessing and classifying the water regime of rivers.

For example in (Harris et al. 2000) authors analyze the water regimes of rivers in the UK using multivariate analysis methods. Average monthly water discharges and temperature regime were separately classified in accordance with the form of their intra-annual distribution. As a result, the authors obtained 3 classes of rivers according to the shape of the hydrograph (peaks in November, December-January, March); these classes were also divided into 2 subclasses by years with different water levels: dry and high-water. In (Kidanewold et al. 2015) Ethiopian scientists have classified national rivers using daily average data and a multivariate (hierarchical) classification method. In general terms, this method is similar to that used in (Haines et al. 1988). The variables used were: average daily runoff modulus (flow water divided by the catchment area), the ratio of the average daily discharge to the average basis flow, dispersion of average daily water discharge, frequency and magnitude of abrupt changes in water discharge, average day of maximum annual discharge, and average number of days when the river dries up. As a result, 208 hydrological gauges were grouped into 3 clusters: «ephemeral» rivers that flow only after precipitation, «seasonal» rivers that flow only at certain times of the year, and «permanent» ones.

In «Classification of natural flow regimes in Iran to support environmental flow management» (Tavassoli et al. 2014), Iranian scientists have already attempted to clusterize water regimes using data from 539 stations over a period of 47 years. The data used were inferred from average daily discharges by converting it into 66 metrics used in the work (Olden and Poff 2003). Metrics were divided into the following groups: monthly water discharge and its statistical characteristics, magnitude and duration of annual maxima and minima of water discharge, dates of extreme discharges (start and end of maximum and minimum), frequency and duration of periods with the difference in average discharge by no less than a standard deviation, rate and frequency of changes in water discharge. As a clustering method, the authors chose the Bayesian mixture of distributions (Webb et al. 2007). This method works by choosing a most likely classification option out of several selected based on existing data. Each of the metrics above was modeled by the authors with a continuous normal distribution. As a result, 12 classes of rivers were obtained, while more than 90% of all stations were unambiguously assigned to any of the classes.

A radically different approach was tried by a team of authors in the article «Identification of Flood Reactivity Regions via the Functional Clustering of Hydrographs» (Brunner et al. 2018). In this work, the classification of hydrographs is carried out by the methods of functional analysis. Unlike other works described in this section, the authors are engaged in the classification of flood hydrographs. The authors propose to decompose the hydrograph into smooth functions and reduce the modeling problem to the identification of appropriate functions and parameters for them, which in total will give the actual values of the hydrograph. The authors use this approach for flood sample values from data collected in 163 Swiss watersheds. From the result obtained, the authors were able to derive three reference hydrographs corresponding to the average values of the clusters. The difference between the hydrographs was in the time that the flood lasts and the intensity of its growth.

The next qualitative leap occurred by using neural networks in this field of hydrology. In the work (Kratzert et al. 2019), the authors use a neural network with a long short-term memory (LSTM network). The method is based on a neural network of a special architecture. In the architecture of the LSTM network there are elements that are able to remember the previous state of a network node and transfer the values between layers distant from each other, which makes it possible to avoid signal blur. Among other things, the authors developed a special version of the LSTM network for solving the prediction problem, which differs in that the incoming signal is fed separately to each layer of the network. The authors were able to teach the network using the CAMELS dataset, which contains daily average precipitation, temperature, humidity, soil composition, and snowfall information for 531 gauging stations across the United States. As a result of training, the neural network was able to form an internal representation and identify two options for clustering the water regime for these gauging stations (with 5 and 6 clusters, respectively). As a result, the authors obtained clusters of water regimes geographically corresponding to: the US Northwest (Oregon and Washington), the Rocky Mountains and California, the Great Plains, the East Coast Southeast, and, finally, the East Coast Northeast and the Appalachians. The key characteristics influencing water regimes were: altitude, aridity, average daily precipitation, catchment area, presence of forests and other vegetation, and the average annual difference in the amount of green vegetation.

This model was successfully applied by the authors to the problems of flow forecasting using an input signal containing precipitation values and other meteorological variables. Finally, the team of authors from (Kratzert et al. 2019) presented the article «Accurate Hydrologic Modeling Using Less Information» (Shalev et al. 2019), in which they showed that a neural LSTM network pre-trained on the CAMELS dataset can learn to predict and classify rivers by water regime only on the basis of averaged data on discharge, temperature, and precipitation, and without taking into account average daily information on precipitation, temperature, humidity, and soil composition and snow cover. The method was applied to the data from Indian rivers. An experiment comparing the performance of models with available data on the static characteristics of the watershed (size, soil type, etc.) with a model without them demonstrated that it is possible to achieve comparable model quality without static characteristics of a watershed

It's rare to find a study with the use of machine learning methods in the problems of classifying the water regime for Russian rivers. In fact, the study (Ayzel 2021) is a unique work. A map of water regime types in the USSR is used as a class reference (Water regime... 2001). In this work the problem of reproducing the types of water regime in 1990 for the North-West of the European territory of Russia is solved by using the «random forest» class of methods on the basis of data on climatic runoff for the period 1979–2016. Then its transformation is estimated based on the calculated values of Future runoff projections (R5CH, 2006–2099) according to the three emission scenarios of the respective RCPs (RCP2.6, RCP6.0, RCP8.5). The calculations are carried out on a regular grid. As a result, the author obtained a very high classification accuracy – 91.6%, the calculations showed that by the end of the 21st century, the water regime of the rivers of the north-west of the ETR will change significantly: low periods of relatively stable water flow will become more intermittent or due to emerging rain floods or due to thaws. The second important aspect will be the transformation of the snowmelt flood – it will become significantly lower and will be observed at an earlier date.

In addition to regional studies, large-scale continental generalizations have begun to appear in recent years, using machine learning methods for problems of hydrological classification. In the work «Spatial patterns and characteristics of flood seasonality in Europe» (Hall and Blöschl 2018), a more general classification of the characteristics of the maximum runoff on the scale of the European continent was carried out. The authors took data from 4,105 measuring stations and used it to extract the maximum flow rates for each year. Then, for each station, a vector of 12 variables was constructed, where each variable corresponds to the frequency with which flood peaks occurred in that month. The K-means algorithm was chosen as the clustering algorithm, and the silhouette coefficient was chosen as the cluster quality assessment metric. The authors considered three options for the number of clusters: 4, 6, 7. As a result of the work, the authors identified 6 main clusters according to the peaks of floods, localized in geographically common subregions.

Another similar work – In «Regional classification, variability, and trends of northern North Atlantic river flow» (Kingston et al. 2011), the team of authors from (Harris et al. 2000) extended the problem of classifying water regime types to the North Atlantic. This time, instead of modeling statistical distributions, the authors used full-fledged clustering algorithms, in particular, several methods were tested:

Agglomerative hierarchical clustering with average pairwise distance metric;

Agglomerative hierarchical clustering with Ward's algorithm;

k-means method;

Agglomerative hierarchical clustering with subsequent application of the K-means method;

Using Principal Components and then Hierarchical Clustering.

The collective of authors came to the conclusion that the second approach is the most optimal in terms of the quality of the obtained clusters. The physical result of the work was the identification of seven different types of hydrographs in the region.

MATERIALS AND METHODS

Selected watersheds

Average monthly water discharges for 351 hydrological gauges located on the European territory of Russia (ETR) were used as a data source for this research. Catchment area size varied from 1000 to 200 000 square kilometers therefore both medium and large rivers were studied. The gauges were selected to cover the entire region of interest from the Far North to the arid south, including the natural zones of the tundra and forest-tundra, taiga, mixed and broad-leaved forests, forest-steppe and steppe.

Hydrological data and observation periods

Average values for monthly runoff of different rivers were used as data for this study. This dataset was created by converting the following publications into a digital format. Data for the period from 1985 to 2007 were purchased from the State Fund VNIIGMI-WDC (http://meteo.ru/). Data for the period from 2007 to 2019 were available online from the AIS GMVO (https://gmvo.skniivh.ru/). The selected parameters were calculated for each year and then averaged over two periods 1945–1977 and 1978–2019. The choice of periods is based on literary analysis, as according to the most modern studies (Long-term fluctuations... 2021; Frolova et al. 2022) in the period from 1978 and up to today hydrological systems start to display different behavior compared to historical period in response to changes in climate.

Feature selection

To carry out the analysis for each year of observation and for each river, the following hydrological characteristics were calculated:

Month number for the maximum average monthly flow (nMax) – the month in which the maximum value of water discharge was observed during the calendar year

Month number for the maximum average minimum flow (nMin) – the month in which the minimum value of water discharge was observed for the calendar year

The share of runoff volume during the spring season (dP) – was determined as the ratio of the sum of runoff volume for March, April, May to the sum of total runoff volume for the entire calendar year

Maximum average monthly discharge per year (Qmax)

Minimum average monthly discharge per year (Qmin)

The ratio of the maximum discharge to the average annual discharge (Qmax / Qyear) – the ratio of the maximum average monthly discharge for a calendar year to the average annual flow rate.

The ratio of the maximum flow to the minimum flow (Qmax / Qmin) – the ratio of the maximum average monthly flow to the minimum average monthly flow for a calendar year.

Coefficient of natural regulation (Phi) – was calculated as the ratio of the sum of the base annual runoff to the total total runoff for the year, where the base runoff is the sum of all discharge values that are less than the average. If the flow rate is greater than the average, then the average flow is used during summation instead.

During the aggregation of values for periods of 1945–1977 and 1978–2019, numerical values were averaged, and for categorical ones (i. e. nMax) a mode (most frequent value) was used.

Clusterization methods

Several algorithms were used to cluster data samples for two previously described periods by types of water regime. The K-means algorithm was first described in 1957 and has been one of most famous algorithms due to its widespread (Xu and Tian 2015). Modern versions of the algorithm optimize its computational complexity to some extent or try to take advantage of various distance metrics. An important feature of the algorithm is the lack of guarantee to find an optimal solution in the global sense; it only finds a local one. Another disadvantage of the algorithm is the requirement to specify the number of clusters into which the data should be partitioned. Therefore this number should be inferred beforehand.

The next clustering algorithm that was used in the work is the EM-algorithm (Expectation–maximization algorithm) (Dempster et al. 1977). In general, this algorithm works similarly to the K-means algorithm. The main difference between them is that the EM-algorithm does not calculate the distance from points to centroids, but instead uses the probability that a point belongs to a particular cluster.

Hierarchical clustering, just like the K-means method, requires choosing a distance metric (usually, Euclidean one is used), but unlike the previous method, it is not that sensitive to changes in this metric. The idea of the algorithm is that a tree of elements is built and for each step of the algorithm the nearest clusters are glued together until only a single set remains. The choice of cutoff at which to stop gluing is left to the discretion of the researcher. The option where individual elements are combined into one is called agglomerative hierarchical clustering (Sasirekha and Baby 2013). The algorithm for determining the distance between the merged nodes also remains at the choice of the researcher, as a rule, the Ward criterion is used. Therefore an algorithm tries to minimize the total value of the variance within each cluster. The main advantage of this class of algorithms is the relative ease of use, which could have influenced their comparative popularity in the works of the 2000s.

Another interesting approach to perform data clustering is the DBSCAN algorithm proposed in (Schubert et al. 2017). Unlike previous algorithms, DBSCAN groups points into clusters according to the density of their distribution in space, and not according to the distances between them. Also, DBSCAN does not require a beforehand knowledge of the number of clusters that the researcher intends to obtain. The method is described in detail in (Schubert et al. 2017).

For all the methods described above their implementations in Python 3 programming language were used. Specifically, the Scikit-Learn machine learning library was used. Other libraries used in data analysis and transformation were Pandas and Numpy. Matplotlib was used as a visualization library. Data preparation consisted of analysis of the parameter variability and its limits, and structuring the data in a way appropriate for drawing maps.

The silhouette coefficient was chosen as a metric for assessing the quality of clustering, similar to (Haines et al. 1988; Hall and Bloshl 2018). The value of the silhouette coefficient S shows how similar the object is to its cluster compared to other clusters, which is described in detail in (Rousseeuw 1987).

The value of the coefficient lies between -1 and 1. The closer the score to 1 the more it indicates that the object is close to the objects in the cluster it was assigned to, and doesn't have much similarity with the objects from «foreign» clusters. If the majority of objects have a high value of this metric, then we can consider the clustering result to be of sufficient quality. If a large number of objects have low or negative silhouette coefficients, then there may be too many clusters, too few clusters, or the data simply isn't structured in a way that could be clusterized.

Classification using Gradient Boosting

During the course of work another approach was tried, gradient boosting algorithms were used to classify the types of water regimes. Unlike clustering algorithms, gradient boosting algorithms are from a family of supervised learning algorithms. First, the algorithm is trained on a labeled piece of data, and then the inferred underlying law is applied to the new data. This family of algorithms (boosting) was chosen because as of now it is a kind of an industry standard. Their implementations are:

Microsoft: LGBM algorithm;

Yandex: CatBoost algorithm;

XGboost algorithm implemented in the open package Sklearn is also widely used.

The popularity of this family of algorithms is the result of their fast speed of work and a relative ease of choosing input parameters. In fact, this algorithm is a special case of an ensemble of decision trees (i.e., a large number of decision trees are built and their average result value is taken). At each step of the algorithm, a temporary intermediate model is created and the residuals of this model are calculated (i.e., the difference between the actual value at the point and the value the algorithm returned). After that, a new ensemble of trees is created that models these residuals and the resulting model is added to the previous solution. This process goes on until the criteria specified at the start of a classification process are met (usually a set number of steps is specified). For a classification of water regime types authors chose the implementation of gradient boosting from Yandex (Prokhorenkova et al. 2019). The available sample was divided into training and test sets to assess the quality of the model. The training data set for 1945–1978 was labeled according to the Water Regime Types map (Water regime… 2001). MultiClass classification metric was chosen as the function to be optimized, i.e. a function that predicts the class of a point among several options and an overall accuracy of the model is calculated as a number of correct predictions divided by the number of datapoints. At the beginning, the authors made an attempt to simply build a model on 2000 steps, but later other parameters had to be adjusted.

The main feature of this algorithm is that it can work on relatively small amounts of data, which is a very useful feature given the amount of data used in this work. The difference between CatBoost and other gradient boosting algorithms also lies in the system for constructing decision trees. CatBoost uses absolutely symmetrical tree construction. To split a tree into branches, a certain metric is needed. In CatBoost, however, the value of the split depends on its ability to approximate the gradient vector. The splitting value is the value that is as close as possible to the gradient. According to the results of testing by the Yandex team, it was found that this mechanism really improves the quality of the algorithm. In the CatBoost algorithm, as in other algorithms, the calculation of the quality of the result is implemented for each split of the tree. The value with the best quality score in the end will be the split point of the tree. However, Yandex developers came up with the idea of adding a certain value to each quality result. This value will depend on the number of iterations passed and on the length of the gradient vector. The use of the CatBoost algorithm in this work took place in several stages, which gave different results at the output.

The basis of the metrics for assessing the quality of classification is the contingency matrix (Townsend 1971). The most common metric is accuracy, which was also used as a metric in the work (Ayzel 2021). This metric was used to evaluate the classification result, despite the fact that it has a significant drawback. It lies in the fact that it assigns the same weight to all classes, regardless of how many points fall into a particular class. However, it is the most common and frequently used metric for assessing the quality of a classification.

RESULTS AND DISCUSSION

Various combinations of parameters were tested by authors in an attempt to cluster water regime types. Three parameters out of the entire dataset were chosen as the optimal number of features to use. Authors were able to identify clusters using only Nmax, Nmin, and Qmax/Qmin. Additional characteristics did not improve the quality of clustering, but increased the instability. Among all clustering methods, K-means and DBSCAN, had the highest silhouette coefficient. By using K-means and setting the number of clusters to 8, authors acquired clusters with a silhouette score of 0.478 for the first period and 0.498 for the second one. The DBSCAN method performed much better. An algorithm found 9 clusters, 5 of significant size and 4 small ones. For the sample of data up to the year of 1978 parameters eps = 1, minPts = 3 were and the resulting silhouette coefficient was 0.610, for the sample after 1978 and parameters eps = 0.6, minPts = 3 the score was 0.720.

The distribution of points across clusters is uneven, 80% of all points fall into the three main clusters, the remaining ones account for less than 20%. At the same time, the clusters were very well localized in the geographical space, despite the fact that zonal characteristics (vegetation, soil, meteorological parameters) did not participate in any way in clustering. As a result, maps of localization of clusters obtained by the DBSCAN method for the period before and after 1977 were built, which are presented in (Fig. 1). The resulting clusters are associated with the types of water regime (TWR) on the map «Water regime of the rivers of Russia and adjacent territories» (Water regime… 2001). The dark blue cluster corresponds to the types numbered 15 and 2. The green cluster can be interpreted as types №14 and 3, and the yellow as 16. The algorithm also singled out the red cluster, which is intermediate between 14 and 16 TWR. The remaining clusters account for less than 20% of the points, of which the orange cluster corresponds to the 21st type of water regime on the map (Water regime… 2001), covering the Kuban basin, and the dark purple cluster corresponds to the 12th type, covering most of the Terek basin.

Table 1. Silhouette Score (SS) for different methods and dataframes for parameters N_{max}, N_{min}, Q_{max}/Q_{min}

Algorithm	Period	Silhouette score (SS) for N кclusters			
		N = 5	N = 6	N = 7	N = 8
K-means	Before 1978	0.438	0.463	0.468	0.478
	After 1978	0.464	0.469	0.482	0.498
EM-method	Before 1978	0.181	0.213	0.083	0.041
	After 1978	0.162	0.233	0.15	0.017
Agglomerative hierarchical clustering	Before 1978	0.423	0.428	0.432	0.437
	After 1978	0.446	0.447	0.455	0.463
		Number of clusters determined by an algorithm		Parameters	
DBSCAN	Before 1978	0.61		eps=1, minPts=3	
	After 1978	0.72		eps=0.6, minPts=3	

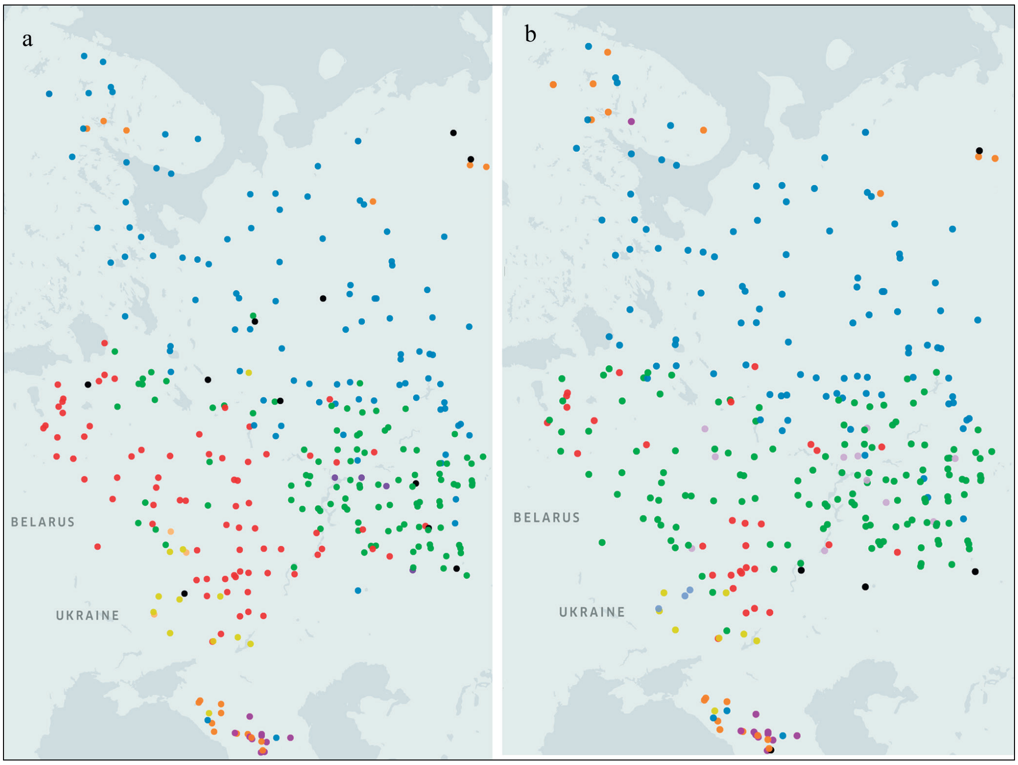

Fig. 1. Scheme of clusters for period 1945–1977 (a) and 19782019 (b) created with DBSCAN algorithm for three parameters: N_{min}, N_{max}, Q_{min}/Q_{max}

The result of clusterization largely corresponds to the map of water regime types created in (Frolova et al. 2021). An algorithm could not identify fractional clusters that differ in continentality conditions in the Central part of the Russian Plain. Figure 1 shows that for the second period there is a noticeable shift of the southern clusters; they are expanding to the north. For example, during the first period the yellow cluster mainly included points within the Seversky Donets basin, right-bank tributaries of the Lower Don. At the present stage, the yellow cluster corresponds to type 16 on the TVR map (Water regime… 2001) and already covers some tributaries of the Middle and Upper Don. The most noticeable changes affected the central zone – the red, intermediate cluster moved north by more than 1000 km, covering most of the Oka and Upper Volga basins, as well as the entire central and eastern part of the Don basin, while the initially dominant green cluster 14-15 TBP has been preserved only to the east of the Volga – in the Kama basin and partly on the Upper Volga. This result corresponds to the data obtained earlier in the work (Frolova et al. 2020), where estimates of the water regime transformation coefficient were given, and it was shown that this calculated coefficient is maximal in this region. At the same time, there is practically no shift of the green cluster to the north compared to the others, which indicates the relative stability of the water regime of the northern regions of the EPR.

The similarity of the obtained results compared to the existing map of water regime types (Water regime… 2001) suggested the possibility of using it to train the supervised model, with the aim of subsequent reproduction on a modern data set. The primary analysis of the «predicted classes» showed a low quality of classification compared to the existing map (about 0.68%). The reason behind this was an inability of the algorithm to recognize relatively similar water regime types: 2 and 14, 3 and 15, as there are relatively few data points in the sample to infer differences between them. As a result, it was decided to combine each pair into one class. After that, on the test part of the data set (1945–1977) with the parameters set to default, the accuracy of determining the type of water regime raised to 78%. This is a very good result, given the volume and quality of the data used by the algorithm. To improve the obtained values, manual selection of parameters of the CatBoost algorithm was carried out. In addition to this selection, a dynamic visualization from a CatBoost package was used to display the process of training the model. With its help, the point at which overfitting began was determined, which in turn made it possible to select the appropriate regularization parameters in order to avoid it. The quality of the algorithm reached 87% in terms of accuracy. In the field of application of machine learning, the result of metrics of 80+% is often considered good. All methods of improving the quality of the algorithm were tried: cross-validation, K-fold validation, One Hot Encoding, regularization, bagging, stacking, normalization and standardization. Subsequent improvements to the algorithm are possible only with the addition of the initial hydrological data. According to the results obtained by using the CatBoost algorithm, a water regime classification map was also built for the past and present periods (Fig. 2). Similar to the clustering, a classification algorithm wasn't able to distinguish between the water regimes for western and eastern regions of ETR. A border between rivers of «northern» (in a relative sense) «central» regions of ETR lies further to the south compared with the existing map and approximately corresponds to the Oka macrovalley. Supervised classification confirmed a noticeable shift of the more «southern» type of water regime (corresponding to No. 16 on the TBP map) to the north, but the shift of the 14th TBP to the north in the case of supervised classification was not detected as supervised training initially sets the classes to match the reference division . On the other hand, class 13 was separately identified, localized in the Ural basin, which compared to a historical period broadened to a larger area.

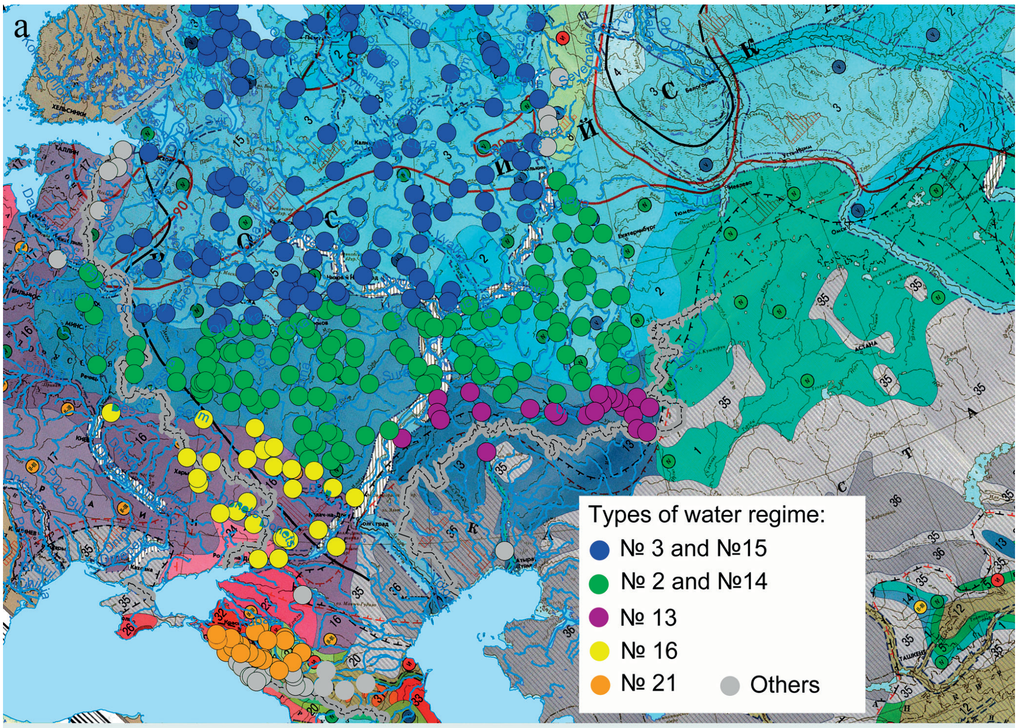

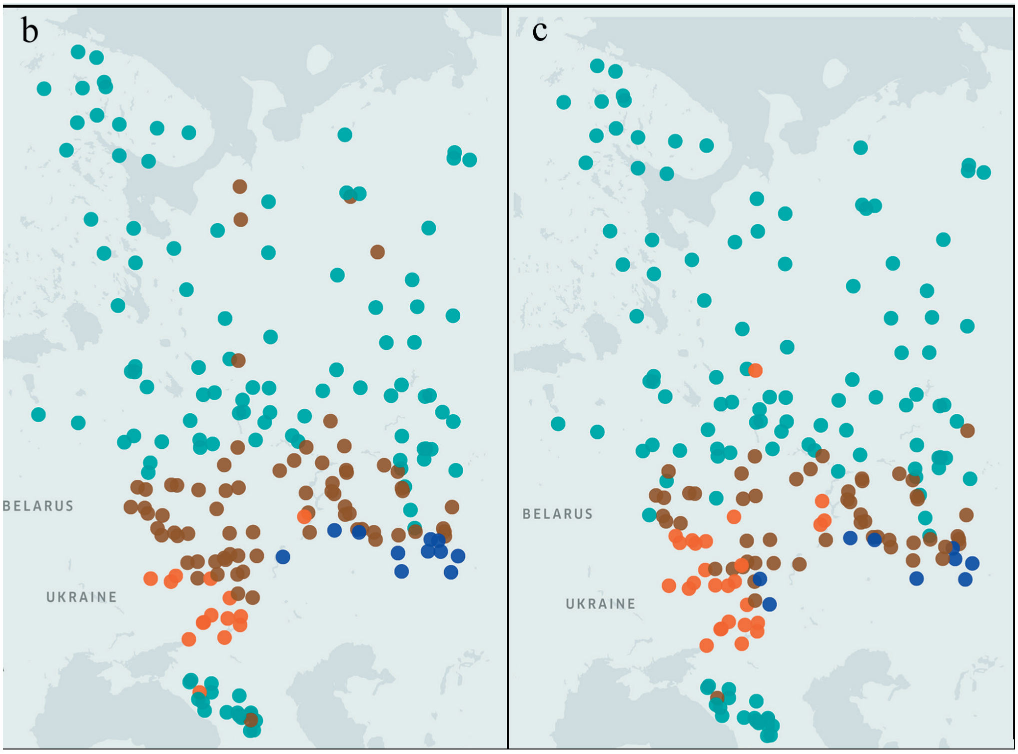

Fig. 2. Classes according to the map of Types of water regime of the rivers of the USSR with points of hydrological gauges (a), classes obtained by training on the test set 1945–1977 (b) and classes obtained using the trained model on modern data for 1978–2018 (c)

CONCLUSIONS

The results obtained allow us to formulate the following main conclusions:

The accumulated volume of hydrological data allows the use of machine learning methods in the problems of classifying water regime types.

The simplest class of methods – clustering methods shows that by selecting a combination of parameters and using data series with a length of 6070 years it is possible to obtain good results. The clustering performed by the DBSCAN method showed a high silhouette coefficient and good localization of clusters in space.

By using clustering methods, it is possible to assess the transformation of the water regime types over the past 40 years by dividing the sample into two periods.

Supervised classification models also show high correspondence with the reference classification, with an accuracy of 87%. However, the initial selection of clusters may not reveal the transitional types that are revealed by using unsupervised methods.

Both clustering methods and classification methods showed a shift of clusters representing southern water regimes. In the central region these regimes expanded by a 1000 km to the north.

REFERENCES

Ayzel G. (2021). Machine Learning Reveals a Significant Shift in Water Regime Types Due to Projected Climate Change. ISPRS Int. J. Geo-Inf., 10, 660, DOI: 10.3390/ijgi10100660.

Blöschl G., Hall J., Parajka J. et al. (2017). Changing climate shifts timing of European floods. Science, 357, 588-590, DOI: 10.1126/science.aan2506.

Blöschl G., Hall J., Viglione A., Perdigão R.A.P., Parajka J., Merz B., Lun D., Arheimer B., Aronica G.T., Bilibashi A., Boháč M., Bonacci O., Borga M., Čanjevac I., Castellarin A., Chirico G.B., Claps P., Frolova N., Ganora D., Gorbachova L., Gül A., Hannaford J., Harrigan S., Kireeva M., Kiss A., Kjeldsen T.R., Kohnová S., Koskela J.J., Ledvinka O., Macdonald N., Mavrova-Guirguinova M., Mediero L., Merz R., Molnar P., Montanari A., Murphy C., Osuch M., Ovcharuk V., Radevski I., Salinas J.L., Sauquet E., Šraj M., Szolgay J., Volpi E., Wilson D., Zaimi K., and Živković N. (2019). Changing climate both increases and decreases European river floods. Nature, 573, 10-111, DOI: 10.1038/s41586-019-1495-6.

Brunner M.I., Viviroli D. Furrer R., Seibert J., and Favre A.C. (2018). Identification of Flood Reactivity Regions via the Functional Clustering of Hydrographs. Water Resources Research, 54(3), 1852-1867, DOI: 10.1002/2017WR021650.

Dempster P., Laird N.M. and Rubin D.B. (1977). Maximum Likelihood from Incomplete Data via the EM Algorithm. Journal of the Royal Statistical Society. Series B (Methodological), 39(1), 1-38.

Djamalov R.G., Frolova N.L., Bugrov A.A., Grigoriev V.Yu., Igonina M.I., Kireeva M.B., Krichevets G.N., Rets E.P., Safronova T .I., Telegina A.A., Telegina E.A., and Fathi M.O. (2014). Renewable Water Resources of the European Part of Russia. Atlas. Moscow: Water Problem Institute of RAN. (In Russian).

Djamalov R.G., Frolova N.L., Kireeva M.B., Rets E.P., Safronova T.I., Bugrov A.A., Telegina A.A., Telegina E.A. (2015). Modern resources of underground and surface waters of the European part of Russia: formation, distribution, use. Moscow: GEOS. (In Russian).

Frolova N.L., Kireeva M.B., Kharlamov M.A., Samsonov T.E., Entin A.L., Lurie I.K. (2020). Mapping the current state and transformation of the water regime of the rivers of the European territory of Russia. Geodesy and Cartography, 7, 14-26, DOI: 10.22389/0016-7126-2020-961-7-14-26. (In Russian).

Frolova N.L., Magritsky D.V., Kireeva M.B., Grigoriev V.Yu., Gelfan A.N., Sazonov A.A., Shevchenko A.I. (2022). Runoff of Russian rivers under ongoing and predicted climate changes: a review of publications. 1. Assessment of changes in the water regime of Russian rivers based on observational data. Water Resources, 49(3), 251-269, DOI: 10.31857/S032105962203004X. (In Russian).

Frolova N.L., Povalishnikova E.S., Kireeva M.B. (2021). Classification and zoning of rivers by their water regime: History, methodology, and perspectives. Water Resources, 48(2), 169-181, DOI: 10.1134/s0097807821020056.

Gelfan A.N., Frolova N.L., Magritsky D.V., Kireeva M.B., Grigoriev V.Yu., Motovilov Yu.G., Gusev E.M. (2021). Influence of climate change on the annual and maximum runoff of rivers in Russia: assessment and forecast Fundamental and applied climatology, 7(1), 36-79, DOI: 10.21513/2410-8758-2021-1-36-79 (In Russian).

Georgievsky V.Yu., and Shalygin A.L. (2012). Hydrological regime and water resources. Methods for assessing the consequences of climate change for physical and biological systems, Moscow: Rosgidromet, 53-86. (In Russian).

Haines A.T., Finlayson B.L., McMahon T.A. (1988). A global classification of river regimes. Applied Geography, 8(4), 255-272, DOI: 10.1016/0143-6228(88)90035-5.

Hall J. and Blöschl G. (2018). Spatial patterns and characteristics of flood seasonality in Europe. Hydrol. Earth Syst. Sci., 22, 3883-3901, DOI: 10.5194/hess-22-3883-2018.

Harris N.M., Gurnell A.M., Hannah D.M., and Petts G.E. (2000). Classification of river regimes: a context for hydroecology. Hydrological Processes, 14(16-17), 2831-2848, DOI: 10.1002/1099-1085(200011/12)14:16/17<2831::AID-HYP122>3.0.CO;2-O.

Kidanewold B.B., Seleshi Y., Demissie S., and Melesse A.M. (2015). Flow Regime Classification and Hydrological Characterization: A Case Study of Ethiopian Rivers Water, 7, 3149-3165, DOI: 10.3390/w7063149.

Kingston D.G., Hannah D.M., Lawler D.M., and McGregor G.R. (2011). Regional classification, variability, and trends of northern North Atlantic river flow. Hydrol. Processes, 25(7), 1021-1033.

Kireeva M., Frolova N., Rets E., Samsonov T., Entin A., Kharlamov M., Telegina E., Povalishnikova E. (2019). Evaluating climate and water regime transformation in the European Part of Russia using observation and reanalysis data for the 1945-2015 period. International Journal of River Basin Management, 18(4), 1-12, DOI: 10.1080/15715124.2019.1695258.

Kratzert F., Klotz D., Shalev G., Klambauer G., Hochreiter S. and Nearing G. (2019). Towards learning universal, regional, and local hydrological behaviors via machine learning applied to large-sample datasets. Hydrol. Earth Syst. Sci., 23, 5089-5110, DOI: 10.5194/hess-23-5089-2019.

Long-term fluctuations and variability of water resources and the main characteristics of the flow of rivers in the Russian Federation. Scientific and Applied Handbook. (2021). St. Petersburg: LLC «RIAL».

Olden J.D., and Poff N.L. (2003). Redundancy and the choice of hydrologic indices for characterizing streamflow regimes. River Research and Applications, 19, 101-121, DOI: 10.1002/rra.700.

Prokhorenkova L., Gusev G., Vorobev A., Dorogush A.V., Gulin A. (2019). CatBoost: unbiased boosting with categorical features. Available at: https://arxiv.org/pdf/1706.09516.pdf%20https://tech.yandex.ru/catboost/ [Accessed Apr. 2020].

Rousseeuw J. (1987). Silhouettes: A graphical aid to the interpretation and validation of cluster analysis. Journal of Computational and Applied Mathematics, 20, 5365, DOI: 10.1016/0377-0427(87)90125-7.

Sasirekha K. and Baby P. (2013). Agglomerative hierarchical clustering algorithm. A review. International Journal of Scientific and Research Publications, 83, 83.

Schubert E., Sander J., Ester M., Kriegel H. P., and Xu X. (2017). DBSCAN revisited, revisited: why and how you should (still) use DBSCAN. ACM Transactions on Database Systems (TODS), 42(3), 1-21, DOI: 10.1145/3068335.

Shalev G., El-Yaniv R., Klotz D., Kratzert F., Metzger A., Nevo S. (2019). Accurate Hydrologic Modeling Using Less Information. Mathematics, Computer Science, Available at: https://arxiv.org/pdf/1911.09427.pdf.

Tavassoli H.R., Tahershamsi A. and Acreman M. (2014). Classification of natural flow regimes in Iran to support environmental flow management. Hydrological Sciences Journal, 59(3-4), 517-529, DOI: 10.1080/02626667.2014.890285.

Townsend J.T. (1971). Theoretical analysis of an alphabetic confusion matrix. Perception & Psychophysics, 9(1), 40-50.

Water regime of the rivers of Russia and adjacent territories. Map for higher educational institutions. (2001). Scale 1:8 000 000, V.M. Evstigneev, N.V. Shenberg, N.V. Anisimova, A.A. Zaitsev (Eds.), Novosibirsk, Roskartografia Cartographic Factory. (In Russian).

Webb J.A., Bond N.R., Wealands S.R., Nally R.M., Quinn G.P., Vesk P.A., and Grace M.R. (2007). Bayesian clustering with AutoClass explicitly recognises uncertainties in landscape classification. Ecography, 30, 526-536, DOI: 10.1111/j.0906-7590.2007.05002.x.

Xu D., and Tian Y. (2015). A Comprehensive Survey of Clustering Algorithms. Ann. Data. Sci., 2, 165-193, DOI: 10.1007/s40745-015-0040-1.

RESEARCH PAPER

DISASTER-INDUCED RESETTLEMENTS: THE RESILIENCE OF FLOOD-AFFECTED HOUSEHOLDS IN DAR ES SALAAM, TANZANIA

Regina John[1*]
[1]School of Spatial Planning and Social Sciences, Ardhi University, P.O.Box 35176, Dar es Salaam, Tanzania
***Corresponding author:** reginajohn2000@gmail.com
Received: March 13th, 2022 / Accepted: August 8th, 2022 / Published: October 1st, 2022
https://DOI-10.24057/2071-9388-2021-027

ABSTRACT. Floods are increasingly affecting cities around the world. As a result, displacement and resettlement of flood-affected households have become the norm in many parts of the world. While resettlement may be necessary to address flood vulnerabilities, including protecting the lives of those affected, empirical studies on the post-resettlement well-being of the resettled population are scarce. This paper presents empirical findings on the livelihood situation of flood-resettled households in Dar es Salaam. The results are based on key informant and household interviews and focus group discussions with resettled households. The findings show that the resettlement area's location in the peri-urban of the city resulted in various challenges, including inaccessibility to basic facilities and high transportation costs, with households spending an average of TZS 2,000 (~US$1) to reach a public transportation facility, i.e., a bus stand. Resettled households also have lower income levels ranging from less than TZS 50,000 (12%) to between TZS 50,000 and TZS 500, 000 (75%). While weak social ties, a lack of trust among household members, and the social stress of loss of privacy were typical challenges among resettled households, vulnerable groups, particularly women and children, were exposed to increased vulnerability. The observed post-resettlement livelihood situation is influenced by the pre-resettlement conditions of the households, characterized by large household sizes ranging from 5 to 6 members (55%) to more than seven members (35%), low education levels (77%), and informal employment, largely petty trading (56%). The paper suggests that when resettling flood-affected households, the context-specific characteristics of the affected population, such as demographic and socio-economic characteristics, and their needs, be considered to improve post-resettlement livelihood sustainability.

KEYWORDS: Displacement, Resettlement, Livelihoods, Disaster, Dar es Salaam

CITATION: John R. (2022). Disaster-Induced Resettlements: the Resilience Of Flood-Affected Households In Dar Es Salaam, Tanzania. Geography, Environment, Sustainability. 3(15), 88-98
https://DOI-10.24057/2071-9388-2021-027

ACKNOWLEDGEMENTS: The author would like to thank all research participants, especially the resettled households, the sub-ward and ward leaders at the resettlement site, and the field assistants, for their cooperation during the data collection. I also wish to thank anonymous reviewers for their constructive comments

Conflict of interests: The author reported no potential conflict of interest.

INTRODUCTION

Natural disasters are increasingly affecting the world at our times. Natural disasters occur worldwide, with developing countries bearing the brunt of the consequences (United Nations International Strategy for Disaster Reduction [UNISDR] 2015). Such hazards have an impact not only on people's lives but also on their property, economic activity, and public infrastructure. The international disaster databases (UNISDR 2012; UNISDR 2015) and the Intergovernmental Panel on Climate Change (IPCC 2012) have noted an increase in hazardous events over the last few decades. According to the United Nations Environmental Program (UNEP 2012), over the last few decades, developing countries have accounted for more than 95 percent of the fatalities associated with extreme events.

Extreme meteorological and climate events such as floods, droughts, and hurricanes are the most common causes of global disasters (UNISDR 2015). Extreme floods and cyclones significantly contribute to disaster events across the African continent. These include Cyclone Eline in 2000, which affected over five million people in Southern African countries, and the 2010 West and Central Africa flood disasters, which affected 17 countries (Reason and Keibel 2004; Holloway et al. 2013). Floods have also affected Tanzania's commercial capital, Dar es Salaam. Severe floods hit the City in 2011, which resulted in the loss of life, destruction of property and public infrastructure, and the displacement of thousands of city dwellers (John et al. 2014). According to the literature, flood events frequently result in catastrophic disasters resulting in the loss of life and the displacement of others (Douglas et al. 2008).

Climate-related disaster events are increasingly causing internal and cross-border displacement of the affected population worldwide. Raheem and Olorunfemi (2013) confirm that the poor's indigenous coping mechanisms are becoming less effective as their livelihood systems become increasingly vulnerable to disaster shocks. Natural disasters displaced an average of 25.4 million people per year between 2008 and 2015, according to the Internal Displacement Monitoring Centre (IDMC 2015). According to IDMC, storm events resulted in disaster displacements of 17.2 million people across 144 countries in 2018. Furthermore, more than 17 million people are at risk of being displaced by floods each year, with towns and cities particularly vulnerable (IDMC 2019).

Disaster-led resettlement is one of the IPCC-identified risk mitigation measures implemented gradually (Tadgell et al. 2018). Although the literature emphasizes that resettlement should be developmental, meaning that resettled populations should be better off as a result of resettlement (Correa 2011; World Bank 2004; Perera 2014), empirical evidence for this is lacking (Vanclay 2017). Both the development and disaster-induced resettlement literature show some evidence of improved physical assets, such as housing and some basic infrastructure (Vickery 2017; Li and Song 2009), with adverse effects related to loss of livelihood resources and impoverishment (Nikuze et al. 2019; Mteki et al. 2017; Patel et al. 2015; Cernea 1997). Recent studies have also identified social-cultural impacts such as changes in dress patterns and marriage customs, the loss of tribal folk art, the destruction of social networks, and increased violence resulting from development-induced displacement (Sikka 2020). Arnall (2019) and Rew et al. (2006) have cautioned that developmental relocations are challenging to achieve in practice due to the operational complexities of resettlement policies both in terms of developing coherent policy and achieving effective implementation on the ground. However, while empirical studies have shown that displaced households are better in safer locations, there are concerns about the impact of resettlement on the affected population. According to the literature, some resettled households return to their original settlements to escape the hardships they face in the resettled areas (Haile et al. 2013; John et al. 2014). While relocation is a typical response to a disaster, 90 percent of those relocated return at some point (Raleigh and Jordan 2010). According to Bronen (2015), in the aftermath of a disaster, decision-makers face significant difficulty implementing measures limiting people's ability to return to where they lived. Resettling disaster-displaced people is thus one of the world's current challenges. Furthermore, Wisner et al. (2012) cautioned that problems associated with the inability to return to one's life or to resettle elsewhere voluntarily are inextricably linked to post-resettlement difficulties.

As Arnall et al. (2013) emphasize, the viability of livelihoods is a critical determinant of whether the resettled individuals stay in their new location or return to their place of origin. Furthermore, Guo and Kapucu (2018) observed that the ease of changing livelihood strategies and their outcomes, supported by livelihood capital and institutional context, determine resettlers' intention to engage in conflicts after resettlement. While Guo and Kapucu (2018) combined the pressure-state response framework and the sustainable livelihoods approach to show specific factors affecting disaster resettlement in a rural setting, understanding the livelihood resilience of non-peasant populations, particularly in urbanization contexts, is critical. According to Gong et al. (2021), livelihood resilience is influenced by the external environment, which includes the socio-economic environment, infrastructure levels, and context-specific development opportunities.

When guided by evidenced-based policy, disaster-induced resettlement offers new opportunities for populations in high-risk locations for whom resettlement may be the best option (Kita, 2017; Black et al. 2013). The literature also shows that resettlement outcomes are better when resettled households choose their relocation sites based on their preferences and livelihood needs (Gong et al. 2021; Nikuze et al. 2019). Scholars argue that resettlement as adaptation should be voluntary by allowing the affected people to choose whether or not to participate in the resettlement process, which may provide them with new opportunities (Lipset 2013; Maldonado et al. 2013; Schmidt-Soltau and Brockington 2007). However, the literature emphasizes the difficulties of implementing voluntary resettlement programmes due to the uncertainties faced by resettlers, as well as the disparities in needs, interests, and experiences of individuals and groups within communities (De Wet 2008; Koenig, 2006). Consequently, it is indisputable that there is uncertainty regarding post-disaster management and how to resettle the affected communities better.

With current and projected climate change scenarios and their impacts, population resettlement due to various disasters is unavoidable, and their impacts on people's livelihoods will remain a challenge. Nonetheless, despite the magnitude of current displacement trends, few studies have examined the impact of disaster-led resettlements on people's livelihoods, in developing countries, particularly in the African region. According to Cernea (2000), resettlement's impact on a population depends on the local conditions, type of project, sector, or nature of displacement. Consequently, the intensity of each risk varies, as does the severity of the outcomes. Moreover, in the context of the urbanized flood-prone informal settlements, there is ongoing uncertainty about the resilience of the resettled communities.

This paper investigates the post-disaster livelihood resilience of flood-resettled households and its implication for the planned resettlement programmes. The analysis looked at the pre-and post-disaster livelihoods of the resettled households as conceptualized in the following section.

Conceptual Framework

Resilience is the ability of a system, community, or society exposed to hazards to resist, absorb, accommodate, adapt to, transform and recover from the effects of a hazard in a timely and efficient manner, including through the preservation and restoration of its essential basic structures and functions through risk management (UNISDR 2009). This study adopts the UNISDR definition and conceptualizes resilience as the ability to recover from a shock determined by the degree to which the community has the necessary resources and is capable of organizing itself before and during times of need. However, addressing the vulnerable population necessitates a greater focus on human livelihoods. As a result, the livelihood approach plays a vital role in analyzing resilience. Tanner et al. (2015) contend that the livelihood perspective contributes to resilience thinking by emphasising human needs and agency, empowerment, and human rights, as well as considering adaptive livelihood systems in the context of broader transformational changes. Livelihood resilience is an individual's or household's ability to maintain and improve their livelihood opportunities and well-being in the face of physical, economic, and social disruptions. A livelihood resilience approach broadens the definition of resilience beyond the technical approach by considering social and economic factors and the overall well-being of the affected population. However, resilience is not directly measurable, and attempts to analyse it has relied mainly on quantifiable surrogates or indicators of resilience (Jones and Tanner 2015), with different scholars employing different methods for determining indicators of resilience. The concept of sustainable livelihood is used in this study to examine household resilience. According to Quandt (2018), the sustainable livelihoods approach is one innovative method for determining resilience indicators.

The study derives the livelihood concept from the sustainable development concept proposed by Chambers and Conway (1992) and further developed by the Department for International Development [DFID] (Carney 1998) as an analytical framework for analysing livelihood changes. According to the framework, people's livelihoods are influenced by trends, shocks, and seasonality, which determine their vulnerability context. The framework includes five types of assets for livelihoods: human, natural, financial, social, and physical capital. The capital asset approach of the sustainable livelihoods framework recognizes the importance of non-monetary factors. It allows the inclusion of various indicators ranging from material to non-material such as social, human, natural, and cultural, considered necessary for measuring resilience. As a result, the capital assets approach to livelihoods appears to be the appropriate way of selecting indicators for assessing flood-resettled households' livelihood resilience. Table 1 presents indicators of livelihood based on the sustainable livelihoods approach.

The Study Area

The research was conducted in Tanzania's commercial capital, Dar es Salaam. Dar es Salaam is East Africa's largest city and, by some accounts, Africa's fastest-growing metropolitan area. According to the 2012 National census, the city had a population of 4.4 million, six times that of the next city, Mwanza (United Republic of Tanzania [URT] 2013). It is estimated that 70-80 percent of the city residents live in informal settlements. Flood risk is a major challenge for the city's sustainable growth because of its rapid urbanization, informal settlement development, and exposure to climate hazards (Pan-African START Secretariat et al. 2011; Picarelli et al. 2017). Floods are common in Dar es Salaam with the population in the low-lying coastal areas and along the river valleys more exposed (Figure 1). Approximately 8% of Dar es Salaam's total area lies in the low-elevation coastal zone below the 10-metre contour line, where flood risk is high (Kebede and Nicholls 2012). The World Bank estimates that floods have affected at least 39% of the population, or 2 million people, in various periods. Floods in 2009, 2010, 2011, 2014, 2015, 2017, 2018, and 2019 claimed lives and impacted various sectors. Furthermore, Kebede and Nicholls (2011) estimated that a 100-year coastal flood in the city would expose 30,000 people and assets worth US$35 billion.

Due to the recurring floods in Dar es Salaam, some of the city residents are in a constant state of recovery, which has a cumulative effect of making them poorer. Floods disproportionately affect vulnerable populations, such as children, the elderly, and women (John et al. 2014). The poor are disproportionately affected at the community and household levels and frequently lack the resources to recover from the flood effects. Households in informal settlements take various flood-prevention measures, including the use of sandbags and tree logs, raised pit latrines and doorsteps, provision of water outlet pipes above plinth level, construction of embankments and protection walls, the elevation of house foundations, as well as seasonal relocation (John 2020; Sakijege et al. 2012,). However, most of these methods are ineffective, particularly during flash floods (John 2020; Sakijege et al. 2014), necessitating the involuntary resettlement of the affected population on several occasions. This study looks at the livelihood resilience of households displaced by the 2011 flash floods in Dar es Salaam.

The research site is in Mabwepande ward, Kinondoni Municipality, about 35 kilometres from Dar es Salaam City centre. Mabwepande Ward had 25,460 people, according to the most recent national population census data in 2012. The Ward covers 52.03 square kilometres and has a population density of 489.4 inhabitants per square kilometre with a total of 6,800 households (URT 2013).

Mabwepande is the resettlement site of the city's 2011 flash floods displaced households. A total of 2,200 households were relocated from flood-prone settlements in the city, including Mchikichini, Tabata, Magomeni, Vingunguti, Kipawa, Kinyerezi, Ukonga, Gongo la Mboto, Majohe, and Charambe (Figure 3). Each resettled household received a plot ranging from 300 to 600 square metres. In addition, each household received one tent for a temporary shelter and 100 bags of cement to help with house construction. Other building materials such as iron sheets and timber were also donated to some of the households by various stakeholders.

Table. 1. Indicators of livelihood resilience based on the Sustainable Livelihood Approach

Concept	Variable	Description
Human asset	Household size	The number of household members: Large household size (-), single parent (-), one-person household (-).
	Age	Age composition of the household members: children and very elderly (-)
	Education	Education level attained by the household head: lower level (-)
Financial asset	Employment	Employment status: formal employment (+)
	Income	Household income level : low income (-)
Social	Social networks	Participation in social groups or associations (+) Social networking: no social network (-)
Physical	Infrastructure facilities	Road accessibility (+), Distance to facilities (Long distance-) Access to health care, education, and markets (+)
	Housing	House ownership (+) Housing quality: high quality (+)
Natural	Land	Ownership of land or plot (+) Size of land/plot (large size (+)

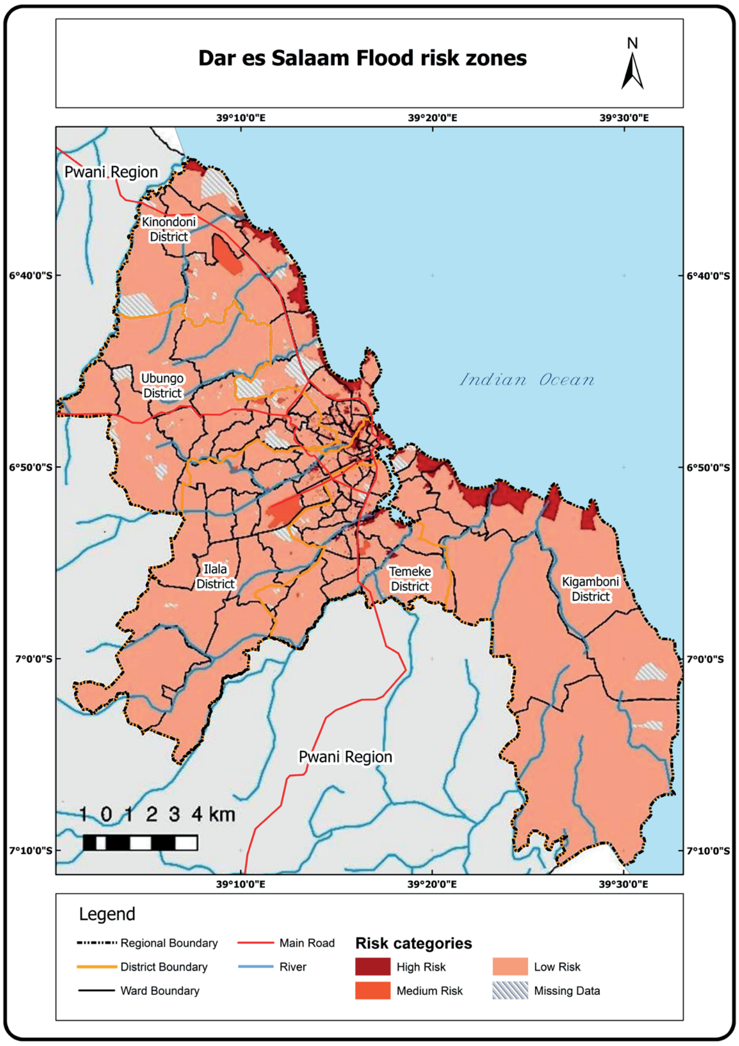

Fig. 1. Map of Dar es Salaam showing flood risk zones (Erman et al. 2019)

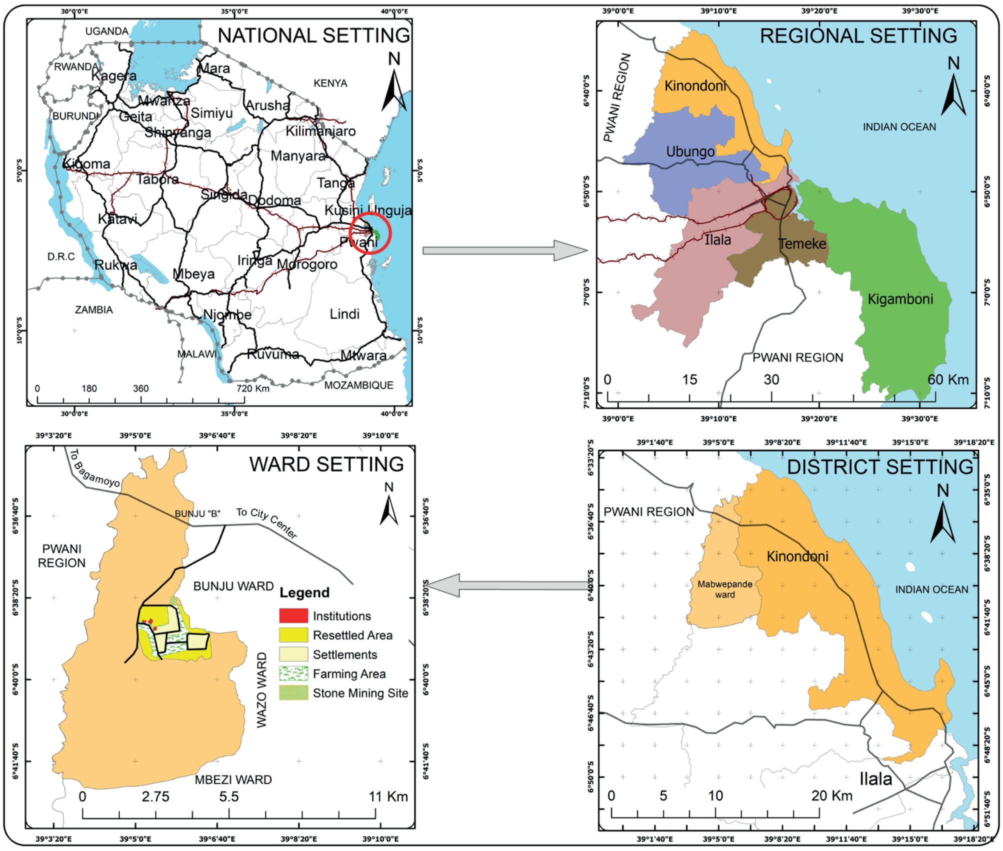

Fig. 2. Location of Mabwepande settlement

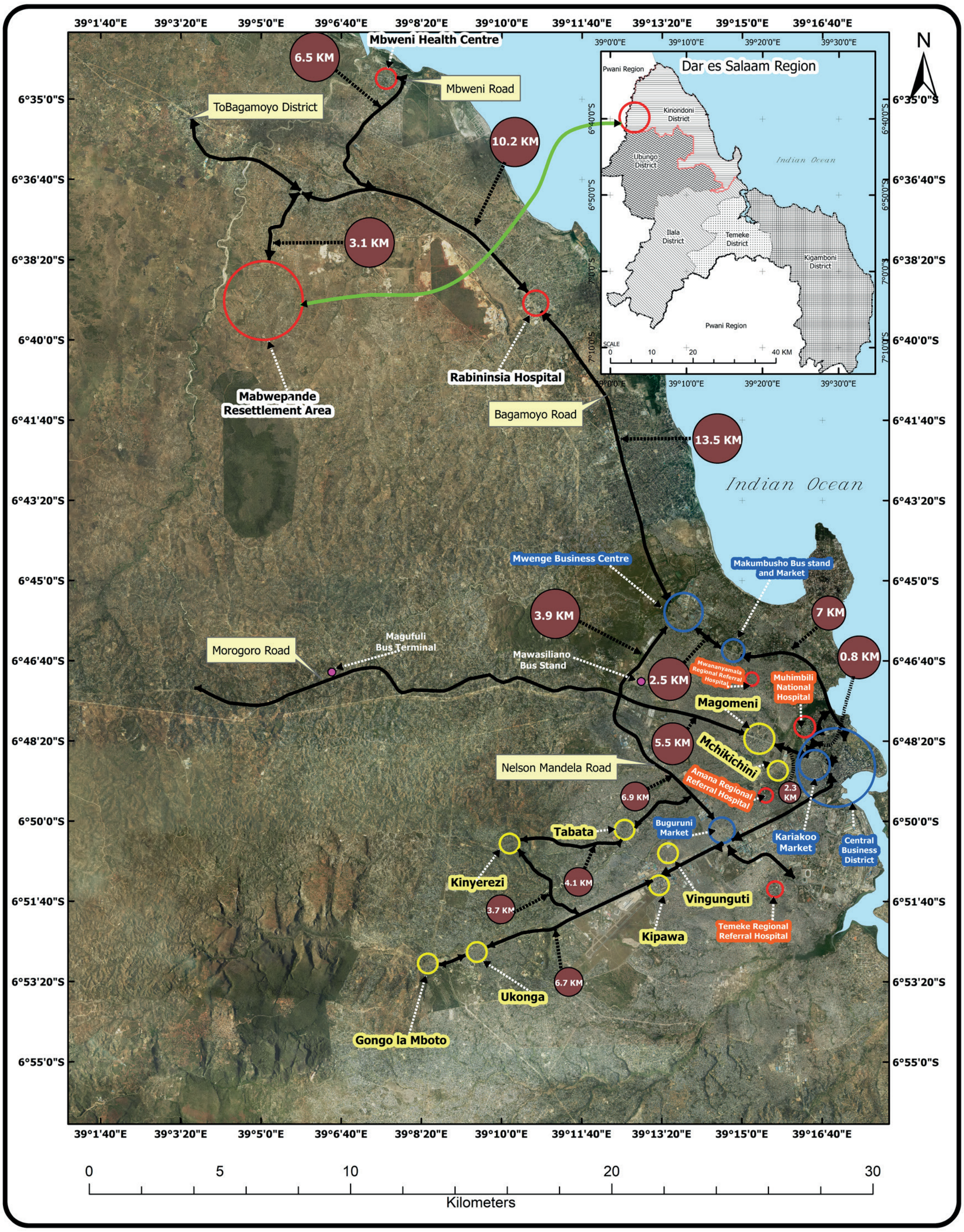

Fig. 3. Location of the resettlement site in relation to the displacement areas, the Central Business District and basic facilities

MATERIAL AND METHODS

The study used a structured questionnaire to conduct interviews with 176 households. For each household, data on livelihood assets were collected regarding the situation before and after the resettlement. Data from household interviews were triangulated with key informant interviews, focus group discussions, and non-participant observations of the physical aspects of household livelihoods. Three focus group discussions were held, one with men, another with women, and one with the youth, to assess their experiences concerning their livelihood situation in the resettled area.

Data was analyzed qualitatively as well as quantitatively. The quantitative analysis entailed the examination of data sets on the socio-economic status of the households, such as age structure, education, and income levels, using descriptive statistics, particularly measures of frequency. The qualitative analysis entailed retrieving and clustering information from focus group discussions, key informants, and household interviews. The qualitative analysis also included extracting direct quotes to illustrate the respondents' responses and contexts. Finally, the study draws analytical conclusions by comparing the study's empirical findings to the existing literature from the previous studies.

RESULTS AND DISCUSSION

The following sections give an analysis of the livelihood resilience of flood-resettled households. The analysis includes a discussion of the households' livelihood assets in the resettled site compared to the situation in the original settlements.

Household Livelihood Assets

The resettled households' livelihoods are characterized by large household sizes and low education levels. According to the household interviews, 55% of the households have 5 to 6 members, 35% have more than seven members, and the remaining 10% have less than five members. In addition, the education level of resettled households was found to be generally low, with 77 percent of the household heads obtaining basic education, i.e., primary, 12 percent obtaining secondary education, and 8 percent obtaining no formal education (Figure 4). Although human assets in terms of household size and education levels were not affected by the resettlement, the assets limited the households' ability to absorb the shock resulting from the resettlement and negatively impacted their livelihoods.

According to the study, most household economic activity was petty trading, followed by employment in the private sector, mechanics, employment in the government sector, masonry, and related works. Food vending, tailoring, quarrying, and general labor were others. Farming, primarily vegetable growing along river valleys, was proportionally lower, and few, i.e., one percent, had no economic activity. Petty trading also predominates the situation after resettlement, accounting for 44% of the household heads, while the percentage of household heads with no economic activity increased (Figure 5).

Most trading activities in the displaced areas occurred in the city centre and at open markets nearby. The resettled area's location in the city's peri-urban area has limited households' access to business and commercial centres, limiting their economic activities. According to the study, 41 percent of the households interviewed chose to conduct their income-generating activities at their homesteads and other locations within the resettled areas, causing businesses to suffer from low sales due to a lack of customers. Those who continued conducting their trading activities in the original areas (59% of the households) had to travel long distances, approximately 35 kilometres, to reach the business location (see Figure 3).

Relapsed economic assets due to location disadvantages

The analysis of household income reveals a decrease, with most households earning less after resettlement than before (Figure 6). Figure 6 depicts an increase in the percentage of households with lower monthly-income levels (below Tanzania Shillings (TZS) 50,000 to TZS 200,000) and a decrease in the percentage of households

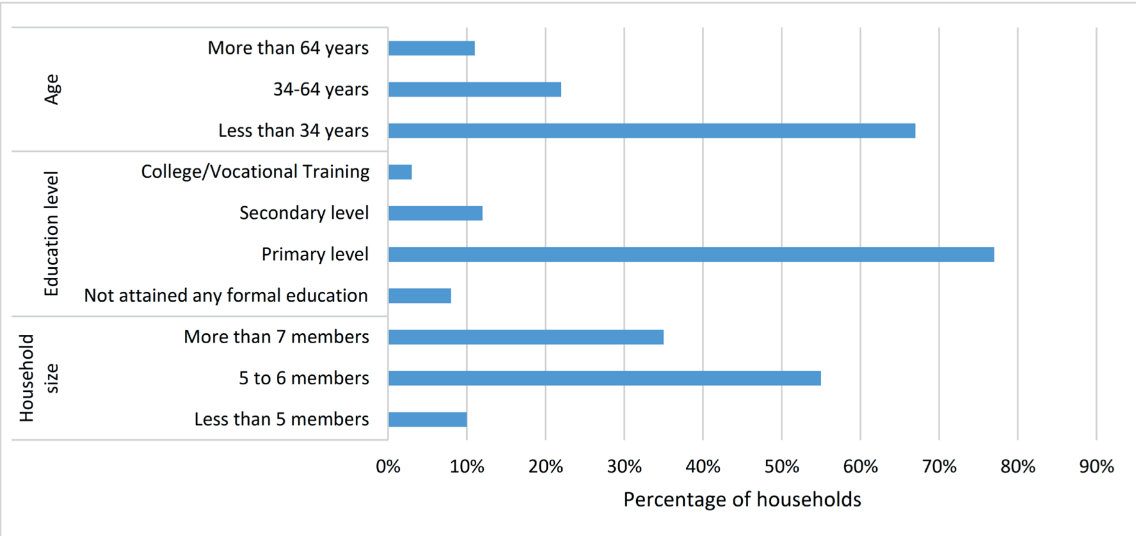

Fig. 4. Household size, education level, and the age structure

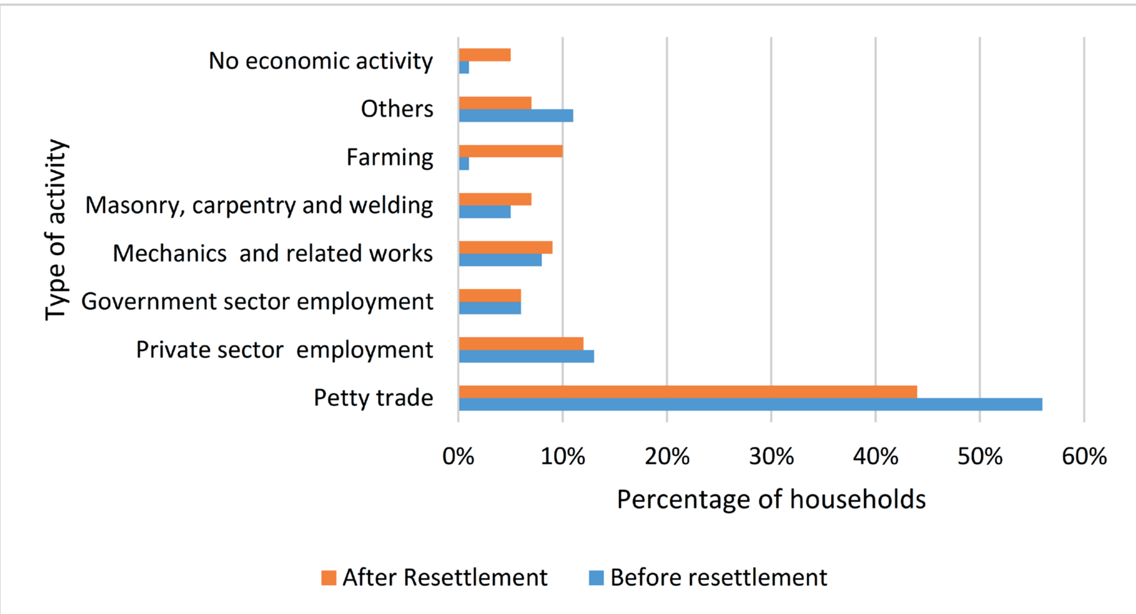

Fig. 5. Household economic activities before and after resettlement

with higher monthly income levels (from TZS 500,000 to above TZS 1,000,000)[1] after resettlement compared to the situation before resettlement.

A focus group discussion with men at the resettlement site revealed that the displacement significantly impacted income generation activities in the new location. While the majority of the households rely on petty trading as a major source of income, the resettlement site's location far from the Central Business District restricts access to trading opportunities within the commercial centres, resulting in a decrease in household income. During an in-depth interview, a resettled woman stated that the new site provides no opportunity for trading activities compared to the former areas, lamenting that she has lost half of her business capital due to a lack of customers in the resettlement area. As a result, the resettlement site's remote location from the business and commercial centres limits households' access to economic opportunities. The findings suggest that locating settlements near business opportunities provides economies of scale for income generation for those who rely on informal employment, such as petty trading. Satiroglu and Narae (2015) contend that a scale of economy that provides abundant livelihood opportunities is the primary reason why displaced people who have returned from the resettlement sites strive to stay in urban centres such as densely populated settlements. The findings suggest that while relocating flood-affected households may address the issue of flood exposure, it may also deprive households of economic opportunities. The findings support the findings of Yong et al. (2017) that resettling people in remote areas reduces resettlers' livelihood resilience.

Destruction of social capital assets

Displacement and resettlement into a new settlement weakened the household's social networks and ties. The separation of household members after the resettlement resulted in diminished social capital. According to the study, 22 percent of households interviewed had members who returned to live near their original settlements for various reasons, including access to schools and income-generating activities. Furthermore, the resettlement impacted networks and ties associated with income-generating activities. One of the male respondents, a masonry worker, stated that his income-generating activities depended on the networks he had established within the former area and its surroundings. He could obtain new clients for his business through social connections, which are scarce in the resettlement area.

Furthermore, findings from focus group discussions and key informant interviews shed light on the disruption of community cohesiveness among the resettled households. According to the women's focus group discussion held at the resettlement site, the diversity of the resettled households' settlements of origin made mobilizing community participation for joint initiatives challenging. An in-depth interview with the Sub Ward Chairperson revealed that a Non-Government Organisation (NGO) that intended to assist resettled households in rebuilding their livelihoods failed due to their unwillingness to cooperate in forming groups due to a lack thereof of trust among them. The findings are consistent with other studies on development-induced resettlement that have confirmed the disintegration of social networks following resettlement (Yntiso 2008; Lupala and John 2012; Singh 2020; Mandishekwa and Mutenheri 2020).

High transportation costs due to increased distance to services

Resettlement resulted in long distances to workplaces and basic infrastructure facilities. While households had close access to health and education facilities and job opportunities in the original settlements, those facilities must be reached over long distances in the resettlement area. For example, whereas a health centre is only 2 kilometres from the settlement, households must travel 35 kilometres to reach high-level health care facilities near the city centre. Similarly, most educational facilities are located up to 25 kilometres away from the resettled settlement. As a result, 30% of the households interviewed sent their children to live with relatives closer to their schools.

Access to public transport is also limited in the resettled settlement compared to the situation in the origin settlements. The resettlement area lacks a public transportation system that connects the settlement to the surrounding areas. As a result, households rely on private transportation, primarily motorcycles, to access various services, including public transportation. The

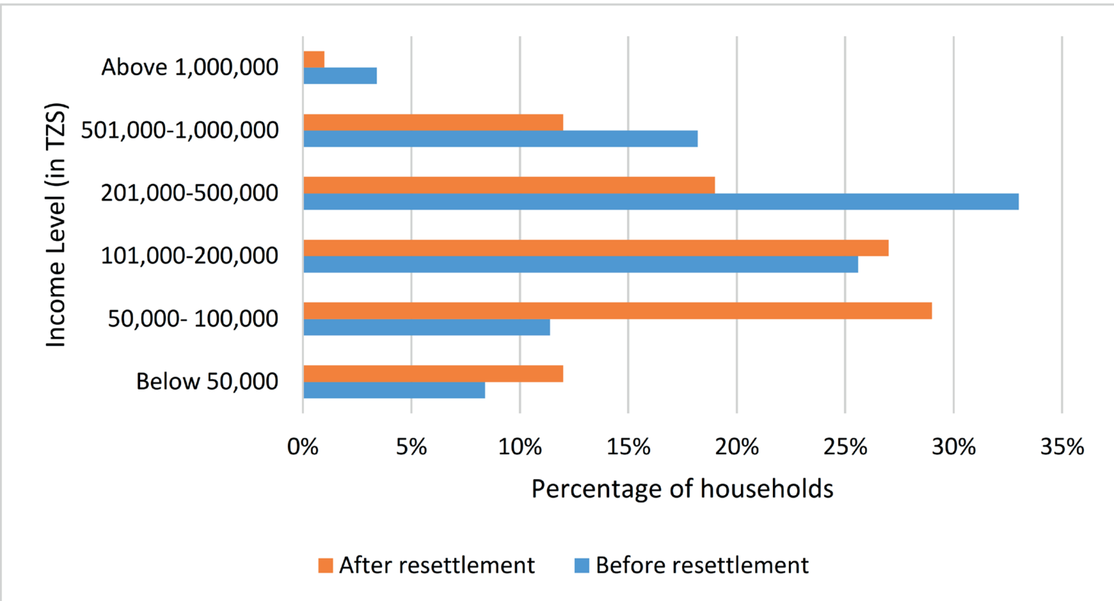

Fig. 6. Monthly household income levels before and after the resettlement

[1] 1 TZS= 0.0042USD (the 2018 exchange rate)

resettled households incur high transportation costs due to an average daily traveling distance of 3 to 5 kilometers in accessing public transportation services, commonly known as daladala. According to the study, it costs at least TZS 2,000 (~US$1) to get to a public transportation facility (bus stop) located approximately 5 kilometres from the resettlement site's centre. The findings are similar to those of Nikuze et al. (2019), who observed that resettlement increased the distance between basic facilities and services, particularly public transportation services. While Nikuze et al. (2019) reported that the resettled households had reasonable access to health and education facilities, this study found out that resettled households had to travel long distances to access both health and education facilities. The preceding suggests that the resettlement site and its proximity to basic infrastructure facilities are essential and may limit resettled households' ability to develop resilient livelihoods.

Social distrust among household members

The increased travel distances have increased transportation costs and altered household travel patterns and behavior. The insights gained from focus group discussions assisted us in better understanding the behavior and social relationships of resettled households. Due to long distances and increased transportation costs in the resettled area, some households, particularly men, frequently stay at their workplaces for a few days or weeks to save money on transportation, according to the study findings. On the other hand, women reported a lack of trust in their husbands when they stayed away from home. A focus group discussion with women revealed that some marriages have become less intact as husbands take advantage of the opportunity to stay outside their homes to engage in cheating. One of the women explained that the husband comes home once a week, sometimes twice a month, to cut transportation costs to work, which creates opportunities for cheating in marriages. Previous scholars, such as Gonzalez and Simon (2008) and Piggott-McKeller et al. (2020), have argued that resettlement can lead to social distrust among community members, particularly when resettled households come from different communities or are resettled in an existing community resulting in a heterogeneous society. However, this study discovered that distrust could occur within a homogenous household, particularly when circumstances entice cheating. The challenge of social distrust among spouses or household members, as opposed to the social distrust between households or community members, reveals a new challenge due to resettlement.

Increased vulnerability of the vulnerable groups

Long walking distances to access schools and health care facilities have increased the vulnerability of vulnerable groups, particularly girls, women, and the youth. Missed classes and school dropouts are common due to the inability of the majority of households to pay for motorized transportation for their school-aged children. A focus group discussion with the youth revealed that most students attend school twice or thrice a week, with others attending only once per week. Poor school attendance leads to school dropouts, as the youth attested during the focus group discussion at the resettlement site. According to the findings, children who drop out of school engage in immoral practices such as smuggling, sexual conduct at early ages, street begging, early marriages, and stealing. According to an elderly respondent, the long distance to school has caused many children to drop out, female students to become pregnant, and others to marry young. In contrast, male students engage in drug abuse and immoral behaviour like robbery.

The study also discovered that the long distances to schools make girls even more vulnerable in the resettled area. Aside from the school dropouts and child pregnancies, the study discovered a case of a female student raped on her way to school. One of the male respondents, the victimised girl's father, bitterly narrated that his daughter was raped on her way to school one morning because she had to walk early to make it in time. The respondent expounded that he reported the incident to the police station and attempted to follow up on it but gave up due to financial constraints. Worse, he pursued the girl from the family, accusing her of causing him double costs: first, the loss of the school fees, and second, the costs of following up the case. The preceding illustrates how vulnerable groups have become even more vulnerable due to resettlement.

Social stress due to loss of privacy

Households in the resettled area experience social stress due to the loss of social intimacy caused by loss of privacy. According to the focus group discussions with men and women, some households are denied privacy to social lives after resettlement. The resettled household structure[2], which depicts the traditional extended families in the African context, poses a challenge in using the limited spaces provided by the one or two-bedroom houses. A female respondent explained that the issue of intimate relationships is a challenge for spouses because the spaces are insufficient to facilitate lovemaking due to sharing the limited space with children and other family members. As a result, lack of space is one of the sources of stress for households struggling to meet their social needs. The lack of privacy observed in this study differs from what was observed by (Nikuze et al. 2019), who found that resettlement caused a lack of privacy due to the design and nature of post-resettlement houses, which allowed households to see what was going on in the neighbouring household. However, Diwakar and Peter (2016) noted related findings of children exposed to their parents' sexual activities due to a lack of space and privacy following involuntary resettlement. The findings support Scudder and Colson's (1982) theory of resettlement, which states that relocation is a stressful experience, whether voluntary or involuntary and that the early stages of the process are the most stressful.

CONCLUSION

This paper investigated the resettlement of flood-affected households and the resulting livelihood conditions. It emphasizes that households in flood-prone areas have poor livelihood assets, such as large household sizes, low education levels, and self-employment primarily in the informal sector. According to the study, displacement and resettlement of flood-affected people from high-risk areas may be considered an appropriate long-term life-saving strategy. However, the ability to sustain life through resettlement does not guarantee livelihood resilience.

[2] The average household was 4 to 6 people, with the majority of households consisting of a father, mother, children, and relatives of both sexes. In-laws were present in some households.

While the resettled households are free from flood hazards, the empirical findings show that the resettlement resulted in several non-flood but place-related challenges, including the inability to access income-generating activities. Other challenges include reduced household income, high costs in accessing public services and facilities, and weakened social capital assets. As a result, the resettled households have been liberated from flood vulnerability but are struggling to build their livelihoods. The findings support the argument that resettlement is a complex phenomenon with various negative socio-economic consequences on the livelihoods of the resettled households.

The study found that the socio-economic characteristics of displaced households influence their post-resettlement livelihood situation. Large family sizes, low education levels, and self-employment primarily in trading activities limit households' ability to employ alternative livelihood strategies in the resettlement area. The study also concludes that a mismatch between household livelihood needs and the resettlement area negatively impacts resettled households. Poor access to the areas for income-generating activities, such as the Central Business District, prevents poor households from earning an income. Policymakers need to pay attention to understanding the displaced households' socio-economic characteristics to optimize the protection of their socio-economic assets and thus improve their livelihood sustainability. The government also needs to understand human choice during resettlement and provide options for resettlement areas for the affected population to make decisions based on their livelihood situations.

The findings also revealed that women and the young, particularly school-age children, are the most vulnerable following resettlement due to challenges in sustaining their livelihoods. School dropouts, early marriages, engagement in smuggling, and other immoral behaviors necessitate reconsidering their needs in the resettlement programs now and in the future. In addition to focusing on physical relocation as a strategy for disaster mitigation, future disaster-led resettlements should consider incorporating support projects for vulnerable groups such as low-income and those employed in the informal sector, women, and youth. ■

REFERENCES

Arnall A. (2019). Resettlement as climate change adaptation: what can be learned from state-led relocation in rural Africa and Asia? Climate and Development, 11(3), 253-263.

Arnall A., Thomas D.S., Twyman C., & Liverman D. (2013). Flooding, resettlement, and change in livelihoods: evidence from rural Mozambique. Disasters, 37(3), 468-488.

Black R., Arnell N.W., Adger W.N., Thomas D., & Geddes A. (2013). Migration, immobility and displacement outcomes following extreme events. Environmental Science & Policy, 27, S32-S43.

Bronen R. (2015). Climate-induced community relocations: using integrated social-ecological assessments to foster adaptation and resilience. Ecology and Society, 20(3), DOI: 10.5751/ES-07801-200336.

Bronen R., & Chapin F.S. (2013). Adaptive governance and institutional strategies for climate-induced community relocations in Alaska. Proceedings of the National Academy of Sciences, 110(23), 9320-9325, DOI:10.1073/pnas.1210508110.

Carney D. (1998). Sustainable Rural Livelihoods: What contribution can we make? London: Department for International Development.

Chambers R. & Conway R. (1992). Sustainable Rural Livelihoods: Practical Concepts for the 21st Century. IDS Discussion Paper, 296, 1-29. Available at: https://www.ids.ac.uk/publications/sustainable-rural-livelihoods-practical-concepts-for-the-21st-century/. [Accessed 10.04.2018].

Cernea M. (1997). The Risks and Reconstruction Model for Resettling Displaced Populations', The World Bank: Environment Department. Washington DC.

Cernea M.M. (2000). Risks, safeguards and reconstruction: A model for population displacement and resettlement. Economic and Political Weekly, 3659-3678.

Correa E., Ramirez F., & Sanahuja H. (2011). Populations at Risk of Disaster: A Resettlement Guide. World Bank, Washington, DC. Available at: https://openknowledge.worldbank.org/handle/10986/27383 License: CC BY 3.0 IGO. [Accessed 24.8. 2018].

De Wet C. (2008). Reconsidering displacement in southern Africa. Anthropology Southern Africa, 31(3-4), 114-122.

Diwakar D., & Peter V. (2016). Resettlement of Urban Poor in Chennai, Tamil Nadu: Concerns in R&R Policy and Urban Housing Programme. Journal of Land and Rural Studies, 4(1), 97-110.

Douglas I., Alam K., Maghenda M., Mcdonnell Y., McLean L., & Campbell J. (2008). Unjust waters: climate change, flooding and the urban poor in Africa. Environment and Urbanization, 20 (1), 187-205.

Erman A. E., Tariverdi M., Obolensky M.A.B., Chen X., Vincent R.C., Malgioglio S., ... & Yoshida N. (2019). Wading out the storm: The role of poverty in exposure, vulnerability and resilience to floods in Dar Es Salaam. World Bank Policy Research Working Paper, (8976). Available at: http://documents1.worldbank.org/curated/en/788241565625141093/pdf/Wad ing-Out-the-Storm-The-Role-of-Poverty-in-Exposure-Vulnerability-and-Resilience-to Floods-in-Dar-Es-Salaam.pd. [Accessed 3.12.2021].

Gong Y., Yao K., Zhang R., Liu B., & Wang F. (2021). Rethinking livelihood resilience after development-induced displacement and resettlement: a case study of Qianping Reservoir. International Journal of Water Resources Development, 37(5), 841-864, DOI: 10.1080/07900627.2020.1790340.

Gonzalez C., & Simon J., (2008). All the glitters is not gold: Resettlement, vulnerability and social exclusion in the Pehuenche Community Ayin Mapu, Chile. American Behavioural Scientist, 51, 1774-1789.

Guo X., & Kapucu N. (2018). Examining the impacts of disaster resettlement from a livelihood perspective: A case study of Qinling Mountains, China. Disasters, 42(2), 251-274. DOI: 10.1111/disa.12242.

Haile T., Kusters K. & Wagesho N. (2013). Loss and damage from flooding in the Gambela region, Ethiopia, International Journalof Global Warming, 5(4), 483-497.

Holloway, A., Chasi, V., de Waal J., Drimie, S., Fortune, G., Mafuleka, G., Morojele, M., Penicela, N. B., Randrianalijaona, M., Vogel, C., & Zweig, P. (2013). Humanitarian Trends in Southern Africa: Challenges and Opportunities. Regional Interagency Standing Committee, Southern Africa. Rome, FAO. Available at: http://reliefwe b.int/ sites/reliefweb.int/files/resources/Final_RIASCO_22July2013.pdf. [Accessed 16.6.2019]

Internal Displacement Monitoring Centre, Norwegian Refugee Council, (IDMC). (2015). Global Estimates 2015 – People Displaced by Disaster, Geneva: IDMC, Norwegian Refugee Council. Available at: http://www.internal-displacement.org/assets/library/Media/201507-globalEstimates-2015/20150713-global-estimates-2015-en-v1.pdf. [12.10.2018].

Internal Displacement Monitoring Centre, Norwegian Refugee Council, (IDMC). (2019). Global Report on Internal Displacement 2019. IDMC, Norwegian Refugee Council. Available at: https://www.internal-displacement.org/global-report/grid2019/.Accessed January 2020.

Intergovernmental Panel on Climate Change (IPCC), 2012. In: Field CB, Barros V, Stocker TF, Qin D, Dokken DJ, Ebi KL, Mastrandrea MD, Mach KJ, Plattner G-K, Allen SK, Tignor M, Midgley PM (eds) Managing the risks of extreme events and disasters to advance climate change adaptation. A special report of working groups I and II of the Intergovernmental Panel on Climate Change (IPCC). Cambridge University Press, Cambridge, UK/New York, 582.

John R. (2020). Flooding in Informal Settlements: Potentials and Limits for Household Adaptation in Dar es Salaam City, Tanzania. American Journal of Climate Change, 9(02), 68.

John R., Jean-Baptiste N., & Kabisch, S. (2014). Vulnerability Assessment of Urban Populations in Africa: the case of Dar es Salaam-Tanzania. In: Edgerton, E., Romice, O., and Thwaites, K., (Eds). Bridging the Boundaries: Human Experience in the Natural and Built Environment and Implication for Research, Policy and Practice, 233-245.Hogrefe Publishing.

Jones L., & Tanner T. (2015). Measuring subjective resilience: using people's perceptions to quantify household resilience, Overseas Development Institute Working Paper 423, DOI: 10.13140/RG.2.1.2438.1289.

Kebede A. S., & Nicholls R. J. (2011). Population and assets exposure to coastal flooding in Dar es Salaam (Tanzania): vulnerability to climate extremes. Global Climate Adaptation Partnership (GCAP).

Kebede A.S., & Nicholls R.J. (2012). Exposure and vulnerability to climate extremes: population and asset exposure to coastal flooding in Dar es Salaam, Tanzania. Regional Environmental Change, 12(1), 81-94.

Kita S.M. (2017). Urban vulnerability, disaster risk reduction and resettlement in Mzuzu city, Malawi. International journal of disaster risk reduction, 22, 158-166.

Koenig D. (2006). Enhancing Local Development in Development-induced Displacement and Resettlement Projects. In De Wet C. (Ed.), Development-Induced Displacement, Problems, Policies, and people (105-140). Berghahn Books.

Li S., & Song Y. (2009). Redevelopment, displacement, housing conditions, and residential satisfaction: a study of Shanghai. Environment & Planning A, 41(1), 1090-1109, DOI: 10.1068/a4168.

Lipset D. (2013). The new state of nature: Rising sea-levels, climate justice, and community-based adaptation in Papua New Guinea (2003–2011). Conservation and Society, 11(2), 144-158.

Lupala J., & John R. (2012). Tracking the Process and Livelihoods of Kurasini Settlement Displacees in Dar es Salaam City, Tanzania. Rural Planning Journal, 14, 80-209.

Maldonado J.K., Shearer C., Bronen R., Peterson K., & Lazrus H. (2013). The impact of climate change on tribal communities in the US: displacement, relocation, and human rights. In Climate change and indigenous peoples in the United States (pp. 93-106). Springer, Cham.

Mandishekwa R. & Mutenheri E. (2020). Mining-Induced Displacement and Resettlement: An analytical Review. Ghana Journal of Development Studies, 17(1), 114-140.

Mteki N., Murayama, T., & Nishikizawa S. (2017). Social impacts induced by a development project in Tanzania: A case of airport expansion. Impact Assessment and Project Appraisal, 35(4), 272-283.

Nikuze A., Sliuzas R., Flacke J., & Maarseveen M. (2019). Livelihood impacts of displacement and resettlement on informal households-A case study from Kigali Rwanda. Habitat International, 86, 38-47.

Pan-African START Secretariat, International START Secretariat, Tanzania Meteorological Agency and Ardhi University, (2011). Urban Poverty and Climate Change in Dar es Salaam, Tanzania: A Case Study. Available at: https://start.org/publication/urban-poverty-and-climate-change-in-dar-es-salaam-tanzania-a-case-study/. [Accessed 15.2.2021].

Patel S., Sliuzas R., & Mathur N. (2015). The risk of impoverishment in urban development-induced displacement and resettlement in Ahmedabad. Environment and Urbanization, 27(1), 231-256, DOI: 10.1177/0956247815569128.

Perera J. (Ed.). (2014). Lose to gain: is involuntary resettlement a development opportunity? Asian Development Bank.

Picarelli N., Jaupart P., & Chen Y. (2017). Cholera in times of floods Salaam. International Growth Centre.

Piggott-McKellar A.E., Pearson J., McNamara K.E., & Nunn P.D. (2020). A livelihood analysis of resettlement outcomes: Lessons for climate-induced relocations. Ambio, 49(9), 1474-1489, DOI: 10.1007/s13280-019-01289-5.

Quandt A. (2018). Measuring livelihood resilience: The household livelihood resilience approach (HLRA). World Development, 107, 253-263.

Raheem U. & Olorunfemi F. (2013). Urban Vulnerability and Adaptation to Extreme Weather Events: A Case Study of Rainstorm Victims in Ilorin, Nigeria. Geography Environment, Sustainability, 6(2), 80-93, DOI: 10.24057/2071-9388-2013-6-2-80-93.

Raleigh C., & Jordan L. (2010). Climate change and migration: emerging patterns in the developing world. Social dimensions of climate change: Equity and vulnerability in a warming world, 103-131.

Reason C. & Keibel A. (2004). Tropical Cyclone Eline and its unusual penetration and impacts over the southern Africa mainland. Weather and Forecasting, 12, 789-805.

Rew A., Fisher E., & Pandey B. (2006). Policy practices in development-induced displacement and rehabilitation. Development-induced displacement: Problems, policies and people, 18, 38-70.

Sakijege T., Lupala J., & Sheuya S. (2012). Flooding, flood risks and coping strategies in urban informal residential areas: The case of Keko Machungwa, Dar es Salaam, Tanzania. Jàmbá: Journal of Disaster Risk Studies, 4(1), 1-10.

Sakijege T., Sartohadi J., Marfai M.A., Kassenga G.R., & Kasala S.E. (2014). Assessment of adaptation strategies to flooding: A comparative study between informal settlements of Keko Machungwa in Dar es Salaam, Tanzania and Sangkrah in Surakarta, Indonesia.

Satiroglu I. & Narae C. (2015). Development-Induced Displacement and Resettlement: New perspectives on persisting problems. Routldge, New York.

Scudder T. & Colson E. (1982). From Welfare to Development: A Conceptual Framework for the Analysis of Dislocated People. In Hansen A. and A. Oliver-Smith (Eds.) Involuntary Migration and Resettlement, 267-287. CO, Boulder: Westview Press.

Sikka G. (2020). Moving Beyond Economic Analysis: Assessing the Socio-Cultural Impacts of Displacement and Resettlement by Sardar Sarovar Project, India. Geography, Environment, Sustainability, 13(3), 90-101, DOI: 10.24057/2071-9388-2019-165.

Singh K.A. (2020) Development Induced Displacement: Issues and Indian Experiences, Journal of the Anthropological Survey of India, 69 (2), 276-289.

Schmidt-Soltau K., & Brockington D. (2007). Protected areas and resettlement: What scope for voluntary relocation? World Development, 35(12), 2182-2202.

Tadgell A., Doberste in B., & Mortsch L. (2018). Principles for climate-related resettlement of informal settlements in less developed nations: a review of resettlement literature and institutional guidelines. Climate & Development, 10(2), 102-115, DOI: 10.1080/17565529.2017.1291401.

Tanner T., Lewis D., Wrathall D., Bronen R., Cradock-Henry N., Huq S., ... & Thomalla F. (2015). Livelihood resilience in the face of climate change. Nature Climate Change, 5(1), 23-26, DOI: 10.1038/nclimate243.

UNISDR. (2009). UNISDR Terminology on Disaster Risk Reduction. Geneva, Switzerland: United Nation.

UNISDR. (2012). Number of climate-related disasters, 1980–2011 – Graphic. Available at http://www.preventionweb.net/english/professional/statistics 2013. [Accessed 12.06.2018].

UNISDR. (2015). Global Assessment Report on Disaster Risks Reduction. Making Development Sustainable; The future of Disaster Risk Reduction. United Nations. Available at https://www.unisdr.org/we/inform/gar. [Accessed 12.06.2018].

United Nations Environment Programme (UNEP). (2012). Early warning systems: a state-of-the-art analysis and future directions. Division of Early Warning and Assessment (DEWA), UNEP, Nairobi.

United Republic of Tanzania (URT). (2013). The United Republic of Tanzania 2012 Population and Housing Census: Population Distribution by Administrative Areas, National Bureau of Statistics, Dar es Salaam.

Vanclay F. (2017). Project-induced displacement and resettlement: from impoverishment risks to an opportunity for development? Impact Assessment and Project Appraisal, 35(1), 3-21, DOI: 10.1080/14615517.2017.1278671.

Vickery J. (2017). Urban Resettlement in Colombo from a Wellbeing Perspective: Does Development- Forced Resettlement Lead to Improved Wellbeing? Journal of Refugee Studies, 30(4), 554-579, DOI: 10.1093/tropej/fmw080.

Wisner B., Gaillard C., & Kelman I. (2012). Handbook of Hazard and disaster reduction Management, Routledge, NewYork.

World Bank. (2004). Involuntary Resettlement Sourcebook: Planning and Implementation in Development Projects. The World Bank. Available at: http://hdl.handle.net/10986/14914. [25.10.2018].

Yntiso G. (2008). Urban Development and Displacement in Addis Ababa: The Impact of Resettlement Projects on Low-Income Households. Eastern Africa Social Science Review, 24(2), 53-77.

Yong C., Yan T., & Yong L. (2017). Post-disaster resettlement and livelihood vulnerability in rural China, Disaster Prevention and Management: An International Journal, 26(1), 65-78, DOI: 10.1108/DPM-07-2016-0130.

RESEARCH PAPER

VERTICAL AND SPATIAL DISTRIBUTION OF MAJOR AND TRACE ELEMENTS IN SOIL CATENA AT THE CENTRAL FOREST STATE NATURE BIOSPHERE RESERVE (SE VALDAI HILLS, RUSSIA)

Polina R. Enchilik[1*], Ivan N. Semenkov[1]
[1]Lomonosov Moscow State University Faculty of Geography, GSP-1, Leninskie Gory, sector A, 17, 119234, Moscow, Russia
*Corresponding author: polimail@inbox.ru
Received: April 2nd, 2021 / Accepted: August 8th, 2022 / Published: October 01st, 2022
https://DOI-10.24057/2071-9388-2022-038

ABSTRACT. In this study, we discussed relationship between the vertical and spatial differentiation of 14 chemical elements (total content and three mobile fractions extracted by NH_4Ac, NH_4Ac with 1% EDTA and 1M HNO_3) and the environmental factors in background Retisols and Stagnosols within a soil catena. In the A soil horizon, the extractability of elements decreased in the series Cd, Mn, Pb> Co, Ni, Cu, Fe> Zn, Bi, As> U, Cr, Mo> Sb. In the O and A horizons, total and exchangeable Mn and Zn were uptaken by plants. In the A horizon, total Bi, Cd, Pb, Sb, Mo, exchangeable As, Bi, Cd, Co, Ni, Mo, as well as As, Cd, Cu, Pb, Zn, Sb bound with Fe-Mn (hydr)oxides were sorbed by soil organic matter; Cr, Fe, Mn formed the organic complexes. In the C horizon, Cd, Fe, Mn, Sb complexes co-precipitated with carbonates. In the Bt horizon, total Cr, Cu, exchangeable Cu, Ni, as well as Cr and U bound with Fe-Mn (hydr)oxides migrated due to the lessivage. On the toeslope's biogeochemical barrier, exchangeable Zn, Mo bound with complexes, As, Bi, and Fe bound with Fe-Mn (hydr)oxides were accumulated. In the lower part of the catena, peat accumulated the exchangeable compounds of As, Bi, Cr, Fe, Mo, Pb, U. The spatial differentiation of elements became less contrasting from the O and A horizons to the E, B and C horizons.

KEYWORDS: heavy metals and metalloids; fractionation; geochemical barrier; mobility; environmental assessment; protected area

CITATION: Enchilik P. R., Semenkov I. N. (2022). Vertical And Spatial Distribution Of Major And Trace Elements In Soil Catena At The Central Forest State Nature Biosphere Reserve (Se Valdai Hills, Russia). Geography, Environment, Sustainability, 3(15), 99-119
https://DOI-10.24057/2071-9388-2022-038

ACKNOWLEDGEMENTS: Field works were financially supported by the RGS-RFBR project No 04/2018/. Data processing was financially supported by the RSF project No 19-77-30004. Interpretation of the results was supported under the Interdisciplinary Scientific and Educational School of the Lomonosov Moscow State University "Future Planet and Global Environmental Change". Investigational analyses were carried out at the Faculty of Geography of the MSU.

Conflict of interests: The authors reported no potential conflict of interest.

INTRODUCTION

Vertical and spatial geochemical differentiation (structure) of landscapes depending on the vertical and lateral flows of compounds in catenas is described using different geochemical ratios. The distribution of substances in landscapes could be explained using the concept of geochemical barriers, i.e. areas where the mobility of chemical elements sharply decreases over a short distance, leading to their accumulation in various forms (Kasimov, Perelman 1992). The vertical geochemical differentiation of landscapes depends on the location of geochemical barriers in the soil horizons. These are biogeochemical, sorption, gley, and, more rarely, carbonate barriers in forest soils (Kasimov, Perelman 1992). The spatial geochemical differentiation of landscapes depends on the contrasting changes of the environments for lateral flows of substances in catenas (Kasimov et al. 2012). A spatial sorption-biogeochemical barrier is the most common in taiga catenas (Avessalomova and Mikliayeva 1997; Samonova et al. 2011; Semenkov et al. 2016; 2019). Coupled analysis of the vertical and spatial distribution of elements depending on the properties and environmental factors depicts the migration ability of elements (Kasimov and Gennadiev 2005).

When characterizing the conditions of migration and accumulation of heavy metals and metalloids (HMMs), the analysis of their total content is usually complemented by the fractionation, closely related to mobility which is often estimated in terms of extractability, i.e. the transition of compounds from soil to solution under the action of various reagents (Burachevskaya et al. 2020; Shao et al. 2020; Sungur et al. 2021). The extracted fractions of HMMs are referred to as F1, F2, F3 in order of their recovery from the solid phase, i.e. decreasing extractability. Water-soluble and exchangeable fractions (F1) are considered to be the most mobile and available to plants (Minkina et al 2018). Fractions bound with complexes (F2), including carbonate and organomineral compounds, are the closest pool available to plants (Minkina et al 2018). Compounds bound with Fe and Mn (hydr)oxides (F3) are mobile only in a gley environment (with a low redox potential), as well as under the long-term exposure to acid exudates of plants. Silicates are usually considered as a residual fraction (F4), the compounds of which are unavailable to plants and move only as a result of mechanical migration (Minkina et al 2018). The ratio of F1+F2+F3 to the total content reflects the mobility of HMMs in soils (Yutong et al. 2016). The F-analysis is a modern approach to studying the migration of chemical elements in soils and landscapes (Bolan et al. 2014; Li et al. 2019; Reimann et al. 2018; Sosorova et al. 2012; Gronflaten, Steinnes 2005; Semenkov et al. 2016, 2019; Huang and Matzner 2007; Sosorova et al. 2012; Motuzova 2014; Popova 2010; Kosheleva et al. 2002, 2015).

As, Bi, Cd, Co, Cr, Cu, Fe, Mn, Mo, Ni, Pb, Sb, U and Zn selected for the study are from different groups of chemical elements (Fig. 1). They differ according to the preferred host phases (Goldshmidt 1924), migration features in surface waters (Krainov et al. 2012), and in plants (Perelman, Kasimov 1992).

Fractionation is commonly used to assess phytoavailability, so the most of HMMs occurrence patterns are studied within agricultural landscapes. Thus, the LUCAS (Land Use/Cover Area frame statistical Survey) and GEMAS (Geochemical Mapping of Agricultural Soil) European projects analyze the Ap-horizon (Reimann et al. 2018). In recent years in the international environmental programs of UNESCO and UNEP, special attention is paid to the assessment of background landscapes, which is mainly carried out in biosphere reserves. The studies of vertical differentiation of the element mobile fractions in Retisols show that F1 fractions of Zn, Mn, Fe (Sosorova et al. 2012), F2 fractions of Mn, Pb, Mo (Gronflaten, Steinnes 2005; Semenkov et al 2016) and F3 fractions of As, Mn, Zn, Co, Pb (Semenkov et al 2016) accumulate in the A-horizon at the biogeochemical barrier. F1 fractions of Ni, Pb, As, Cu (Huang and Matzner 2007; Sosorova et al. 2012; Motuzova 2014), F2 fractions of Zn (Popova 2010) accumulate at the sorption geochemical barrier in the A- and Bt-horizons and is depleted in the E-horizon. F3 fractions of Fe, Co, Cr, Cu (Tolpeshta and Sokolova 2010; Semenkov et al 2019; Adriano 2001) are removed from the topsoil. Their content increases monotonously in the subsoil horizons.

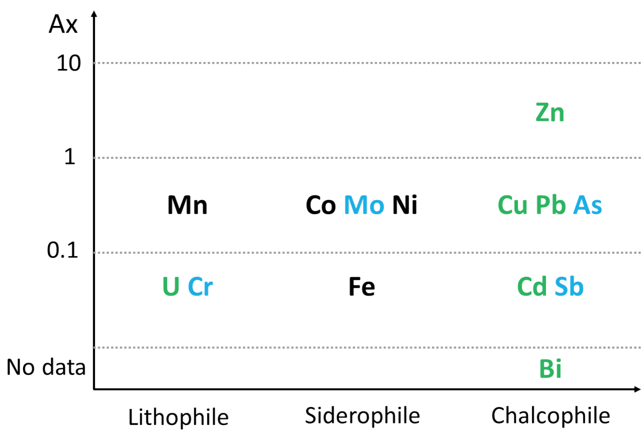

Fig. 1. Groups of chemical elements according to the main migration properties. The classification of Goldschmidt (1924) is displayed on the horizontal axis. The vertical axis shows the values of the Ax index (Perelman, Kasimov 1999) the ratio of the content of an element in the plant ash to the content in the parent rock. The prevailing form of migration in surface waters are shown in color (Kraynov et al. 2012): green – complex, black – cationic and complex, blue – anionic

Few studies of spatial differentiation of element mobile fractions in background taiga landscapes show that F1 fractions of Cu, Zn, Mn, Co and F2 fractions of Cu, Co accumulate in the upper parts of the catenas (Semenkov et al. 2019; Semenkov et al. 2016). The content of F1 fractions of Ni Co, Fe, F2 fractions of Fe, Zn, Ni, Sr, Pb and F3 fractions of Fe, Mn, Cr и Ni increases down the catena (Kosheleva et al. 2002; Semenkov et al. 2019; Semenkov et al. 2016).

Coupled studies of vertical and spatial differentiation of various compounds of HMMs, which are in demand for the environmental assessment, are uncommon. Such a coupled analysis of the chemical composition of landscape components of background ecosystems in ecological monitoring is necessary for solving theoretical and applied problems of landscape geochemistry.

The aim of the work is to determine the environmental factors affecting the vertical and spatial distribution of As, Bi, Cd, Co, Cr, Cu, Fe, Mn, Mo, Ni, Pb, Sb, U and Zn fractions and their mobility in background Retisols and Stagnosols within a soil catena located in the Central-Forest Natural Reserve with coniferous-broadleaved southern taiga landscapes. The following tasks were solved: 1 – the average concentration of chemical element mobile fractions were evaluated in background soils; 2 – chemical elements extractability and proportion of fractions were identified in each genetic horizons; 3 – geochemical barriers in soil horizons which affect the vertical distribution of chemical elements fractions in soils were determined; 4 – geochemical barriers in soil catena landscapes which affect the spatial distribution of chemical elements fractions were found.

MATERIALS AND METHODS

Object of study

The survey was taken within the Central Forest Nature Biosphere Reserve, (Fig. 2), located in the Valdai Hills. The background southern taiga landscapes of the Central Forest Nature Reserve were chosen, because here we can study the migration of HMMs between landscape components in natural conditions. Here, the structure, dynamics and functioning of the reference ecosystems of the southern taiga is monitored. Which makes it possible to study the background soil-geochemical structure of the catenas of the region in more detail. In addition, the data getting from the Central Forest Nature Reserve territory can be used for a comparative analysis of pollution levels in the Moscow region.

A 187 m long soil catena was studied on the southeastern gentle (<2°) slope in the southern part of the Central Forest Nature Reserve protected area. It begins at the top of a hill at 265 m a.s.l., crosses the slope and ends in a small gully on a flat terraced surface (Fig. 3). Despite small slopes and short distance, soils and vegetation change drastically (Fig. 3, Table 1) due to the repartitioning of surface water. The summit and the backslope of well-drained hill are covered by coniferous-broadleaved forest on Albic Stagnic Retisols with O–OA–E–BE–Bt–BC and O–OA–Ah–AE–E–BE–Bt–C horizons, respectively (Table A.1, Fig. 2). The coniferous-broadleaved forest on Endocalcaric Glossic Albic Gleyic Histic Stagnosols with O–H–A–Eg–Btg–Cg-horizons covers the footslope, too. The toeslope position of a bogged gully with a temporary stream is occupied by coniferous forest on Endocalcaric Glossic Albic Histic Stagnosols with O–H–Eg–Btg–Cg-horizons. The parent rocks are mantle loams underlain by carbonate moraine loams at a depth of 90-190 cm deposited during the Valday (MIS-2) glaciation

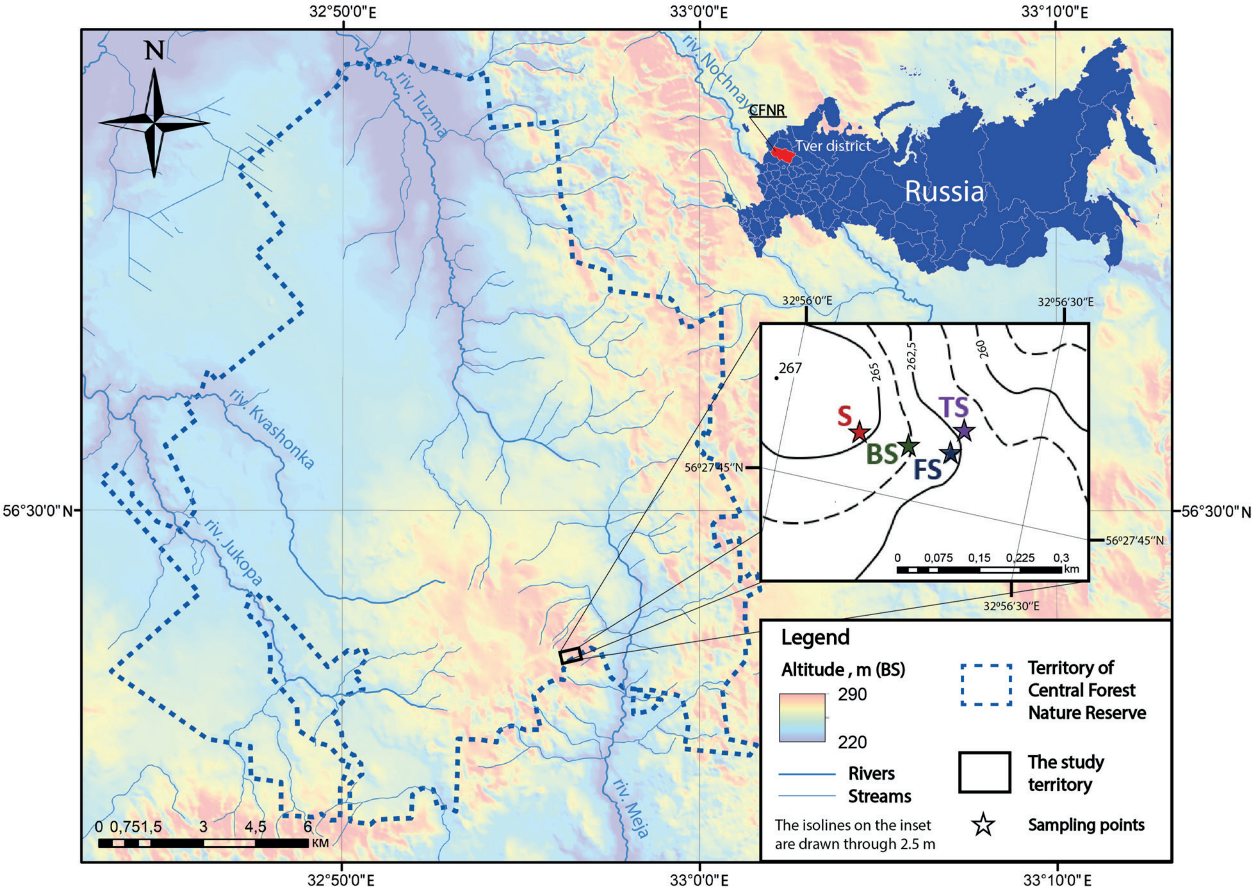

Fig. 2. Study object location. Toposequence in the Central Forest Nature Reserve; positions (hereinafter in the figures and tables): S – summit (interfluve); BS – backslope; FS – footslope, TS – toeslope

(Karavanova and Malinina 2009; Puzachenko et al. 2013). Due to the low water permeability of parent rocks, the toeslope position is waterlogged (Puzachenko et al. 2013). According to I.S. Urusevskaya (1990), the catena is a subordinate hydromorphic soddy-podzolic-marsh one. According to N.S. Kasimov et al. (2012), it is a typical monolithic watershed-marsh catena from the autonomous summit landscape to the superaqueous one at the bottom of a temporary watercourse with a relatively uniform composition of soil-forming rocks (binary: mantle loams on moraine).

Research methods

In the last decade of June 2017, 30 samples were taken from all soil horizons (Table 1). The pH value in suspension was measured on the Expert-pH pH-meter under static conditions (error ±0.07 pH units). The soil organic matter (SOM) content was determined by titrimetry using the bichromate oxidation method. The granulometric composition was analyzed on the Analysette 22 comfort laser granulometer (Fritsch, Germany) separating seven granulometric fractions (Kachinsky 1958): clay (<1 μm); fine, medium and coarse silt (1–5, 5–10, and 10–50 μm,

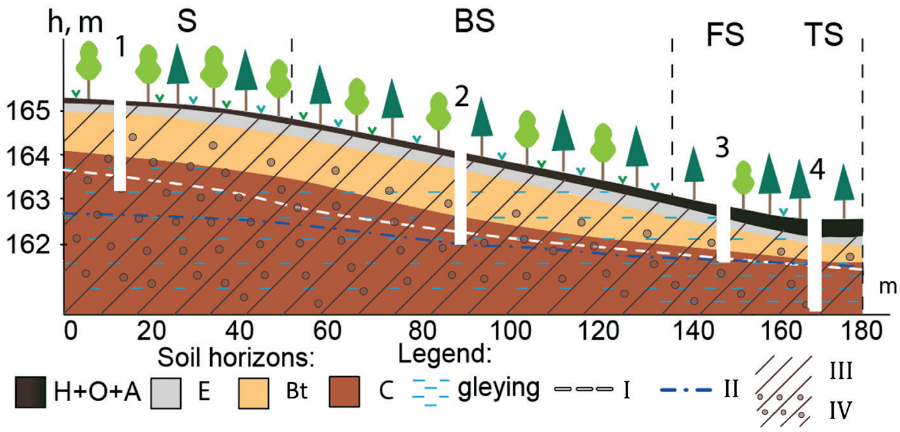

Fig. 3. Toposequence of soils: 1 – Summit position – Endocalcaric Albic Neocambic Stagnic Glossic Retisols under coniferous-deciduous forest; 2 – Backslope position – Endocalcaric Albic Neocambic Stagnic Glossic Retisols under coniferous-deciduous forest; 3 – Footslope position – Endocalcaric Glossic Albic Gleyic Histic Stagnosols under coniferous-deciduous forest и 4 – Toeslope position – Endocalcaric Glossic Albic Gleyic Histic Stagnosols under coniferous forest. Horizons: O – organic, H – histic, A – humus, E – albic, Bt – argic, C – parent material. I – upper boundary of effervescence with 10% HCl; II – ground water level, III – mantle like loams, IV – carbonate moraine deposits

respectively); fine, medium and coarse sand (50–250, 250–500 and 500–1000 μm).

Mobile fractions of elements were extracted by the method of parallel extraction (Minkina et al. 2018) with incubation for 18 hours with solutions of NH_4Ac with pH 4.8, NH_4Ac + 1% EDTA with pH 4.5 (soil to solution ratio 1:5) and 1M HNO_3 (soil to solution ratio 1:10). An exchangeable fraction (F1), represented by easily and moderately soluble salts and complexes, was extracted with NH_4Ac. The fraction of compounds bound with carbonate or organic complexes (F2) corresponded the difference in the content of elements in NH_4Ac + 1% EDTA and NH_4Ac extracts. The fraction of compounds bound with Fe-Mn (hydr)oxides (F3) was calculated as the difference in the content of elements in 1M HNO_3 and NH_4Ac. An open system acid digestion method was used for the dissolution of soil samples prior to the total elemental analysis (Karandashev et al. 2017). 5% of all samples were measured in duplicates. The content of chemical elements in solutions was measured using the Elan-6100 ICP-MS System and the Optima-4300 DV ICP-AES System. Blank solutions of NH_4Ac, NH_4Ac+1% EDTA and 1M HNO_3 were analyzed, too.

Mobility, as a set of loosely bound fractions, is the total proportion of exchangeable (F1), complex (F2), and sorbed by Fe-Mn (hydr)oxides (F3) fractions in the total content of an element (Bolan et al. 2014; Li et al. 2019). Basing on the mobility (%), the HMMs are divided into low mobile <5, moderately mobile 5-25, mobile 25-50, and highly mobile >50.

Based on the chemical and morphological properties of the horizons, biogeochemical, sorption (by soil organic matter, silt particles, Fe-Mn nodules) and alkaline geochemical barriers were identified in the studied soils. The alkaline barrier was implemented through an increase in pH value and carbonate content in Bt and C-horizons. The biogeochemical barrier characterized of the topsoil with a high content of soil organic matter. The sorption barrier appeared in case of increasing of the content of the clay fraction in the Bt-horizon or Fe-Mn nodules in the E and Bt-horizons. The possibility of accumulation of HMMs at the geochemical barrier was diagnosed according to two criteria: i. an increase in the content of chemical element fraction in the soil horizon; ii. the existence of a positive significant correlation with the soil property, which can be an indicator of a particular geochemical barrier (Semenkov and Koroleva 2020, Kosheleva et al. 2015). We understand that it is impossible to unambiguously confirm or refute the accumulation of chemical elements fractions on the geochemical barrier by the presence or absence of a significant correlation with indicator soil properties. However, in the studied soils, we have identified properties and barriers that are more likely to determine the formation of certain patterns vertical partitioning of chemical elements.

The correlation analysis of the content of elements and the physicochemical properties of soils was carried out using the STATISTICA program. The accumulation of elements at geochemical barriers was justified by the presence of a significant ($p<0.05$) Spearman rank correlation ratios (r) between the contents of HMMs and soil properties calculated using the whole data set obtained. The relationship with the pH value indicates the presence of an alkaline barrier; a sorption barrier is associated with the content of clay fraction (<1μm), and a biogeochemical barrier is associated with the content of SOM. The variable content of fractions of chemical elements in the A-horizon was evaluated using the coefficients of variation (Cv) calculated based on the data on the A horizon in all cross-sections.

The regional geochemical specialization of soils was estimated using element abundances (CC), i.e. the ratio of the total contents of HMMs in soils and their concentrations in the upper part of the continental Earth's crust (Rudnick and Gao 2003), and concentration coefficients (Cc), i.e. comparisons of the contents of mobile (F1, F2, F3) fractions of HMMs in soils with average values reported for the A-horizon of the Retisols at the East European Plain and the Albic Luvisols of Western Siberia (Samonova et al. 2018, Semenkov et al. 2019; Semenkov et al. 2016). As a Cc ranged from 0.5 to 2.0, the content of elements was similar with the standards. Since the territory of the reserve is far from sources of pollution, the main reason for going beyond these limits was considered to be the local natural peculiarities of soils and rocks.

To characterize vertical and spatial distribution of As, Bi, Cd, Co, Cr, Cu, Fe, Mn, Mo, Ni, Pb, Sb, U and Zn, varied ratios were calculated. Accumulation and dispersion of HMMs in the soil horizons (Chor) relative to the rock (Crock) was diagnosed using the coefficient (1) of vertical differentiation R (Kasimov and Perelman 1992):

$$R = Chor / Crock \tag{1}$$

The spatial differentiation was described using the coefficient L (2) characterized the difference between soils located on the slope (Csub) and soils sampled in the interfluve (Cint) (Kasimov and Perelman 1992):

$$L = Csub / Cint \tag{2}$$

When the coefficients R and L exceed 2.0, the element was considered to be concentrating. If it was less than 0.5, the element was considered as dispersing. According to Rozanov (2004), four types of the element vertical distribution in soils were identified: (i) accumulative, with maximum concentration of an element in the A-horizon and monotonic decrease with depth due to accumulation at the biogeochemical barrier; (ii) accumulative-eluvial-illuvial, with accumulation at the sorption geochemical barrier in the A- and Bt-horizons and removal from the E-horizon; (iii) eluvial, with removal from the topsoil and monotonous increase in concentration in the subsoil horizons; (iv) ground-accumulative, with removal from the upper and middle part of the profile and residual accumulation in the soil-forming rock, or accumulation on the alkaline geochemical barrier.

RESULTS AND DISCUSSION

Soil properties

Retisols and Stagnosols of the southern taiga catena have clearly distinguishable E- and Bt-horizons, and eluvial-illuvial type of clay fraction distribution (Table A.1). The development of soils on binary sediments is confirmed by E-horizon enriched in silt fractions, and by Bt-horizon and parent rock enriched in clay fraction (Fig. 4), which is typical for the Central Forest Nature Reserve territory (Puzachenko et al. 2013), for similar soils of Karelia (Lukina et al. 2019) and Tobolsk Upland (Semenkov et al. 2019). The pH value varies from strongly acidic (pH=3.7) in the topsoil horizons (Table 1) to slightly alkaline (pH=7.5) in the C-horizon, which corresponds to the parameter spread in Albeluvisols in the Central Forest Nature Reserve (Sokolova et al. 2014). The SOM content decreases sharply with depth, which is also typical of taiga soils (Lukina et al. 2019). In general, the studied soils of the southern taiga catena have all features and parameters specific to texture-differentiated soils of southern taiga landscapes on mantle loams underlain by a carbonate moraine.

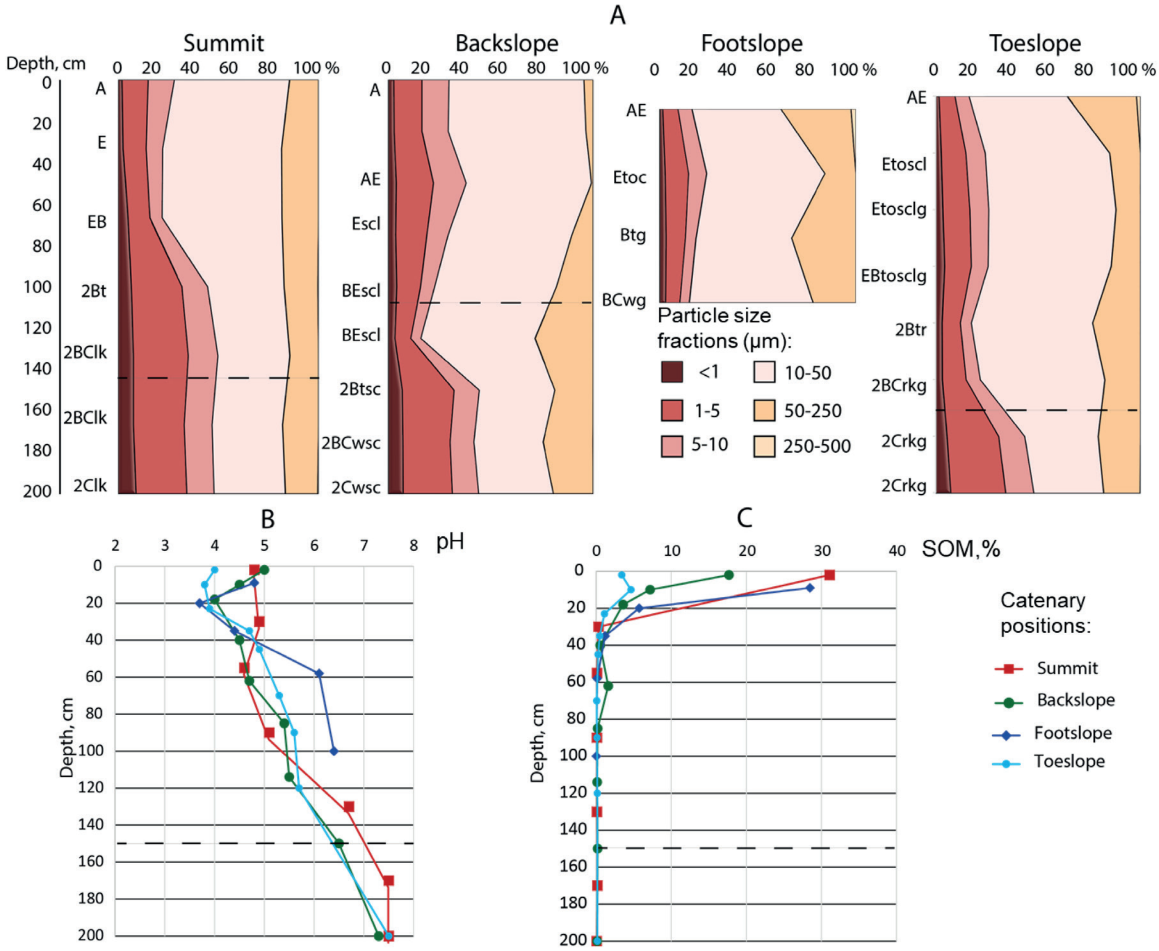

Fig. 4. The vertical differentiation of the Retisols studied. A – granulometric fractions in μm. B – pH value. C – SOM. Dotted line – upper boundary of effervescence with 10% HCl

Average concentration of chemical elements

Total content. Elemental composition of the A-horizon of soils studied differs slightly with the upper continental Earth's crust (subscript is for CC): Bi$_{1.8}$ Sb$_{1.6}$ Zn$_{1.1}$ Mn$_{0.7}$ Mo$_{0.6}$ U$_{0.5}$. The reduced content of As Cu$_{0.4}$ Cr Co Fe Ni$_{0.2}$ is due to lower concentration of the elements in the mantle loam, which was also noted (Avessalomova 2017). Higher content of Cd$_7$ in the A-horizon can be explained by its uptake by woody plants and that of Pb$_2$ by its accumulation in *Picea abies* needles (Enchilik et al. 2020). The total content of most elements (Bi, Co, Cr, Cu, Mn, Mo, Ni, U and Zn) in the A-horizon of studied soil is similar (Fig. 5) to the data on agricultural soils in Europe (Reimann et al. 2018). The content (subscript is for Cc) of As$_{0.3}$ and Fe$_{0.4}$ is slightly reduced, and that of Cd$_{3.5}$ Sb and Pb$_{2.2}$ is increased. The increased content of Cd and Pb results from participating of the elements in the biological cycle of woody plants (Enchilik et al. 2020). Sb is a component of humic acids (Kabata-Pendias and Szteke 2015), which are insoluble under acidic conditions. The total elemental composition of the E-, Bt- and BCk-horizons of soils studied differs slightly with the upper continental Earth's crust. (Table 1). According to variability of the total content (subscript index - *Cv*, %), the elements form the following series: Mn$_{73}$> Cd$_{55}$ Zn Ni$_{51}$ Sb$_{47}$ Bi$_{41}$ Fe$_{40}$ As$_{37}$ Mo$_{33}$ Pb$_{32}$ Cr, Co$_{28}$ U$_{22}$ and Cu$_{19}$. It means that the total content of most elements in the A-horizon shows low to medium variability. Based on the data on the environmental conditions, phisyco-chemical properties and elemental composition, we think that the studied catena can be considered as background for the purpose of regional soil geochemical monitoring in the center of the East European Plain.

Exchangeable fraction (F1). The content of exchangeable (subscript is for Cc) Mn As$_{>100}$ Ni Fe$_{>10}$ U$_7$ Cd Cr$_5$ Pb, Zn$_4$ (Fig. 5, Table 1, Table A.3) in the A-horizon is higher than their average concentration in background Albic Luvisols (Semenkov et al. 2019). Essential Mn and beneficial for plants Pb and Cr are fixed by organic matter at the biogeochemical barrier (Table A.5). Zn is involved in the synthesis of chlorophyll (Boyd, 2020; Kabata-Pendias and Szteke 2015) and accumulates in the acid A-horizon with the litter of photosynthetically active plant organs (Enchilik et al. 2020) due to immobilization by soil microorganisms (Perelomov and Chulin 2014) and sorption by organic matter. Increased content of Mn, Ni, Fe, Pb, and Zn relative to soils of the Tobolsk Upland (Semenkov et al. 2019) could be also due to the lower degree of gleying of the studied soils and, as a result, more favorable conditions for elements preservation in the A-horizon. The content of Fe$_{2.3}$ and Zn$_{4.1}$ Ni$_{2.6}$ Mn$_{2.0}$ in the E- and Bt-horizons, respectively, is higher than in the soils of the Mezen-Vychegda Plain (Semenkov et al. 2016) which could be supported by the change of redox conditions and the formation of a complex redox barrier in these horizons under poorly-permeable soil-forming rocks and the proximity of groundwater in the lower part of the catena. The content of Fe$_{16}$ Mn$_{11}$ Co$_{10}$> Zn$_5$ Cd$_4$ Ni$_3$ in carbonate horizons is higher than in soils of the Mezen-Vychegda Plain (Semenkov et al. 2016) since the elements accumulate at the contrasting carbonate barrier under higher pH values (Fig. 5). The accumulation of exchangeable Co and Ni at the alkaline barrier is in accordance with a positive correlation with $CaCO_3$ content (Table A.5).

Variability of the content of F1 of elements (subscript is for *Cv*, %) is higher than that of the total content: Mo Fe As U Cr$_{100}$ Mn$_{97}$> Zn$_{70}$> Co$_{54}$ Pb Bi$_{47}$> Cd$_{38}$ Cu$_{33}$ Ni$_{28}$.

Fraction bound with complexes (F2). The content of complexes of Pb_{15} Bi_{10}>$Cu_{8.4}$ $Mo_{4.4}$ in the A-horizon (Fig. 5, Table 1, Table A.3) exceed the data available in the literature (Semenkov et al. 2019), apparently due to the regional biogeochemical specialization of plants of the Valdai Hills, which accumulate these elements in their aerial tissues (Enchilik et al. 2020). F2 compounds could migrate as a part of dissolved organic matter and organic complexes (Moiseenko et al. 2013). In the E-horizon, concentration of $Cd_{0.4}$ $Fe_{0.3}$ $Mn_{0.2}$ $Cu_{0.1}$ (subscript is for *Cc* values) is lower than in Luvisols of the Mezen-Vychegda Plain, probably due to the lower proportion of clay fraction in the studied soils; and the content of Pb is the only one higher (Fig. 4, Table A.2). Concentration of Cd_{59}> Cr_9 $Ni_{4.4}$ $Zn_{4.2}$ $Pb_3$$Co_{2.7}$ in the Bt-horizon is higher than in more acidic Bt-horizon sampled in the Mezen-Vychegda Plain; and that of $Cu_{0.3}$ is lower probably due to the lower content of clay fraction in the studied Retisols which shows positive correlation with the element (Table A.5). The content of F2 of Ni_4 is the only one increased in the BCk-horizon. According to variability of the content of F2 (subscript is for *Cv*, %), the elements form the series: As Mn Fe_{100} Sb_{96}> Mo_{82} Zn_{78} Cr_{74}> Co_{51}> Cd_{39} Cu_{36} Ni_{33}> Bi_{17} Pb_{13}.

Fraction bound with Fe-Mn (hydr)oxides (F3). In A-horizon, the content of $Mn_{0.4}$ Fe Bi $Cd_{0.3}$ As $Co_{0.1}$ Ni Cr Mo Sb $U_{<0.1}$ (subscript is for Cc values; Fig. 5, Table 1) is lower than in soils of the Tobolsk Upland (Semenkov et al. 2019), where gleying is more intense. Retisols (Loamic) of the middle and southern taiga are enriched with F3 of elements in the lower part of the E-horizon (Sokolova et al. 2014). For example, the content of F3 of $Mn_{2.2}$ $Pb_{1.6}$ and $Ni_{8.1}$ $Mn_{1.6}$ in the E- and Bt-horizons of the studied Retisols, respectively is increased relative to the soils of the Mezen-Vychegda Plain. The concentration of $Ni_{2.4}$ slightly increases in the carbonate horizon probably due to higher pH values (Fig. 4) than in the same soil horizons within the Mezen-Vychegda Plain (Semenkov et al. 2016). According to the variability of the content of F3 (subscript is for *Cv*, %), the elements form the series: Bi Sb Mn_{100} Cr_{98} U_{92} Zn_{85} Co_{82} Cd_{77}> Fe_{52} Ni_{51}> Pb_{43} As_{39} Cu_{35}.

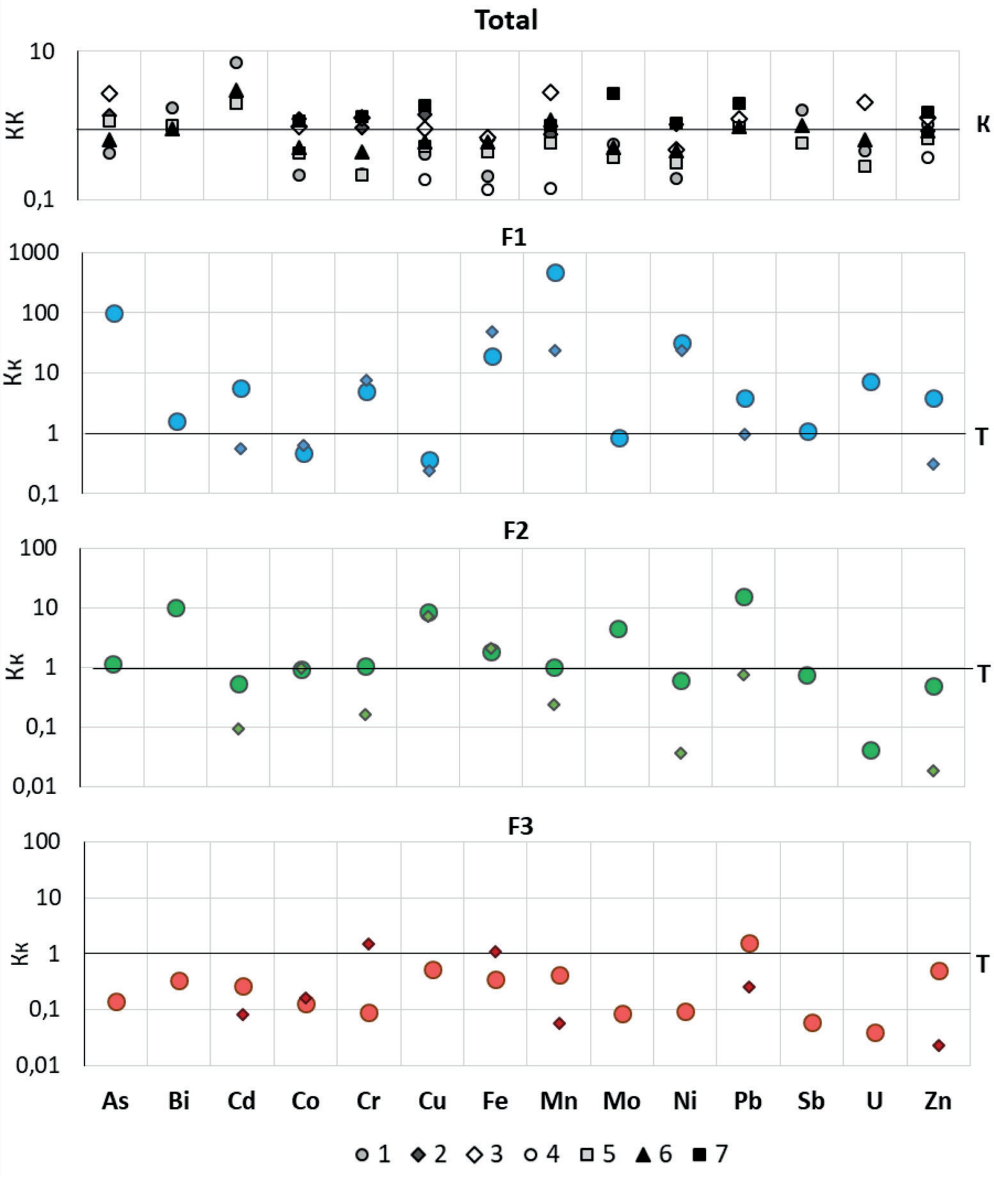

Fig. 5. Differences in average element concentrations in the humus horizons of the site and background datasets. Total element content is normalized to element abundances of the upper part of the continental Earth's crust (Rudnick and Gao 2003), mobile fractions (F1, F2, F3) content is normalized to Albic Luvisols in the Tobolsk upland (Semenkov et al. 2019). Soils:1 – Albic Retisols and Stagnosols in the Central Forest Nature Reserve (present study), 2 – Albic Retisols in the Mezen-Vychegda Plain (Semenkov et al. 2016), 3 –Albic Luvisols in the Tobolsk upland (Semenkov et al. 2019), 4 – Albic Retisols in the Central Forest Nature Reserve (Karavanova and Malinina 2009), 5 – Europe agricultural soils – GEMAS (Reimann et al. 2018), 6 – Regosols of the Smolensk-Moscow Upland (Samonova et al. 2018), 7 – soils of the Southern Russia (Dyachenko and Matasova 2016)

The *Cv* of the content of the mobile fractions (F1, F2, F3) in the A-horizon of soils of the southern taiga catena are above 30% for all chemical elements, except for the F1 of Ni and F2 of Bi and Pb. The content of F1 of most elements is higher than in Albic Luvisols of the Tobolsk Upland (Table 2), where the gleying of the entire soil profile provides more favorable conditions for the removal of elements. The content of F3 of many studied elements in the A-horizon of studied Retisols is slightly lower than in Albic Luvisols of the Tobolsk Upland (Table 1), which is due to the lower degree of gleying of the studied soils. The F3 accounts for the major share of the total content of HMMs, which may indicate their high contribution to the physicochemical migration in Central Forest Nature Reserve soils and is typical for soils at the southern taiga (Semenkov et al. 2019).

Mobility of chemical elements in the soil catena.

Extractability of HMMs (Table 1) which correlates with phytoavailability is the highest in the acidic O-horizon and lower in the subsoil horizons with the near-neutral environment (Fig. 4). The ratio of fractions depends on the properties of soil horizons and chemical elements. Among the mobile fractions of Co, Mn, Cd and Zn in the A-horizon, F2 and F3 account for practically the same proportion, which confirms their active participation in biogenic migration in the southern taiga landscapes of the Central Forest "Reserve". The biological cycle plays a greater role in the migration of Cd, Mn, Pb and Zn in the Central Forest Nature Reserve soils than for As, Bi, Cu, Fe and Ni, which is reflected in the increased proportion of exchangeable fractions (F1>10% of the total), the most readily available to plants from the A- and O-horizons of soils (Gabarrón et al. 2019; Li et al. 2017).

According to their mobility, the chemical elements are divided into 3 groups (Table 1). The first group (Sb, Mo, Cr and U) is characterized by relatively low mobility in the soils. Permanently low mobility of Sb in the vast majority of the samples is due to the presence of insoluble clay minerals (Bolan et al. 2022; Kabata-Pendias and Szteke 2015). Low mobility of Sb in soils is also associated with just slight involvement of its F1 compounds in the biological cycle by plants (Table A.1) and the removal of easily soluble compounds of the element within slightly acidic, close to neutral (pH = 5.2-6.8) surface waters of the Mezha River (Minaeva and Andreev 2008).

Elements of the second group (As, Bi, Zn, Fe, Cu and Ni) are the highly mobile in the A- and O-horizons sampled in the summit and footslope positions (>25%) while in other horizons they are moderately mobile (5-25%). This could be explained for Bi by the probable accumulation of dissolved organic matter in the soils of the lower part of the slope, because the element is captured in the organic-mineral forms (Kabata-Pendias and Szteke 2015). Mobile fractions of Zn enter the soil with plant litter of deciduous plants in

Table. 1. Mobility of chemical elements in the soil catena, %

Horizons	Sb	Mo	Cr	U	As	Bi	Zn	Fe	Cu	Ni	Co	Pb	Mn	Cd
	Summit													
A	2,8	7	8	5	35	53	91	52	68	69	79	100	100	100
E	2	3,8	10	11	9	17	13	37	16	8	41	41	31	40
Bt	0,6	9	7	15	6	12	17	16	16	32	50	40	66	78
C	1,1	1,9	4,8	22	5	6	15	8	17	36	46	29	67	62
	Backslope													
A	3,6	7	6	3,8	25	42	91	56	61	23	81	100	100	100
E	6	7	8	8	8	18	19	39	21	12	33	58	60	54
Bt	1,1	10	8	11	6	11	11	18	18	21	42	38	44	49
C	2,5	9	6	16	7	11	16	14	18	40	60	50	73	81
	Footslope													
H	4,9	8	12	24	57	67	43	100	70	59	52	100	24	100
E	1,3	3,2	8	12	23	12	15	16	21	11	8	44	3,8	51
Bt	1,3	10	11	11	11	16	22	35	34	44	67	35	69	75
C	1,6	12	12	12	8	16	29	19	23	40	54	32	65	69
	Toeslope													
H	1,3	56	6	6	21	100	77	45	79	28	14	100	8	100
E	1,3	8	8	11	24	15	12	35	17	9	16	42	12	46
Bt	1,1	8	10	15	6	13	17	31	30	28	46	37	72	69
C	0,8	9	9	14	4,7	9	15	20	20	34	60	27	68	29

Color indicates mobility (%): <5 5-25 25-50 >50 the catena upper part (Enchilik et al. 2020). Fe, Cu and Ni are highly mobile in the (sub)surface soil horizons (A, H and E).

Elements of the third group (Co, Pb, Mn and Cd) are highly mobile (>25% in most horizons), which is explained by their active involvement in the biological cycle (Enchilik et al. 2020). Mn, as an essential element for plants, accumulates in the topsoil due to active plant uptake (Enchilik et al. 2020). Readily available to plants F3 compounds of Co (Kabata-Pendias and Szteke 2015) contribute a lot to the extractability of the metal in the A-horizon sampled in the summit and backslope positions (F3=36% and 41%, respectively). Pb forms complexes with soil organic matter (Fan et al. 2015). The maximum mobility of Mn and Pb was also found in other texture-differentiated soils (Semenkov et al. 2016). Cd becomes more soluble in the acidic humus horizon (Kabata-Pendias and Szteke 2015). Cd and Pb remain highly mobile in the E-horizon due to sorption by Mn (hydr)oxides (Violante 2013; Vodyanitskii 2010). Cd, Mn and Pb are highly mobile in the subsoil due to the vertical migration of dissolved organic matter (Fan et al. 2015).

Vertical soil-geochemical structure of the catena

The vertical distribution of chemical elements is determined by geochemical barriers occurring in the soil horizons. Biogeochemical, sorption, gley and carbonate geochemical barriers were diagnosed in Retisols of the Central Forest Nature Reserve. The ability of chemical elements to accumulate at (no) one or several vertical geochemical barriers defines four types of vertical distribution.

Accumulative distribution. The total content of Bi and Cd are retained in the topsoils (Table A.3). The accumulation of HMMs in the O- and A-horizons is primarily due to the presence of a biogeochemical barrier. Topsoil accumulation of the total content of Cd (Fig. B.1a) is apparently due to the return of plant litter enriched with the element to the soil surface (Enchilik et al. 2020).

F1 compounds of As, Bi, Cd, Cr, Mn, Mo, Pb and Zn accumulate in the topsoil (Table A.4). There is a direct correlation of F1 of As, Bi, Cd, Cr, Mn, Mo, Pb and Zn (Fig. 6a, Fig. 7, Table A.3) with SOM content (Table A.5). Mn enters the soil surface in the backslope position with abundant plant remains – the fresh leaf litter horizon is thicker in this part of the catena (Enchilik et al. 2020). Exchangeable Mo is weakly mobile under acidic conditions and binds to SOM (Kabata-Pendias and Szteke 2015).

F2 compounds of Cd, Cr, Cu, Pb, Sb, Zn accumulate in the topsoil (Table A.4). The content of F2 compounds of Bi, Sb and essential Ni and Zn (Fig. 6b) correlates with SOM (Table A.5). The formation of Ni complexes with dissolved organic matter was pointed in (Semenkov et al. 2016; Avessalomova 2017). The O-horizon and especially peat are highly capable of absorbing the anionic Cr (Kyziol et al. 2006). Its association with humic substances is confirmed by high values of the stability constant with fulvic acids (Moiseenko et al. 2013).

The F3 fraction of Pb and Sb accumulates in the topsoil (Fig. B.1b). Anionic Sb accumulates in the A-horizon since it is weakly mobile in the acidic media (Manaka 2006), is sorbed by organic matter (Table A.5), and forms compounds with humic acids (Bolan et al. 2022). Vertical distribution of the total content and F3 compounds of HMMs shows in Annex (Fig. B.1).

Accumulative-eluvial-illuvial distribution. The total content of Sb increases at the biogeochemical barrier in the A-horizon (Fig. 7) as a part of insoluble humin. Correlation with SOM content (Table A.5) is positive for all fractions of the element. The total content of Sb is also higher in the Bt-horizon, which indicates its possible presence in poorly soluble primary clay minerals (Bolan et al. 2022; Kabata-Pendias and Szteke 2015). The complexes (F2) of Sb with organic matter are formed in the topsoil and with carbonates in the BCk-horizon. Zn accumulates at the sorption barrier in the Bt-horizon. F1 and F2 compounds of Ni accumulates in the waterlogged toeslope position due to the conservation of F1 compounds in the H-horizon, which is typical for such conditions (Semenkov et al. 2016; Avessalomova 2017). Its F1 fraction tends to accumulate at the alkaline geochemical barrier (Table A.5, Fig. 7). The content of F3 fraction of Pb correlates with the content of SOM, and that of Cu and Zn with clay particles (Table A.5, Fig. 7).

Eluvial distribution. Slightly mobile As under acidic conditions could be sorbed by iron nodules accumulated in the lower part of the E-horizon (Lee et al. 2011; Vodyanitskii 2010). The content of Cu increases in the subsoil (Table A.5) due to its accumulation at alkaline and sorption geochemical barriers (Boyd 2020; Kabata-Pendias and Szteke 2015). The Zn content in the slope soils increases under alkaline conditions in the parent rocks due to the increase in carbonates.

The content of the F1 fraction of Fe in the summit Retisols and Ni in the slope Retisols increases in the middle part of the soil profile (Table A.4). Exchangeable Cu accumulates at the alkaline geochemical barrier in the subsoil (Table A.4, Fig. 7).

The F2 fraction of Fe accumulates in the Bt-horizon which confirms its ability to form compounds with carbonates (Thompson et al. 2006). Accumulation in the middle part of the Retisols is characteristic of the F2 fraction of Cu due to the migration of its organic complexes (Kabata-Pendias and Szteke 2015; Moiseenko et al. 2013).

High content of the F3 fraction of Fe and Cr is observed in the E-horizon due to their accumulation in abundant ferruginous nodules (Vodyanitskii 2010) and in the BCk-horizon at the alkaline geochemical barrier (Table A.4). The F3 fraction of As, Bi, Cd, Pb accumulates in the middle part of the Retisols due to the abundance of Fe–Mn nodules in the horizons (Lee et al. 2011; Violante 2013). As is absorbed with iron (hydr)oxides. And Cd and Pb are absorbed with manganese (hydr)oxides (Vodyanitskii 2010). Accumulation of Cu in the middle part of the Retisols seemed to result from the influence of the manganese (hydr)oxides, too (Perelomov and Chulin 2014). Bi leaches out from the A-horizon and accumulates in the middle part of the Retisols due to the adsorption by clay (Pasieczna 2012). Cr and U accumulate in the lower part of the Retisols, since the distribution of these elements is related to the eluvial-illuvial distribution of clay particles (Table A.5, Fig. 7).

The ground-accumulative distribution is characteristic of total Bi, Cd, Ni, Pb and Sb, exchangeable Co, Ni, and U, F2 of Co, Mn and Mo, and F3 of Bi, Co, Cr, Fe, Mn and Ni. The concentration of exchangeable Ni and Cu correlates with the distribution of clay (Table A.4, A.5, Fig. 7). Complexes of Mn are carried out to the parent rocks in the waterlogged toeslope position.

F1 of As, Bi, Cd, Cr, Mn and Pb and F3 of Pb and Sb accumulate at the biogeochemical barrier (Fig. 7, Table A.5) of soils studied due to sorption by organic matter. Formation of organic complexes with As, Bi, Cr and Zn might be the reason for a positive correlation between the content of F2 fraction of these elements and SOM (Table A.5). The accumulative-eluvial-illuvial distribution of the total content of Sb and Zn, F2 of Fe and F3 of Cu, Pb and Zn depends on the content of soil organic matter and clay. The eluvial distribution of the total content of As, Co, Cu and Cr, F1 of Cu and F3 of Cr is governed by clay and co-precipitation with carbonates (Table A.5). The ground-accumulative distribution is determined by the accumulation of compounds with fine particles and with carbonates and hydroxides at the alkaline barrier in the subsoil horizons (Table A.5).

a) F1

b) F2

Fig. 6. The vertical differentiation (R) of the F1 (a) and the F2 (b) fraction of the HMMs in the soil catena studied

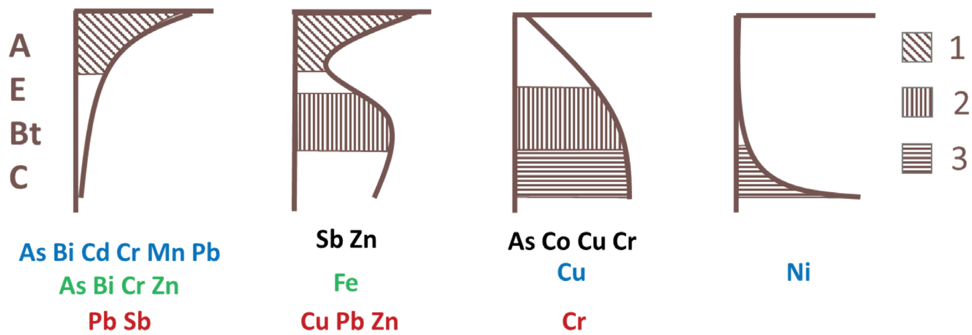

Fig. 7. Accumulation sites of HMMs at the barriers in the soil horizons sampled in the catena located in the Central Forest Nature Reserve. The colors indicate the forms of chemical elements: black – total content, blue – F1, green – F2, red – F3. Geochemical barriers: 1 – biogeochemical, 2 – sorption, 3 – alkaline. The presented elements have the same type of vertical distribution in soils of two or more positions and accumulate on geochemical barriers, confirmed by correlation coefficients (Table A.4)

Spatial soil-geochemical structure of the catena

The intensity of lateral flows of chemical elements depends on the migrational contrasts (Perel'man 1967). The most considerable role in the distribution of HMMs in forest soils is played by the spatial sorption-biogeochemical barrier. Therefore, two variants of the contrasting distribution of elements in the studied catena within the Central Forest Nature Reserve were identified depending on the location of the barrier.

Accumulation in the backslope position. In the backslope position, HMMs mainly accumulate at the biogeochemical barrier. Here the biomass reaches its maximum and the abundant leaf litter enriched with Cd, Zn, Mn, and Ni enters the soil surface (Enchilik et al. 2020). The total content of Bi, Cd, Pb, Sb and Zn is maximal in the A-horizon, too. Total As, Mn and Ni accumulate to a greater degree in the A-horizon sampled in the backslope position (Fig. B.2a).

F1 fractions of Zn accumulates in the A-horizon in the backslope position (Fig. 8a, Fig. 9) due to the transformation of plant litter (Enchilik et al. 2020, Table A.4).

The content of exchangeable compounds of Mn is maximal (Fig. 9) in the E-horizon sampled in the backslope position.

F2 of Mo accumulates (Fig. 8b) in the A-horizon sampled in the backslope position. F2 of Bi, Cd, Pb and Sb accumulates (Fig. 9) in the E-horizon. Slope soils tend to accumulate F3 of As at the spatial geochemical barrier in the A-horizon (Fig. B.2b), Sb at the eluvial and As again at the E-horizon. Spatial distribution of the total content and F3 fraction is given in the Annex (Fig. B.1).

Accumulation in the footslope and toeslope positions. The migration slows down in the toeslope positions of the catena. And the total content of many HMMs increases at the spatial geochemical barrier of peaty soils (Fig. B.2a). The role of oxidative and reductive barriers in the E-horizon increases in this position. The total content of As in the A-horizon is maximal in the soils sampled at the footslope position probably due to the accumulation of humic substances washed away from the summit position. Peat of the toeslope position is enriched in Fe which accumulates in sphagnum more actively than other elements (Enchilik et al. 2020), and depleted in Mo due to its lower phytoavailability in acidic Fe-saturated soils (Kabata-Pendias and Szteke 2015).

The content of F1 of As, Bi, Cr, Fe, Mo and U in the O-horizon increases down the catena (Fig. 8a). The spatial geochemical barrier in peaty soils at the toeslope positions was previously reported in the taiga catenas (Avessalomova 2017; Semenkov et al. 2019; Semenkov et al. 2016). F1 of Mo is absorbed by Fe-Mn nodules in the E-horizon sampled at the toeslope position. The content of Bi, Cd and Pb in the E-horizon increases when moving down the catena. F1 of Co, Cr, Fe and Mn in the Bt-horizon also accumulates in the lower part of the catena (Fig.9).

F2 of As, Fe, Mo and Sb accumulates at the spatial biogeochemical barrier in the H-horizon of the toeslope position (Fig. 8b) due to migration of organic compounds from the upper-situated landscapes. The distribution of As is associated with soil organic matter (Table A.4). Fe compounds with high stability constants with humic acids (Moiseenko et al. 2013) actively migrate downslope with surface runoff under the acidic conditions and accumulate in the soils of the lower catena part. F2 of anionic Cr accumulates in the E-horizon sampled in the footslope and toeslope positions probably due to the slower migration of the element under strongly acidic conditions (pH=3.7 and 3.9, respectively, Fig. 4). F2 of Bi, Cd, Mo, Sb and Zn accumulates in the C-horizon of the footslope position (Fig. 9), which could be provoked by frequent changes in redox conditions near shallow groundwater table (Fig. 3) and the formation of complex oxygen and gley barriers. F3 of Fe accumulates in the H-horizon sampled in the footslope position (Fig. B.2b), As in the Bt-horizon, and Mo in the Ck-horizon (Fig. 9).

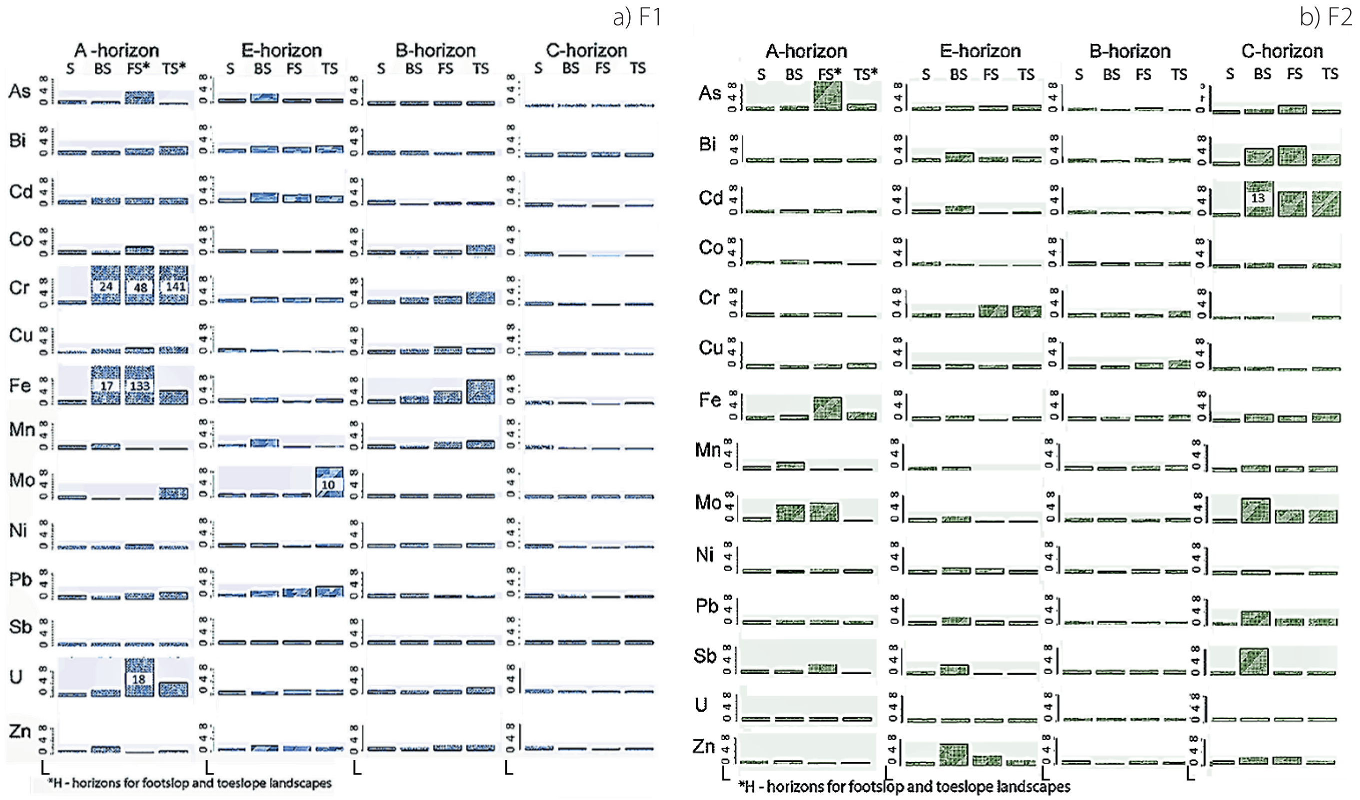

Fig. 8. The spatial differentiation (L) of the F1 (a) and the F2 (b) fraction of the HMMs in the soil catena studied

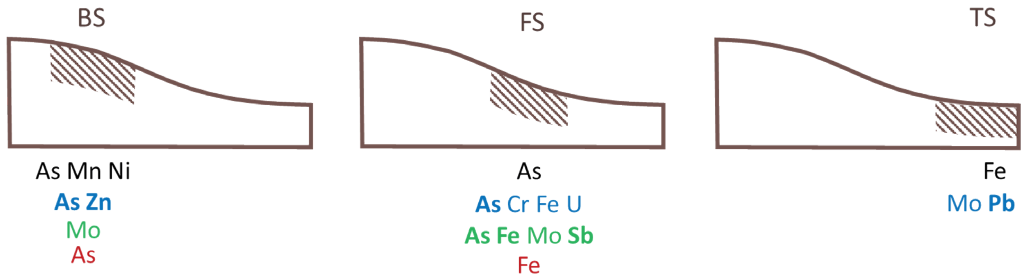

Fig. 9. Accumulation sites of HMMs at the lateral biogeochemical barrier in catena soils (hatching): BS– backslope, FS – footslope, TS – toeslope. The colors indicate the forms of chemical elements: black – total content, blue – F1, green – F2, red – F3. Bold (italic) - accumulation of elements at geochemical barriers is confirmed by correlation with soil properties (Table A.5).

The contrast of spatial differentiation of elements generally decreases along A–E–Bt–Ck series of horizons, which is due to the lithogeochemical homogeneity of the catena and weakening of the influence of the heterogeneity of the vegetation cover in the underlying soil horizons. The exchangeable and complex compounds of many elements accumulate on the biogeochemical barrier of peaty soils of the foot slope position (Fig. 9), which is confirmed by positive correlation with SOM (Table A.5) for F1 of As and F2 of As, Fe and Sb. The exchangeable fraction total content of Zn increases at the biogeochemical barrier of soils sampled at the backslope position due to the transformation of plant litter (Enchilik et al. 2020).

CONCLUSIONS

The studied background Retisols and Stagnosols of the southern taiga catena at the Central Forest Nature Reserve have relatively high content of F1 of most of the studied elements in the acid A-horizons.

The high content of the F1 in the E- and Bt-horizons is due to the change in redox conditions and the increase of pH values in the parent rocks. The leaching water regime results in the lower content of F3 fraction of HMMs in the A-, H- and O-horizons. HMMs accumulated in Fe-Mn nodules in the E-horizon. The variability of the total content of elements in the A-horizon is within the range of 20-75%. The F1 fraction of Mo, Fe, As, U and Cr, F2 of As, Mn and Fe, and F3 of Bi, Sb, and Mn show the highest variability in the horizon.

The highest *extractability* of elements is characteristic of organic horizons, where the share of F2 and F3 fractions is practically the same. The proportion of the F1 fraction in the A-horizon is maximum for Cd, Mn, Pb and Zn. Cd, Co, Pb, and Mn are highly mobile.

The extractability decreases significantly towards the underlying subsoil horizons. Both Cd and Pb are highly mobile (40-58%) in the E-horizon of all soils. Mobility of As, Bi, Zn, Fe, Cu. Ni and Co decreases to 8%. Only Cd, Pb, and Mn are mobile (>25%) in the Bt- and C-horizons.

The *vertical* distribution of F1 of elements depends considerably on biogeochemical processes (absorption by plants from subsoil horizons, return with litter to the soil surface, humus accumulation) and sorption by soil organic matter. The key factors of F2 distribution are the content of SOM and carbonates. As, Cd, Cu, Pb, Zn and Sb accumulated on the biogeochemical barrier in the A-horizon. As, Bi, Cd and Pb accumulated on the sorption barrier of Fe-Mn nodules in the E- and Bt-horizons. Migration with silt is important for the distribution of F3 fraction of Cr and U. The biological cycle plays the greatest role in the migration of highly-mobile Cd, Mn and Pb in soils of the catena, since their F1 are observed to accumulate in the topsoil.

The *spatial* distribution of the total content of Bi, Cd, Pb, Sb and Zn, F1 of Zn, F2 of Mo and F3 of As, Fe and Bi depends on the biological cycle in the backslope landscape. Here, the abundant leaf litter enriched with HMMs mobile fraction enters the soil surface. Mobile forms of As, Mo and Sb (F2), and Fe (F2, F3) accumulated at the spatial biogeochemical barrier in the H-horizon sampled at the footslope position due to the accumulation of humic substances washed off from summit positions. Fe and the most mobile (F1) fraction of As, Bi, Cr, Fe, Mo, Pb and U accumulate on the spatial geochemical barrier of peat soils in the lower part of the catena. This process indicated the ability of peat to conserve the most biologically available F1 fractions of both mobile Pb, Fe, Bi and As and less mobile U, Cr and Mo.

Thus, both total content and the concentration of F3 of elements increases in the A-horizon of the slope soils, and F2 in the H-horizon of the footslope position, while the peat of the waterlogged toeslope position entraps F1. The contrast of spatial differentiation of the mobile fractions decreases from the topsoil horizons to the parent material, which is mainly due to the smaller effect of vegetation cover and biological factor on deep soil horizons.

REFERENCES

Avessalomova I.A. (2017). Biogeochemistry of the high-mountain landscapes of the Elbrus region. Geochemistry of landscapes. To the 100th anniversary of the birth of Alexander Ilyich Perelman, 168-188. (in Russian)

Avessalomova I.A. and Mikliayeva I.M. (1997). Structural and functional peculiarities of meadows and swamps in landscapes of the central Meschera. Vestnik Moskovskogo Universiteta, 5(1), 43-48.

Bolan N., Kumar M., Singh E., Kumar A., Singh L., Kumar S., Keerthanan S., Hoang S.A., El-Naggar A., Vithanage M., Sarkar B., Wijesekara H., Diyabalanage S., Sooriyakumar P., Vinu A., Wang H., Kirkham M.B., Shaheen S.M., Rinklebe J. and Siddique K.H.M. (2022). Antimony contamination and its risk management in complex environmental settings: A review. Environment International, 158, 106908, DOI: 10.1016/J.ENVINT.2021.106908.

Bolan N., Kunhikrishnan A., Thangarajan R., Kumpiene J., Park J., Makino T., Kirkham M.B. and Scheckel K. (2014). Remediation of heavy metal(loid)s contaminated soils - To mobilize or to immobilize? Journal of Hazardous Materials, 266(15), 141-166, DOI: 10.1016/j.jhazmat.2013.12.018.

Boyd C.E. (2020). Water Quality Protection. In: Water Quality. USA: Aubrun University, DOI: 10.1007/978-3-030-23335-8_18.

Burachevskaya M., Minkina T., Bauer T., Mandzhieva S., Gülser C., Kızılkaya R., Sushkova S. and Rajput V. (2020). Assessment of extraction methods for studying the fractional composition of Cu and Zn in uncontaminated and contaminated soils. Eurasian Journal of Soil Science, 9(3), 231-241, DOI: 10.18393/ejss.734601.

Enchilik P.R., Semenkov I.N., Aseeva E.N., Samonova O.A., Iovcheva A.D. and Terskaya E. V. (2020). Catenary biogeochemical differentiation in the southern taiga landscapes (Central Forest Reserve, Tver Oblast). Vestnik Moskovskogo Universiteta, 5(1), 121-131.

Fan T.-T., Wang Y.-J., Li C.-B., Zhou D.-M. and Friedman S.P. (2015). Effects of Soil Organic Matter on Sorption of Metal Ions on Soil Clay Particles. Soil Science Society of America Journal, 79(3), 794-802, DOI: 10.2136/sssaj2014.06.0245.

Gabarrón M., Zornoza R., Martínez-Martínez S., Muñoz V.A., Faz Á. and Acosta J.A. (2019). Effect of land use and soil properties in the feasibility of two sequential extraction procedures for metals fractionation. Chemosphere, 218, 266-272, DOI: 10.1016/j.chemosphere.2018.11.114.

Grønflaten L.K. and Steinnes E. (2005). Comparison of four different extraction methods to assess plant availability of some metals in organic forest soil. Communications in Soil Science and Plant Analysis, 36(19-20), 2699-2718, DOI: 10.1080/00103620500303764.

Huang J.H., Matzner E. (2007). Fluxes of inorganic and organic arsenic species in a Norway spruce forest floor. Environmental Pollution, 149(2), 201-8, DOI: 10.1016/j.envpol.2007.01.004.

Kabata-Pendias A., Szteke B. (2015). Trace elements in abiotic and biotic environments. Boca Raton: CRC Press, Taylor, Francis Group.

Karavanova E.I., Malinina M.S. (2009). Spatial differentiation of the chemical composition of solid and liquid phases in the main soil types of the Central Forest State Natural Biospheric Reserve. Eurasian Soil Science, 42, 725–737, DOI: 10.1134/S1064229309070035.

Kasimov N.S., Gennadiev A.N. (2005). Landscape geochemistry and soil geography: Main concepts and approaches. Vestnik Moskovskogo Universiteta, 5(2), 10-17.

Kasimov N.S. and Perelman A.I. (1992). The geochemistry of soils. Eurasian Soil Science, 24(4), 59-76.

Kasimov N.S., Gerasimova M.I., Bogdanova M.D., Gavrilova I.P. (2012). Landscape-geochemical catenas: concept and mapping. Geochemistry of landscapes and geography of soils. 100th Anniversary of the Birth of M.A. Glazovskaya, 59-81. (in Russian).

Kosheleva N.E., Kasimov N.S. and Samonova O.A. (2002). Regression models for the behavior of heavy metals in soils of the Smolensk-Moscow Upland. Eurasian Soil Science, 8, 954-966.

Kosheleva N. E., Kasimov N. S. and Vlasov D. V. (2015) Factors of the accumulation of heavy metals and metalloids at geochemical barriers in urban soils // Eurasian Soil Science ,48(5), 476-492.

Kraynov S.N., Ryzhenko B.N., Shvets V.M. (2012). Geochemistry of underground waters. Theoretical, applied and environmental aspects. Moscow, TsentrLitNefteGaz (In Russian).

Kyziol J., Twardowska I. and Schmitt-Kopplin P. (2006). The role of humic substances in chromium sorption onto natural organic matter (peat). Chemosphere, 63(11), 1974-82, DOI: 10.1016/j.chemosphere.2005.09.042.

Lee S.H., Jung W., Jeon B.H., Choi J.Y. and Kim S. (2011). Abiotic subsurface behaviors of As(V) with Fe(II). Environmental Geochemistry and Health, 33(1), 13-22, DOI: 10.1007/s10653-010-9360-4.

Li Y., Wang S., Nan Z., Zang F., Sun H., Zhang Q., Huang W. and Bao L. (2019). Accumulation, fractionation and health risk assessment of fluoride and heavy metals in soil-crop systems in northwest China. Science of the Total Environment, 663, 307-314DOI: 10.1016/j.scitotenv.2019.01.257.

Li Y., Wang S., Prete D., Xue S., Nan Z., Zang F. and Zhang Q. (2017). Accumulation and interaction of fluoride and cadmium in the soil-wheat plant system from the wastewater irrigated soil of an oasis region in northwest China. Science of the Total Environment, 595, 344-351, DOI: 10.1016/j.scitotenv.2017.03.288.

Lukina N. V., Orlova M.A., Bakhmet O.N., Tikhonova E. V., Tebenkova D.N., Kasakova A.I., Kryshen A.M., Gornov A. V., Smirnov V.E., Shashkov M.P., Ershov V. V. and Knyazeva S. V. (2019). The Influence of Vegetation on the Forest Soil Properties in the Republic of Karelia. Eurasian Soil Science, 52, 793–807, DOI: 10.1134/S1064229319050077.

Manaka M. (2006). Amount of amorphous materials in relationship to arsenic, antimony, and bismuth concentrations in a brown forest soil. Geoderma, 386, 114906, DOI: 10.1016/j.geoderma.2006.02.002.

Minaeva T.Y., Andreev V.S. (2008). Dynamics and hydrochemistry of surface waters. Chronicle of nature. Dynamics of phenomena and processes in the natural complex of the reserve. Federal State Institution «Central Forest Reserve». (in Russian)

Minkina T.M., Mandzhieva S.S., Burachevskaya M.V., Bauer T.V. and Sushkova S.N. (2018). Method of determining loosely bound compounds of heavy metals in the soil. MethodsX, 5, 217-226, DOI: 10.1016/j.mex.2018.02.007.

Moiseenko T.I., Dinu M.I., Gashkina N.A. and Kremleva T.A. (2013). Occurrence forms of metals in natural waters depending on water chemistry. Water Resources, 40(4), 407-416, DOI: 10.1134/S009780781304009X.

Reimann C., Fabian K., Birke M., Filzmoser P., Demetriades A., Négrel P., Oorts K., Matschullat J., de Caritat P., Albanese S., Anderson M., Baritz R., Batista M.J., Bel-lan A., Cicchella D., De Vivo B., De Vos W., Dinelli E., Ďuriš M., … Sadeghi M. (2018). GEMAS: Establishing geochemical background and threshold for 53 chemical elements in European agricultural soil. Applied Geochemistry, 88, 302-318, DOI: 10.1016/j.apgeochem.2017.01.021.

Perel'man A.I. (1967). Geochemistryof Epigenesis. New York: Plenum Press.

Perelomov L.V. and Chulin A.N. (2014). Molecular mechanisms of interaction of microelements with microorganisms in the environment. Direct biological transformation of microelement compounds. Biology Bulletin Reviews, 4(4), 285-299, DOI: 10.1134/s2079086414040070.

Popova L.F., Repnitsyna O.N., Nikitina M.V. (2010) Transformation of mobile forms of zinc in the soils of Arkhangelsk. Northern (Arctic) Federal University named after M.V.Lomonosov, 65-71. (in Russian).

Rozanov B.G. (2004) Soil morphology. Moscow: Academic project press.

Rudnick R.L. and Gao S. (2003). Composition of the Continental Crust. In: Rudnick, R.L. (Ed.), The Crust. Treatise on Geochemistry. Oxford: Elsevier-Pergamon.

Puzachenko Y., Sandlersky R. and Sankovski A. (2013). Methods of evaluating thermodynamic properties of landscape cover using multispectral reflected radiation measurements by the landsat satellite. Entropy, 15, 3970-3982, DOI: 10.3390/e15093970.

Samonova O. A., Kasimov N.S. and Aseeva E.N. (2011). Mobile forms of metals in the soils of erosional forms in the South-Eastern part of the Smolensk-Moscow Upland. Vestnik Moskovskogo Universiteta, 5(6), 67-75

Semenkov I. and Koroleva T. (2020) Heavy metals content in soils of Western Siberia in relation to international soil quality standards. Geoderma Regional, 21, e00283.

Semenkov I., Krupskaya V. and Klink G. (2019). Data on the concentration of fractions and the total content of chemical elements in catenae within a small catchment area in the Trans Urals, Russia. Data in Brief, 25, 104224, DOI: 10.1016/j.dib.2019.104224.

Semenkov I.N., Kasimov N.S. and Terskaya E.V. (2019). Lateral differentiation of metal fractions in loamy soil catenas of the central part of Western Siberia Plain. Vestnik Moskovskogo Universiteta, 5(3), 25-37.

Semenkov I.N., Kasimov N.S. and Terskaya E. V. (2016). Lateral distribution of metal forms in tundra, taiga and forest steppe catenae of the east European plain. Vestnik Moskovskogo Universiteta, 5(6), 87-95.

Shao S., Liu H., Tai X., Zheng F., Li J. and Li Y. (2020). Speciation and migration of heavy metals in sediment cores of urban wetland: bioavailability and risks. Environmental Science and Pollution Research, 27(19), 23914-23925, DOI: 10.1007/s11356-020-08719-y.

Sokolova T.A., Tolpeshta I.I. and Maksimova Y.G. (2014). Al, Fe, and Si compounds in Tamm and Mehra-Jackson extracts from mucky-peaty-podzolic gley soil: Contents, reserves, and profile and particle-size distributions. Eurasian Soil Science, 47(5), 392-399, DOI: 10.1134/S1064229314050214.

Sosorova S.B., Gyninova A.B., Merkusheva M.G., Ubugunov L.L. and Boloneva L.N. (2012). The content of microelements and iron in soils and plants in the basin of Lake Kotokel' in Western Transbaikalia. Eurasian Soil Science, 45(4), 376-385, DOI: 10.1134/S1064229312040138.

Sungur A., Kavdir Y., Özcan H., İlay R., Soylak M. (2021). Geochemical fractions of trace metals in surface and core sections of aggregates in agricultural soils. Catena, 197, 104995, DOI: 10.1016/j.catena.2020.104995.

Thompson A., Chadwick O.A., Rancourt D.G. and Chorover J. (2006). Iron-oxide crystallinity increases during soil redox oscillations. Geochimica et Cosmochimica Acta, 70(7), 1710-1727, DOI: 10.1016/j.gca.2005.12.005.

Tolpeshta I.I. and Sokolova T.A. (2010). Mobile aluminum compounds in soils of the southern taiga (soils of the central forest reserve as an example). Eurasian Soil Science, 43(8), 893-904, DOI: 10.1134/S1064229310080065.

Urusevskaya I. (1990). Soil catenas in the non-chernozem zone of the USSR. Environmental Science. Pochvovedenie, 9, 12-27.

Violante A. (2013). Elucidating Mechanisms of Competitive Sorption at the Mineral/Water Interface. Advances in Agronomy, 118, 111-176, DOI: 10.1016/B978-0-12-405942-9.00003-7.

Vodyanitskii Y.N. (2010). Iron hydroxides in soils: A review of publications. Eurasian Soil Science, 43(11), 1244-1254, DOI: 10.1134/S1064229310110074.

Yutong Z., Qing X. and Shenggao L. (2016). Chemical fraction, leachability, and bioaccessibility of heavy metals in contaminated soils, Northeast China. Environmental Science and Pollution Research, 23(23), 24107-24114, DOI: 10.1007/s11356-016-7598-9.

APPENDICES

Table A.1. Morphological properties of the studied soils

Position	Photos of soil pits	Soils and horizons (Barham et al., 2006; IUSS Working Group WRB, 2014)		Coordinates of soil pits	Plant dominants		
					Trees	Shrubs	Herbs and mosses
Summit		Endocalcaric Albic Neocambic Stagnic Glossic Retisols (Geoabruptic, Chromic, Loamic)	Oi–Oe–Oa–OAh–E–BE–2Btk–2BClk	N56°27′48.7″ E32°57′45″	*Picea abies, Tilia cordata, Acer platanoides, Ulmus glabra*	*Corylus avellana*	*Stellaria holostea, Anemone nemorosa, Lamium galeobdolon, Oxalis acetosella, Pteridium aquilinum, Aegopodium podagraria*
Backslope		Endocalcaric Albic Neocambic Stagnic Glossic Retisols (Geoabruptic, Lamellic, Loamic, Ochric)	Oi–Oe–Oa–OAh–Ah–AhE–Escl–BEscl–Bescl–2Btsc–2CBwsc	N56°27′47.5″ E32°56′15.4″	*Picea abies, Tilia cordata, Acer platanoides*	*Corylus avellana, Sorbus aucuparia, Lonicera xylosteum*	*Hepatica nobilis, Galium odoratum, Pteridium aquilinum, Lamium galeobdolon, Asarum europaeum, Equisetum sylvaticum, Pulmonaria obscúra, Anemone nemorosa, Stellaria holostea, Oxalis acetosella*
Footslope	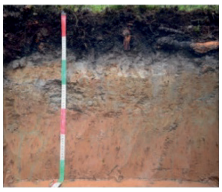	Endocalcaric Glossic Albic Gleyic Histic Stagnosols (Geoabruptic, Loamic)	Oi–Oe–Ha–Ah–AhEl–Etosc–Btg	N56°27′47.1″ E32°56′19.8″	*Picea abies, Tilia cordata, Acer platanoides*	*Sorbus aucuparia*	*Vaccinium myrtillus*
Toeslope		Endocalcaric Glossic Albic Histic Stagnosols (Geoabruptic, Loamic)	Oi–Oe–Ha–HaE–Eoscl–Eoscl–BEtoscl–Bg–2Crk	N56°27′48.0″ E32°56′21.1″	*Picea abies, Tilia cordata, Acer platanoides, Salix caprea*	*Sorbus aucuparia*	*Pteridium aquilinum, Oxalis acetosella, Vaccinium myrtillus, Sphagnum*

Table A2. Physicochemical properties of Retisols studied

			Granulometric fractions (μm)									
Position	Horizons	Sampling depth, cm	500–1000	250–500	50–250	10–50	5–10	1–5	<1	pH	$CaCO_3$,%	TOC, %
Summit	OAh	2-6	0	0	15	58	13	13	2	4.8	na	31
	E	20-30	0	0	19	59	8	11	2	4.9	na	0.3
	BE	45-55	0	0	18	60	6	11	5	4.6	na	0.32
	2Btk	70-90	0	0.2	17	38	13	25	6	5.1	na	0.12
	2BCk	110-130	0	0	14	36	15	27	8	6.7	na	0.10
	2BClk	150-170	0	0	18	35	14	25	8	7.5	7.8	0.10
	2Clk	200	0	0.3	16	36	14	25	9	7.5	10.4	0.17
Backslope	OAh	2,5-4	0	0	5	66	13	14	3	5.0	na	18
	Ah	5-10	0	0	4	67	13	14	3	4.5	na	7.19
	AhE	12-18	0	0	1	61	16	18	4	4.0	na	3.60
	E	30-40	0	0	10	60	10	15	4	4.5	na	0.55
	EB	52-62	0	0	18	59	7	12	4	4.7	na	1.62
	EB	75-85	0	0	28	56	5	8	3	5.4	na	0.19
	2Btl	104-114	0	0	19	37	12	25	7	5.5	na	0.14
	2BCl	140-150	0	0.1	24	34	12	23	7	6.5	na	0.20
	2Cl	200	0	0.03	19	36	13	24	7	7.3	4.8	0.13
Footslope	Ah	9-14	na	na	na	na	na	na	na	4.8	na	28
	AhE	17-20	0	2.4	36	45	7	8	2	3.7	na	5.74
	E	25-35	0	0	16	60	9	12	3	4.4	na	1.19
	Btg	48-58	0	0	33	49	5	10	3	6.1	na	0.14
	BCl	100	0	0	22	63	5	7	3	6.4	na	0.04
Toeslope	Ha	0-8	na	na	na	na	na	na	na	4.0	na	3.41
	HaE	8-12	0	1.9	34	48	7	8	2	3.8	na	4.65
	E	17-23	0	0	15	61	10	12	3	3.9	na	1.10
	E	28-35	0	0	12	62	9	13	3	4.7	na	0.48
	BEl	39-45	0	0	14	60	8	13	4	4.9	na	0.25
	2Bl	60-70	0	0	23	59	6	9	3	5.3	na	0.07
	2BClk	80-90	0	0	17	61	7	12	3	5.6	na	0.11
	2Clk	110-120	0	0	21	36	13	25	5	5.7	na	0.15
	2Clk	200	0	0.2	18	34	14	27	7	7.5	3.0	0.15

Table A3. Content of HMMs in the Retisols studied

Position	Horizons	Sampling depth, cm	As	Bi	Cd	Co	Cr	Cu	Fe	Mn	Mo	Ni	Pb	Sb	U	Zn
Total content																
Summit	OAh	2-6	1.4	0.37	0.69	3.4	20	12	4700	600	0.80	9	34	1.10	1.3	91
	E	20-30	3.8	0.13	0.12	9.2	29	10	13800	1100	0.56	11	18	0.20	2.4	43
	BE	45-55	3.1	0.17	0.11	12.4	38	22	15000	1000	0.40	17	17	0.26	2.6	50
	2Btk	70-90	2.3	0.18	0.16	10.2	47	21	16200	800	0.37	22	16	0.64	1.8	66
	2BCk	110-130	3.7	0.18	0.24	9.1	47	22	15900	600	0.43	26	15	0.34	1.8	67
	2BClk	150-170	3.0	0.15	0.21	10.1	41	18	14100	800	0.49	24	14	0.31	1.7	59
	2Clk	200	2.6	0.15	0.18	7.5	41	17	12900	500	0.41	20	13	0.27	1.7	58
Backslope	OAh	2,5-4	1.7	0.28	0.98	3.8	19	12	3800	1400	0.58	23	35	0.69	1.3	112
	Ah	5-10	2.5	0.42	0.54	5.1	29	7	8300	900	0.66	9	36	0.62	2.0	70
	AhE	12-18	3.0	0.24	0.26	5.1	29	7	9600	300	0.55	8	25	0.41	2.1	45
	E	30-40	3.3	0.13	0.09	7.3	37	7	10800	700	0.33	10	14	0.19	2.2	39
	EB	52-62	3.0	0.15	0.11	7.3	38	17	12900	600	0.26	15	14	0.24	2.4	47
	El	75-85	1.5	0.11	0.10	5.6	28	14	9700	500	0.09	12	13	0.19	2.0	36
	2Btl	104-114	3.1	0.19	0.16	10.8	52	23	17500	800	0.52	29	17	0.38	1.6	78
	2BCl	140-150	2.6	0.15	0.20	9.2	40	19	14400	700	0.39	21	19	0.26	1.5	63
	2Cl	200	1.8	0.14	0.20	8.3	44	18	13200	700	0.45	21	14	0.27	1.8	73
Footslope	Ah	9-14	3.5	0.26	0.64	3.1	17	10	8700	100	0.61	7	33	0.66	1.2	29
	AhE	17-20	1.0	0.13	0.14	2.0	27	6	3900	200	0.46	6	16	0.27	2.3	25
	E	25-35	0.7	0.11	0.08	2.8	28	6	6300	300	0.25	7	13	0.20	2.4	25
	Btg	48-58	2.7	0.12	0.13	8.2	33	16	11800	900	0.27	17	14	0.23	1.9	41
	BCl	100	2.5	0.11	0.12	6.3	28	13	10100	600	0.18	12	13	0.19	1.8	36
Toeslope	Ha	0-8	2.1	0.11	0.09	5.9	32	13	10600	400	0.27	14	13	0.23	1.3	39
	HaE	8-12	1.2	0.14	0.14	1.8	26	7	4400	200	0.36	5	16	0.30	2.3	29
	E	17-23	0.6	0.11	0.08	2.0	27	4	4500	200	0.21	5	13	0.18	2.3	24
	E	28-35	1.7	0.12	0.09	3.5	30	10	7300	300	0.24	8	14	0.22	2.4	36
	BEl	39-45	3.8	0.16	0.09	13.4	44	16	17700	1200	0.44	18	16	0.28	2.7	43
	2Bl	60-70	2.6	0.14	0.23	10.4	35	20	12900	500	0.32	21	15	0.26	2.4	46
	2BClk	80-90	2.9	0.13	0.12	9.0	37	18	13300	800	0.31	19	14	0.26	1.6	50
	2Clk	110-120	0.8	0.20	0.61	1.6	15	10	2600	100	0.43	6	27	0.64	0.6	38
	2Clk	200	2.9	0.15	0.19	10.6	46	20	15700	700	0.51	24	15	0.31	1.8	55
Exchangeable compounds (F1)																
Summit	OAh	2-6	0.05	0.019	0.20	0.27	0.01	0.17	8	577	0.042	0.50	3.40	<0.001	0.02	9.7
	E	20-30	<0.01	0.004	0.02	0.20	0.45	0.19	284	27	<0.002	0.27	0.41	<0.001	0.08	1.15
	BE	45-55	<0.01	0.005	0.01	0.14	0.17	0.75	262	17	<0.002	0.27	0.65	<0.001	0.19	0.75
	2Bwk	70-90	<0.01	0.004	0.01	0.03	0.06	0.40	54	12	<0.002	0.32	0.65	<0.001	0.12	0.65
	2BCk	110-130	<0.01	0.005	0.04	0.01	0.06	0.19	9	8	<0.002	0.75	0.31	<0.001	0.10	0.32

Summit	2BClk	150-170	<0.01	0.003	0.09	0.25	0.19	0.41	72	137	<0.002	0.85	0.65	<0.001	0.17	0.95
	2Clk	200	<0.01	0.003	0.10	1.00	0.25	0.60	90	212	<0.002	1.15	1.30	<0.001	0.14	2.95
Backslope	OAh	2,5-4	<0.01	0.015	0.53	0.15	0.01	0.29	11	1141	<0.002	0.31	2.50	<0.001	0.02	27.5
	Ah	5-10	0.07	0.019	0.26	0.33	0.60	0.18	266	787	<0.002	0.43	2.85	<0.001	0.04	14.0
	AhE	12-18	0.05	0.016	0.10	0.16	0.45	0.14	577	113	<0.002	0.37	2.00	<0.001	0.06	3.25
	E	30-40	<0.01	0.004	0.02	0.16	0.50	0.15	427	35	<0.002	0.17	0.40	<0.001	0.11	1.48
	EB	52-62	<0.01	0.005	0.01	0.09	0.41	0.50	188	13	<0.002	0.32	0.60	<0.001	0.14	0.50
	El	75-85	<0.01	0.003	0.01	0.02	0.16	0.45	111	5	<0.002	0.25	0.37	<0.001	0.11	0.60
	2Btl	104-114	<0.01	0.005	0.01	0.01	0.05	0.32	32	6	<0.002	1.00	0.60	<0.001	0.06	0.25
	2BCl	140-150	<0.01	0.004	0.02	0.01	0.06	0.26	16	8	<0.002	0.42	0.70	<0.001	0.09	0.47
	2Cl	200	<0.01	0.003	0.07	0.13	0.11	0.36	61	75	<0.002	0.50	0.65	<0.001	0.12	1.00
Footslope	Ah	9-14	0.21	0.029	0.34	0.64	0.62	0.31	1114	15	<0.002	0.64	6.10	<0.001	0.29	3.60
	AhE	17-20	<0.01	0.008	0.06	0.13	0.35	0.16	58	3	<0.002	0.16	1.95	<0.001	0.21	1.90
	E	25-35	<0.01	0.005	0.01	0.04	0.50	0.11	201	2	<0.002	0.11	0.80	<0.001	0.17	1.15
	Bwg	48-58	<0.01	0.003	0.02	0.02	0.13	0.60	124	19	<0.002	0.50	0.25	<0.001	0.11	0.80
	BCl	100	<0.01	0.004	0.01	0.01	0.05	0.24	7	8	<0.002	0.21	0.27	<0.001	0.08	0.60
Toeslope	Ha	0-8	<0.01	0.043	0.35	0.30	1.84	0.37	36	20	0.147	0.37	7.01	<0.001	0.07	9.35
	HaE	8-12	<0.01	0.018	0.07	0.11	0.30	0.11	129	4	0.036	0.24	3.46	<0.001	0.17	2.11
	E	17-23	<0.01	0.005	0.01	0.04	0.48	0.15	236	2	0.012	0.11	1.05	<0.001	0.16	0.55
	E	28-35	<0.01	0.004	0.00	0.12	0.42	0.12	270	8	<0.002	0.21	0.65	<0.001	0.16	1.15
	BEl	39-45	<0.01	0.004	0.01	0.10	0.32	0.47	383	31	<0.002	0.50	0.47	<0.001	0.31	0.75
	2Bl	60-70	<0.01	0.002	0.02	0.02	0.10	0.48	87	13	<0.002	0.75	0.25	<0.001	0.10	0.85
	2BClk	80-90	<0.01	0.004	0.01	0.02	0.15	0.40	74	9	<0.002	0.70	0.43	<0.001	0.08	0.60
	2Clk	110-120	<0.01	0.003	0.01	0.02	0.08	0.25	25	6	<0.002	0.44	0.55	<0.001	0.06	0.41
	2Clk	200	<0.01	0.002	0.05	0.07	0.05	0.20	26	40	<0.002	0.32	0.40	<0.001	0.08	0.49
Compounds bound with complexes (F2)															
Summit	OAh	2-6	0.16	0.179	0.315	1.21	0.92	4.03	1511	820	0.008	2.74	21.4	0.011	<0.0001	30
	E	20-30	0.04	0.003	0.003	0.74	0.19	0.24	342	49	0.011	0.09	1.2	0.003	<0.0001	0.3
	BE	45-55	0.11	0.008	0.011	3.75	0.19	0.65	772	213	0.0175	0.20	1.8	<0.0005	<0.0001	0.2
	2Btk	70-90	0.13	0.006	0.041	3.71	0.16	0.60	445	301	0.0305	1.15	2.8	<0.0005	<0.0001	0.7
	2BCk	110-130	0.14	0.008	0.123	3.38	0.20	1.06	254	399	0.0315	6.02	3.0	<0.0005	<0.0001	1.3
	2BClk	150-170	0.06	0.001	0.010	3.44	0.20	0.84	86	321	0.008	5.27	1.1	<0.0005	<0.0001	0.6
	2Clk	200	0.06	0.001	0.002	0.94	0.20	0.80	72	36	<0.001	2.22	0.9	<0.0005	<0.0001	0.7
Backslope	OAh	2,5-4	0.22	0.142	0.420	2.03	1.28	4.01	1249	2583	0.031	2.13	26.5	0.007	<0.0001	43
	Ah	5-10	0.14	0.115	0.130	1.71	0.34	1.53	2286	1005	0.05	1.04	20.8	0.011	<0.0001	9.9
	AhE	12-18	0.10	0.038	0.045	0.63	0.39	0.81	1549	232	0.037	0.66	8.9	0.013	<0.0001	4.8
	E	30-40	0.03	0.006	0.002	0.63	0.14	0.33	273	48	0.0165	0.05	0.9	0.004	<0.0001	0.2
	EB	52-62	0.08	0.003	0.003	1.05	<0.0011	0.35	314	73	0.0175	0.02	0.8	<0.0005	<0.0001	0.1
	El	75-85	0.10	0.005	0.014	1.27	0.24	0.36	370	124	0.0195	0.68	1.1	<0.0005	<0.0001	0.2

	2Btl	104-114	0.06	0.003	0.050	3.73	0.19	0.84	239	323	0.031	2.82	3.3	<0.0005	<0.0001	0.3
Backslope	2BCl	140-150	0.12	0.008	0.107	3.83	0.19	1.14	250	407	0.055	4.51	6.9	0.008	<0.0001	1.5
	2Cl	200	0.06	0.003	0.040	3.11	0.19	0.80	128	291	0.0165	3.92	2.0	<0.0005	<0.0001	1.1
	Ah	9-14	1.41	0.145	0.320	0.99	1.01	4.49	10374	9.4	0.044	2.85	23.7	0.030	<0.0001	7.5
	AhE	17-20	0.08	0.014	<0.0002	<0.0001	0.54	0.69	244	0.3	0.0135	0.36	2.5	<0.0005	<0.0001	1.4
Footslope	E	25-35	0.09	0.002	0.005	<0.0001	0.79	0.22	270	0.01	0.0013	0.04	1.2	<0.0005	<0.0001	0.2
	Btg	48-58	0.12	0.008	0.045	3.17	0.12	1.30	426	404	0.022	3.12	1.8	<0.0005	<0.0001	1.0
	BCl	100	0.16	0.006	0.045	2.13	<0.001	0.62	146	278	0.0185	1.91	2.2	<0.0005	<0.0001	1.5
	Ha	0-8	0.30	0.125	0.229	0.39	<0.001	5.23	3490	8.0	<0.001	2.12	19.1	<0.0005	<0.0001	10
	HaE	8-12	0.14	0.014	<0.0002	<0.0001	0.34	0.69	874	0.01	<0.001	0.28	2.4	<0.0005	<0.0001	0.1
	E	17-23	0.10	0.003	0.005	<0.0001	0.66	0.23	343	0.3	<0.001	0.07	1.0	<0.0005	<0.0001	0.5
	E	28-35	0.07	0.005	0.004	0.08	0.77	0.36	383	2.6	0.0085	<0.003	0.9	<0.0005	<0.0001	0.7
Toeslope	BEl	39-45	0.06	0.006	0.007	3.64	0.27	2.39	561	232	0.01	0.27	1.7	<0.0005	<0.0001	0.3
	2Bl	60-70	0.09	0.006	0.119	3.67	0.38	1.98	469	672	0.042	5.27	2.0	<0.0005	<0.0001	0.8
	2BClk	80-90	0.08	0.005	0.048	3.42	0.22	1.01	357	353	0.0245	2.47	2.5	<0.0005	<0.0001	0.6
	2Clk	110-120	0.06	0.003	0.023	2.07	0.13	0.61	149	158	0.0215	1.14	1.9	<0.0005	<0.0001	0.5
	2Clk	200	0.06	0.003	0.065	4.12	0.19	0.71	110	328	0.008	4.30	2.2	<0.0005	<0.0001	0.9
Compounds bound with Fe and Mn (hydr)oxides (F3)															
	OAh	2-6	0.26	<0.0001	0.455	1.2	0.7	3.8	904	893	<0.002	3.0	25.8	0.019	0.048	43.0
	E	20-30	0.26	0.011	0.031	2.3	2.9	0.8	5316	219	<0.002	0.4	5.5	<0.001	0.089	3.9
	BE	45-55	0.20	0.020	0.019	1.8	2.7	2.6	3815	127	<0.002	1.1	4.7	<0.001	0.209	5.5
Summit	2Btk	70-90	0.02	0.011	0.024	0.9	2.7	2.3	2403	56	<0.002	1.2	3.4	<0.001	0.134	8.3
	2BCk	110-130	0.04	0.008	0.073	1.6	3.7	2.4	1993	148	<0.002	5.9	2.1	<0.001	0.189	11.2
	2BClk	150-170	0.12	0.005	0.030	1.7	1.9	1.7	1025	117	<0.002	4.1	1.2	<0.001	0.224	6.7
	2Clk	200	0.05	0.006	0.015	0.8	1.2	1.6	744	45	<0.002	2.2	2.6	<0.001	0.224	5.3
	OAh	2,5-4	0.24	<0.0001	0.390	1.5	0.0	3.9	707	1787	<0.002	2.1	24.0	<0.001	0.020	52.0
	Ah	5-10	0.40	0.002	0.200	1.4	0.5	1.9	2259	781	<0.002	1.1	22.9	0.026	0.038	20.3
	AhE	12-18	0.28	0.003	0.045	0.8	1.2	1.1	2632	202	<0.002	0.7	10.9	0.025	0.044	4.8
	E	30-40	0.10	0.011	0.018	1.8	2.1	0.8	3897	173	<0.002	0.4	3.8	<0.001	0.088	3.8
Summit	EB	52-62	0.09	0.011	0.014	1.0	2.9	2.4	2972	65	<0.002	1.1	2.5	<0.001	0.129	5.5
	El	75-85	0.09	0.013	0.020	0.7	2.8	2.3	2364	51	<0.002	1.3	2.3	<0.001	0.114	4.6
	2Btl	104-114	<0.002	0.004	0.028	1.1	2.9	2.2	1711	64	<0.002	2.4	3.7	<0.001	0.099	6.8
	2BCl	140-150	<0.002	0.007	0.044	1.7	2.8	2.2	1950	120	<0.002	3.6	4.3	<0.001	0.124	9.9
	2Cl	200	0.09	0.007	0.045	1.7	1.9	1.8	1421	128	<0.002	3.3	2.2	<0.001	0.204	7.2
	Ah	9-14	0.37	<0.0001	<0.0001	0.0	0.3	2.1	2394	0	<0.002	0.9	7.4	<0.001	<0.0001	1.4
	AhE	17-20	0.12	<0.0001	0.036	0.1	1.0	1.0	325	6	<0.002	0.6	4.6	<0.001	0.084	1.7
Footslope	E	25-35	0.10	0.001	0.004	0.1	1.4	0.3	558	8	<0.002	0.2	1.7	<0.001	0.094	1.5
	Btg	48-58	0.16	0.009	0.038	2.3	3.5	3.7	3589	197	<0.002	3.8	2.6	<0.001	0.114	7.1
	BCl	100	0.05	0.007	0.028	1.3	3.4	2.1	1728	106	<0.002	2.6	1.7	<0.001	0.134	8.2

Toeslope	Ha	0-8	0.13	<0.0001	0.149	0.2	0.0	4.3	1257	3	<0.002	1.4	13.0	<0.001	0.006	10.2
	HaE	8-12	0.17	<0.0001	0.025	0.1	0.8	1.1	592	5	<0.002	0.4	4.1	<0.001	0.056	2.1
	E	17-23	0.15	0.000	0.010	0.1	1.1	0.3	665	9	<0.002	0.1	1.6	<0.001	0.074	0.9
	E	28-35	0.20	0.008	0.013	0.7	1.7	0.7	2182	50	<0.002	0.3	2.8	<0.001	0.144	2.3
	BEl	39-45	0.07	0.011	0.017	2.6	3.6	2.4	4988	184	<0.002	1.2	4.5	<0.001	0.204	5.1
	2Bl	60-70	0.14	0.009	0.047	1.0	3.0	3.1	3010	97	<0.002	2.7	2.5	<0.001	0.139	7.1
	2BClk	80-90	0.07	0.008	0.022	1.1	3.6	2.7	2705	75	<0.002	2.3	3.2	<0.001	0.109	7.4
	2Clk	110-120	<0.002	0.004	0.015	0.8	2.4	1.9	1517	37	<0.002	1.6	2.3	<0.001	0.054	4.9
	2Clk	200	0.02	0.013	0.032	1.1	1.8	1.7	1229	84	0.052	3.1	1.7	<0.001	0.189	6.1

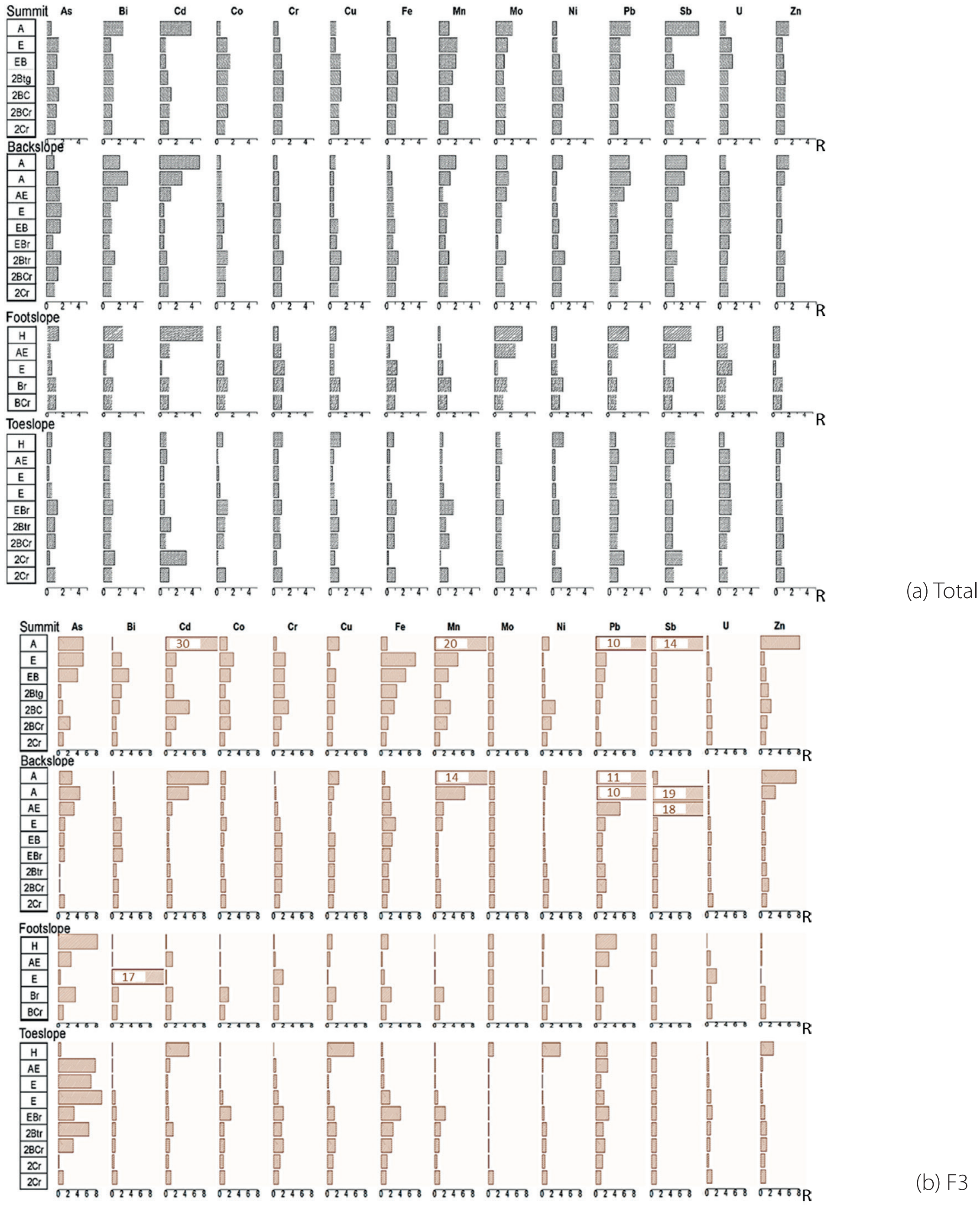

Fig. B.1. The vertical differentiation (R) of the total content (a) and the F3 fraction (b) of the HMMs of the soils of the catena

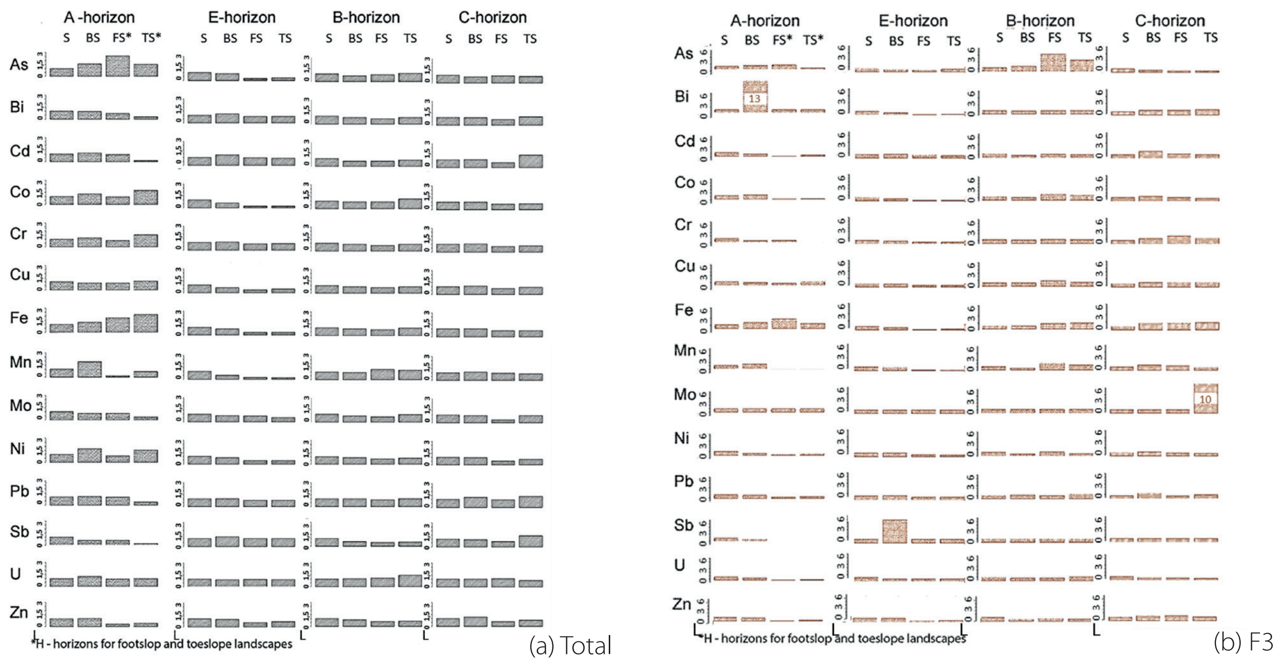

Fig. B.2. The spatial differentiation (L) of total content (a) and the F3 (b) fraction of the HMMs of the soils of the catena

Table A.4. Vertical differentiation of the HMMs in the Retisols studied

HMMs fractions	Accumulative	Accumulative-eluvial-illuvial	Eluvial	Subsoil-accumulative	Undifferentiated
SUMMIT. Endocalcaric Albic Neocambic Stagnic Glossic Retisols					
Total	**Cd Bi***	**Sb Zn**	**As Co Cu Fe** U	Ni	
F1	**As Cd Mn Mo Pb Zn**	Bi	**Cr Cu Fe** U	Co **Ni**	Sb
F2	**Cr Cu Zn** Fe Mo **Pb** Sb	As Bi Cd Mn	Co	Ni	U
F3	**Pb Sb**	**As Cd** Co **Cu** Mn Ni **Zn**	**Cr Bi**	Fe	Mo U
BACKSLOPE. Endocalcaric Albic Neocambic Stagnic Glossic Retisols					
Total	**Cd**	Bi Mn Mo Pb **Sb Zn**	As **Co Cr Cu Fe** Ni	-	U
F1	**As Bi Cd Mn Zn Cr Pb**	Co **Cu**	**Fe** U	**Ni**	Mo Sb
F2	**Bi Cd Cr Cu** Mn **Zn As Pb**	Mo **Ni** Sb	Co Fe	-	**U**
F3	Cd Mn Zn As **Pb Sb**	**Cu**	**Bi Fe Cr**	-	Co **Mo** Ni U
FOOTSLOPE. Endocalcaric Glossic Albic Gleyic Histic Stagnosols					
Total	As **Bi Cd**	Mo Pb **Sb**	**Co Cr** Fe Mn Ni U	-	Cu
F1	**As Pb Cr** Fe **Bi**	Cd **Co** Mn **Ni** Zn	**Cu**	U	**Mo Sb**
F2	**As Cd** Cr Mo **Pb** Sb **Zn Bi**	Cr Cu Fe **Ni**	-	Co **Mn**	U
F3	-	**As Cd Cu** Fe **Pb**	U	Bi Co Cr Mn Ni	**Mo** Sb Zn
TOESLOPE. Endocalcaric Glossic Albic Gleyic Histic Stagnosols					
Total	Ni	-	**As Co Cu Cr** Mn U	Pb Sb Bi Cd	Mo Zn
F1	**Cd** Co **Cr** U **Bi Mo Pb Zn**	**Cu Ni**	Cr	-	As Mn **Sb**
F2	**Cd Cr** Ni **Pb Zn**	As Bi Co Cu **Fe**	W	**Mn** Mo	Sb
F3	Ni	**Cd Cu Pb Zn**	As Co **Cr Fe** Mn	-	Bi **Mo** Sb **U**

Bold - elements, the type of distribution of which is preserved in the soils of two or more positions. Dash - elements with this type of distribution were not found.

Table A.5. Accumulation of elements at geochemical barriers and correlation with soil properties (in brackets)

HMMs fractions	Geochemical barriers			Carbonate ($CaCO_3$)	Don't accumulate on barriers
	Alkaline (pH)	Sorption (clay)	Biogeochemical (SOM)		
Total	$As_{0.32}$ $Co_{0.42}$ $Cr_{0.43}$ $\mathbf{Cu_{0.64}}$ $Fe_{0.55}$ $Mn_{0.23}$ $Ni_{0.68}$	$As_{0.32}$ $Co_{0.36}$ $Cr_{0.49}$ $\mathbf{Cu_{0.55}}$ $Fe_{0.51}$ $Ni_{0.54}$ $Zn_{0.22}$	$Pb_{0.38}$ $S\mathbf{b_{0.19}}$	-	Bi Cd *Mo* U
F1	$\mathbf{Cu_{0.44}}$ $Ni_{0.47}$	$\mathbf{Cu_{0.33}}$ $Ni_{0.32}$	$As_{0.32}$ $Bi_{0.59}$ $Cd_{0.39}$ $Co_{0.6}$ $Cr_{0.29}$ $Fe_{0.38}$ $Mn_{0.2}3$ $Pb_{0.63}$ $\mathbf{Sb_{0.26}}$ $Zn_{0.54}$	$Co_{0.62}$ $Ni_{0.56}$	U
F2	$Cd_{0.20}$ $Co_{0.50}$ $\mathbf{Cu_{0.41}}$	$Co_{0.32}$ $\mathbf{Cu_{0.24}}$	$As_{0.23}$ $Bi_{0.44}$ $Cr_{0.53}$ $Fe_{0.54}$ $\mathbf{Sb_{0.33}}$ $Zn_{0.31}$	-	Mn *Mo* Ni Pb
F3	$Cr_{0.40}$ $\mathbf{Cu_{0.34}}$ $U_{0.40}$ $Zn_{0.45}$	$Cr_{0.26}$ $\mathbf{Cu_{0.21}}$ $U_{0.35}$ $Zn_{0.4}$	$As_{0.30}$ $Mn_{0.20}$ $Pb_{0.20}$ $\mathbf{Sb_{0.37}}$	-	Bi Cd Co Fe Mo Ni

Numbers - values r with p value <0.05. Bold (italic) - elements that in all (three of four) forms accumulate at the same geochemical barrier.

ges.rgo.ru/jour/

ISSN 2542-1565 (Online)